Press Forming and Formability of Polypropylene, Dry Fabrics and Fabric-Reinforced Polypropylene

by

Chandra Kishore Reddy Emani

A dissertation submitted in partial fulfillment
of the requirements for the degree of
Doctor of Philosophy
(Mechanical Sciences and Engineering)
in the University of Michigan - Dearborn
2022

Doctoral Committee:

Professor Pankaj K Mallick, Chair
Assistant Professor Lei Chen
Associate Professor Jian Hu
Associate Professor German Reyes-Villanueva

Chandra Kishore Reddy Emani

emani@umich.edu

ORCID iD: 0000-0003-4504-6013

Dedication

This dissertation work is dedicated to all my family members.

Acknowledgements

I would like to express sincere gratitude to my advisor Dr. Pankaj Mallick for his unwavering patience, motivation, and support. Dr. Mallick's guidance and insights helped me greatly in pursuing research and in writing this dissertation. I have learnt a lot during my discussion with him and this work as it stand today is due to his endeavor and effort. I could not have asked for a better mentor for my doctoral studies, Thank you.

I would like to thank my doctoral committee: Dr. German Reyes-Villanueva, Dr. Jian Hu and Dr. Lei Chen for their valuable time and advice. Their insightful comments and questions pushed me to broaden my research perspectives. I would like to specially thank Dr. German Reyes-Villanueva for his help in extending the lab facilities required for my experimental work.

I thank my fellow colleagues Caroline Kella and Monish Urapakam Ramakrishnan for the fascinating discussions and fun we have had in the lab over the last four years.

I would like to thank all the staff members of Mechanical Engineering Department and technicians of MSEL lab at UM-Dearborn for their prompt assistance. Thank you, Rebekah Awood for your administrative support. Thanks to Shawn Simone and Matthew Brown for your kind cooperation in carrying out my experimental work.

Table of Contents

List of Tables

List of Figures

Abstract

With recent technological advancements, the need for reduced manufacturing costs and improved damage tolerance of composite structures, thermoplastic matrix composites are being increasingly considered for a variety of automotive and aerospace applications. Not only do they have low density, high strength, excellent fatigue durability and design flexibility, but also lower processing time, better damage tolerance and higher recyclability compared to thermoset matrix composites. Press forming is the leading manufacturing process for making fabric-reinforced thermoplastic composite parts since it is a fast, repeatable and cost-effective process.

The objective of the current research is to develop process simulation models to study press forming and predict press formability of polypropylene, glass fabric, and glass fabric-reinforced polypropylene. Polypropylene is selected as the matrix since it is a widely used thermoplastic polymer for automotive applications. Plain glass fabrics are selected as the reinforcement based on their low cost, high strength and good drapeability on mold surfaces.

Press forming of polypropylene involves a warm deep drawing process which is different from thermoforming processes commonly used for thermoplastics. The forming temperature, which is much lower than the usual thermoforming temperature, and forming speed are selected to make the production rate high. A modified temperature and strain-rate dependent material model was developed to conduct the finite element simulations. It is shown that the deep drawability of polypropylene cups is influenced by the blank holder force, initial blank temperature, die corner radius and forming speed. The failure modes that limited the formability of polypropylene are

flange wrinkling and tearing of the cup wall either at the top corner radius or near the bottom corner radius.

To simulate fabric deformation behavior for preforming fabric shapes, a superimposed finite element model of membrane and shell elements was used with the in-plane shear behavior governed by the membrane elements and the out-of-plane bending behavior governed by the shell elements. Using this approach, a study on the effect of the shear-tension coupling on the deformation of an E-glass fabric shows that with increasing applied tensile loads, the fabric exhibits a stiffer shear response. The limits of the press forming operation are determined by the ability to form the shape and retain it without defects such as fiber distortion, wrinkling, and tearing of the fabric. A safe window in which the forming limit of the fabrics is determined as a function of blank holder force and forming depth is presented. The punch corner radius, which controls the shape of the fabric during draping, plays an important role on the forming limit of the fabric.

A comparison of the experimental and simulated results of the bias-extension tests and press forming shows that the superimposed approach can reasonably accurately predict the outer shape profile and the force required for fabric deformation. A numerical method to simulate the press forming of woven fabric-reinforced polypropylene is presented. It uses the concept of a superimposed approach with the fabric layers superimposed on the matrix layers. The failure occurs first in the polypropylene layer at the location of the maximum shear deformation in the fabric layer, which is along the diagonal at the die entry radius. Fabric layer exhibits buckling tendency after failure is initiated in the polypropylene layer. Draw depths of the fabric-reinforced polypropylene do not vary much on either the forming temperature or the punch corner radius.

Chapter 1 Introduction

1.1 Background

Fiber reinforced polymer composites are being increasingly used in automotive and aerospace structures owing to their low density and high strength and modulus-to-weight ratios characteristics that are important to meet the demand for reducing fuel consumption and carbon footprint. Corrosion resistance, excellent fatigue durability, vibration damping, and design flexibility are some of the other reasons for their increasing use [1]. Most recent aerospace examples include the Boeing 787 which is 80% composite by volume, 50% by weight [2] and the Airbus A350 which constitutes 53% by weight of composites used in fuselage, wings, tail, doors, and interior [3]. Among the automotive examples is the BMW 7 series vehicles which are 130 kg lighter than their predecessors due to the use of carbon fiber reinforced polymers in their body structures and panels [4]. Figure 1.1(a) illustrates the percentage composition of weight distribution for different materials used in Boeing 787 and Figure 1.1(b) provides an overview of the types of composite materials used in BMW 7 series vehicles.

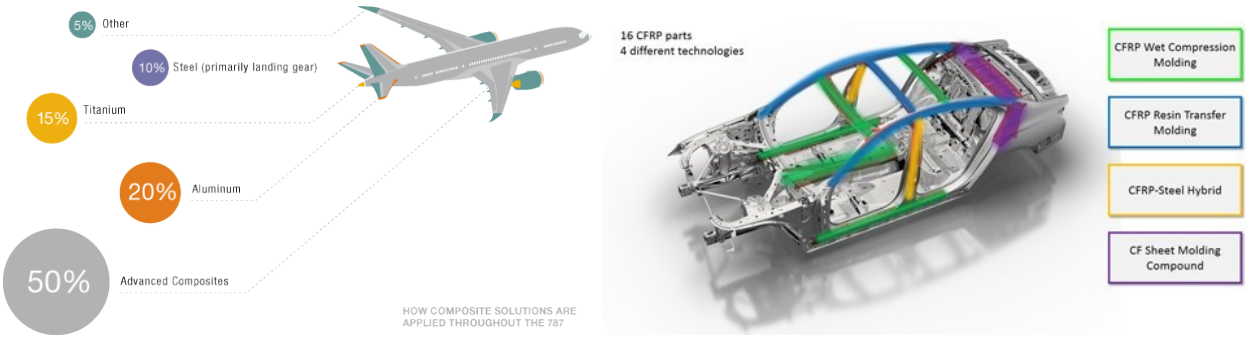

Figure 1.1: (a) Boeing 787 material weight distribution [2], (b) BMW 7series using composite materials [4].

Fiber reinforced polymers also called polymer matrix composites (PMCs), consist of fibers of high strength and modulus embedded in a polymer matrix with distinct interfaces between them so that both fibers and matrix retain their physical and chemical identities and produce a combination of properties that cannot be achieved with either of the constituents acting alone. In general, fibers are the principal load carrying members, while the surrounding matrix keeps them in the desired locations and contributes to load transfer between the fibers [1]. Some of the commonly used fibers are glass, carbon, and aramid. For matrix materials, there is a wide range of thermosets such as epoxies, polyesters, phenolics and thermoplastics, such as polypropylene, polyamide 6, polyetherimide, polyphenylene sulfide and polyether ether ketone. The fibers can be continuous or discontinuous in length. Continuous fibers provide higher modulus and strength than discontinuous fibers and are therefore selected for many structural applications.

However, while the modulus and strength of unidirectional continuous fiber composites are very high in the fiber direction, they are much lower in the normal to the fiber direction. In aerospace applications, laminated constructions of multiple layers of unidirectional continuous fibers are used. The fiber orientations in these layers are varied depending on the design requirements of the components being considered. For many automotive structural components, biaxially-oriented continuous fibers, such as woven fabrics, are preferred. Woven fabrics are constructed of interlaced fiber yarns oriented in two mutually perpendicular directions (Figure 1.2), called warp and weft directions, and provide a more balanced modulus and strength in these two directions. They can be draped on mold surfaces with complex geometries much easier than unidirectional continuous fibers.

Matrix material used in PMCs is either a thermosetting or a thermoplastic polymer. Thermosets are a group of polymers that are obtained by curing a low-viscosity liquid pre-polymer

or resin to an irreversibly hardened solid material. Curing is induced by mixing the pre-polymer with a catalyst and by applying heat. Curing is a chemical reaction that creates cross-links between polymer molecules. Fibers are embedded in the thermosetting polymer before the start of the curing reaction when the pre-polymer is in a very low viscosity liquid state. Thermoplastic polymers, on the other hand, do not require curing. They are formed into shape either by melting (as in injection molding) or by heat-softening (as in thermoforming) and then cooling to room temperature. Even in the liquid state, the viscosity of the thermoplastic polymers is very high so that embedding fibers in thermoplastic polymers is considerably more difficult than in thermosetting polymers.

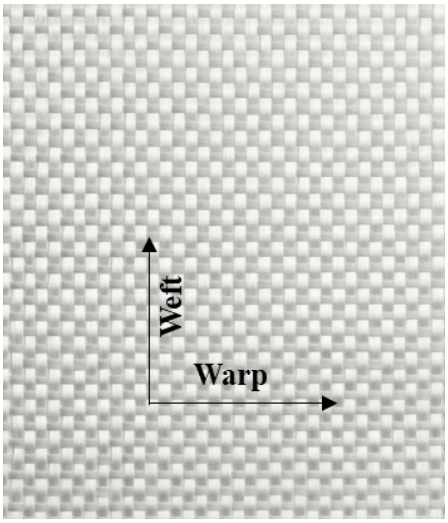

Figure 1.2: Photograph of a plain E-glass fabric with the warp and weft directions shown.

Traditionally, thermosetting polymers have been used as a matrix material in polymer matrix composites. However, in recent years, thermoplastics are gaining more importance which can be attributed to their many advantages over thermosetting polymers. In general, the key benefits of thermoplastic matrix composites over thermoset matrix composites are [5]:

i. Enhanced mechanical properties, in terms of impact resistance and fracture toughness.

ii. Unlimited shelf life of raw materials.

iii. Environmentally benign (since there are no exothermic reactions, toxic fume, or solvent emissions).

iv. Faster cycle times, and therefore, higher production rate.

v. Ability to be reprocessed and recycled.

vi. Ability to mold large integrated complex parts in one operation, which leads to lower manufacturing costs.

vii. Ease of joining and repair by welding, solvent bonding, etc.

Because of the above advantages, continuous fiber thermoplastic matrix composites, particularly woven fabrics, can be a very attractive material for structural automotive applications. However, unlike discontinuous fiber thermoplastic matrix composites, they have not yet found widespread application in the automotive industry principally for two reasons: (1) lack of a low-cost process for making continuous fiber reinforced thermoplastic sheets and (2) lack of manufacturing processes that are amenable to mass production.

Injection molding is the most common manufacturing process for making thermoplastic matrix composite parts, however, it can only be used with short or discontinuous fibers, typically 1-2 mm in length. The manufacturing processes for continuous fiber thermoplastic matrix composites are diaphragm forming and press forming. Diaphragm forming is performed in an autoclave, while press forming is performed in a heated press. Press forming is selected in this research since it has the potential for becoming the leading manufacturing process for thermoplastic matrix composites in the automotive industry. It is a much simpler operation than diaphragm forming and is similar to metal stamping processes that are used for manufacturing steel and aluminum body panels and body structure components for automobiles. It can also be

automated, making it a suitable process for high volume, low cost production processes for fiber reinforced composites.

1.2 Press Forming

Press forming is a fast, repeatable, and cost-effective process for manufacturing both thermoplastic polymer and thermoplastic matrix composite parts. It involves placing either a preheated flat thermoplastic polymer blank or a thermoplastic prepreg blank in the lower half of a heated matched-die mold and forming the part by the application of pressure. After the molding operation is over, parts are removed from the mold and cooled to room temperature outside the mold. Subsequent trimming can be performed to obtain the final shape of the product. An illustration of the press-forming operation of thermoplastic composite matrix materials is shown in Figure 1.3.

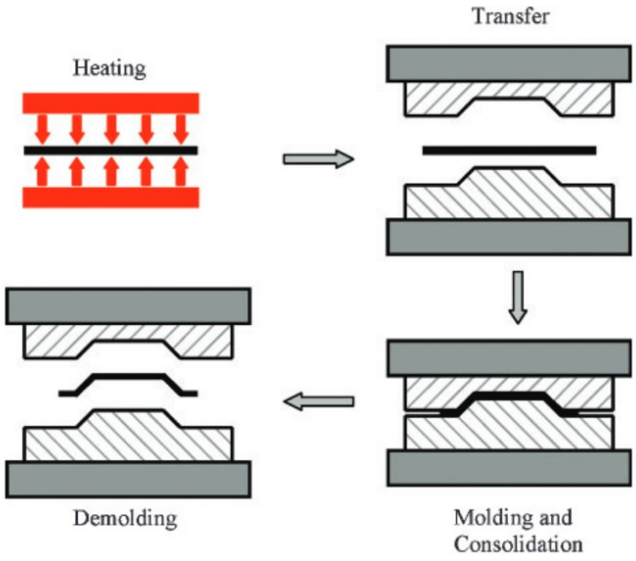

Figure 1.3: Illustration of press forming of thermoplastic composite matrix materials [6].

Press forming is also used for making dry fiber preforms that have shapes very close to that of the final composite part, but without any resin. The preform may contain layer or layers of woven fabrics, random fiber mats, or their combinations. They are used to manufacture composite parts by liquid composite molding (LCM) processes, such as resin transfer molding (RTM). To

make the preforms, flat dry fiber sheets are placed on the preforming mold and pressed into the shape of the composite part. It is then transferred to the composite part mold, and a liquid thermosetting resin mix is injected into the perform and cured to manufacture the composite part. Preforming is done to replace the manual operation of draping dry fiber blanks in the mold. It reduces the part production time and improves the quality and repeatability of the composite part.

1.2.1 Press Forming of Thermoplastic Matrix Composites

During press forming, a flat blank cut from a pre-consolidated thermoplastic matrix composite sheet is placed in a heated mold and deformed to the shape of the mold to produce the composite part. The blank is usually mounted in a frame that keeps the material under slight tension until forming is complete. Before placing the blank on top of the die half of the mold, it is heated to the forming temperature T_f either in the mold or outside the mold. The forming operation can be conducted either in an isothermal or a non-isothermal condition [7]. Figure 1.4 illustrates the temperature and pressure profiles for the isothermal and non-isothermal press forming process. In the isothermal process, the sheet material is heated to the forming temperature after placing it in the mold. In the non-isothermal process, the sheet material is preheated to the forming temperature outside the mold and transferred to the mold, which is also preheated.

The blank for press forming thermoplastic matrix composites is a prepreg that contains a layer of reinforcement, commonly a woven fabric, embedded in one or two layers of a thermoplastic polymer. There are several different processes for making prepregs, such as melt impregnation, solution impregnation and resin film infusion. If multiple layers of prepregs are used, they are consolidated into a single prepreg blank prior to placing it in the mold. Consolidation is a time-temperature-pressure dependent process and is typically done on heated flat mold surfaces to join the prepreg layers and remove gaps and air pockets between them. Good fluid flow

is required during the consolidation of prepreg layers and for the removal of air between them. Process induced defects, such as voids, uneven distribution of fibers, resin-starved areas and interlayer cracks are influenced by fiber flow [1, 8].

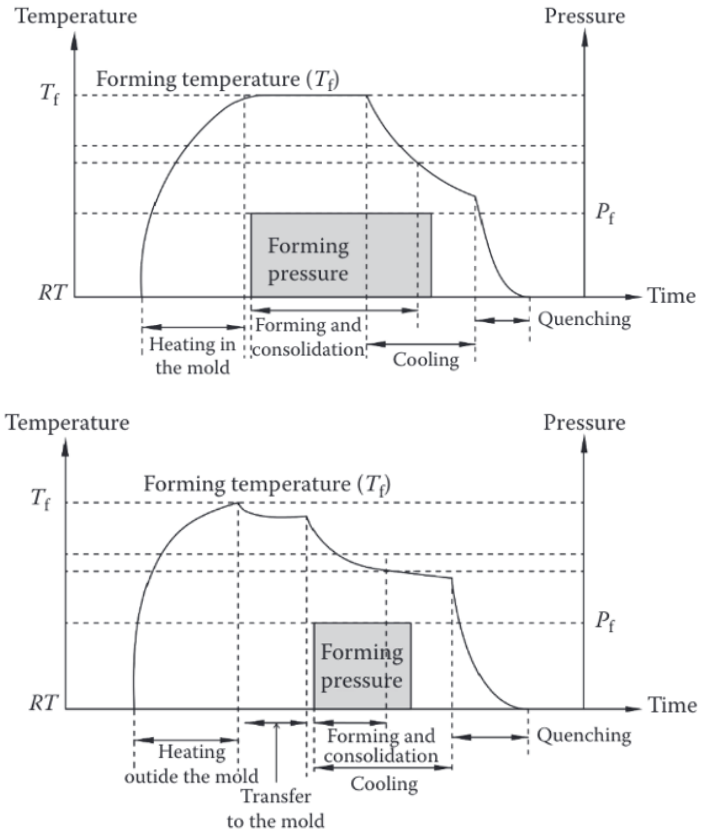

Figure 1.4: Temperature and pressure profiles during (a) Isothermal (b) non-isothermal process [7].

1.2.2 Press Formability of Dry Fabrics and Fabric-Reinforced Thermoplastics

In both preforming of dry woven fabric blanks and press forming of woven fabric embedded thermoplastic prepreg blanks, the primary mode of deformation experienced by the fabric to conform to the shape of the mold is shearing between the warp and weft yarns. Tensile and bending deformations may also be present in some areas of the fabric where it is stretched or bent to follow the curvatures in the mold. The blank holder force used in press forming also induces tension in the fabric, which when coupled with the shear deformation can increase the fabric stiffness and its

resistance to draping around the mold surface. A deeper understanding of the various deformation modes and their interactions is needed to develop the process parameter for producing successful composite parts using woven fabrics as the reinforcement material.

Press formability of woven fabric reinforced thermoplastics depends on the formability characteristics of the polymer matrix, the fabric, as well as the fabric reinforced polymer prepreg. Unlike liquid composite molding processes such as resin transfer molding (RTM) used for thermoset matrix composites, there is very little fluid flow of liquid polymer during the press forming of thermoplastic matrix composites. However, as the consolidated prepreg is draw-bended into the shape of the mold or die, there will be a considerable amount of deformation of both the polymer matrix and the woven fabric embedded in the polymer matrix. Although the thermoplastic polymer by itself may be capable of stretching and bending at the processing temperatures used for press forming, the fabric reinforcement, being nearly inextensible, will restrict its press formability. Furthermore, the fiber yarns in the fabric are interlocked, which makes the shape formation possible mostly through their rotations about their crossovers, i.e., by shear deformation. The limits of shear deformation depend on several yarn characteristics, such as yarn width and thickness, yarn spacing, filament counts in yarns, etc. As the shear deformation increases, the shear stiffness of the fabric increases until shear locking occurs when the warp and weft yarns start to press against each other, and an out-of-plane buckling occurs that appears as wrinkling of the fabric, which is considered a major defect on the press-formed composite part. Other defects in press formed parts include fiber rupture, ply separation (if the prepreg layers are not fully consolidated) and non-uniform thickness distribution.

The process parameters for the press forming operation include the preheating temperature, mold temperature, forming speed and applied pressure. The design of the part and the mold,

including the corner radii, curvatures, and depth of draw, also influence the molded part quality. An acceptable press formability window is a combination of these parameters that produce parts without unacceptable surface and internal defects, such as wrinkling, fiber breakage, yarn shifting, voids, poor surface quality and intense thinning [9]. Other parameters that affect the formability window are the friction at the prepreg-mold interface and the blank holder force.

1.3 Research Needs for Press Forming of Thermoplastic Matrix Composites

Press forming is a common manufacturing operation with sheet metals and is used extensively in the automotive industry for stamping body panels and body structure components of steel and aluminum alloys. However, there are significant differences between the press forming processes of sheet metals and thermoplastic matrix composites. These differences are highlighted below.

1) Sheet metals are usually press formed at room temperature, but for thermoplastic matrix composites, forming must be done at elevated temperatures so that the thermoplastic matrix is in a heat-softened state and flexible enough to deform or in a liquid state if matrix flow is required in the forming operation.
2) Thermoplastic matrix composite sheets have a layered structure in which the fiber orientation may vary from layer to layer, whereas sheet metals have a monolithic structure. The shape change during the press forming of sheet metals at room temperature takes place through plastic deformation. Excessive thinning (necking) and fracture of the sheet metal blank are the two failure modes that limit the press-formability of metals. For thermoplastic matric composites, the shape change may include viscoplastic deformation of the layers that include inter-ply and intra-ply shear, fiber movement and viscous flow of the polymer matrix. The formability of thermoplastic matrix composites is a relatively unexplored area of study. The formability parameters are the processing conditions, such as sheet temperature, forming

pressure and mold temperature. Depending on the part design, thinning can be one of the failure modes; but more importantly, fiber buckling and disorientation, ply shift and ply-to-ply deconsolidation are the major defects that can limit the formability of the thermoplastic matrix composites.

3) Post-forming behaviors of metals and thermoplastic matrix composites are also different. For example, formed metal parts exhibit spring back, while formed thermoplastic matrix composites exhibit spring forward.

The available literature on press forming of thermoplastic matrix composites shows that past research on this topic has concentrated principally on understanding the process conditions and the deformation mechanisms during press forming. Unlike sheet metals, formability and forming limit studies have not been explored. There are no published studies that have considered the effects of process variables on the press formability of thermoplastic matrix composites. Such studies will be useful in adopting press forming on a larger scale for the production of structural composite parts.

1.4 Objective and Methodology

The objective of the current dissertation is to develop process simulation models to study press forming and predict the press formability of polypropylene and glass fabric reinforced polypropylene. Polypropylene is selected as the matrix since it is a widely used thermoplastic polymer for automotive applications, such as instrument panels, seat backs, bumper beams, etc. Among its advantages are its low cost, good environmental resistance, and relatively low processing temperature range. Plain glass fabrics are selected as the reinforcement based on their low cost, high strength and good drapeability on mold surfaces.

The limits of press forming glass fabric reinforced polypropylene are determined by the ability to form the shape and retain it without generating defects such as fiber distortion, wrinkling and fracture. The numerical models were developed using LS-Dyna, a commercially available and widely used finite element software for non-linear analysis of structures and processes. Shear deformation characteristics of fabrics under shear-tension coupling and the formability of fabrics were investigated using numerical modeling. Experiments were conducted to determine the material parameters needed to numerically study the formability of fabric-reinforced polypropylene.

The dissertation is divided into the following four phases.

a) Development of a numerical model to understand the process parameters that influence the press forming of polypropylene
b) Development of a numerical model to determine the fabric deformation characteristics needed for preforming fabric shapes
c) Development of press-formability limits and processing windows of fabric preforms, and
d) Development of press formability of a fabric-reinforced polypropylene composite

1.5 Chapter Distribution

The dissertation is divided into the following chapters to present the methodology, results, and outcomes:

- Chapter 2: Literature review. This chapter presents a brief review of the published literature on different material characterization techniques to determine fabric deformation, draping models and material models that are available in LS-Dyna finite element software to study the fabric deformation behavior and the techniques to include the out-of-plane bending stiffness to capture true fabric deformation.

- Chapter 3: Press forming of polypropylene by warm deep drawing. Press forming of polypropylene by warm deep drawing is studied in this chapter. The material model used for the analysis considers the effects of varying temperature and strain rate during the drawing process on the depth of draw. The effects of the process and material variables on the depth of draw are determined. Thickness, temperature and strain variations in the drawn cups, punch forces, and failure modes are also determined.
- Chapter 4: Modeling of forming characteristics of fabrics. In this chapter, forming characteristics of dry woven fabrics are explored and a numerical modeling approach is developed to study the deformation behavior of woven fabrics in a biaxial bias-extension test which induces shear-tension coupling in the fabric, a commonly observed deformation mode in press forming of fabrics. One of the goals of this study is to examine specimen design and test parameters needed to produce consistent deformation patterns. The simulation approach is then applied to study the fabric deformation during press forming of dry fabrics and to develop a forming limit diagram that can be utilized to select the blank holder force and forming depth that influences the development of wrinkling and tearing in a preformed dry fabric.
- Chapter 5: Formability of fabrics and fabric-reinforced polypropylene. In this chapter, the experimental results of the uniaxial bias-extension test and press forming of three E-glass fabrics are presented. The results of the experimental uniaxial bias-extension test are used to determine the simulation material input parameters using superimposed approach. In the second part of the chapter, an approach to simulate the press forming of fabric-reinforced polypropylene is presented and the draw depths attained before failure at different temperatures are compared with that of the draw depth attained for press forming of single layer polypropylene using the same die-punch setup.

- Chapter 6: Conclusions. This chapter presents a summary of results and recommendations for future work for press forming thermoplastic polymers, dry fabrics, and fabric-reinforced thermoplastic polymers.

1.6 References

[1] P. K. Mallick, Processing of Polymer Matrix Composites, Boca Raton, FL: CRC Press: Taylor & Francis Group, 2018.

[2] Boeing. [Online]. Available: https://www.boeing.com/commercial/aeromagazine/articles/qtr_4_06/article_04_2.html.

[3] Airbus A350 XWB. [Online]. Available: https://en.wikipedia.org/wiki/Airbus_A350_XWB#Materials.

[4] Composite World. [Online]. Available: https://www.compositesworld.com/articles/is-the-bmw-7-series-the-future-of-autocomposites.

[5] U. K. Vaidya and K. K. Chawla, "Processing of fiber reinforced thermoplastic composites," *International Materials Reviews,* vol. 53, no. 4, pp. 185-218, 2008.

[6] B. Tomastrom, "Chapter 2 Thermoplastic composite sheet forming: Materials and manufacturing techniques," *Composite Materials Series,* vol. 11, pp. 27-73, 1997.

[7] A. G. Gibson and J.A. Manson, "Impregnation technology for thermoplastic matrix composites," *Composites Manufacturing,* vol. 3, no. 4, pp. 223-233, 1992.

[8] R. Brooks, "11 - Forming Technology for Thermoplastic Composites," in *Composites Forming Technologies*, Elsevier Ltd, 2007, pp. 256-276.

[9] K. Friedrich, M. Hou and J. Krebs, "Chapter 4 Thermoforming of continuous fiber/thermoplastic composite sheets," *Composite Materials Series,* vol. 11, pp. 91-162, 1997.

Chapter 2 Literature Review

Press forming is considered to be the leading manufacturing process for fabric-reinforced thermoplastic matrix composites. It typically starts with preheating a fabric-reinforced thermoplastic prepreg outside the mold, followed by pressing it in the mold and then cooling the formed composite part outside the mold. It is similar to the warm forming process for sheet metals and is suitable for mass-production applications, particularly for body panels and structures in automobiles, since it is a relatively fast, reliable, and easily adaptable manufacturing process. However, there are several aspects of the press forming operation that need to be addressed before it is accepted as a regular production process in the composite part manufacturing industry. Among them are the deformation mechanism of the woven fabric reinforcement during both preforming and press forming so that fiber yarns in the fabric are not distorted or misaligned, no wrinkles are formed and there is no tearing in the fabric as it is pressed or draped to fit the mold surface. The thermoplastic matrix during press forming is also subjected to severe deformation, partly due to the mismatch of its properties and the fabric properties, and is prone to failure by tearing, uneven surface appearance, etc. In recent years, many publications have appeared in the literature on these topics, some of which are experimental while others are theoretical or numerical in nature. This chapter reviews a few key findings, methodology developments and results from these publications and involves the following areas of study:

- Deformation mechanisms in the press forming processes.
- Draping models.
- Material characterization tests for fabrics.

- Review of the material models available in LS-Dyna to capture fabric deformation.
- Study of the existing techniques/ approaches to capture true fabric deformation.
- Forming limit curves for fabrics.
- Process variable for press forming process.

2.1 Deformation Mechanisms in Press Forming Processes

The different deformation mechanisms during press forming of thermoplastic matrix composites can be enumerated as follows:

- Intra-ply shear: Intra-ply shearing occurs when the fibers within each ply move past each other by in-plane shearing. This mechanism is more common when the prepreg stack is deformed over a doubly curved surface, such as a spherical dome. This occurs in the form of a trellis effect in which the angle between the initially orthogonal fiber tows is decreased. The shear stress needed to induce intra-ply shearing also decreases with increasing temperature and increases with increasing forming speed and is usually higher than the shear stress needed for interplay slip [1]. The extent to which the fibers can rotate is limited, by the shear locking of the fibers in the warp and weft direction commonly denoted as the locking angle. Figure 2.1 represents the intra-ply shear mechanism during forming of thermoplastic matrix composites.

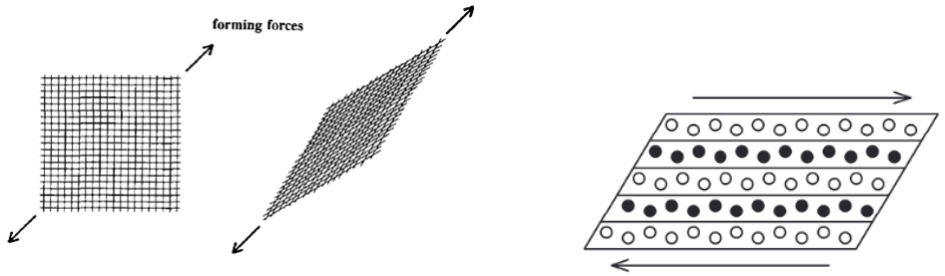

Figure 2.1: Intra-ply slip [2, 3].

- Inter-ply slip or interlaminar slip occurs through the slippage or sliding of adjacent layers relative to each other as the flat prepreg stack is deformed over a singly curved surface. Figure

2.2 shows the sliding of adjacent layers relative to each other during the press forming process. It is helped by the liquid polymer which acts as a lubricant between the adjacent layers. It is also the principal mechanism that prevents the buckling and wrinkling of the prepreg layers during the shape forming. The minimum shear stress needed to induce interplay slip decreases with increasing temperature and increases with increasing slip velocity [3].

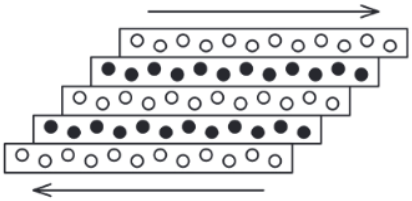

Figure 2.2: Inter-ply slip [2].

- Inter-ply rotation, also a shearing mechanism that creates a rotational slip of one layer relative to its adjacent layer as shown in Figure 2.3. The viscosity of the liquid polymer between the layers controls the resistance to inter-ply rotation. Since viscosity decreases with increasing temperature, shear stress needed for inter-ply rotation also decreases with increasing temperature [2].

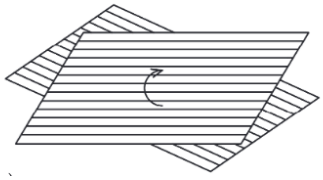

Figure 2.3: Inter-ply rotation [2].

- Fiber straightening: Straightening of fibers is another deformation mechanism taking place in the plane of a ply and it occurs if fibers are not fully stretched before forming. In fabrics, where fiber bundles are interlaced with some degree of curvature, stretching reduces the curvature, leading to an increase in mechanical properties in the loading direction. But the curvature in the perpendicular direction may increase, leading to a reduction in mechanical properties in that direction [1, 4]. Figure 2.4 (a) represents the fiber along the warp and weft before the

application of force and Figure 2.4 (b) represents the stretching of fibers along the warp direction with the application of force.

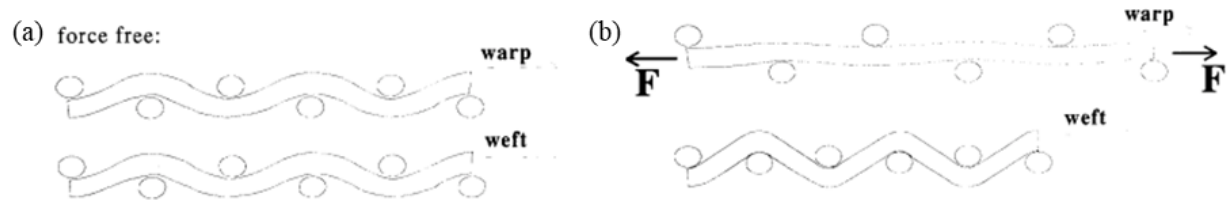

Figure 2.4: Fiber straightening in the warp and weft direction [1].

- Fiber deformation: Because of Hookean behavior, fiber elongation is purely elastic. Hence, elastic elongation of the fiber reinforcements is not a deformation that can be used to shape composite products [1, 4]. However, high residual stresses that occur due to stretching and cooling of the composite part can lead to premature failure or mismatch of the product. Since during forming, fibers are surrounded by the heat-softened matrix with a very low modulus, fiber buckling can occur in areas where the compressive stresses on the fibers are high.
- Resin percolation: The flow of liquid polymer between the fibers and along the layers in the prepreg stack is fundamental to fiber impregnation, consolidation, and evacuation of air from the fiber bundles in each layer as well as between the layers. It is also needed for the uniform distribution of the matrix in the composite part [2, 5]. If resin percolation is not sufficient, consolidation quality will be negatively affected, and voids remain in the material. Figure 2.5 represents the resin percolation around the fibers during the press forming operation. Since thermoplastic polymers have high viscosity even at temperatures higher than their melting point, resin percolation may not be as effective as with thermosetting polymers which have relatively low viscosity. Because of this, the consolidation quality of thermoplastic prepreg layers may not be as good as that of thermosetting prepregs.

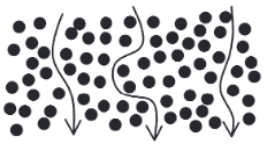

Figure 2.5: Resin percolation around fibers [2].

- Transverse flow is a process by which the prepreg stack spread out in the transverse direction of fibers due to the pressure gradient that develops during the processing. Figure 2.6 represents the fiber flow along the transverse direction. There is very little axial flow since the resistance to flow in the axial direction is much higher than in the transverse direction. Barnes et al. [5] gave Equation (2.1) to measure transverse flow velocity by

$$Viscosity = \frac{F\,H^2}{2\,V\,W^2 L} \qquad \text{(Eq. 2.1)}$$

where F is the applied normal force, H is specimen thickness, W is the specimen width, L is specimen length and V is the transverse flow velocity.

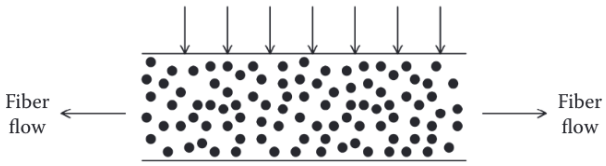

Figure 2.6: Transverse flow.

- Bending: Limited experimental data on the flexural response of thermoplastic matrix composites in forming conditions estimate the laminate response to be somewhere in between Kirchhoff bending and transverse shear [1, 4]. Figures 2.7 (a) and (b) represent Kirchhoff bending and intra-ply shear respectively, and Figure 2.7 (c) represents the combination of two bending modes with inter-ply shear which is often observed in thermoplastic matrix composites during press forming operation.

Figure 2.7: (a) Kirchhoff bending, (b) intra-ply shear, (c) combination with intra-ply shear [1, 4].

- Frictional interaction occurs between the forming tools (dies, punch, and blank holder) and the surface of the thermoplastic matrix composite which are in contact with each other. Experimental work has shown that the frictional interaction depends on temperature, pressure and sliding velocity [1, 4].

A brief review of the deformation modes for stacked reinforcement plies and the corresponding flow mechanism is shown in Figure 2.8.

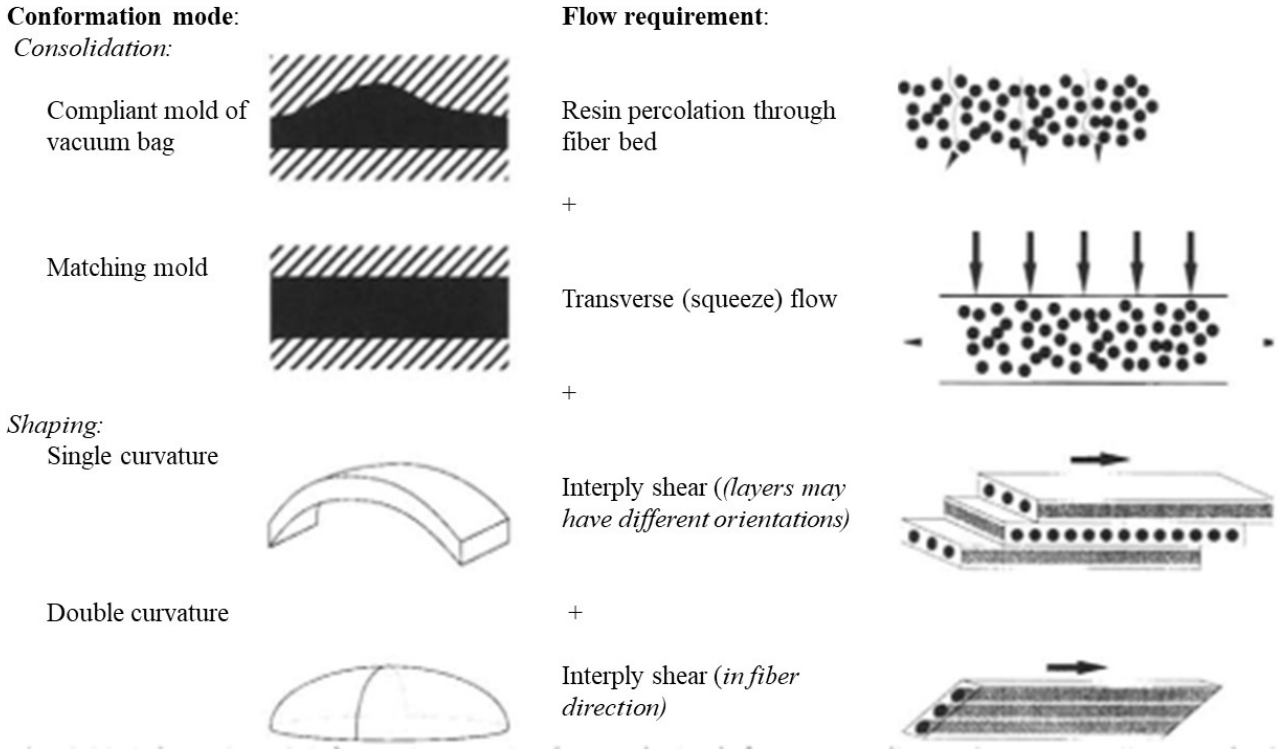

Figure 2.8: Different modes of stacked plies and the corresponding flow mechanisms.

2.2 Draping Models

Draping describes the manner in which fabrics are laid over a mold and the way the fibers within the fabrics change in orientation as they are pressed onto the mold surface to conform to the mold geometry. Draping is the most important factor in determining the manufacturability and performance of woven fabric composite structures. Physical and mathematical models proposed to predict the draping behavior during press forming of fabric preforms and fabric-reinforced thermoplastic composite prepregs are described in this section.

1. Fishnet or kinematic models

Fishnet or kinematic models [6, 7] represent the fabric as a pin-jointed net of interlocked fibers, neglecting yarn extension or slippage. The other assumptions include no sliding at the intersection between the warp and weft yarns and free rotations between the warp and weft yarns. These models are relatively simple and efficient to determine fabric deformation; however, they do not account for load boundary conditions (sliding of the fabric relative to the tools) and mechanical phenomena such as fiber distortion and shear locking. These models are limited to the draping of fabrics without holes, bridges, or around complex curves.

2. Continuum models

Continuum models [7] assume that the woven fabric is a homogenous sheet of material. They primarily depend on the constitutive model of the fabric and the definition of material properties. These models track and update the fiber orientation as the material deforms by using a non-orthogonal or anisotropic formulation. The limitation of this approach is that it cannot predict yarn slippage and also out-of-plane behavior is often neglected. The two most widely used continuum models are hyperelastic and hypoelastic models.

a) Hyperelastic models [8]: These account for large deformation, anisotropy and non-linear elasticity, so these models find their application in the material which are subjected to very high strains such as rubbers or elastic foams. They work by calculating stress from a strain energy functional, and can accurately predict fiber directions during textile draping.

b) Hypoelastic models [8]: These continuum models relate stress increments directly to strain increments with constitutive tensor that contains tensile and shear material properties. These models are quite effective for materials with reversible non-linear behavior and are typically used for isotropic analyses at large strains. Non-orthogonal hypoelastic models at the mesoscale and macroscale have been developed and are for determining draping behavior.

3. Discrete models

Discrete models [8] avoid macroscale homogenization of the woven fabric, and instead physically represent the mesoscale or microscale features of the fabric, considering the arrangement and interaction of discrete yarns or even fibers within the fabric. These models represent yarns as beams or truss elements and use springs to simulate interactions or shear effects. This model employs enriched kinematic beam models along with advanced fiber friction and contact algorithms, to predict fabric behavior. These models are computationally expensive and are not feasible for modeling a full part. Figure 2.9 shows the fabric sheet using the discrete method which is skeletonized into a network of interconnected nodes of grid-point by Sze et al. [9].

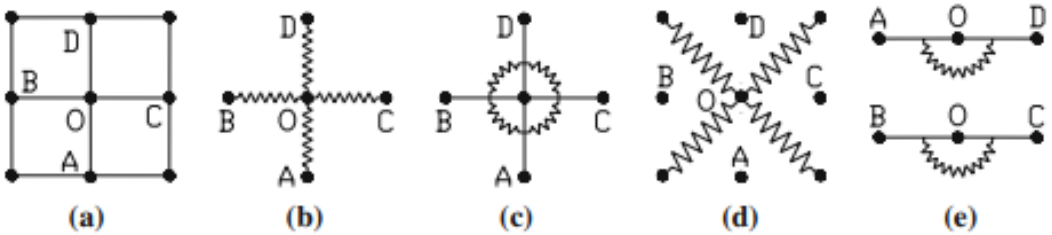

Figure 2.9: Skeletal method, in which a fabric sheet is skeletonized into a network of interconnected nodes of grid points [9].

4. Semi-discrete models

Semi-discrete model by Hamila et al. [10, 11] combines aspects of discrete methods with continuum finite-element practices. In this model, the fabrics are composed of a discrete number of unit woven cells. This model also has the feature to incorporate bending behavior for better wrinkle simulation. Semi-discrete methods require less comprehensive material characterization than continuum methods and are more efficient than discrete methods, however; the model overestimates in-plane stiffness when compared to the continuum method as the yarn slippage is neglected [8].

The semi-discrete model by Hamila et al. [10] uses the principle of virtual work. Fabric reinforcement is seen as a set of a discrete number of unit woven cells submitted to biaxial tension, in-plane shear and bending loads (Figure 2.10). A three-node triangular shell finite element has been defined from the simplified form of the principle of virtual work, details of the formulation of which can be found in Ref. [10].

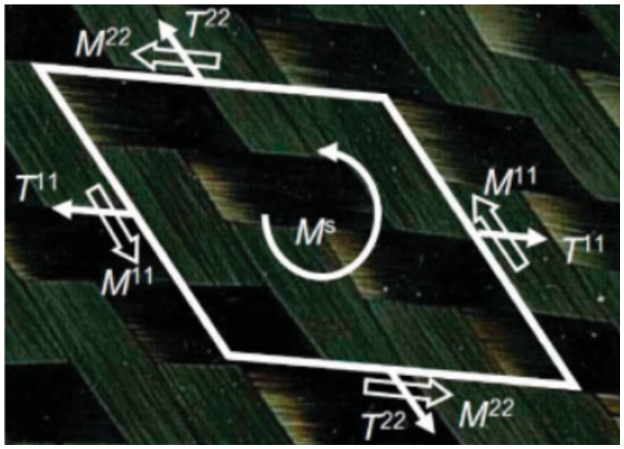

Figure 2.10: Unit woven cell subjected to tension, in-plane shear and bending loads [11].

2.3 Material Characterization Techniques

All the modeling approaches mentioned in Section 2.2 to capture fabric deformation using finite element simulations may require different mechanical properties to simulate the fabric behavior.

To understand the behavior of dry fabrics and fabric-reinforced thermoplastic polymers during press forming, the characterizations of tensile, in-plane shear and bending properties remain a priority. These properties of the fabrics are characterized experimentally.

2.3.1 Tensile Characterization

Tensile stress-strain diagrams obtained from single filament test of reinforcing fibers (yarns) are almost linear up to the point of failure as shown in Figure 2.11 [12]. They exhibit very low strain-to-failure and brittle failure mode. This behavior indicates the essential inextensibility of the fibers.

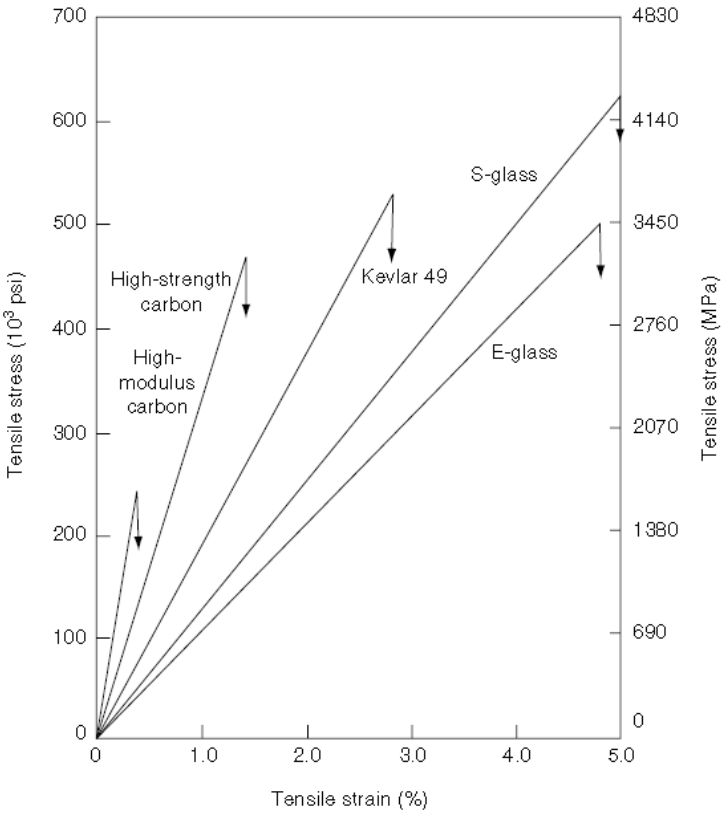

Figure 2.11: Tensile stress-strain diagrams for various reinforcing fibers [12].

For woven fabrics, because of the undulation of fibers along warp and weft directions, a biaxial tensile characterization test can be done to study the effect of variation of tensile load along warp and weft directions. Under the application of the tensile load, the undulations in the yarns

tend to straighten and become flat in the direction of the applied tensile load. In the extreme case (for example, if the tensile load is applied to only one yarn and the yarns in the other direction are free to displace), then the loaded yarns become straight and the other strongly undulated. The deformation of the fibers in the woven fabric under the application of tensile load is shown in Figure 2.12. Under intermediate conditions, the fibers in both directions show undulation variations. The co-efficient of biaxial tension *k* is the ratio of the deformations along the warp and weft directions. It also helps quantify the degree of interaction between warp and weft yarns. Biaxial testing equipment for testing of plain fabric and the influence of the co-efficient '*k*' are shown in Figure 2.13 [13, 14].

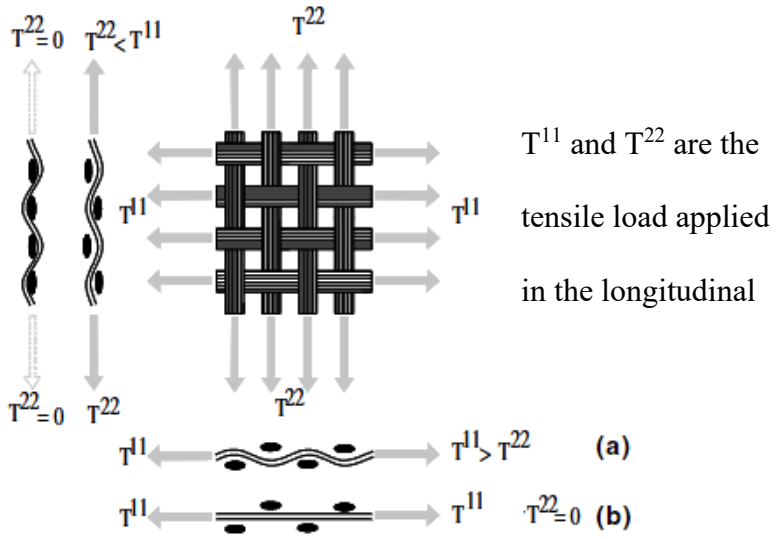

Figure 2.12: Undulation variations in case of warp (1-direction) and weft (2-direction) tensions [15].

Most of the studies on biaxial tensile tests are for dry fabrics. Studies conducted by Wang et al. [16] indicate that the influence of resin can be neglected. However, biaxial rigs that test cruciform-shaped samples in both warp and weft yarn directions at various loading rates are challenging to build and operate. As a result, there is no biaxial test standard, and uniaxial "grab" and "strip" tests are often employed, under the common assumption that the biaxial behavior is negligible [13].

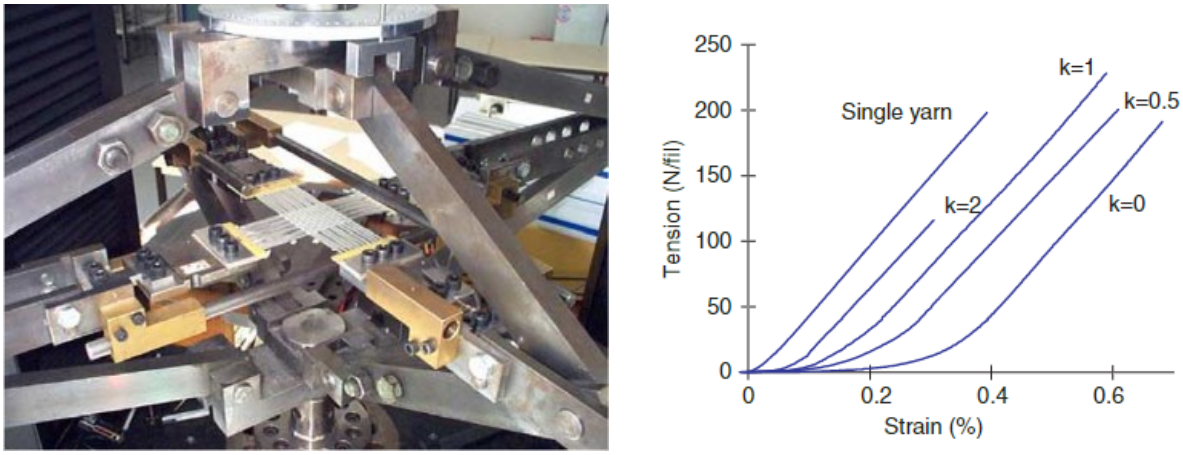

Figure 2.13: Biaxial tension test device and measuring results for different ratios [15].

From Figure 2.13 irrespective of the ratio *k* there is a small non-linear portion in the tensile stress-strain curves which is a characteristic of woven fabrics and is attributed to the crimping in yarns. Studies by Shim et al. [17] have shown that the areal density of the fabric reduces by 3% if the yarns are fully straightened and the resulting uniaxial stress-strain shows the crimping to 1.5% of total strain. Since the static failure strain of the fibers is usually low, it is necessary to incorporate the crimp effects.

2.3.2 In-Plane Shear Characterization

The shear behavior of woven fabrics tends to be highly non-linear. After overcoming initial friction at the crossover locations at low loads, fabric yarns are relatively free to rotate under shear loading; however, the shear resistance increases rapidly until they ultimately reach a locked state [13] as shown in Figure 2.14. Compared to the high tensile stiffness, the in-plane shear stiffness of fabrics is so low that this type of deformation is the most dominant deformation mode for reinforcement and prepreg in the forming.

The in-plane shear behavior can be divided into three parts as represented in Figure 2.14.

- Stage 1: Characterized by low shear angles, yarns freely rotate against each other in a rigid body motion and the shear stiffness, which is mainly due to the frictional resistance between the yarns, is very weak.
- Stage II: The locking angle in this stage corresponds to the angle after which the geometry of the weaving does not allow any further rotation, yarns are now in contact with their neighbors and are laterally compressed leading to an increase in shear stiffness.
- Stage III: After the locking stage, there is no further rotation of the yarns causing the shear stiffness to increase very rapidly and the appearance of out-of-plane wrinkles.

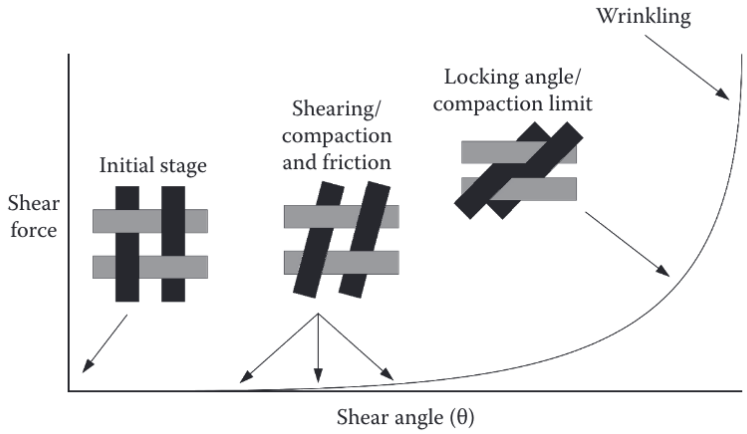

Figure 2.14: Shear force vs. shear angle plot describing in-plane shear characteristics of a fabric [2].

The two test methods that are commonly used to characterize fabric shear response and locking angle are the picture frame test and the bias-extension test.

2.3.2.1 Picture Frame Test

In this test, the fabric is cut into a square shape specimen and fixed in a pin-jointed frame with its warp and weft yarns oriented as shown in Figure 2.15. The bottom pin of the frame remains stationary, and as the top pin of the frame is displaced upward, it starts to change from the initial square configuration to a stretched configuration that causes a pure shear deformation in the fabric.

This test assumes that the shear deformation in the specimen is homogenous. This test requires careful handling and alignment during clamping. Misalignment of the yarns introduces parasitic tensile stresses, which will significantly affect the results due to a much higher tensile stiffness of the fabric compared to its shear stiffness. For this test, the shear angle can be directly calculated from the displacement *d* and length of the frame L_{frame} [18, 19] as shown in Equation (2.2).

$$\gamma = \frac{\pi}{2} - \theta = \frac{\pi}{2} - 2cos^{-1}\left(\frac{1}{\sqrt{2}} + \frac{d}{2L_{frame}}\right) \quad \text{(Eq. 2.2)}$$

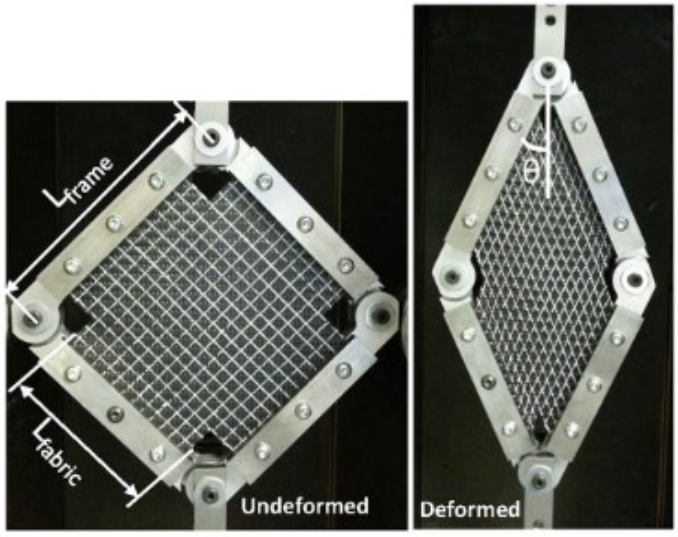

Figure 2.15: Picture frame test showing the un-deformed and deformed fabric specimen [20].

2.3.2.2 Uniaxial Bias-Extension Test

Uniaxial bias-extension (UBE) test involves clamping a rectangular specimen of the woven fabric to the grips of a tensile testing machine and applying an axial displacement in the length direction of the fabric so that the fabric is subjected to a uniaxial tensile force. The warp and weft yarns of the fabric are oriented initially at ±45° to the direction of the applied tensile force. A schematic representation of the test specimen before and after deformation is shown in Figure 2.16.

The length of the fabric specimen is to be kept more than twice the width of the specimen to get a region of pure shear deformation in the middle where the restraining effects of the clamps

become insignificant [21]. Because of the higher tensile stiffness of the woven fabrics compared to other stiffnesses, two different shear zones and a shear-free zone are observed on the deformed fabric specimen. Figure 2.16 shows the shear deformation regions in uniaxial bias extension test specimens.

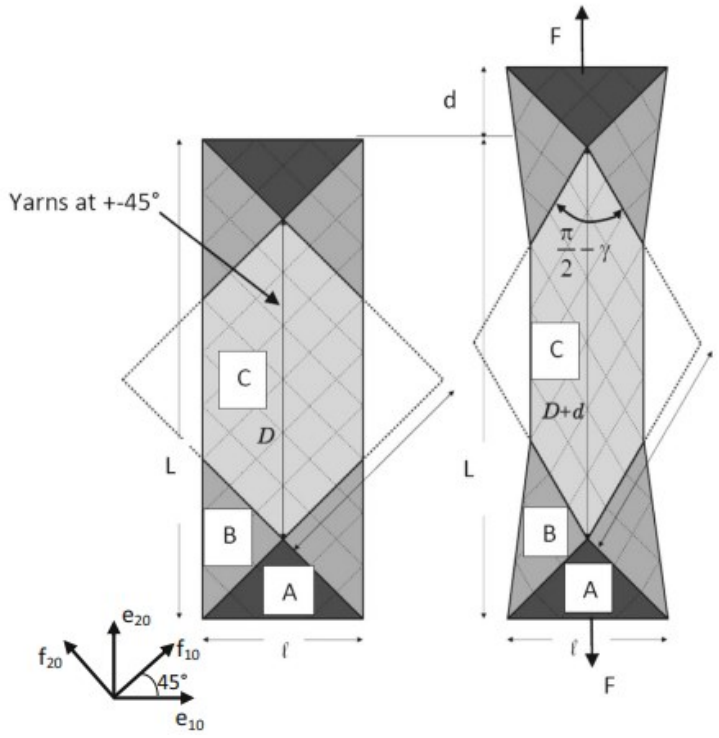

Figure 2.16: Uniaxial bias-extension test specimen showing the un-deformed and deformed shapes of the fabric specimen [22].

Yarns in the central region ‘A’ are free at both ends; deformation in this region is trellising and is pure shear. Shear in the region B is half of that of the shear deformation in A; in this region, one end of the yarns is clamped, and the other end is free [23]. Region C is the region under clamps and undergoes zero shear deformation since in this region one end of both warp and weft yarns are fixed in the clamp. Several authors have expressed the shear angle in the central region as a function of the moving crosshead displacement of the testing machine by Equation (2.3) [21, 22]. The shear angle in the central region was found to vary linearly with displacement. The theoretical

shear angle (γ) measured using Equation (2.3) and the experimentally measured shear angles show a linear relationship between each other up to a certain angle beyond which they mismatch due to the wrinkle formation and measuring the shear angle experimentally becomes difficult [24].

$$\gamma = \frac{\pi}{2} - 2\,cos^{-1}\left(\frac{D+d}{\sqrt{2}D}\right) \quad \text{(Eq. 2.3)}$$

Among the several characterization tests to characterize the in-plane shear response of fabrics, the UBE test is widely used due to its simplicity in carrying out the test. It can be carried out on any tensile testing machine with the fabrics oriented at ±45°. Another advantage of this test is the absence of spurious tensions in the yarns of the sheared zones [22]. In the picture frame test, all yarns are clamped in the frame and any misalignment of the specimen will lead to an increase in the load required for fabric deformation. Comparison studies between the picture frame and UBE tests have shown a higher shear load for the picture frame than the shear load in BE test due to the presence of spurious tension, setting these to zero matches the results of the BE test [22].

2.3.2.3 Effect of Shear-Tension Coupling on Deformation of Fabrics

During press forming of complex geometries, many process-induced defects are observed on the fabric if there is no in-plane tension. Application of the in-plane tension with the help of blank holder force or using a clamping device mitigates these defects and also controls final fiber orientation distribution across the component after forming [24]. The shear compliance of woven fabrics has also shown a relation to the in-plane tension acting along the two sets of yarns within the fabrics. Hence characterizing the shear-tension coupling is extremely important to determine the variation of the shear stiffness of the fabrics with applied tension and also to study the final fiber orientation of the deformed fabrics. Several studies have been conducted by providing an extension to the existing shear characterization tests to determine the effect of the in-plane tension on the shear behavior of woven fabrics. Specimens used to study the shear-tension coupling

characteristics are called biaxial bias extension (BBE) specimens. Harrison et al. [24] used a square ±45° fabric specimen to determine shear extension coupling. The fabric was clamped over a fraction of the length along its four edges and an increasing tensile load similar to that of the uniaxial bias-extension test was applied to the vertical clamps, while a constant transverse load is applied to the horizontal clamps. The corresponding force vs. shear angle was recorded. Similar to the UBE specimens, the BBE specimens also exhibited a pure shear deformation in the center region of the specimen, which is surrounded by regions of half shear and zero shear. Force vs. shear angle curves (Figure 2.17), taken from Ref. [24] show an increase in slope as the applied transverse load is increased, representing an increase in shear stiffness of the woven fabric with the applied transverse load.

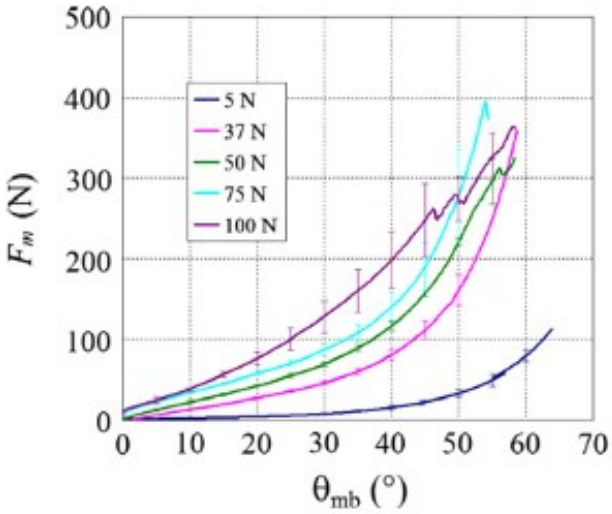

Figure 2.17: Material deformation force vs. shear angle curves at different applied transverse loads [24].

Another attempt to characterize shear-tension coupling on the fabric behavior was done by Sharma et al. [25] by varying biaxial boundary conditions on a cruciform specimen with ±45° warp and weft orientations shown in Figure 2.18. The test method is displacement-controlled with the horizontal and vertical arms displaced at different velocities. The ratio of the vertical velocity to

horizontal velocity was maintained to be greater than 0.5 and less than or equal to 1.4. Velocity ratios lower than 0.5 produced inaccurate stress results and were not considered for the study. No significant increase in the shear resistance of the material was observed.

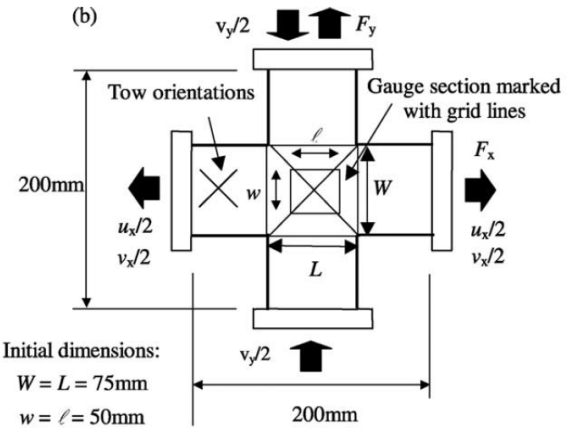

Figure 2.18: Cruciform fabric test specimen [25].

Rashidi et al. [26] also used cruciform specimens with different dimensions from that of Sharma et al. [25] to study the shear tension coupling effect on woven fabrics. Tensile forces were applied for all four arms in the outward direction and the fabric deformation was studied for varying transverse forces. Severe wrinkling was observed along the arms of the cruciform fabric specimen.

The results from Harrison et al. [24] and Sharma et al. [25] are contradictory, while Harrison et al. [24] observed a change in fabric stiffness behavior with a change in the applied transverse loads, Sharma et al. [25], on the other hand, did not observe any major change in the fabric stiffness for varying transverse loads.

2.3.3 Bending Characterization

The bending stiffness of fabrics is very low compared to their tensile and in-plane shear stiffnesses. Several studies have shown that it plays a key role in determining wrinkle formation. The most

common method to characterize the bending stiffness of fabrics is the cantilever beam bending test in which a strip of fabric is embedded on a horizontal board which is tilted slowly at the hinge until the tip of the fabric strip touches the tilted board with a 41.5° deflection angle. A standard cantilever bending experiment test setup is represented in Figure 2.19. Bending moment *M* is a linear function of the curvature *k* (of a bent beam, plate or shell depending on the complexity of the model) and is shown in Equation (2.4). The bending stiffness can be calculated by the measurement of the bending length *l* and is shown in Equation (2.4).

$$M = G \times b \times k \quad \text{(Eq. 2.4)}$$

where *G* is the flexural rigidity per unit width and *b* is the width of the strip.

$$S = \frac{l^3}{8} \cdot \frac{\cos \emptyset/2}{\tan \emptyset} \quad \text{(Eq. 2.5)}$$

where *S* is the ratio of the flexural rigidity to the weight *w* per unit length and $\emptyset$ is the bent angle.

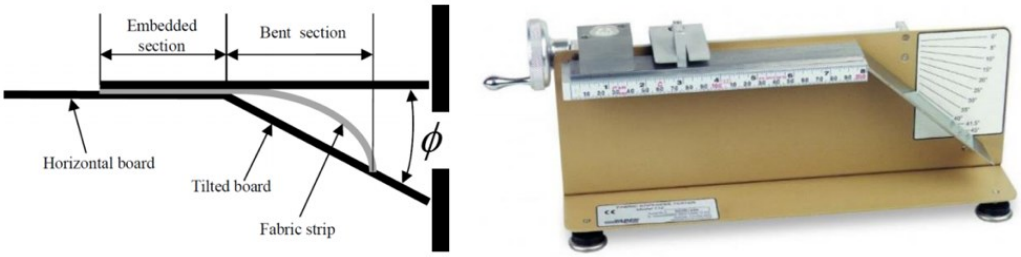

Figure 2.19: Standard cantilever bending experiment [27].

2.4 Material Models to Simulate Fabric Deformation in LS-Dyna

There are several material models available in LS-Dyna that can be used to determine fabric deformation during press forming. The desirable characteristics that are expected from these models are that they should be able to capture the inherent characteristics of the fabric reinforcement, predict the local fiber orientation and final fiber volume fraction. Some of the material models available in LS-Dyna with these capabilities include the Viscoelastic loose fabric

model (MAT_234), Micromechanics dry fabric model (MAT_235) and Anisotropic hyperplastic model (MAT_249). All of them take into account the reorientation of the yarns as the fabric is deformed and are also able to simulate the locking phenomenon exhibited by the fabric [28, 29].

2.4.1 Viscoelastic Loose Fabric (MAT_234)

One of the material models suitable for press forming simulation of dry fabrics is MAT_VISCOELASTIC_LOOSE_FABRIC (MAT_234). It was originally developed by Ivanov and Tabiei [30] for modeling ballistic impact on woven fabrics used in body armors, airbags, etc. It is based on a micro-mechanical model of loosely woven fabrics and is compatible with the membrane element formulation being used to simulate the draping behavior of fabrics. This model uses a representative volume cell, which is commonly used for micro-mechanical studies and accounts for fiber reorientation, the trellis mechanism of the yarn, and both the elastic and viscoelastic response of the fibers.

The modeling of the flexible fabric behavior under the membrane and transverse loading is a challenging task. The difficulty comes from the architecture of the loosely woven fabrics. The undulation of the yarns allows their straightening which causes more flexibility and redistribution of the strain energy between the yarns. The shearing of the fabrics resembles a trellis mechanism that causes significant reorientation of the yarns. The rotation in the yarns is accompanied by rotational friction at the crossover locations, and if the deformation of the fabric is large, the rotating yarns may reach the locking angle between them at which the fabric becomes packed in a block that has the highest area density.

The representative volume (RVC) technique shown in Figure 2.20, is utilized in MAT_234. RVC of the loosely woven fabric material model is extracted from the deformed pattern of the material. The RVC consists of an undulated fill yarn crossed over an undulated warp yarn. The

parameters of the RVC are the yarn span (*s*), fabric thickness (*t*), yarn width (*w*), and yarn cross-sectional area (*S*).

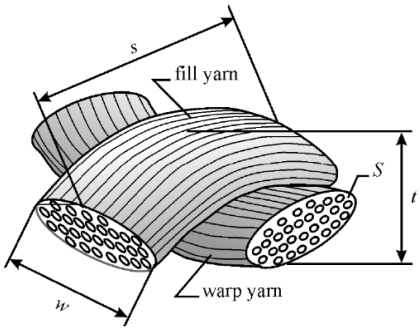

Figure 2.20: Representative volume cell (RVC) of a loose woven fabric.

Woven fabrics behave like a trellis mechanism when they are stretched in any non-yarn direction or sheared in the plane. The initially orthogonal yarns are free to rotate in the plane of the fabric up to the minimum braid angle θ_{min} after which the lateral contact between the yarns causes the locking of the trellis mechanism and the packing of the yarns as shown in Figure 2.21.

The minimum braid angle θ_{min} can be calculated from the yarn width *w* and the span between the yarns, *s*:

$$\sin(2\theta_{min}) = \frac{w}{s} \qquad \text{(Eq. 2.6)}$$

The other constraint angles are the locking range angle θ_{lock} and the maximum braid angle θ_{max} . They can be determined as

$$\theta_{lock} = 45^o - \theta_{min} \ , \qquad \theta_{max} = 45^o + \theta_{lock} \qquad \text{(Eq. 2.7)}$$

Initially the braid angles of yarns θ_f and θ_w are $45^o$and -45^orespectively.

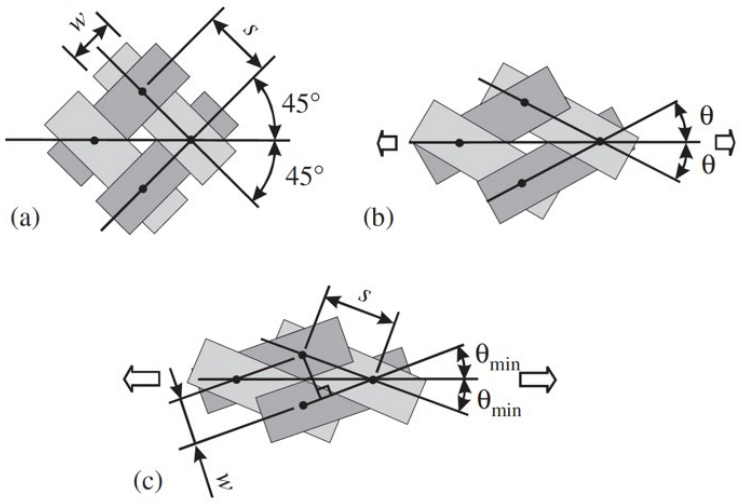

Figure 2.21: Trellising mechanism of fabrics (a) un-deformed state, (b) slightly deformed fabric, (c) fabric deformed to interlock.

The total in-plane stretch of the yarns and the strain increment tensor of the RVC can be determined from Ref. [30]. The material behavior of the woven fabrics is described by a combination of a spring with spring constant K_a in series with the Kelvin-Voigt element as depicted in Figure 2.22.

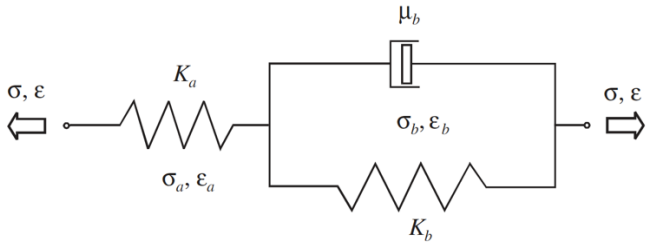

Figure 2.22: Three-element viscoelasticity model.

The differential equation of viscoelasticity can be derived from the model equilibrium in the form

$$(K_a + K_b)\sigma + \mu_b\dot{\sigma} = K_aK_b\varepsilon + \mu_bK_a\dot{\varepsilon} \qquad \text{(Eq. 2.8)}$$

where,

K_a = Hookean spring constant of the spring element

μ_b = Viscosity coefficient of the Kelvin-Voigt element

K_b= Hookean spring constant of the Kelvin-Voigt element

The main advantage of this model is that it contains two failure criteria that can be used to predict failure of the fabric: one for the Hookean spring providing the instantaneous response which is considered to determine the primary molecular bond failure,

$$\varepsilon_a = \frac{\sigma}{K_a} > \varepsilon_{a\,max} \quad \text{(Eq. 2.9)}$$

and the other is for the Kelvin-Voigt element providing the delayed response which is considered to determine the secondary molecular bond failure.

$$\varepsilon_a = \varepsilon - \varepsilon_a > \varepsilon_{b\,max} \quad \text{(Eq. 2.10)}$$

The input parameters for the viscoelasticity model of the material are static Young's modulus E_1, the Hookean spring coefficient K_a, the viscosity coefficient μ_b, the static ultimate strain ε_{max} and the Hookean spring ultimate strain $\varepsilon_{a\,max}$. The other parameters can be obtained as

$$K_b = \frac{K_a E_1}{K_a - E_1}, \qquad \varepsilon_{b\,max} = \frac{K_a - E_1}{K_a}\varepsilon_{max} \quad \text{(Eq. 2.11)}$$

2.4.2 Micromechanics Dry Fabric (MAT_235)

This material model utilizes the micro-mechanical approach and the homogenization technique commonly used in modeling the mechanical behavior of composite materials. It accounts for the reorientation of the yarns and the fiber architecture. In this material model, the behavior of the flexible fabric material is achieved by discounting the shear moduli of the material in the free state, which allows the simulations of the trellis mechanism before shear locking is attained [31].

Similar to MAT_234, this material model supports under-integrated and fully-integrated membrane elements. The material model MAT_235 does not consider the effects of the out-of-

plane bending stiffness. In the free state, the fabric material behavior resembles a trellis mechanism with the warp and weft yarns mutually perpendicular to each other. The load is carried by the yarns in their axial directions and the load applied in any other direction causes the yarns to rotate up to the locking angle. When the yarns have attained shear locking, the area density of the fabric is the highest and the yarns are packed in a block that has anisotropic properties.

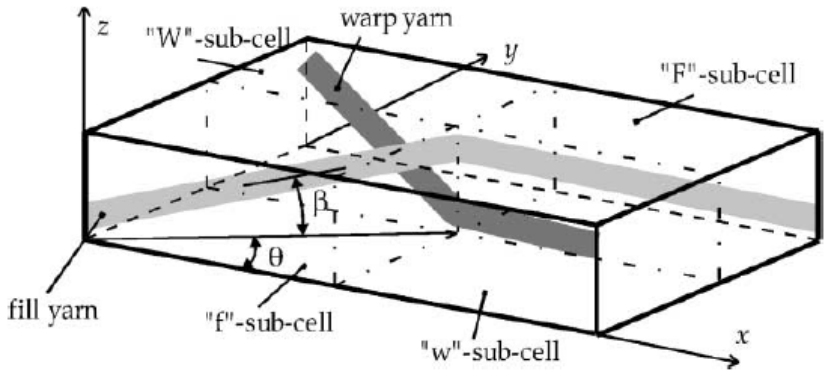

Figure 2.23: Representative Volume Cell showing the angles required to define the direction of each yarn in the MAT_235 material model [31].

The material model uses the RVC approach shown in Figure 2.23 which is divided into four sub-cells, two anti-symmetric sub-cells containing the undulated fill-yarn and two other anti-symmetric sub-cells containing the warp yarn. The direction of each yarn is defined by two angles; the braid angle θ and the undulation angle of the yarn, which are different for the fill and warp yarns. They are β_f and β_w, respectively.

The yarn stiffness matrix has a discount factor that scales the shear stress and is a function of the braid angle with values ranging from 0 to 1. In the free stress state, the discount factor has a small value, and the material has a very small resistance to shear deformation. When shear locking occurs, the fabric yarns are packed, and they behave like elastic media with discount factor

equal to unity and the fabric material now resists the shear with its real shear moduli. The details of the stress calculation and the homogenization procedure can be found in Ref. [31].

To predict the reorientation of the yarns during the deformation, a non-linear method has been utilized [31]. This method is a strain-controlled incremental approach of the semi-discretization spatial method employed in the explicit non-linear finite element code. The initial values of the yarn are given by the user with the braid angle equal to 45° in the free state. The undulation angle is changing along the yarn, and it varies from zero to some maximal value less than 90°, the maximum values are used as a characteristic of the crimping. The undulation angle can be approximated to be the angle at which the tangent is half of the fabric thickness divided by the distance between the yarns.

Hill et al. [32] attribute 93% of the total variance to the initial braid angle, locking angle, undulation angle and reorientation damping coefficient. The initial response of the fabric behavior is controlled by varying the discount factor, and angle tolerance for locking determines the transition from the trellis mechanism to the stiffer behavior exhibited by the fabrics.

2.4.3 Anisotropic Hyperelastic Model (MAT_249)

This material model in LS-Dyna describes a reinforced thermoplastic composite material and can be used to model unidirectional layers as well as woven and non-crimped fabrics. In this material model, the reinforcement is defined as an anisotropic hyper-elastic material with up to three distinct fiber directions and the matrix is modeled with a simple thermal elastoplastic material formulation [33]. The MAT_249 can model fabrics with different fibers along the warp and weft direction and the properties of the individual fibers can be assigned to the fiber family. Different options to model shear response between the fiber families i.e., the warp and weft direction can be defined using the METH12 control card in the material model. Up to three fiber families can be

defined using this material model. The matrix model uses an elastic-plastic material formulation with a von-Mises yield criterion. The matrix material can be assigned a parameter for mixed hardening i.e., either pure kinematic hardening or pure isotropic hardening by defining the extreme values. Intermediate values will define the matrix material as mixed hardening.

The material model features an additive split of the matrix and reinforcement contribution to the stress. The combined stress response is given in Equation (2.12) where σ^m is the matrix stress and σ^f the fiber stress.

$$\sigma = \sigma^m + \sigma^f \quad \text{(Eq. 2.12)}$$

2.5 Modeling Approaches for Fabrics

Modeling and accurate representation of the fabric behavior is a challenging task. The difficulty comes from the dual behavior of the fabric. In the free state, the fabric behavior resembles the trellis mechanism with the reorientation of the yarns up to some locking angle. The fabric slightly resists shear strain due to friction between yarns. When the yarns are completely packed, i.e., the angle between the yarns have reached a locking angle, the area density of the fabric becomes the highest, and the yarns are packed in a block that has anisotropic properties [31]. The material models MAT_234 and MAT_235 to simulate fabric deformation are based on representative volume cell approach and work with under-integrated and fully integrated membrane shell elements.

The flexural rigidity of the fabrics is quite low when compared to its tensile rigidity and also fabrics are highly susceptible to buckling when subjected to in-plane compression. To simplify the numerical determination of the behavior of fabrics, it is common practice to disregard bending stiffness and use membrane assumption. In tension, the behavior of the fabrics is governed by the material model, while in compression the fabric behavior is governed by the buckling

phenomenon owing to the lack of flexural stiffness in membrane elements. In this way, the membrane-shell element formulation and material models are mutually complemented to represent the true fabric nature [30].

Studies have shown that out-of-plane bending stiffness even when they are very low compared to the tensile stiffness are quite significant and including them will represent true fabric deformation and also play a key role in capturing wrinkle onset, shape and size [34, 35]. Element formulation in finite element software which can capture the low out-of-plane bending stiffness while preserving the high tensile stiffness of the fiber direction are not present. To overcome this, authors have presented different modeling approaches to include the in-plane shear behavior and out-of-plane bending stiffness for the fabrics so that they represent the true fabric deformation.

Jauffers et al. [36] propose a discrete approach based on an explicit FE formulation using a hypoelastic description. The fabric is modeled using a combination of beam and shell elements (1-D and 2-D). The 1-D elements account for the tensile contribution of the yarns and capture the evolution of the orientation of the principal load paths as the yarns rotate and 2-D elements account only for the shearing resistance of the fabric and have no tensile stiffness.

Harrison et al. [37] included out-of-plane bending stiffness by using a constrained pantographic beam and membrane mesh approach. Membrane elements provide the in-plane shear behavior while the beam elements provide the axial stiffness, and their cross-sectional width and heights are manipulated to represent the true fabric behavior.

Nishi et al. [38] proposed modeling the fabric behavior using coupled membrane-shell hybrid model. In this model, in-plane shear is captured using the membrane elements, while the out-of-plane bending stiffness is captured with the shell elements which are at a certain offset to the membrane elements and are duplicated on the membrane elements to couple bending stiffness

to it. The thickness of the shell elements on either side is half of the value of the membrane elements. The offset of the shell reference surface is applied so that in-plane properties will not be affected.

Thompson et al. [39] proposed modeling the fabrics using shell and membrane elements which are superimposed on one another, sharing the same nodes. In-plane shear properties are controlled by the membrane elements and out-of-plane behavior (i.e. bending) is controlled by the shell elements. The hypoelastic material model is applied to both membrane and shell elements. Membrane elements are assigned the tensile modulus of the fibers and the non-linear shear stiffness of the fabric, while the shell elements are assigned Young's modulus equivalent to the flexural modulus of the material (the value to be obtained experimentally from the fabric's bending rigidity) [37, 39] and is shown in Equation (2.12). The shear rigidity of the shell elements is set to zero and so the fabric shear is controlled solely by the membrane elements. 'G' is the flexural rigidity of the fabric material and '*h'* is the thickness of the fabric. 'E' is the modulus obtained from the flexural rigidity by rearranging the terms and is to be given as an input for shell elements.

$$G = \frac{Eh^3}{12} \qquad \text{(Eq. 2.13)}$$

2.6 Forming Limit Diagrams for Fabrics

Forming limit diagrams are graphical representations of process parameter limits up to which a fabric can be successfully press-formed without any defects in the fabric preform. They can be generated either by experiments or by simulations. They can help select the process parameters that will lead to defect-free preforms and a better alternative to trial-and-error approaches commonly used in making the preforms.

Dessenberger and Tucker [40] developed an experimental method for determining the formability of random-fiber mats and also included a mathematical framework to express their

results. The forming limit maps the combinations of principal stretch ratios λ_1 and λ_2 that cause the material to fail. The forming limit curves were obtained by combining uniaxial and constrained tests. The uniaxial tests determine the wrinkling behavior when the mat is free to contract in the lateral direction and the constrained test gives the limit when lateral contraction is prohibited. The results are expressed in a formability function of the stretch ratios in which the forming limits are incorporated through a quadratic penalty function. The formability curve is shown in Figure 2.24.

Viisainen et al. [41] proposed a process-specific forming limit diagram, showing the range of shear strain and blank holder forces leading to wrinkling for non-crimp fabrics with the help of an experimental set-up using digital image correlation. They also proposed a finite element modeling technique to predict the corresponding variations in shear strain during the forming process. Wrinkles were identified by measuring the wrinkle amplitude. The forming limit diagram by Viisainen [41] is shown in Figure 2.25.

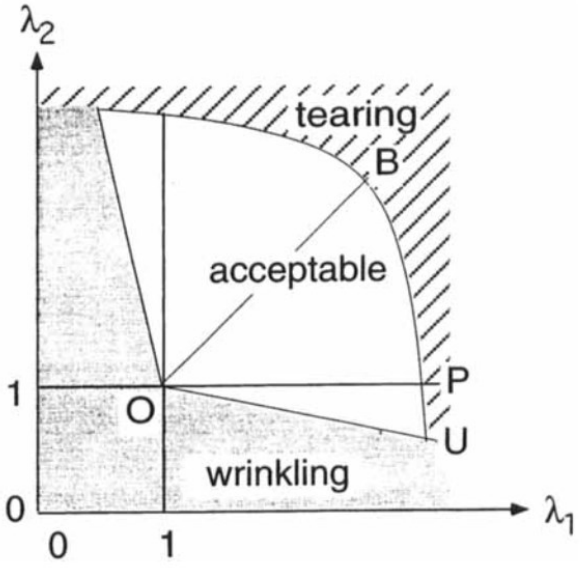

Figure 2.24: Forming limit curve as a function of the stretch ratios [40].

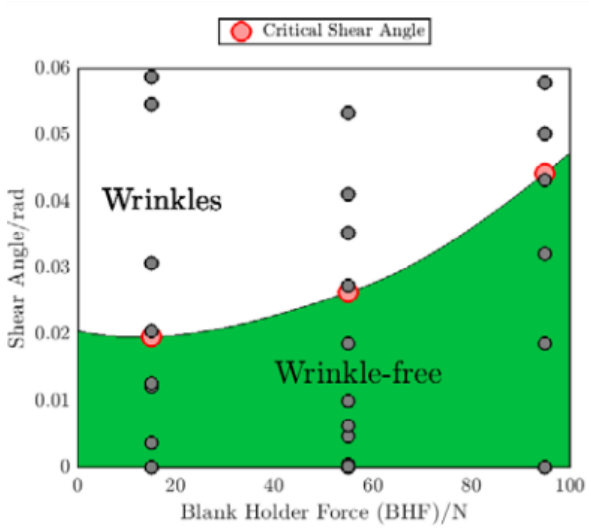

Figure 2.25: Forming limit curve expressed as a function of shear angle and blank holder force [41].

The other approach to develop forming limit diagrams for fabrics due to Vanclooster et al. [42] who investigated two-layered thermoplastic reinforced fabric laminates with different yarn orientations in different layers. A forming limit diagram was presented as a function of the shear angle and the relative yarn orientations between the layers. The decrease in the formability was characterized by a decrease in in-plane shear stiffness and an increase in wrinkling of the laminates. The forming limit diagram concept proposed by Vanclooster et al. [42] is shown in Figure 2.26.

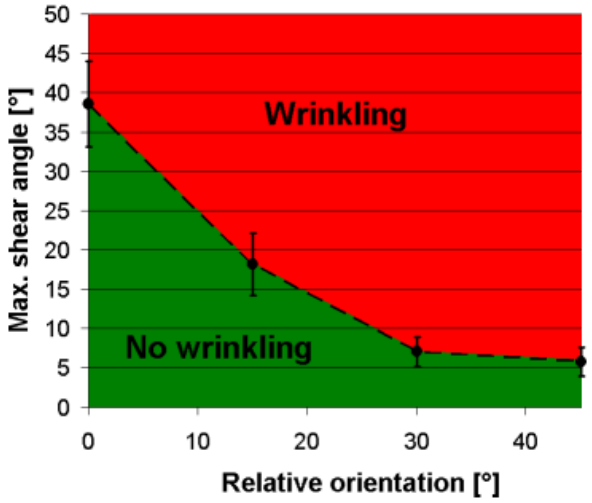

Figure 2.26: Forming limit expressed as a function of shear angle and relative orientation between plies [42].

2.7 Process Variables for Press Forming Operation

The following are the process variable for press forming of thermoplastic matrix composites.

a) Processing temperature**:** There is usually a range of processing temperatures for press forming thermoplastic matrix composites. A higher temperature outside this range can result in the thermal degradation of the polymer matrix. Lower temperatures can cause the thermoplastic polymer to be too stiff to draw-bend in the mold and form the desired shape. Also, the spring forward for the final press-formed part will be on the lower side for parts pressed under non-isothermal compared to that with isothermal forming.

b) Forming pressure: Press forming to produce thermoplastic matrix composites requires the application of an optimal value of pressure. Application of high pressure on a fiber network can be self-defeating as higher pressure compacts the fiber bundles and reduces the pores available for the resin to impregnate resulting in resin-devoid areas [43]. Also, it has been reported that closely packed fiber networks (such as in woven fabric) tend to carry the increasing load on compaction, due to the establishment of a greater number of fiber-to-fiber contacts, which results in reduced pressure available for the polymer to impregnate in fiber network and possibly in the formation of the void within the composite.

c) Holding type: During solidification, pressure has to be maintained until the part cools down below the glass transition temperature if it is an amorphous polymer and much lower than the melting point if it is a semi-crystalline polymer. This is done to suppress the shrinkage in the mold and help control the dimensional stability of the composite part. The holding time required can be achieved in two ways: (a) load holding (i.e., applying constant peak load) and (b) position holding (i.e., at the constant position after the peak load is obtained) [44]. The flexural strength of the formed part obtained with load holding was on the higher side. The

enhancement of strength of the part made through the load-holding motion was brought through the improvement of micromechanics of bonding between fibers and resin. Hence, load holding will be the optimum one to give a higher flexural strength to the press formed part.

d) Punch velocity: Optimum punch velocity has to be used for press forming thermoplastic matrix composite parts. For parts formed with very low punch velocity, the temperature of the surface can reduce below the forming temperature, leading to a reduction in formability.

e) Cooling rate: Mechanical strength of the final part will be higher if gradual cooling is used instead of fast cooling. Enhancement of strength can be attributed to higher time for the improvement of bonding between the fibers and resin. Also, the cooling rate affects the crystallization rate for semi-crystalline thermoplastic polymers. The degree of crystallinity and spherulite size decreases with an increasing cooling rate. Mechanical properties such as modulus and tensile strength increase with increasing degree of crystallinity and decreasing size of spherulites and other properties such as impact strength and fracture toughness are lower with a higher degree of crystallinity and increasing size of spherulites. Specific volume vs temperature graphs as shown in Figure 2.27 can be used to determine the cooling rate. Some of the models which have been developed for the evaluation of crystallinity level in the semi-crystalline polymer are: (a) Ozawa's crystallization kinetics model, (b) Velisaris and Seferis crystallization kinetics model, (c) Choe and Lee crystallization kinetics model, (d) Icenogle's crystallization kinetics model, etc. [45, 46].

Other process variables such as blank holder force, die clearance, press load, type of material used for dies (which affects the conduction heat transfer), etc. can affect the final shape of the press-formed part.

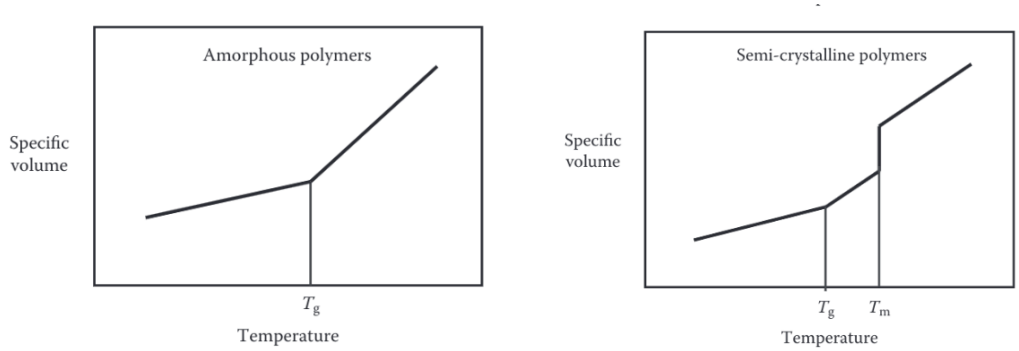

Figure 2.27: Specific volume vs. temperature diagrams of amorphous and semi-crystalline thermoplastic polymers [2].

2.8 References

[1] F. Saraiva, "Development of press forming techniques for thermoplastic composite: Investigation of a multiple step forming approach," MSc Thesis, Delft University of Technology, 2017.

[2] P. K. Mallick, Processing of Polymer Matrix Composites, Boca Raton, FL: CRC Press: Taylor & Francis Group, 2018.

[3] J. Krebs, K. Friedrich and D. Bhattacharyya, "A direct comparison of matched-die versus diaphragm forming," *Composites Part A: Applied Science and Manufacturing,* vol. 29, no. 1-2, pp. 183-188, 1998.

[4] L. M. J. Robroek, "The development of rubber forming as a rapid thermoforming technique for continuous fibre reinforced thermoplastic composites: Quality control by process control," Ph.D. Thesis, Technical University Delft, 1994.

[5] J. A. Barnes and F. N. Cogswell, "Transverse flow processes in continuous fiber-reinforced thermoplastic composites," *Composites,* vol. 20, no. 1, pp. 38-42, 1989.

[6] F. Van Der Ween, "Algorithms for draping fabrics on doubly-curved surfaces," *International Journal of Numerical Methods in Engineering,* vol. 31, pp. 1414-1426, 1991.

[7] P. Boisse, "Simulations of woven composite reinforcement forming," in *Woven Fabric Engineering*, 2010, pp. 387-414.

[8] R. S. Pierce and B. G. Falzon, "Simulating resin infusion through textile reinforcement materials for the manufacture of complex composite structures," *Engineering 3,* vol. 3, no. 5, pp. 596-607, 2017.

[9] K. Y. Sze and X. H. Liu, "A new skeletal model for fabric drapes," *International Journal of Mechanics and Materials in Design,* vol. 2, no. 3-4, pp. 225-243, 2005.

[10] N. Hamila, P. Boisse, F. Sabourin and M. Brunet, "A semi-discrete shell finite element for textile composite reinforcement forming simulation," *International Journal for Numerical Methods in Engineering,* vol. 79, no. 12, pp. 1443-1466, 2009.

[11] N. Hamila and P. Boisse, "A meso–macro three node finite element for draping of textile composite preforms," *Applied Composite Materials,* vol. 14, no. 4, pp. 235-250, 2007.

[12] P. K. Mallick, Fiber-Reinforced Composites: Materials, Manufacturing, and Design, Bosa Roca: CRC Press, 2007.

[13] H. Xiong, "Simulation of forming, compaction and consolidation of thermoplastic composites based on solid shell elements," Ph.D. Thesis, Université de Lyon, 2018.

[14] K. Buet-Gautier and P. Boisse, "Experimental analysis and modeling of biaxial mechanical behavior of woven composite reinforcements," *Experimental Mechanics,* vol. 41, no. 3, pp. 260-269, 2001.

[15] P. Boisse, B. Zouari and A. Gasser, "A mesoscopic approach for the simulation of woven fiber composite forming," *Composites Science and Technology,* vol. 65, no. 3, pp. 429-436, 2005.

[16] P. Wang, N. Hamila, P. Boisse, P. Chaudet and D. Lesuer, "Thermo-mechanical behavior of stretch-broken carbon fiber and thermoplastic resin composites during manufacturing," *Polymer Composites,* vol. 36, no. 4, pp. 694-703, 2015.

[17] V. P. W. Shim, V. B. Tan and T. E. Tay, "Modelling deformation and damage characteristics of woven fabric under small projectile impact," *International Journal of Impact Engineering,* vol. 16, no. 4, pp. 585-605, 1995.

[18] F. Dumont, "Contribution to the experimentation and modeling of the mechanical behavior of reinforcements of woven composites," Ph.D. Thesis, University of paris, 2003.

[19] B. Zouari, J. Daniel and P. Boisse, "A woven reinforcement forming simulation method. Influence of the shear stiffness," *Computers & Structures,* vol. 84, no. 5-6, pp. 351-363, 2006.

[20] M. A. Khan, C. Pasco, N. Reynolds and K. Kendall, "Shear deformability characteristics of a rapid-cure woven prepreg fabric," *International Journal of Material Forming,* vol. 14, no. 1, pp. 133-142, 2021.

[21] I. Taha, Y. Abdin and S. Ebeid, "Comparison of picture frame and bias-extension tests for the characterization of shear behaviour in natural fibre woven fabrics," *Fibers and Polymers,* vol. 14, no. 2, pp. 338-344, 2013.

[22] P. Boisse, N. Hamila , E. Guzman-Maldonado, A. Madeo, G. Hivet and F. dell'Isola, "The bias-extension test for the analysis of in-plane shear properties of textile composite reinforcements and prepregs: a review," *International Journal of Material Forming,* vol. 10, no. 4, pp. 473-492, 2017.

[23] N. Hamila and P. Boisse, "Locking in simulation of composite reinforcement deformation. Analysis and treatment," *Composite. Part A, Applied science and Manufacturing,* vol. 53, pp. 109-117, 2013.

[24] P. Harrison, F. Abdiwi, Z. Guo, P. Potluri and W. R. Yu, "Characterising the shear–tension coupling and wrinkling behaviour of woven engineering fabrics," *Composites Part A: Applied Science and Manufacturing,* vol. 43, no. 6, pp. 903-914, 2012.

[25] S. B. Sharma, M. P. F. Sutcliffe and S. H. Chang, "Characterisation of material properties for draping of dry woven composite material," *Composites Part A: Applied Science and Manufacturing,* vol. 34, no. 12, pp. 1167-1175, 2003.

[26] A. Rashidi and A. S. Milani, "A multi-step biaxial bias extension test for wrinkling/de-wrinkling characterization of woven fabrics: Towards optimum forming design guidelines," *Materials & Design,* vol. 146, pp. 273-285, 2018.

[27] F. T. Pierce, "26-The handle of cloth as a measurable quantity," *Journal of the Textile Institute Transactions,* vol. 21, no. 9, pp. 377-416, 2008.

[28] H. Yildirim and F. Ozturk, "A benchmark study of the material models for forming simulation of woven fabrics," *The Journal of the Textile Institute,* vol. 113, no. 6, pp. 1027-1038, 2021.

[29] A. Tabiei and R. Murugesan, "Thermal structural forming simulation of carbon and glass fiber reinforced plastics composites," *International Journal of Composite Materials,* vol. 5, no. 6, pp. 182-194, 2015.

[30] I. Ivanov and A. Tabiei, "Loosely woven fabric model with viscoelastic crimped fibers for ballastic impact simulations," *International Journal for Numerical Methods in Engineering,* vol. 61, no. 10, pp. 1565-1583, 2004.

[31] A. Tabiei and I. Ivanov, "Computational micro-mechanical model of flexible woven fabric for finite element impact simulation," *International Journal for Numerical Methods in Engineering,* vol. 53, no. 6, pp. 1259-1276, 2002.

[32] J. L. Hill, "Mechanical property determination for flexible material systems," Ph.D. Thesis, Georgia Institute of Technology, 2016.

[33] "LS-Dyna Keyword User's Manual Volume II R11.0," Livermore Software Technology Corporation (LSTC), 2018.

[34] P. Boisse, N. Hamila, E. Vidal-Salle and F. Dumont, "Simulation of wrinkling during textile composite reinforcement forming. Influence of tensile, in-plane shear and bending stiffnesses," *Composites Science and Technology,* vol. 71, no. 5, pp. 683-692, 2011.

[35] B. Liang, N. Hamila, M. Peillon and P. Boisse, "Analysis of thermoplastic prepreg bending stiffness during manufacturing and of its influence on wrinkling simulations," *Composites Part A: Applied Science and Manufacturing,* vol. 67, pp. 111-122, 2014.

[36] D. Jauffres et al., "Discrete mesoscopic modeling for the simulation of woven-fabric reinforcement forming," *Internation Journal of Material Forming,* vol. 3, no. 2, pp. 1205-1216, 2010.

[37] P. Harrison, "Modelling the forming mechanics of engineering fabrics using a mutually constrained pantographic beam and membrane mesh," *Composites Part A: Applied Science and Manufacturing,* vol. 81, pp. 145-157, 2016.

[38] M. Nishi and T. Hirashima, "Approach for dry textile composite forming simulation," *19th International Conference on Composite Materials,* pp. 7486-7493, 2013.

[39] A. J. Thompson, J. P. Belnoue and S. R. Hallett, "Modelling defect formation in textiles during the double diaphragm forming process," *Composites Part B: Engineering,* vol. 202, p. 108357, 2020.

[40] R. Dessenberger and C. L. Tucker III, "Forming limit measurements for random fiber mats," *Polymer composites,* vol. 19, no. 4, pp. 370-376, 1998.

[41] V. Viisainen, J. Zhou and M. P. Sutcliffe, "Development of a composite forming diagram: A feasibility study," in *22nd International Conference on Composite Materials*, Melbourne, Australia, Aug 2019.

[42] K. Vanclooster, S. V. Lomov and I. Verpost, "On the formability of muti-layered fabric composites," in *ICCM International Conferences on Composite Materials*, Edinburgh, Scotland, 2009.

[43] T. G. Gutowski, "A brief introduction to composite materials and manufacturing process," in *Advanced composite manufacturing*, New York, John Wiley & Sons, 1977.

[44] D. Tatsuno, T. Yoneyama, K. Kawamoto and M. Okamoto, "Hot press forming of thermoplastic CFRP sheets," *Procedia Manufacturing,* vol. 15, pp. 1730-1737, 2018.

[45] C. Ageorges and L. Ye, "Crystallisation Kinetics," in *Fusion Bonding of Polymer Composites*, London; New York, Springer, 2002, pp. 135-160.

[46] T. A. Osswald and G. Menges 1923, Materials Science of Polymers for Engineers. (2nd ed.), Munich; Cininnati: Hanser Publishers, 2009.

Chapter 3 Press Forming of Polypropylene by Warm Deep Drawing

3.1 Introduction

Deep drawing is a well-established metal forming process [1] and is widely used with steels, aluminum alloys and other metals in the automotive as well as non-automotive industries. Even though several articles have been published on deep drawing of polymers [2, 3, 4, 5, 6, 7], it has not found widespread applications in the plastics industry. One of the common manufacturing processes in the plastics industry is called thermoforming in which a preheated thin plastic sheet is placed on a mold and vacuum formed into the shape of the mold [8]. The preheating temperature is much above the glass transition temperature for amorphous polymers and close to or slightly above the melting point for semi-crystalline polymers. There are several variations of the thermoforming process, one of which is called plug-assist vacuum forming. In all these variations, the major deformation mode of the preheated sheet is biaxial stretching. In deep drawing operation, on the other hand, the deformation of the sheet takes place by a combination of drawing and stretching.

During the past several years, polypropylene (PP) has found an increasing number of applications in automotive components such as instrument panels and housings, and in household products, such as containers. The reasons for selecting PP in many such applications can be attributed to its low density of 0.9 g/cm^3, relatively low cost and a balance of mechanical properties. In addition to weight and cost savings, the other qualities offered by PP are very low water absorption, good chemical resistance, high food safety and low electrical conductivity.

Manufacturing polypropylene products using deep drawing process has not been much explored in the past. Research on deep drawing of polymers has dealt mostly with amorphous polymers, such as acrylonitrile-butadiene-styrene (ABS) and polycarbonate [2, 3, 4, 5, 6, 7]. In these studies, the emphasis was more on the relationship of deep drawability with material parameters and not with process parameters. In addition to several amorphous polymers, Evans [3] performed cup drawing tests on polypropylene at 23°C and observed failure by necking in the cup wall. Machida and Lee [7] reported experimental results on the cup drawing of propylene-ethylene copolymer under isothermal and differential heating conditions at temperatures up to 130°C. Although cups could be formed under both heating conditions, differential heating in which the flange area of the blank was at a higher temperature than the punch area produced a higher draw depth than isothermal heating in which the flange and punch areas of the blank were at the same temperature.

In the current work, deep drawing of a polypropylene homopolymer was numerically studied using LS-DYNA, a commercially available and widely used finite element software for non-linear analysis of structures and processes. PP has a glass transition temperature of -20°C and a melting point of 170°C [9]. It exhibits brittle behavior at temperatures at or below -10°C, and above the melting point, it transforms into a liquid state. A manufacturing process called solid phase stretch forming is used with polypropylene to produce cylindrical and rectangular containers. The recommended initial sheet temperature to successfully form these containers is 150-160°C, which is in the thermoforming temperature range of 145-166ºC of polypropylene.

In this study, the processing window for deep drawing of PP was selected to be between 25°C and 125°C, which is much below its thermoforming temperature range [9]. The initial die/punch temperature was set at 25°C. The forming speed was set at 100 mm/s. The effects of

temperature and strain rate variations in the PP blank during deep drawing were accounted for in the numerical study using the material constitutive model described below. Because of the relatively low forming temperature and high forming speed, viscoelastic effect during deep drawing was not considered. The deep drawability of PP was determined by the depth of draw and drawing limit for successful forming of circular blanks to round cup shapes. The effects of blank holder force, initial blank temperature and blank diameter were also studied.

3.2 Tensile Characteristics of Polypropylene

The following three-parameter nonlinear constitutive model proposed by Zhou and Mallick [10] was used to develop a series of tensile stress-strain curves of PP needed as an input for finite element simulations of the deep drawing process.

$$\sigma = \frac{E(\dot{\varepsilon}, T)\,\varepsilon}{1 + E(\dot{\varepsilon}, T)\,\beta(\dot{\varepsilon}, T)\,\varepsilon^{m}} \qquad \text{(Eq. 3.1)}$$

In Equation (3.1), the stress σ is expressed as a function of strain ε, modulus E, and compliance factor β and strain exponent m. Both E and β depend on the strain rate $\dot{\varepsilon}$ and temperature T, but m is considered a constant.

Zhou and Mallick [11] also presented the experimental tensile stress-strain curves for an unfilled polypropylene at various strain rates and temperatures. They are shown in Figure 3.1. The corresponding modulus and yield strength (at 0.2% of strain), compliance factor β and strain exponent m are given in Table 3.1. It is evident from Table 3.1 that both modulus and yield strength values are temperature and strain rate dependent. Compliance factor shows an increasing trend with temperature and a decreasing trend with strain rate. Strain exponent m on the other hand does not show any trend with either temperature or strain rate; hence it is considered to be independent

of both temperature and strain rate. The values of *m* in Table 3.1 were averaged to obtain the value of the strain exponent m as 1.31.

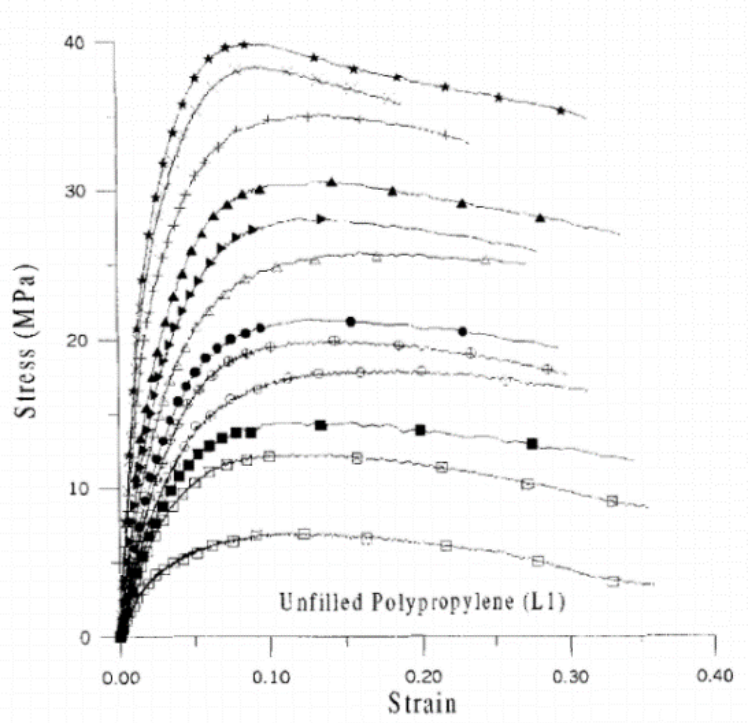

Stress-strain curves of unfilled polypropylene in the flow (L) direction at various strain rates and temperatures. + 21.5°C, 0.05 min⁻¹; × 21.5°C, 0.5 min⁻¹; ★ 21.5°C, 5 min⁻¹; △ 50°C, 0.05 min⁻¹; ▶ 50°C, 0.5 min⁻¹; ▲ 50°C, 5 min⁻¹; ○ 75°C, 0.05 min⁻¹; ⊕ 75°C, 0.5 min⁻¹; ● 75°C, 5 min⁻¹; □ 100°C, 0.05 min⁻¹; ⊡ 100°C, 0.5 min⁻¹, ■ 100°C, 5 min⁻¹.

Figure 3.1: Experimental stress-strain curves of an unfilled PP at various strain rates and temperatures [11].

To account for the effects of varying temperature and strain rate on the modulus, yield strength and compliance factor of the PP during the deep drawing operation, a parametric equation of the general form given by Equation (3.2) was used. In this equation, the parameters *a*, *b*, and *c* are different for the modulus, yield strength and compliance factor. T_0 and $\dot{\varepsilon}_0$ in Equation (3.2) are the reference temperature and strain rate, respectively. The parameters *a*, *b* and *c* were determined using MATLAB Curve Expert to fit the data given in Table 3.1. Their values are listed in Table 3.2. The reference temperature and strain rate were 21.5°C and 0.05 s^{-1}, respectively.

$$E, \sigma_y, \beta = a\left(1 + b \cdot \ln\left(\frac{\dot{\varepsilon}}{\dot{\varepsilon}_0}\right)\right) \cdot exp\left(c.\left(T - T_0\right)\right) \qquad \text{(Eq. 3.2)}$$

Table 3.1: Constitutive parameters of PP determined from experimental curves in Figure 3.1.

Temp (°C)	Strain rate (min^{-1})	Modulus (MPa)	Yield strength (MPa)	m	β (MPa^{-1})
21.5	0.05	1420	15.62	1.2425	0.03813
21.5	0.5	1760	18.18	1.2595	0.03781
21.5	5	1901	18.87	1.2714	0.03729
50	0.05	735	10.46	1.3182	0.05514
50	0.5	866	11.25	1.3281	0.05198
50	5	1040	11.76	1.2969	0.04649
75	0.05	480	6.36	1.3585	0.08082
75	0.5	523	6.83	1.3916	0.07903
75	5	613	7.79	1.35	0.06988
100	0.05	287	4.16	*	*
100	0.5	381	4.49	1.3445	0.12906
100	5	465	4.75	1.2947	0.09757

Using Equations (3.1) and (3.2), theoretical stress-strain curves were generated for temperatures ranging from 20 to 130°C in intervals of 10°C and at strain rates of 0.1, 10, 100 s^{-1}. Theoretical stress-strain curves were compared with the available experimental curves in Figure 3.1, and they showed a very small difference. Figure 3.2 shows the theoretical curves for a strain rate of 0.1 s^{-1} at respective temperatures. The theoretical stress-strain curves thus generated were given as input for the FE simulations of the deep drawing behavior of PP. The variations of yield strength and modulus of PP with temperature at 0.1 s^{-1} strain rate are shown in Figures 3.3 and 3.4. These diagrams were obtained from Equation (3.2) and were used as input to the FE simulations.

Table 3.2: Parameters in Equation (3.2) to determine the variations in modulus, yield strength and compliance factor β as functions of strain rate and temperature.

	a	b	c
Modulus (E)	1420	0.07132	-0.01992
Yield strength (σ_y)	15.62	0.0597	-0.0174
β	0.034105	0.005165	0.015245

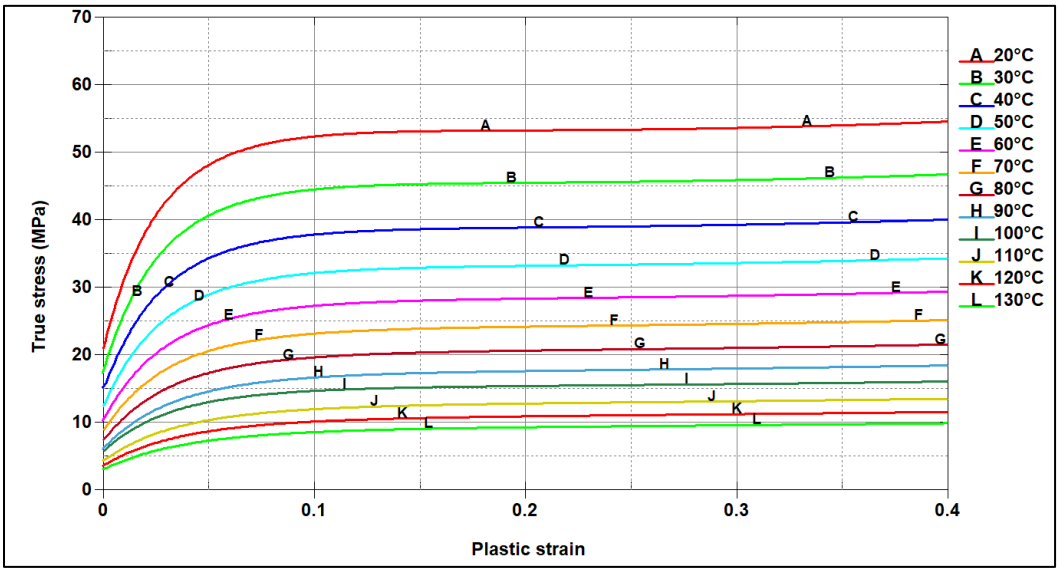

Figure 3.2: Stress-strain curves at 0.1 s^{-1} and different temperatures ranging from 20 to 130˚C.

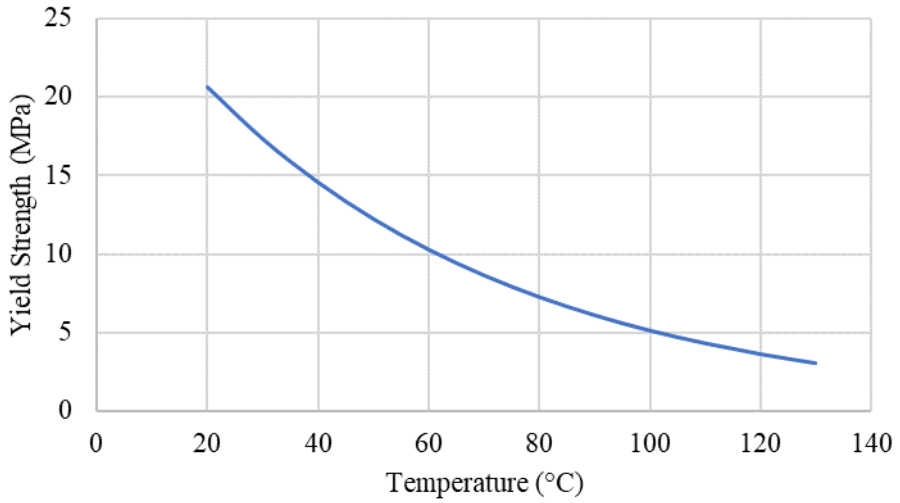

Figure 3.3: Yield strength variation of PP as a function of temperature at a strain rate of 0.1 s^{-1}.

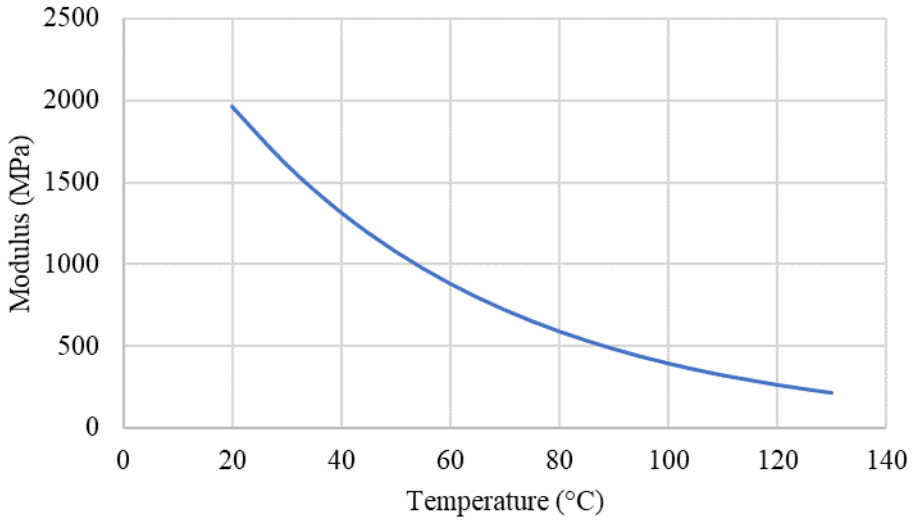

Figure 3.4: Modulus variation of PP as a function of temperature at a strain rate of 0.1 s^{-1}.

3.3 Deep Drawing Setup

Figure 3.5 shows the die-punch setup consisting of an open die, a flat-bottomed punch and a circular blank holder used in this study. A circular polypropylene blank of 1.2 mm thickness and a punch diameter of 50 mm were selected. To study the effect of blank diameter on the depth of draw, three different blank diameters, namely 80, 90 and 100 mm, were used. The remaining die-punch dimensions based on the guidelines prescribed by Donaldson et al. [12] for sheet metal deep drawing were as follows: die-punch clearance = 1.4 mm, die opening diameter = 52.8 mm, punch and die corner radii = 8 mm. The die, punch and blank holder material was aluminum.

Deep drawing parameters used in the study are listed in Table 3.3. Deep drawing simulation studies on PP were conducted using LS-Dyna to study the variation of depth of draw or cup draw depth, punch force, blank temperature distribution, blank thickness and plastic strain with process and material variables. The variables under consideration for this study are (1) blank holder force, (2) initial blank temperature, (3) blank diameter, (4) blank thickness, (5) friction co-efficient, (6) die corner radius, (7) punch corner radius, (8) punch velocity and (9) failure strain.

Table 3.3: Deep drawing parameters considered in the study.

Study	Deep drawing parameters
Effect of blank holder force	Blank diameter = 90 mm, Initial blank temperature = 100°C, Punch velocity = 100 mm/s, **Blank holder force = 200, 500, 1000, 1500 N**.
Effect of initial blank temperature	Blank diameter = 90 mm, **Initial blank temperature = 25, 50, 75, 100 and 125°C**, Punch velocity = 100 mm/s, Blank holder force = 500 N.
Effect of blank diameter	**Blank diameter = 80, 90 and 100 mm**, Initial blank temperature = 100°C, Punch velocity = 100 mm/s, Blank holder force = 500 N
Effect of blank thickness	Blank diameter = 90 mm, Initial blank temperature = 100°C, Punch velocity = 100 mm/s, Blank holder force = 500 N, **Blank thickness = 0.8, 1, 1.2, 1.4 mm**.
Effect of friction co-efficient	Blank diameter = 90 mm, Initial blank temperature = 100°C, Punch velocity = 100 mm/s, Blank holder force = 500 N, **Static and dynamic friction co-efficient = 0.1, 0.2, 0.3, 0.4**.
Effect of die corner radius	Blank diameter = 90 mm, Initial blank temperature = 100°C, Punch velocity = 100 mm/s, Blank holder force = 500 N, **Die corner radius = 4, 6, 8, 10 mm**.
Effect of punch corner radius	Blank diameter = 90 mm, Initial blank temperature = 100°C, Punch velocity = 100 mm/s, Blank holder force = 500 N, **Punch corner radius = 4, 6, 8, 10 mm**.
Effect of failure strain	Blank diameter = 90 mm, Initial blank temperature = 100°C, Punch velocity = 100 mm/s, Blank holder force = 500 N, **Failure strain = 0.3, 0.6, 0.9, 1.2, no failure strain**.
Effect of punch velocity	Blank diameter = 90 mm, Initial blank temperature = 100°C, Blank holder force = 500 N, **Punch velocity = 5, 20, 50, 100, 200 mm**/s.

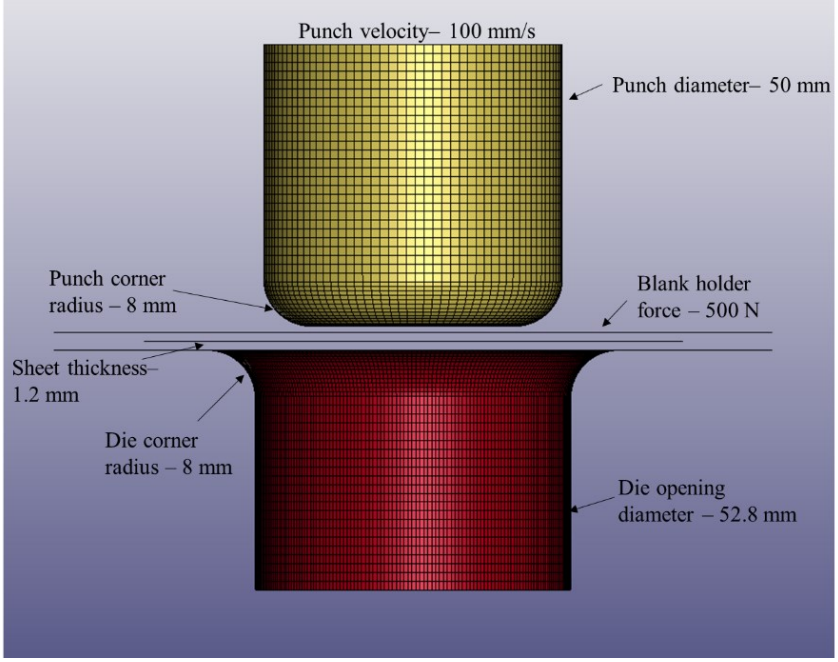

Figure 3.5: Deep drawing setup

3.4 Finite Element Modeling

The mesh size for the die and the punch was selected as 1.5 mm with higher mesh density at both die and punch corner radii as shown in Figure 3.6. For the blank, the mesh size was 1 mm. A higher mesh density was used at the punch and die corner radii so that the blank can accommodate the geometrical inconsistences.

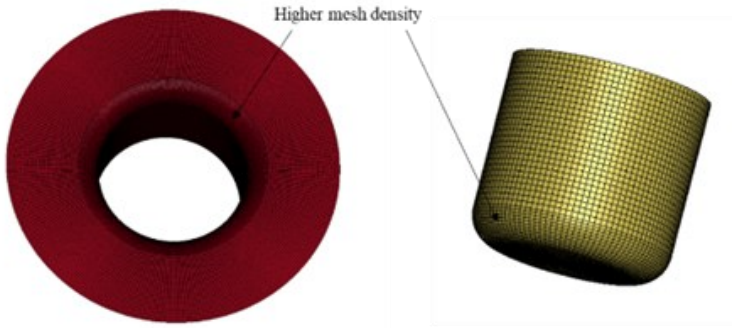

Figure 3.6: Higher mesh density at critical locations.

The material model used to simulate the behavior of PP during the warm deep drawing operation was MAT_106 (MAT_ELASTIC_VISCOPLASTIC_THERMAL). Since the behavior

of PP is both temperature and strain rate dependent; the material model which considers both temperature and strain rate effects was selected. Theoretical curves depicted in Figure 3.2 were given as an input for FE simulation. The aluminum die-punch set was modelled using rigid shell elements and material model MAT_20 (MAT_RIGID). Thermal properties of both PP and aluminum, tabulated in Table 3.4, were incorporated using the material model T_01 (THERMAL_ISOTROPIC).

Blank temperature changes from its initial value as the punch contacts the blank and draws it into the die due to conduction heat transfer between the blank and the punch/die surfaces. Some amount of heat will be generated because of friction at the surfaces of contact, and also due to the plastic deformation of PP. This will also contribute to the changes in the blank temperature with time. Variations of yield strength and modulus due to changes in blank temperature were given as inputs for the FE simulations. Examples of such variations are shown in Figures 3.3 and 3.4. Variation of plastic strain at failure with temperature (Figure 3.7), was given as an input to predict failure of the PP blank during the deep drawing operation. Figure 3.7 was obtained from Figure 3.1 which shows that the plastic strain at failure increases with temperature, but the effect of strain rate is relatively small.

Table 3.4: Thermal properties of aluminum and PP.

Parameter	Aluminum [13]	Polypropylene [14]
Heat Capacity (J/kg. k)	900	1800
Thermal conductivity (W/m. K)	205	0.14

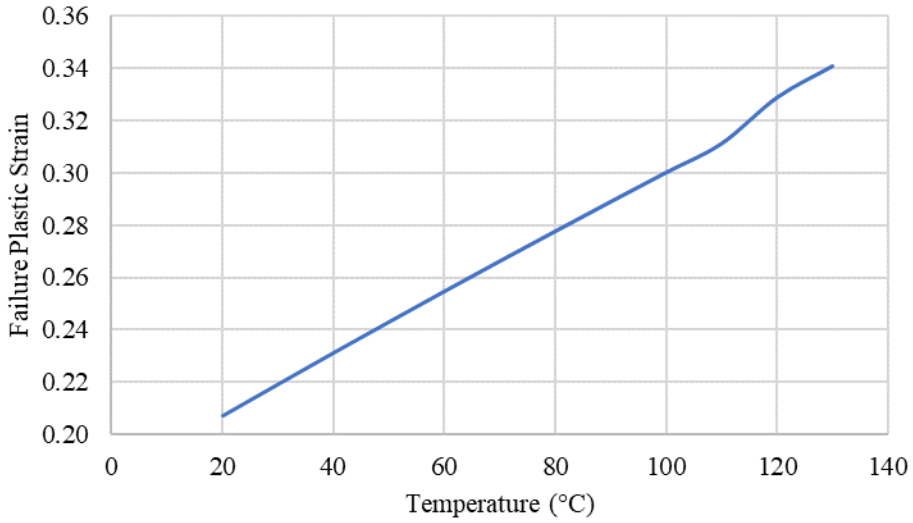

Figure 3.7: Failure plastic strain variation of PP as a function of temperature.

Three regions of contact were considered in the FE simulations: (1) contact between the punch and the blank, (2) contact between the blank holder and the blank, and (3) contact between the die wall and the blank. Friction conditions at these contact areas play an important role in the deformation of PP blanks. Also, the friction conditions will be different at different temperatures and will include sliding friction at lower temperatures and sticking friction at higher temperatures. Friction coefficient variation as a function of temperature shown in Figure 3.8 is from the study by Chung et al. [15] and was given as an input for the FE simulations.

Thermal contact conductance value was given as in input based on the study conducted by Marotta et al. [16]. The thermal conductance values govern the conduction heat transfer that occurs between the PP and the aluminum surfaces during the deep drawing operation. Thermal contact conductance of PP with aluminum was found to be between 276.7 – 324 W/m^2 K [16]. An intermediate value of 300 W/m^2 K was selected for this study.

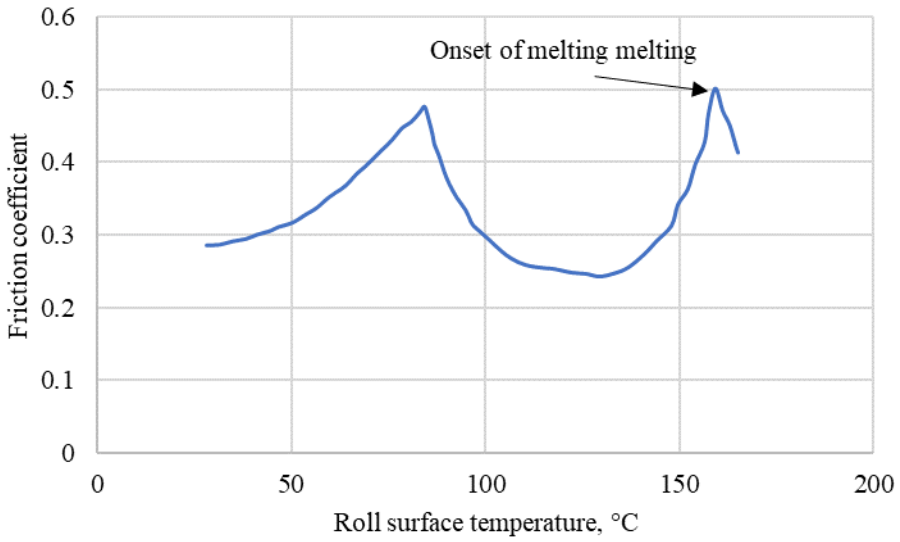

Figure 3.8: Friction co-efficient between PP and aluminum surfaces as a function of temperature [15].

3.5 Results

Deep drawing simulation studies on PP were conducted using LS-Dyna to study the variation of depth of draw or cup draw depth, drawing limit, punch force, blank temperature distribution, blank thickness, and plastic strain with process variables. The drawing limit, as defined by Machida and Lee [7], is equal to $\left[1-\left(\frac{d_f}{d_o}\right)\right]$, where d_f is the final flange diameter and d_o is the initial blank diameter. The process variables under consideration for this study are (1) blank holder force, (2) initial blank temperature, (3) blank diameter, (4) blank thickness, (5) friction co-efficient, (6) die corner radius, (7) punch corner radius, (8) failure strain and (9) punch velocity.

3.5.1 Blank Holder Force

Blank holder force plays a very important role in deep drawing since it affects the flow characteristics of a circular blank. As the blank is drawn into the die, its flange is subjected to a tensile stress in the radial direction and a compressive stress in the circumferential direction [1]. Too low a blank holder force can cause the edges of the blank to lift off the top surface of the die

and can result in the formation of wrinkles due to the circumferential compressive stress. Too high a force may prevent the flow of the blank material into the space between the die and the punch and can cause failure of the blank due to excessive thinning and tearing at or near the top corner radius due to high radial tensile stress. In this study, blank holder forces considered were 200 N, 500 N, 1000 N and 1500 N. The cup draw depths attained just before failure at these blank holder forces are given in Table 3.5 and the locations of failure are shown in Figure 3.9.

Table 3.5: Draw depth just before failure and failure locations at different blank holder forces (with 100°C initial blank temperature).

Blank holder force	200 N	500 N	1000 N	1500 N
Draw depth attained just before failure (mm)	12.89	18.87	18.34	17.31
Max. punch force (N)	1371.4	2476.4	2705.5	2843.2
Drawing limit = $(1- d_f/d_o)$	0.0649	0.1391	0.1160	0.0940
Failure location	Wrinkling in the flange area	Plastic strain exceeding failure strain at the top corner radius		Tearing at the bottom corner radius

Failure in the blank at 200 N can be attributed to the formation of wrinkles along the flange area. Failure at 500 and 1000 N blank holder forces was observed when the plastic strain in the PP cup at the top corner radius exceeds the failure limit. At 1500 N blank holder force, the failure can be attributed to excessive thinning and tearing of the blank along the cup wall near the bottom corner radius due to a high resistance to the flow of the blank material. The highest depth of draw just before failure was observed with 500 N blank holder force. Similar observation can be made by considering the variation of drawing limit as a function of blank holder force plotted in Figure

3. 10. It shows that at a blank temperature of 100ºC, the highest drawing limit was obtained at 500 N blank holder force.

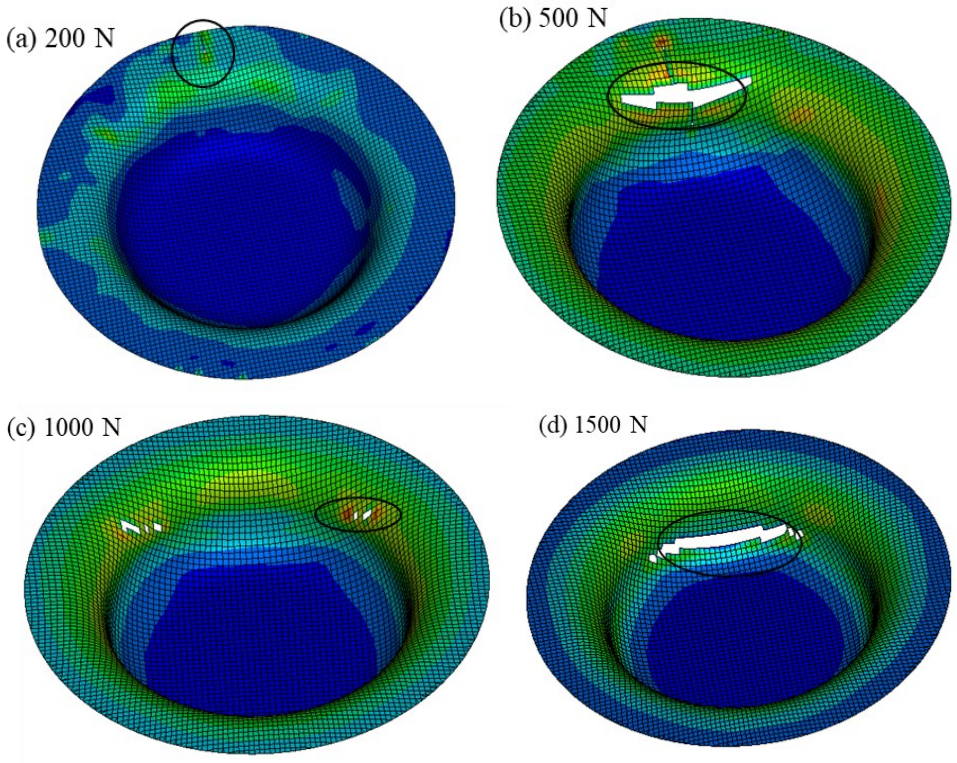

Figure 3.9: Failure locations at different blank holder forces.

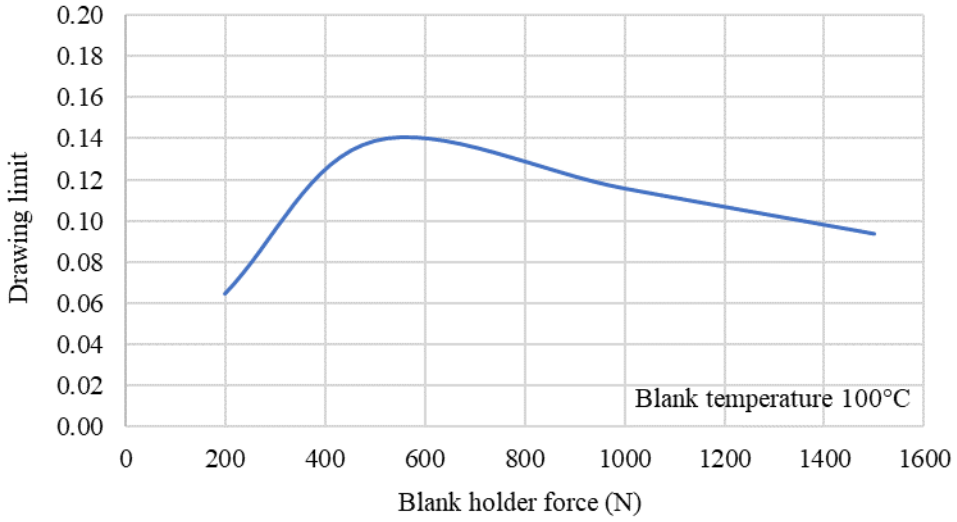

Figure 3.10: Drawing limit as a function of blank holder force for a blank diameter of 90 mm and initial blank temperature of 100°C.

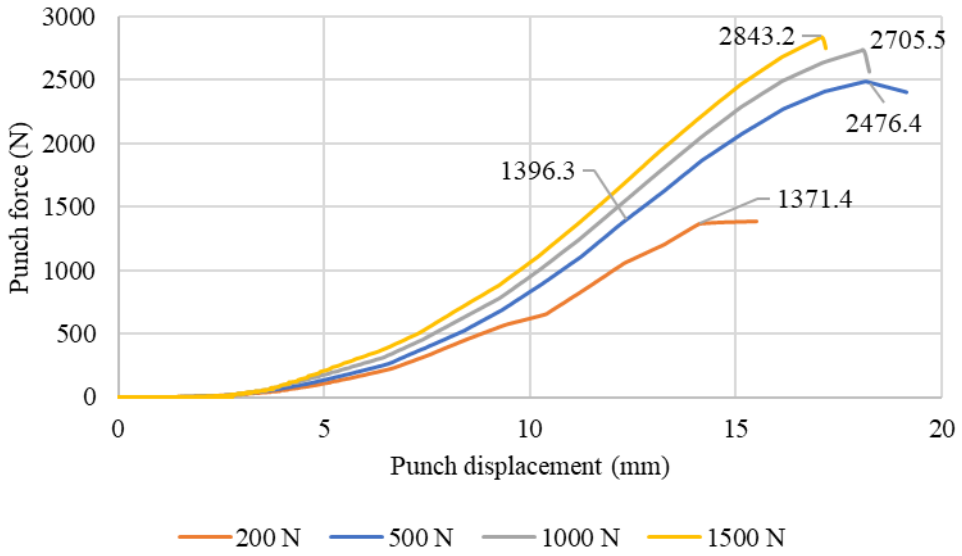

Figure 3.11: Effect of blank holder force on punch force vs. punch displacement diagrams.

Figure 3.11 represents the effect of blank holder force on punch force vs. punch displacement diagrams. The punch force required to deep draw the blank increases with increase in blank holder force which can be attributed to the higher resistance offered by the material to the drawing of the blank. Sudden drop in load is due to the failure of the blank which is either due to wrinkling, plastic strain exceeding the failure strain or excessive thinning and tearing of the blank.

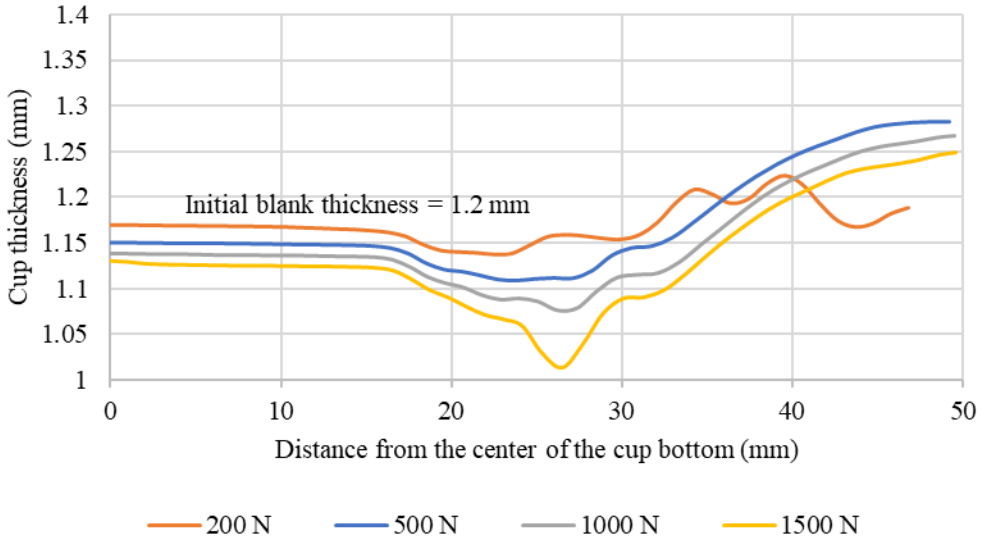

Figure 3.12: Cup thickness variations in deep-drawn cups at different blank holder forces.

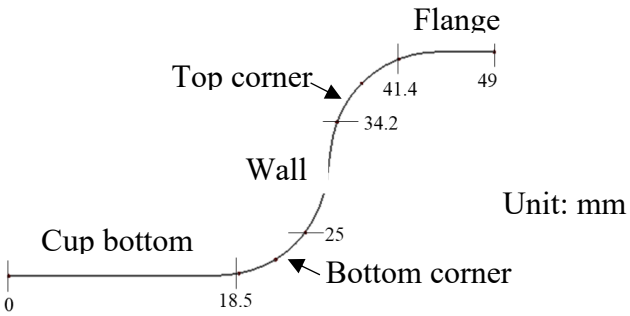

Figure 3.13: Distance markers from the center of the cup bottom to the end of the flange in deep-drawn cups.

The cup thickness variations in the deep-drawn cups just before failure are plotted in Figure 3.12 along the distance from the center of their cup bottom to the end of their flange. The distance markers are shown in Figure 3.13. Thickness of the cup in the cup bottom and cup wall at the draw depth attained just before failure was observed to decrease with increase in blank holder force. Increase in cup thickness in the flange area was found to be lower for the higher blank holder forces (Figure 3.12), which can be attributed to the higher resistance to the flow of the blank material, thus restricting the increase in thickness of the blank. At 200 N blank holder force, the cup thickness shows very little variation, which can be attributed to the failure of the blank at a lower draw depth due to the formation of wrinkles in the flange area. Cup thickness variation at 1500 N shows a much higher decrease in thickness of the cup wall which can be attributed to the high amount of stretching of the blank at 1500 N blank holder force.

For the blank drawn at 500 N blank holder force, the thickness variations with time in the cup bottom, cup wall and flange area are shown in Figure 3.14. At the end of the draw, cup thickness along the flange area shows an increase in thickness from 1.2 to 1.28 mm, while the thickness along the cup bottom and cup wall shows a decrease to 1.15 and 1.13 mm, respectively. Cup thickness in the cup bottom decreases to 1.15 mm after which it remains constant, while the thickness along the cup wall continues to decrease indicating the thinning of the blank.

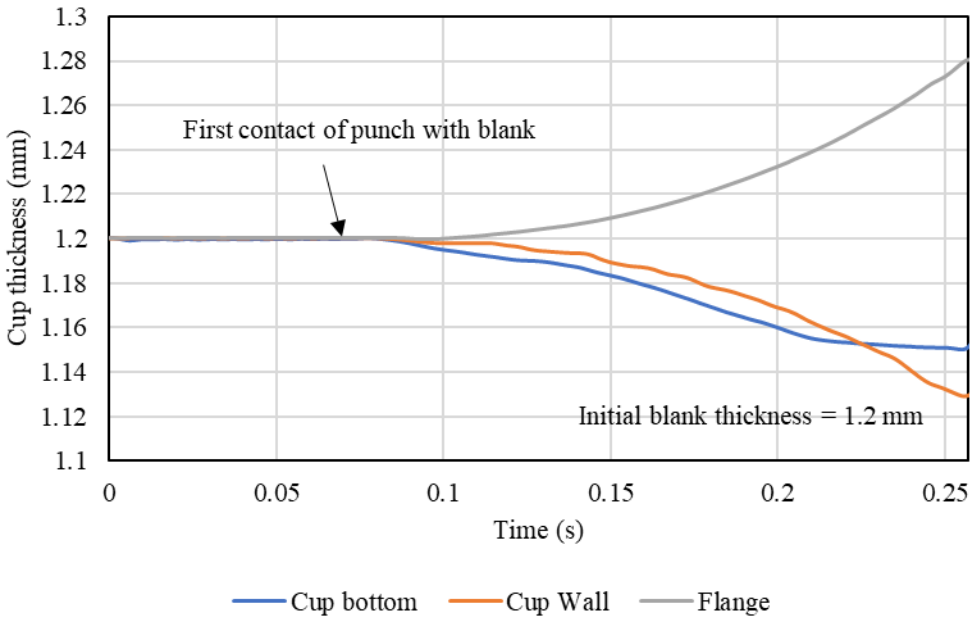

Figure 3.14: Cup thickness variation at different regions of the deep drawn PP cup at 500 N blank holder force as a function of time. The arrow indicates the time at which the punch contacts the blank.

Temperature distribution profiles at the cup bottom and cup wall were found to be almost similar for deep drawing with 500 N, 1000 N and 1500 N blank holder forces, which is evident from Figure 3.15. Deep drawing with 200 N blank holder force shows a lower drop in temperature which can be attributed to the failure of the blank at lower draw depth and therefore, shorter time of contact with the punch. Temperature along the flange showed a higher drop compared to the cup bottom since flange area is in contact with both blank holder and die, while the cup bottom is only in contact with the punch. Temperature decrease in different regions of the blank just before failure at 500 N blank holder force is shown in Figure 3.16. The highest temperature was found along the bottom corner radius which can be attributed to the heat generation due to thinning and due to lesser contact surface area.

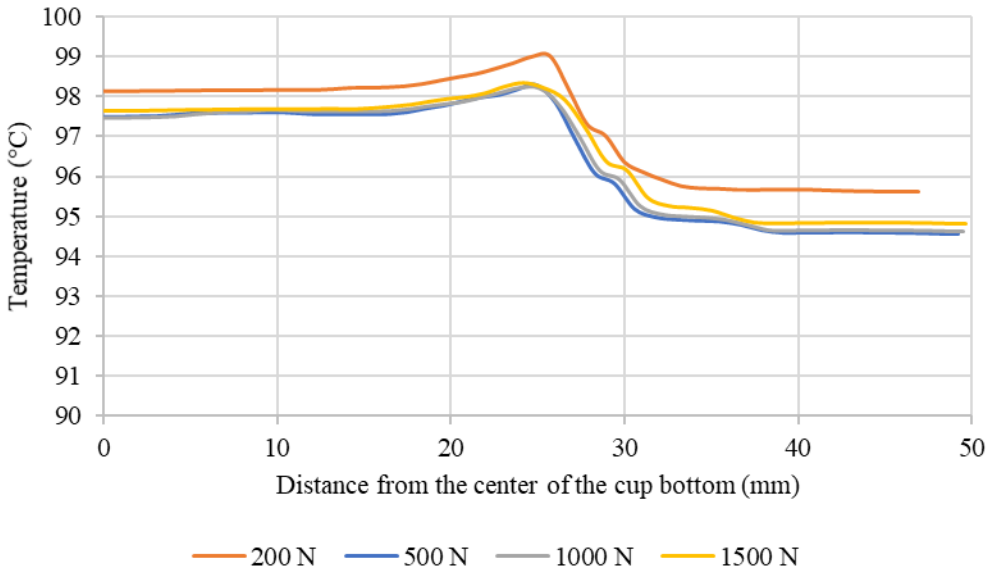

Figure 3.15: Temperature distributions at different blank holder forces just before failure.

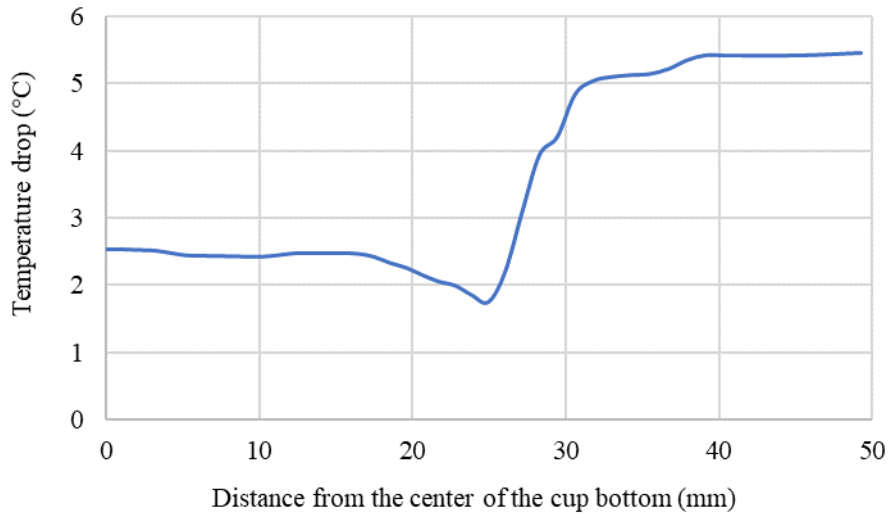

Figure 3.16: Temperature drop from the initial blank temperature of 100°C at the end of deep drawing at 500 N blank holder force.

Effective plastic strain variation in deep drawn cups just before failure is shown in Figure 3.17. Plastic strain at the cup bottom was found to increase only slightly with blank holder force, since the cup bottom does not experience much stretching. Plastic strains are much higher in the cup wall due to increased amount of stretching with increasing blank holder force and they reach a peak at the die entry radius where the blank undergoes bending and unbending. For deep drawing

at 1500 N blank holder force, the plastic strain at the die entry radius was found to be less compared to those at 500 and 1000 N, but higher in the cup wall near the bottom corner radius which is the failure location in the cup at 1500 N blank holder force. Figure 3.17 also indicates that stretching and thinning of the blank increase with increase in blank holder force.

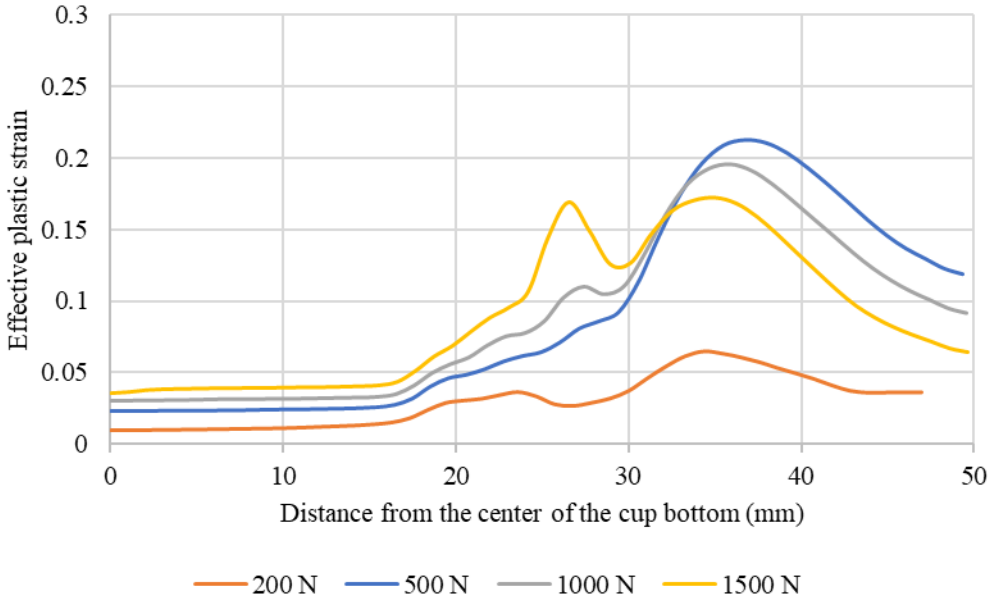

Figure 3.17: Effective plastic strain variations at different blank holder forces just before failure.

3.5.2 Initial Blank Temperature

Blank temperature plays an important role in deep drawing of PP sheets, since decreasing the blank temperature decreases the failure strain of PP and increasing the blank temperature too high can cause the PP blank to lose its stiffness and cause sagging before the punch comes in contact with the blank. In this section, deep drawability of PP sheet is studied at five different initial blank temperatures, namely 25°C, 50°C, 75°C, 100°C and 125°C. The blank holder force was maintained at 500 N. The draw depths with these five initial blank temperatures are reported in Table 3.6.

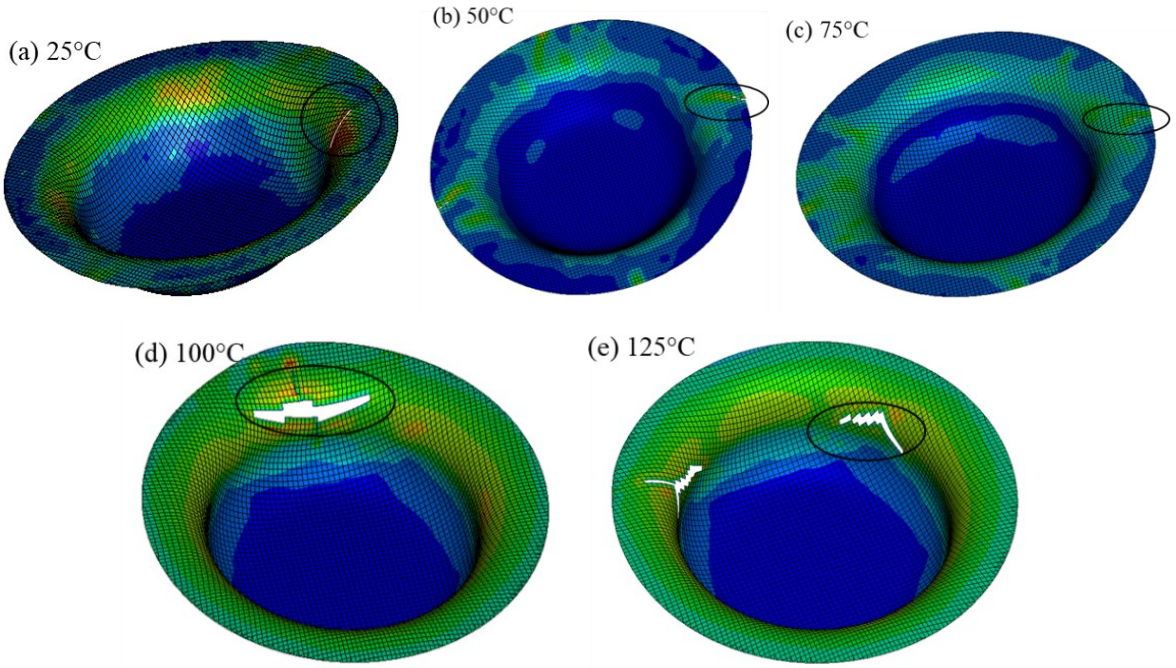

Figure 3.18: Failure locations at different initial blank temperatures.

Table 3.6: Draw depth just before failure and failure location at different initial blank temperatures (with blank holder force at 500 N).

Initial blank temperature	25°C	50°C	75°C	100°C	125°C
Draw depth attained just before failure (mm)	10.63	11.33	13.79	18.87	20.64
Max punch force (N)	1674.3	1516.0	1686.1	2476.4	1618.3
Drawing limit = $(1- d_f/d_o)$	0.0433	0.0482	0.0744	0.1391	0.1471
Failure location	Strain exceeding failure strain in flange area			Strain exceeding failure strain at top corner radius	

Failure in the flange area (Figure 3.18) with initial blank temperatures at 25°C, 50°C and 75°C can be attributed to the blank exhibiting higher stiffness at these temperatures and therefore, offering higher resistance to flow. Draw depth attained at 25°C is low due to low failure strain of PP at this

temperature. Wrinkles were also observed on the flange surface at 50°C and 75°C. For deep drawing at 100°C and 125°C, failure occurred at the top corner radius when the strain exceeded the respective failure strain. The draw depth attained before failure increases with increase in initial blank temperature as can be seen in Table 3.6. Drawing limit as a function of blank temperature is plotted in Figure 3.19 for a blank diameter of 90 mm and a blank holder force of 500 N. It shows a slowly increasing trend with blank temperature similar to that observed by Machida and Lee [7] in their deep drawing experiments with propylene-ethylene copolymer under isothermal heating condition. The drawing limit values are similar to the experimental values reported in their work [7].

Force required to draw the PP blank decreases with increasing initial blank temperature as can be seen in Figure 3.20. Decrease in the slopes of the punch force vs. punch displacement diagram can be attributed to lower stiffness and lower stress-strain behavior of PP at higher temperatures so that the force required to produce the deformation in the blank decreases with increase in initial blank temperature.

Figures 3.21-3.23 show the variations in cup thickness, temperature and effective plastic strain at the draw depth before failure for deep drawing at different initial blank temperatures. Cup thickness variation plots show that deep drawing at 100°C and 125°C have the lowest thickness along the cup wall near the bottom corner radius indicating stretching and thinning as can be seen in Figure 3.21, while deep drawing at 50°C and 75°C produces the lowest cup thickness in the flange area and the top corner radius indicating lower deformation due to higher stiffness of the blank material at these temperatures. The up and down thickness variations in the flange area at 50°C and 75°C occur due to periodic fold formation. Along the cup bottom, the blank at 125°C showed a greater decrease in blank thickness compared to 100°C. Cup thickness variation for blanks at 50°C and 75°C showed almost a similar trend.

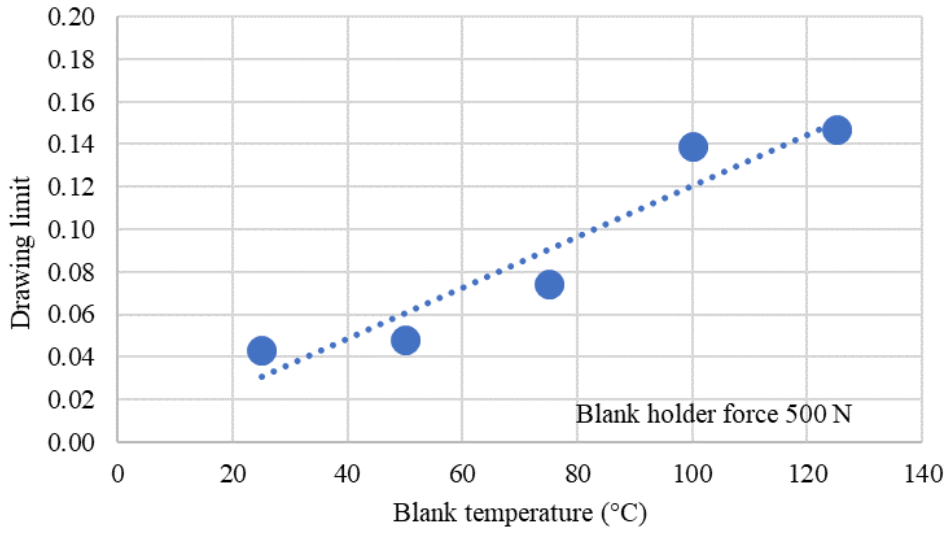

Figure 3.19: Drawing limit as a function of blank temperature for a blank diameter of 90 mm and a blank holder force of 500 N.

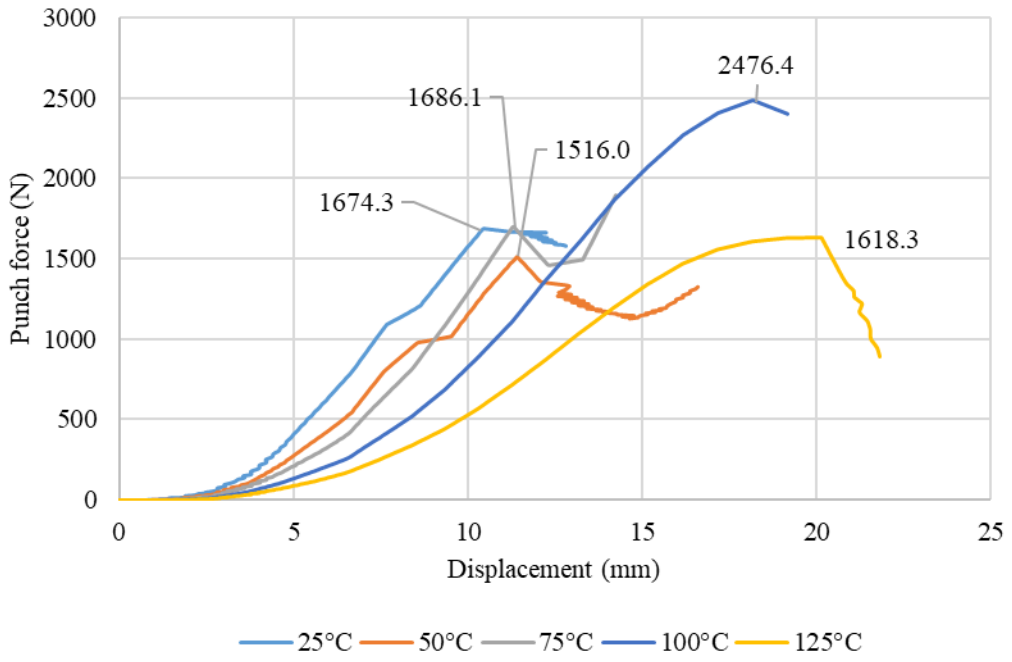

Figure 3.20: Effect of initial blank temperature on punch force vs. punch displacement diagrams (blank holder force = 500 N and blank diameter = 90 mm).

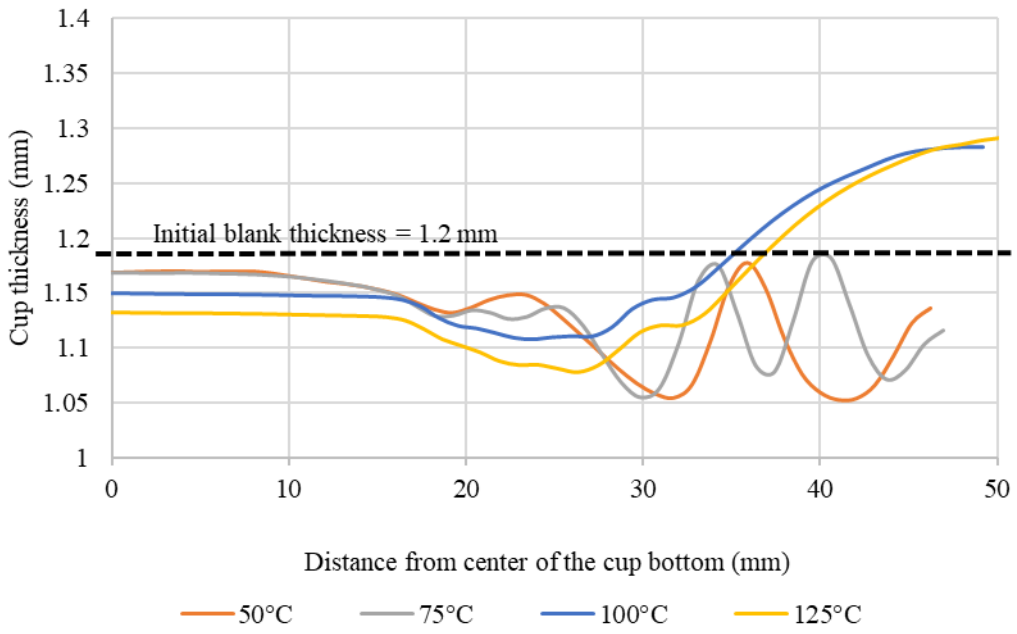

Figure 3.21: Cup thickness variations at different initial blank temperatures (Blank holder force = 500 N).

Heat lost by the blank to the die-punch set up due to conduction heat transfer increases with increase in temperature as can be seen from Figure 3.22. At higher temperatures, there is a clear distinction between the regions for contact of the blank with die-punch set up, while at lower temperatures, the temperature distribution profile was found to be almost linear with no variation. The little variation in the temperature profiles for 50°C and 75°C blank temperatures can be attributed to the failure of blank at lower draw depths, thus reducing the time of contact for the conduction heat transfer to occur.

Plastic strain variations show that the maximum strain occurred at the top corner radius irrespective of the initial blank temperature as can be seen from Figure 3.23. At this location, the blank bends first and then unbends as it enters the space between the punch and the die. For deep drawing at 50°C and 75°C, plastic strain in the flange area was found to be almost the same as the strain at the top corner radius which can be attributed to a higher stiffness of the blank at lower temperatures. Along the cup bottom, plastic strain increased with increase in initial blank temperature.

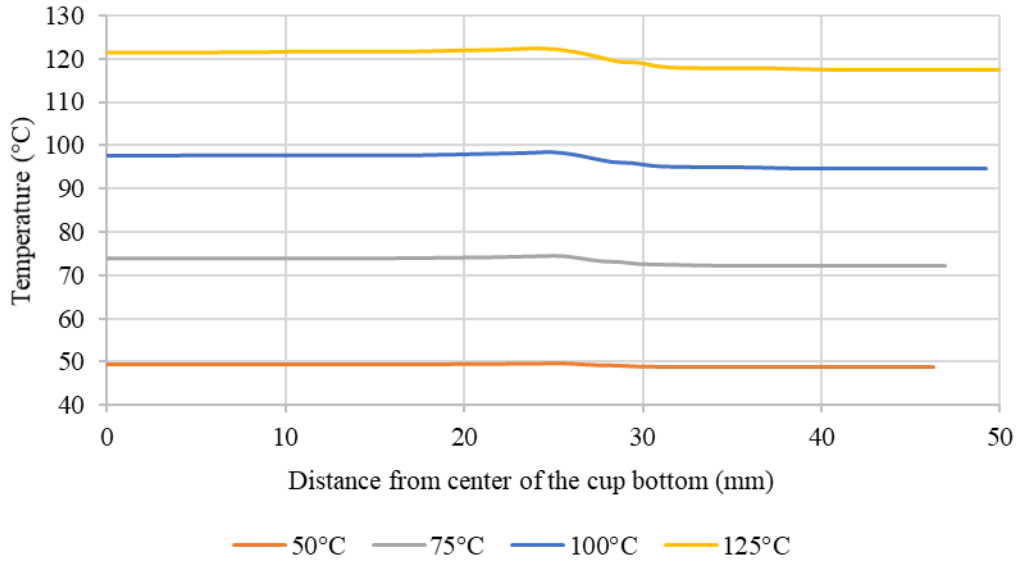

Figure 3.22: Temperature distributions at different initial blank temperatures just before failure.

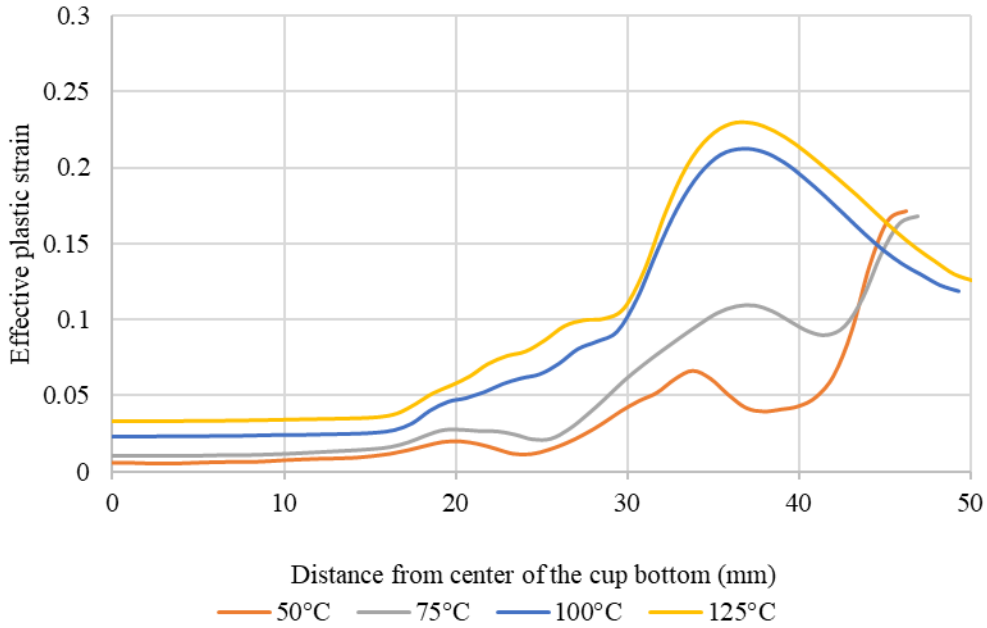

Figure 3.23: Effective plastic strain variations at different initial blank temperatures just before failure.

3.5.3 Blank Diameter

Selection of blank diameter depends on the draw depth required and on the die design. Higher draw depth can be attained with higher blank diameter, but care must be taken to ensure that the die-punch setup is able to accommodate the increase in flange thickness which will occur with

increase in blank diameter. Process variables suitable for a particular blank diameter may not be suitable for another blank diameter. Also, a higher blank diameter increases the resistance against flow of the blank because of the increased surface area of contact between the blank and the die, while lower blank diameter causes an early release of the blank from the blank holder which leads to the formation of wrinkles at the flange surface or on the top rim of the cup and subsequent failure of the blank. Hence, determination of the correct blank diameter suitable for deep drawing under given process conditions is very important.

To determine the effect of blank diameter on draw depth, three different blank diameters, namely 80 mm, 90 mm, and 100 mm, were considered with the initial blank temperature at 100°C and the blank holder force at 500 N. Table 3.7 lists the draw depths attained before failure and the failure locations for deep drawing with different blank diameters. Failure locations are shown in Figure 3.24.

Table 3.7: Draw depth just before failure and failure location for different blank diameters (with 100°C initial blank temperature and 500 N blank holder force).

Blank diameter	80 mm	90 mm	100 mm
Draw depth attained just before failure (mm)	16.49	18.87	13.38
Max. punch force (N)	1650.4	2476.4	1656
Failure location	Plastic strain exceeding failure strain at the top corner radius		Wrinkling in the flange area

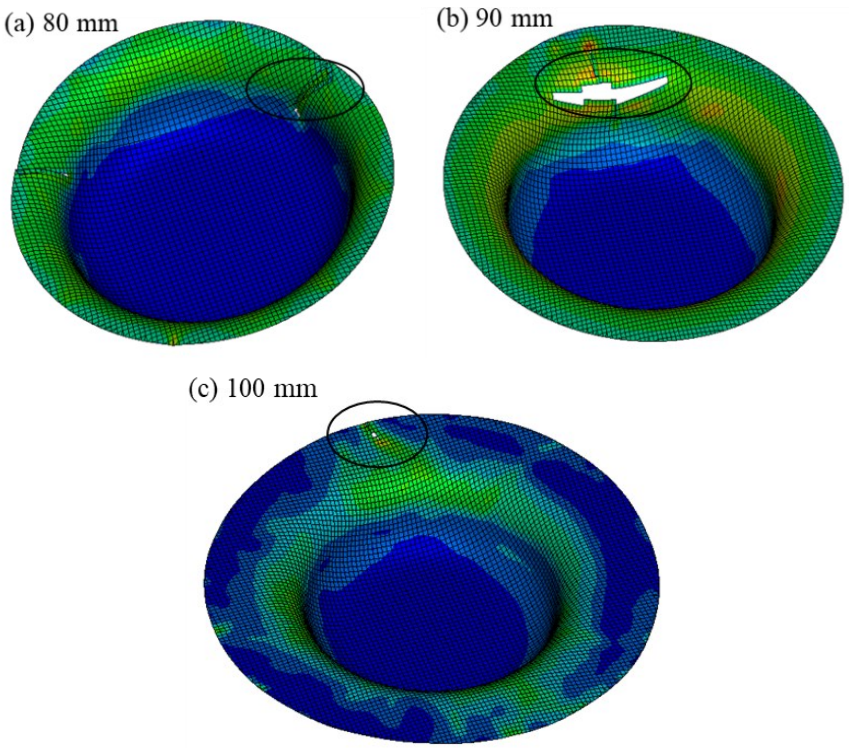

Figure 3.24: Failure locations for different blank diameters.

Failure of the 80 mm diameter blank occurs when the flange area of the blank loses contact with the blank holder and plastic strain exceeds the failure strain. For the 90 mm blank diameter, failure was observed at the top corner radius where the blank entered the space between the punch and die. For the 100 mm blank diameter, failure occurred at a lower draw depth compared to 90 mm which is due to the initiation of flange wrinkling attributed to a combination of higher circumferential compressive stress in the flange and lower modulus of the material at 100°C. The corresponding punch force is also lower than that with the 90 mm flange.

Figure 3.25 shows the variation of the cup thickness just before failure along the distance from center of the cup bottom to the flange region. Cup thickness variation was found to be lower for 80 mm and 100 mm diameter blanks when compared to 90 mm blank diameter (Figure 3.25). For the 80 mm blank, the lower variation in thickness can be attributed to the less surface area of

the blank in contact with the lower die and blank holder, which did not cause enough stretching of the blank material and for the 100 mm blank, the lower variation in blank thickness can be attributed to failure at a lower draw depth. For the 100 mm blank, the failure at lower draw depth can be attributed to the increase in resistance observed against the flow of the blank material with increase in surface contact area of the blank with the die and the blank holder.

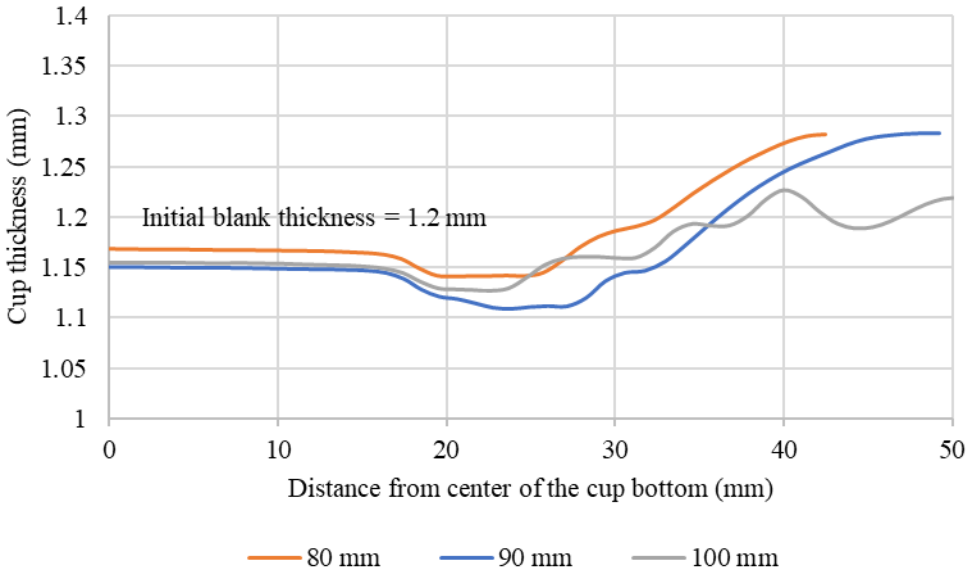

Figure 3.25: Cup thickness variation for different blank diameters.

Temperature distribution was found to be almost similar irrespective of blank diameter as can be seen from Figure 3.26. Small variations in the temperature distribution can be attributed to the failure of the blanks at different draw depths and therefore, different times of contact between dies and the blank. For all the blanks, the lowest temperature was recorded in the flange area and the highest at the cup wall near the bottom corner radius. Plastic strain variation plots until failure for different blank diameters show that irrespective of the blank diameter, the maximum strain occurs at the top corner radius which can be observed in Figure 3.27.

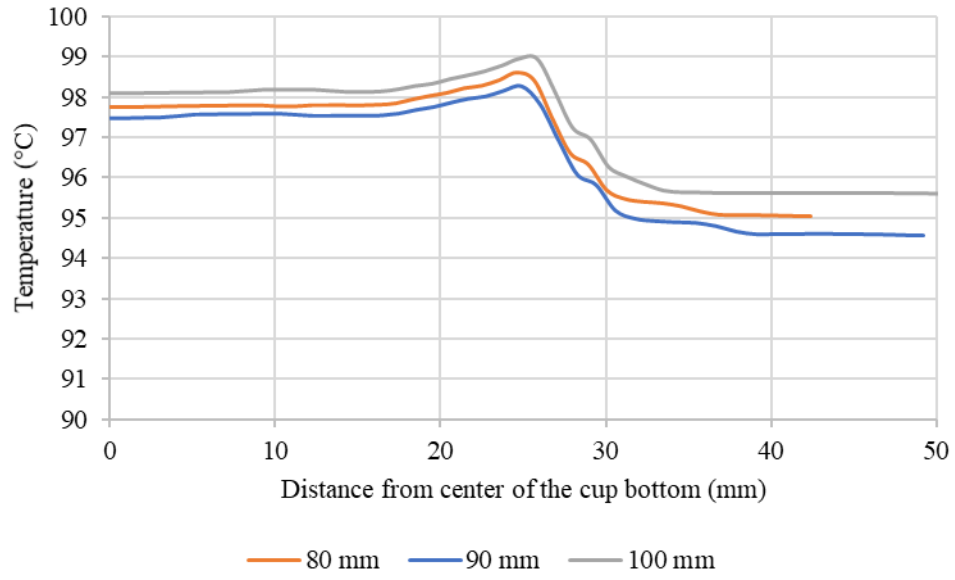

Figure 3.26: Temperature distributions for different blank diameters just before failure.

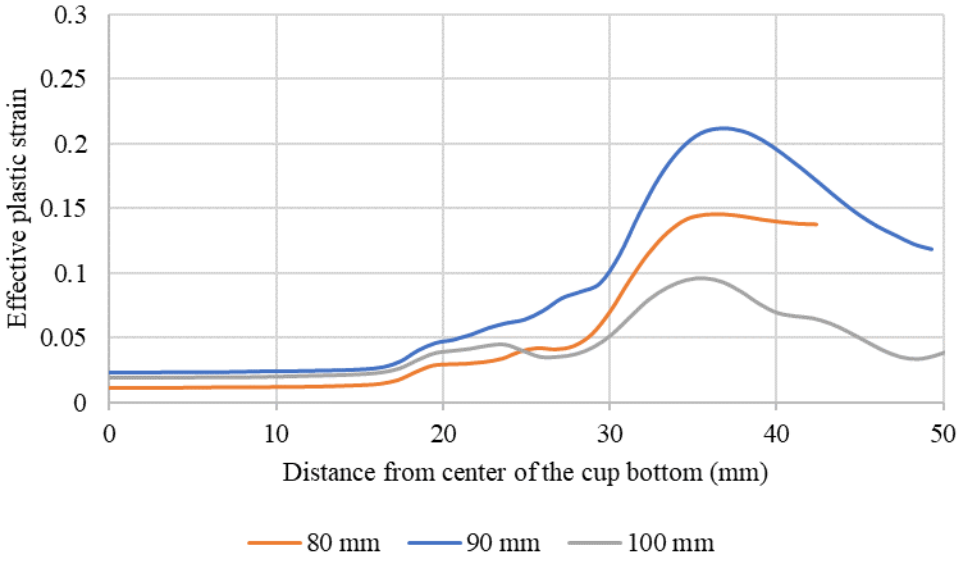

Figure 3.27: Effective plastic strain variations for different blank diameters just before failure.

3.5.4 Blank Thickness

Blank thickness plays a very important role in warm deep drawing, since it not only influences the die-punch gap to be used in the tool so that ironing does not occur, but also the punch force, heat conduction from the blank to the die and punch, and final thickness of the formed part. The conduction heat transfer between the blank and the die/punch will be affected by the thickness of

the blank. A blank with lower thickness loses heat at higher rate compared to that of a blank with higher thickness.

In this section, deep drawability of PP sheet is studied at four different blank thicknesses, namely 0.8 mm, 1.0 mm, 1.2 mm, and 1.4 mm. The blank holder force was maintained at 500 N and the initial blank temperature was set at 100°C. Table 3.8 lists the draw depths and the failure regions for deep drawing of PP blank with different blank thicknesses. Successful draw depth decreases with increasing blank thickness and the maximum punch force also increases with blank thickness. Figure 3.28 shows the failure regions in the deep drawn parts with different blank thicknesses.

Table 3.8: Draw depth just before failure and failure location at different initial blank thicknesses (with blank holder force at 500 N).

Blank thickness	0.8 mm	1.0 mm	1.2 mm	1.4 mm
Draw depth attained just before failure (mm)	19.11	19.04	18.87	17.72
Max. punch force (N)	1718.1	2089.6	2476.4	2517.9
Failure location	Plastic strain exceeding failure strain at the top corner radius			Flange area and at the top corner radius

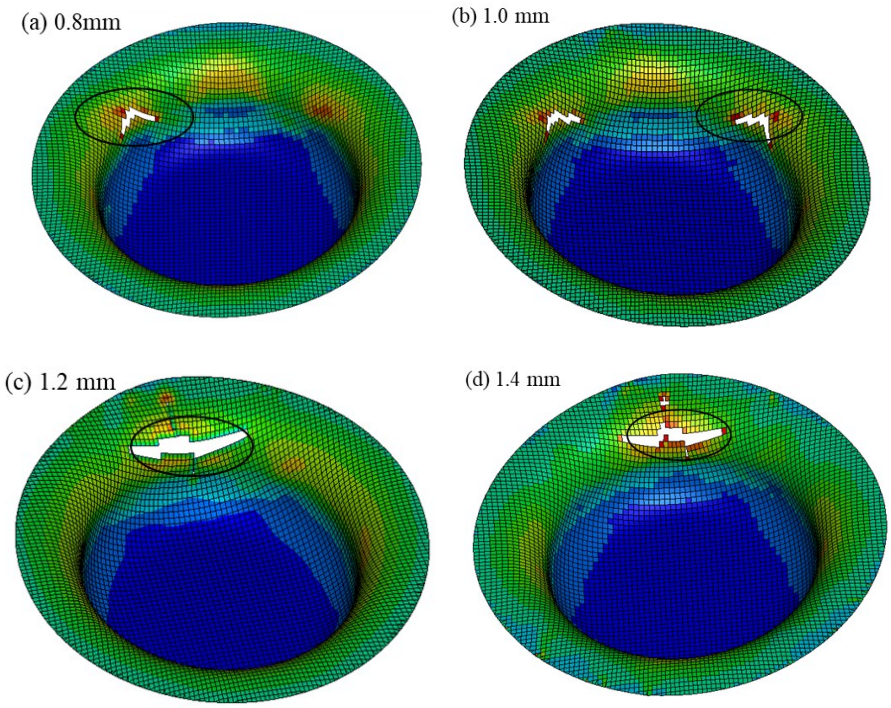

Figure 3.28: Failure location in cups with different blank thicknesses.

Failure locations in cups with different blank thicknesses are shown in Figure 3.28. For blanks with thicknesses at 0.8, 1.0 and 1.2 mm, failure can be attributed to the plastic strain exceeding the failure strain along the top corner radius. For a blank with1.4 mm thickness, failure occurred in the flange area and the top corner radius. Failure in the flange area is due to ironing effect (compressive stresses) as the space between the punch and die was not able to accommodate the increase in thickness along the flange area. The slope of the punch force vs. punch displacement curve (Figure 3. 29) increases with increase in the blank thickness indicating that the punch force required to deep draw the cup increases with increase in blank thickness.

Cup thickness variation plots shown in Figure 3.30 was found to be similar irrespective of the initial blank thickness. Cup thickness shows a drop near the end of the bottom corner radius indicating thinning and stretching of the blank and it increases near the flange area indicating thickening of the blank along the flange region. The percentage increase in thickness along the

flange area was found to be higher for 1.2 and 1.4 mm thickness compared to the other two blank thickness. Reduction in thickness value along the cup bottom was found to be similar for all blanks.

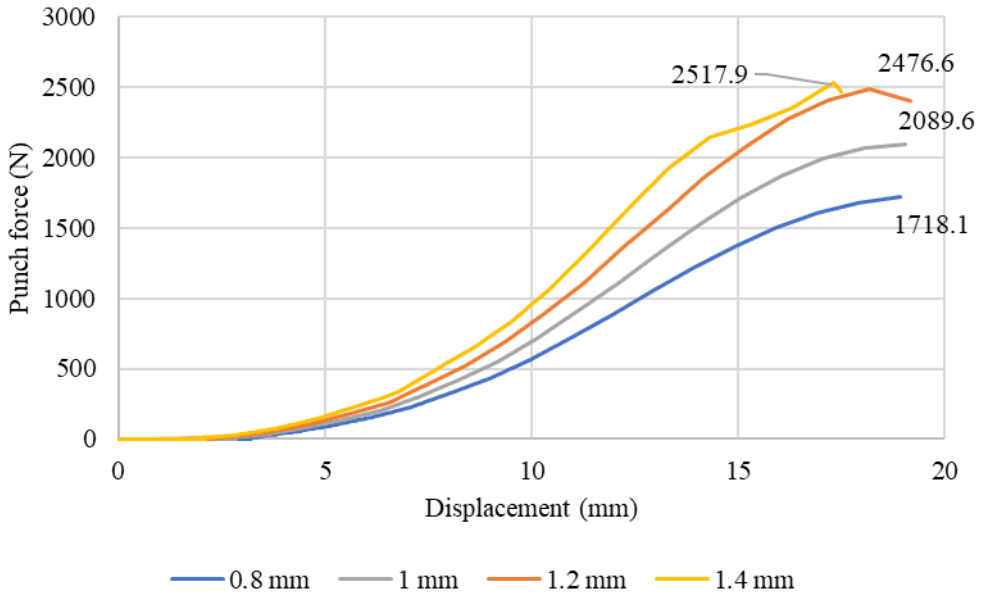

Figure 3.29: Punch force vs. punch displacement diagrams for deep drawing with different blank thicknesses.

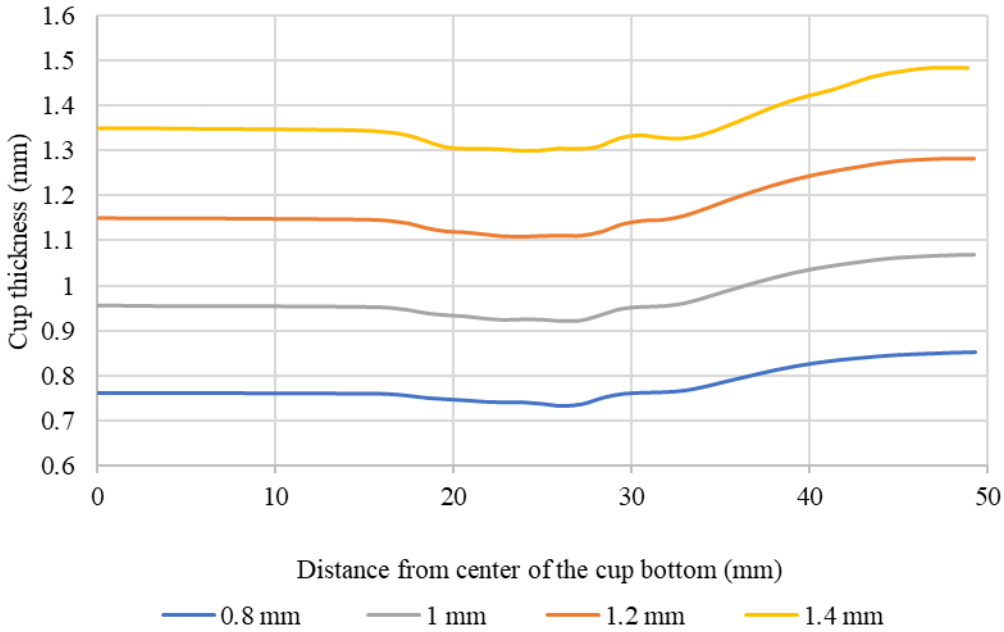

Figure 3.30: Cup thickness variations for deep drawing with different blank thicknesses.

Heat lost by the blank to the die-punch set up due to conduction heat transfer decreases with increase in blank thickness as can be seen from Figure 3.31. Temperature drops from the initial blank temperature of 100°C along the cup bottom are inversely related to the blank thickness, i.e., with decrease in blank thickness, the conduction heat loss increases causing greater decrease in temperature; however, the temperature drop was found to be higher along the cup wall and flange area almost by a factor of 2 when compared to the cup bottom. From Figure 3.31, we can conclude that higher the thickness of the blank lesser will be the conduction heat transfer between the blank and dies.

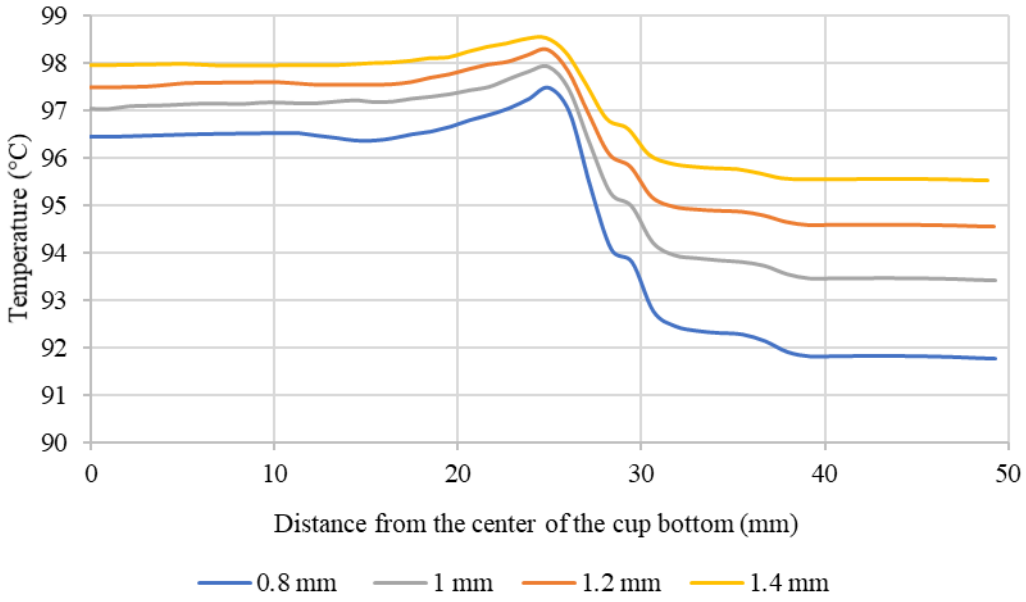

Figure 3.31: Temperature distributions just before failure at different blank thicknesses.

Effective plastic strain variation just before failure was found to be similar irrespective of blank thickness as can be seen from Figure 3.32. Maximum plastic strain variation for deep drawn cups with different blank thickness was found to be at the die entry radius. Plastic strain at the end of cup bottom was found to be highest for the drawn cup with blank of 0.8 mm, the higher plastic

strain compared to the other blank thickness suggests the possibility of thinning with decrease in thickness of the blank.

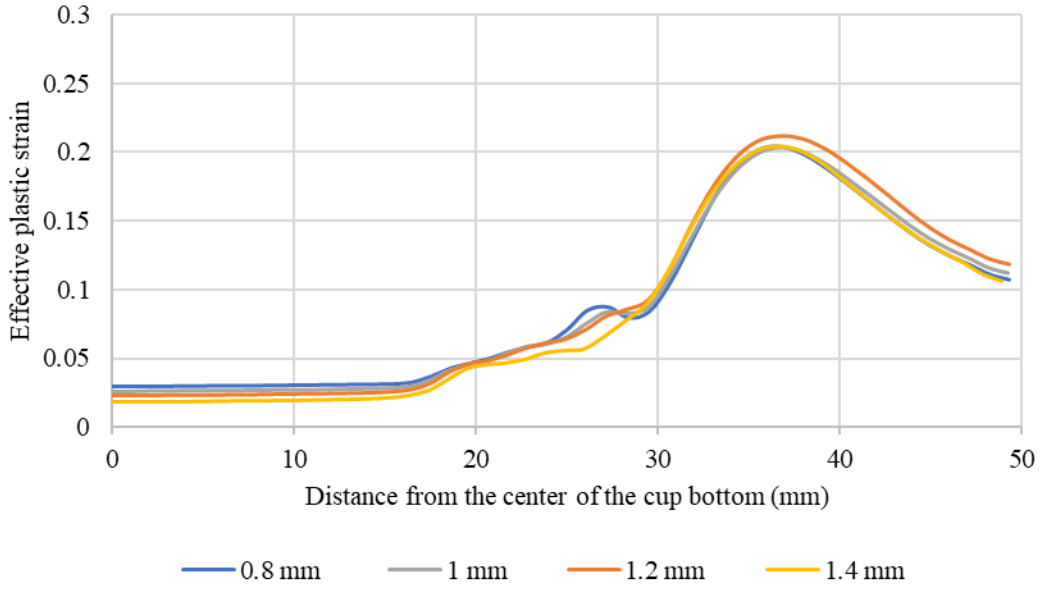

Figure 3.32: Effective plastic strain variation just before failure for different blank thicknesses.

3.5.5 Friction Coefficient

Friction at the tool-blank interfaces plays a very important role in deep drawing operations since it is one of the sources of resistance to flow of the blank material into the die. The force of friction between the blank and die surface has to be overcome for the material to flow into the space between the die and punch. The force of the blank holder adds significantly to the force of friction. As friction increases, the punch force to form the cup also increases.

Values of friction coefficient at the aluminum tool surfaces and PP at the initial blank temperatures were given as an input for the FE simulations. As has been observed in the previous sections, the temperature variation in the PP blank during deep drawing is not very significant, and therefore, it is expected that there will also not be much variation in the friction coefficient in the deep drawing of PP cups. Figure 3.8 shows that the friction coefficient at 100°C blank temperature is 0.305. Using this as the baseline value, deep drawability of PP sheet is studied at three other

friction coefficients, namely 0.1, 0.2, and 0.4. The blank holder force was maintained at 500 N and the initial blank temperature of 100°C. Draw depths attained just before failure with different friction coefficients are given in Table 3.9 and the locations of failure are shown in Figure 3.33.

Table 3.9: Draw depth just before failure and failure location at different friction conditions (at 500 N blank holder force).

Friction coefficients	0.1	0.2	0.305	0.4
Draw depth attained just before failure (mm)	17.69	19.47	18.87	18.18
Max punch force (N)	1762.1	2135.7	2476.4	2380.2
Failure location	Wrinkling in the flange area		Strain exceeding failure strain at the top corner radius	

Figure 3.33 presents the failure locations for drawn cups of PP at different friction conditions. Failure at 0.1 and 0.2 friction coefficients can be attributed to the wrinkling and circumferential buckling which occurs due to the lower resistance offered for the flow of blank. As a result of the lower resistance, the blank does not undergo enough stretching and buckles as the blank flows into the space between the punch and die. At higher friction coefficients, the resistance offered for the flow of the blank will be higher and requires higher punch forces for the blank to be deep drawn. Failure in the deep drawn cup at higher friction coefficients was observed at the die entry radius. Draw depth attained just before failure increases and then decreases with increase in friction conditions as can be seen from Table 3.9. Maximum draw depth was found to be for the deep drawn cup with 0.2 friction coefficient. The decrease in draw depths with increase in friction coefficient at higher values of friction coefficient can be attributed to the higher resistance offered for the flow of blank.

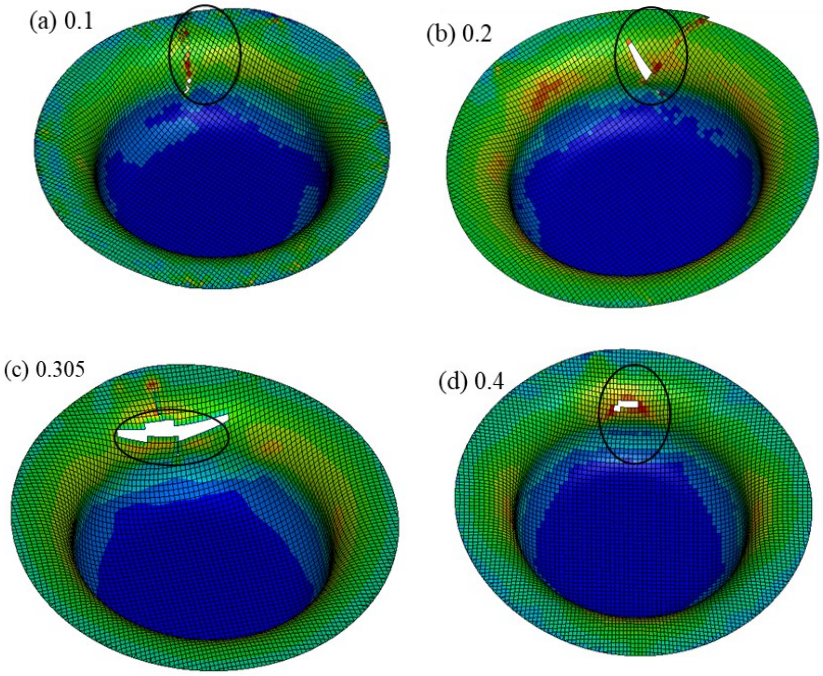

Figure 3.33: Failure locations at different friction conditions.

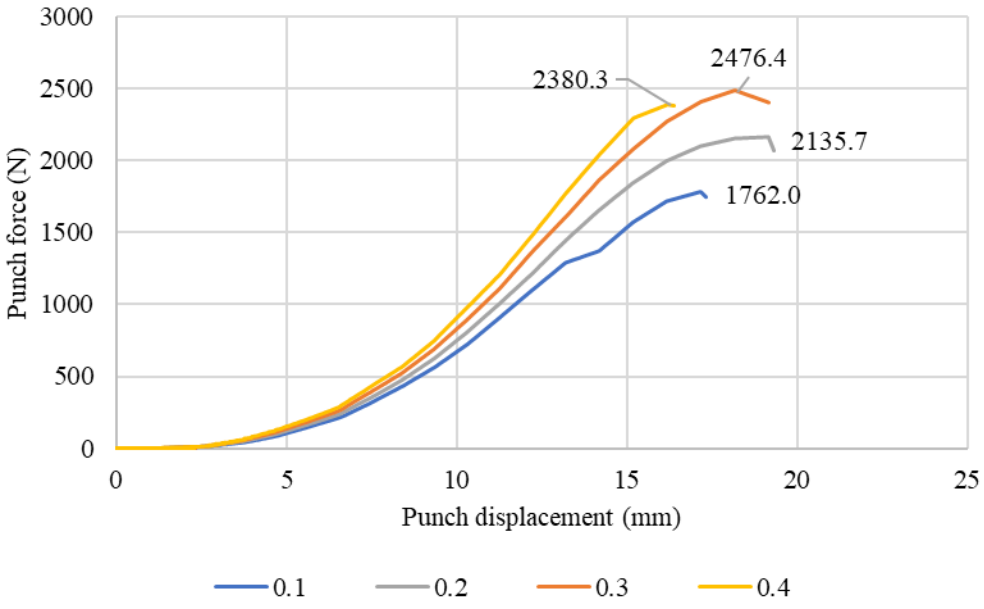

Figure 3.34: Effect of friction coefficient on punch force vs. punch displacement diagrams.

Force required to deep draw the cup increases with increase in friction conditions as can be seen from Figure 3.34. However, as shown in Figures 3.35 - 3.37, cup wall thickness decreases

and effective plastic strain increases with increasing friction coefficient, but the temperature distribution is not affected much.

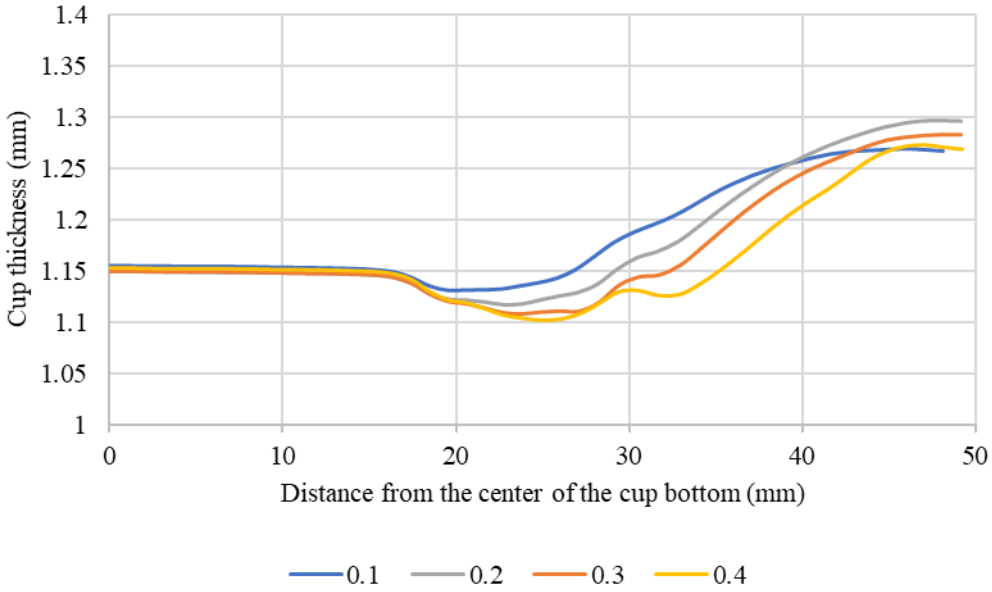

Figure 3.35: Cup thickness variations for deep drawing at different friction coefficients.

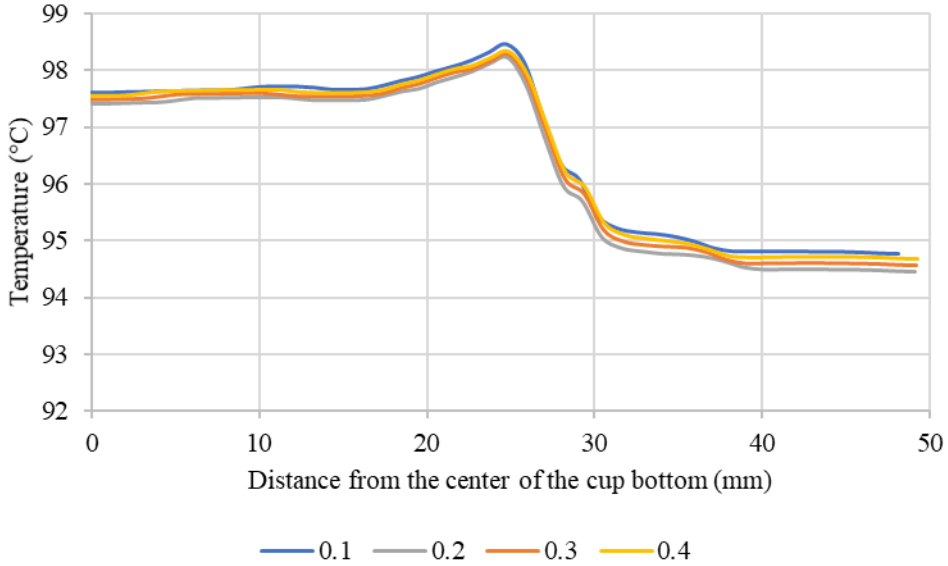

Figure 3.36: Temperature distributions at different friction coefficients just before failure.

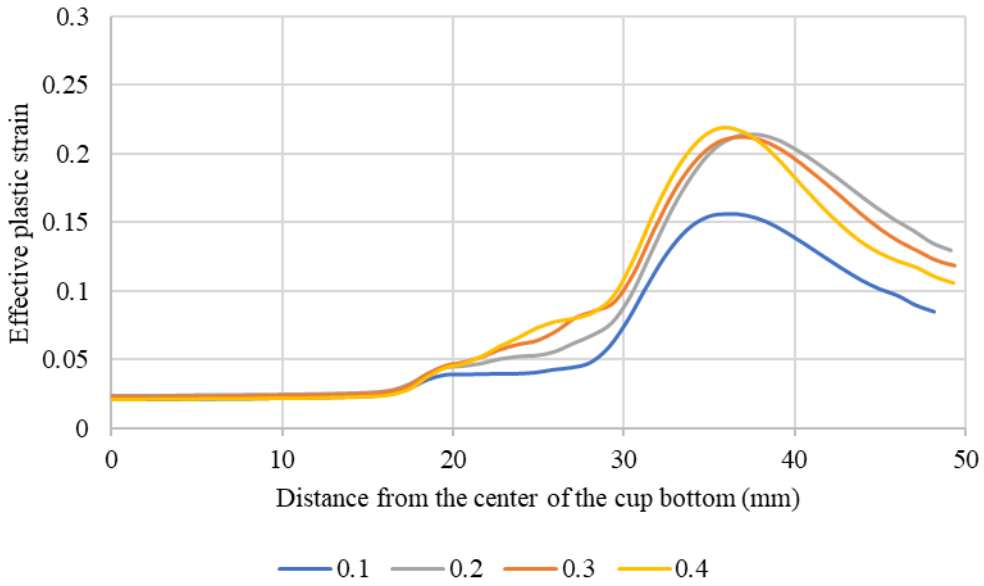

Figure 3.37: Effective plastic strain variation at different friction conditions just before failure.

3.5.6 Die Corner Radius

Die corner radius should be as large as possible to permit smooth flow of PP into the space between the die and the punch as it passes over the die corner radius. However, if it is too large the blank will be released by the blank holder too soon and wrinkling will result in the deep drawn cup. Too sharp a radius will hinder the normal flow of the material and cause uneven thinning and tearing of the cup wall.

In this section, deep drawability of PP sheet is studied for four different die corner radii of 4, 6, 8 and 10 mm with blank holder force of 500 N, initial blank temperature of 100°C and punch corner radius of 8 mm. Table 3.10 lists the draw depth just before failure for four different die corner radii and Figure 3.38 shows the locations of failure.

Failure in the blank for deep drawing with 4 mm die corner radius occurred due to circumferential buckling along the flange area as the sharp die corner radius restricts the flow of the blank material into the space between the die and the punch. Failure for die corner radius of 6 and 8 mm was observed along the die entry radius as can be seen from Figure 3.38. Deep drawing

with 10 mm die corner radius showed progressive failure, with failure originating along the die entry radius and progressing over the flange area.

Table 3.10: Draw depth just before failure and failure location at different die corner radii (at 500 N blank holder force)

Die corner radius	4 mm	6 mm	8 mm	10 mm
Draw depth attained just before failure (mm)	13.09	17.07	18.87	20.67
Max. punch force (N)	1704.7	2463.7	2476.6	2394.3
Failure location	Wrinkling in the flange area	Strain exceeding failure strain at the top corner radius		

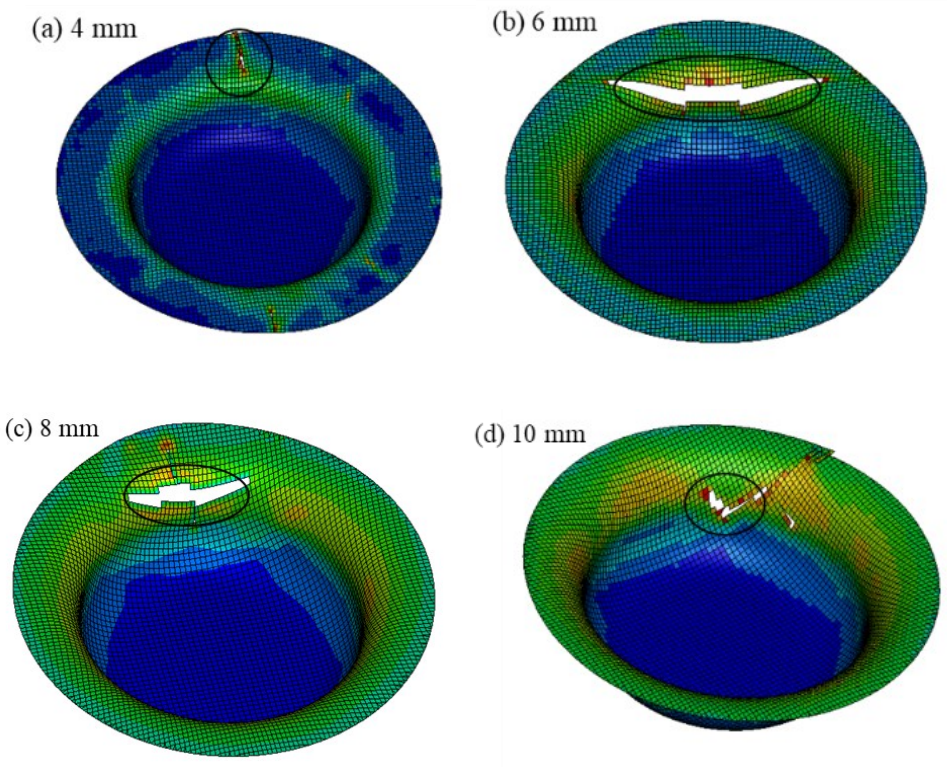

Figure 3.38: Failure location at different die corner radius.

Force required to deep draw the PP blank decreases with increase in die corner radius as can be seen in Figure 3.39. The decrease in punch force with increase in die corner radius can be attributed to the less hindrance offered for the flow of blank material. Also, with increase in die corner radius the blank was released by the blank holder early, which in turn results in lower resistance to the flow of the blank material into the die.

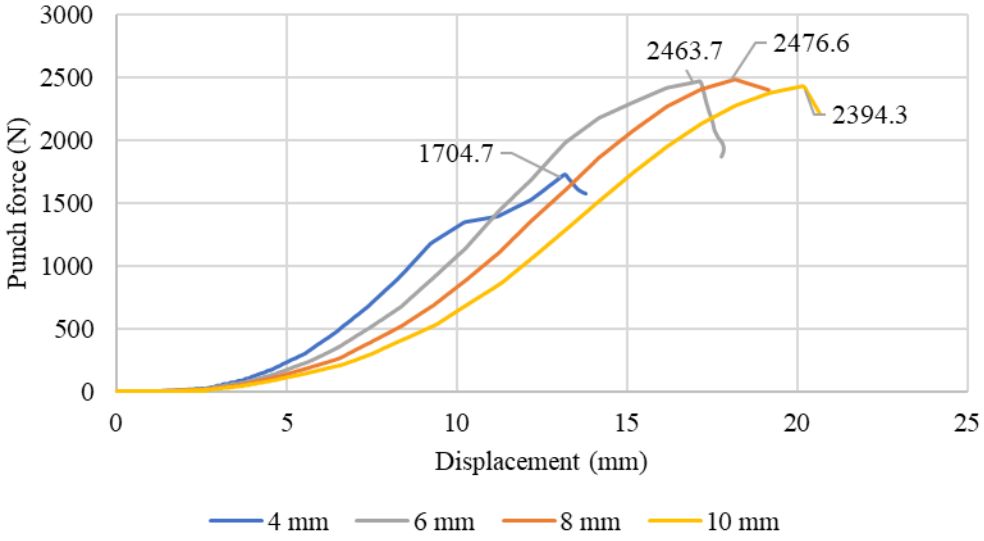

Figure 3.39: Effect of die corner radius on punch force vs. punch displacement diagrams.

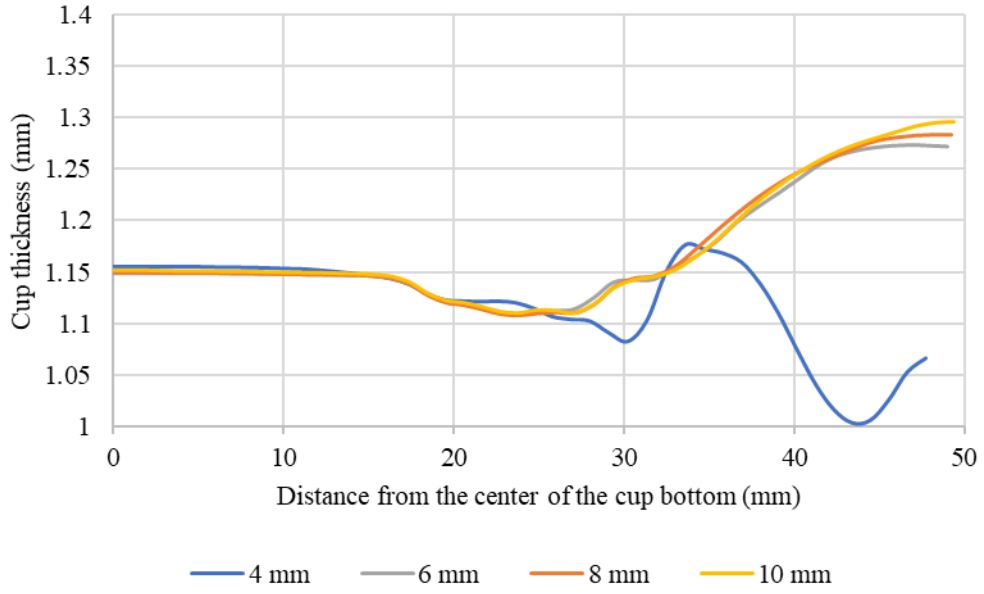

Figure 3.40: Cup thickness variation just before failure at different die corner radii.

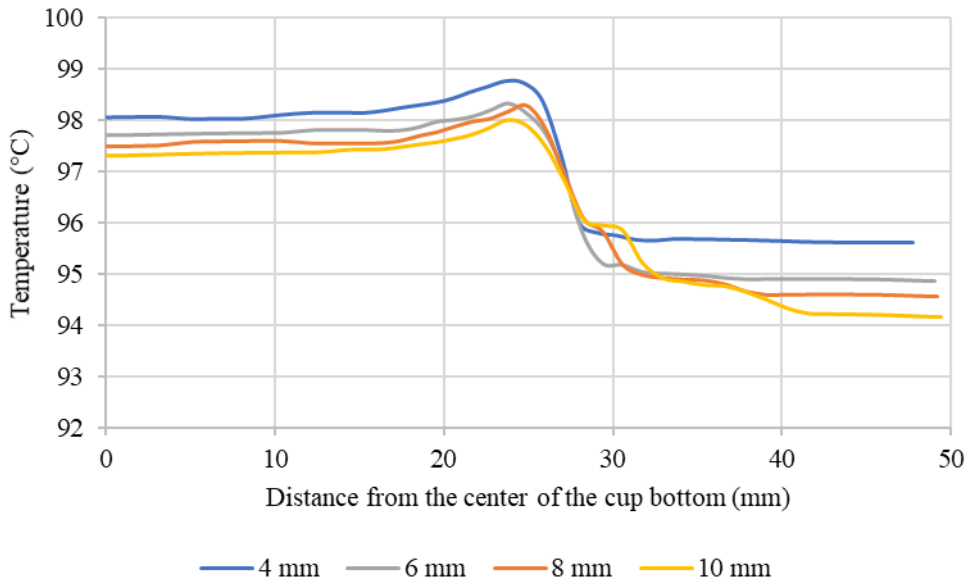

Figure 3.41: Temperature distributions just before failure for different die corner radii.

Figures 3.40–3.42 show the variations in blank thickness, temperature and effective plastic strain at the draw depth just before failure for deep drawing with different die corner radius. Cup thickness variation for the deep drawn cups just before failure at the cup bottom was almost the same irrespective of the die corner radius. Blank thickness shows a decrease in value at the cup bottom near the end of punch corner radius and shows an increase in the thickness value along the flange area as can be seen from Figure 3.40. Increase in thickness along the flange area increases with increase in die corner radius which can be attributed to the higher draw depth attained just before failure owing to the lesser resistance offered for the flow of blank material. Blank thickness variation exhibited by the blank with die corner radius of 4 mm can be attributed to the early failure of the blank along the flange area at a lower draw depth.

Temperature distribution profiles shown in Figure 3.41 were found to be almost similar for all die corner radius. Difference in temperature drop along the cup bottom, cup wall and flange area can be attributed to the different failure draw depths. The temperature drop at the die entry radius reduces with increase in die corner radius which can be attributed to the release of the blank

in contact with the blank holder which in turn reduces one surface for conduction heat transfer to occur between the blank and die.

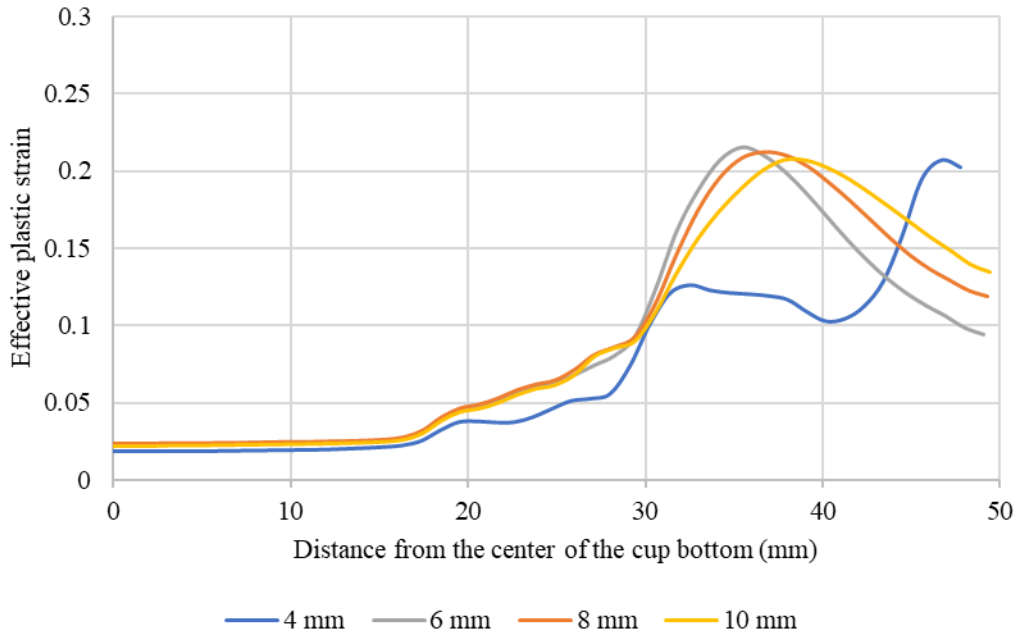

Figure 3.42: Effective plastic strain variation just before failure at different die corner radius.

Effective plastic strain variation just before failure as can be seen from Figure 3.42 shows that the maximum strain occurs at the die entry radius irrespective of the die corner radius. The peak plastic strain values shows a shift towards the right side with the increase in die corner radius. Plastic strain variation at the cup bottom was almost same irrespective of the die corner radius. The different plastic strain variation exhibited by the drawn cup with 4 mm die corner radius can be attributed to the failure of the blank at low draw depth.

3.5.7 Punch Corner Radius

The convexity of the punch corner radius affects the final shape of the bottom of the drawn cup. Studying the effect of punch corner radius in important to determine the draw depth attained just before failure for deep drawing of PP sheet. A sharper radius will require higher punch force when the blank is folded around the punch corner and result in excessive thinning or tearing at the bottom

of the cup. A larger radius may distort the shape and produce close to a round bottom cup instead of having a flat bottom cup. In this section, deep drawability of PP sheet is studied at four different punch corner radii of 4, 6, 8 and 10 mm with the applied blank holder force at 500 N, the initial blank temperature of 100°C and a die corner radius of 8 mm. The cup draw depths attained just before failure at different punch corner radius are given in Table 3.11 and the locations of failure are shown in Figure 3.43.

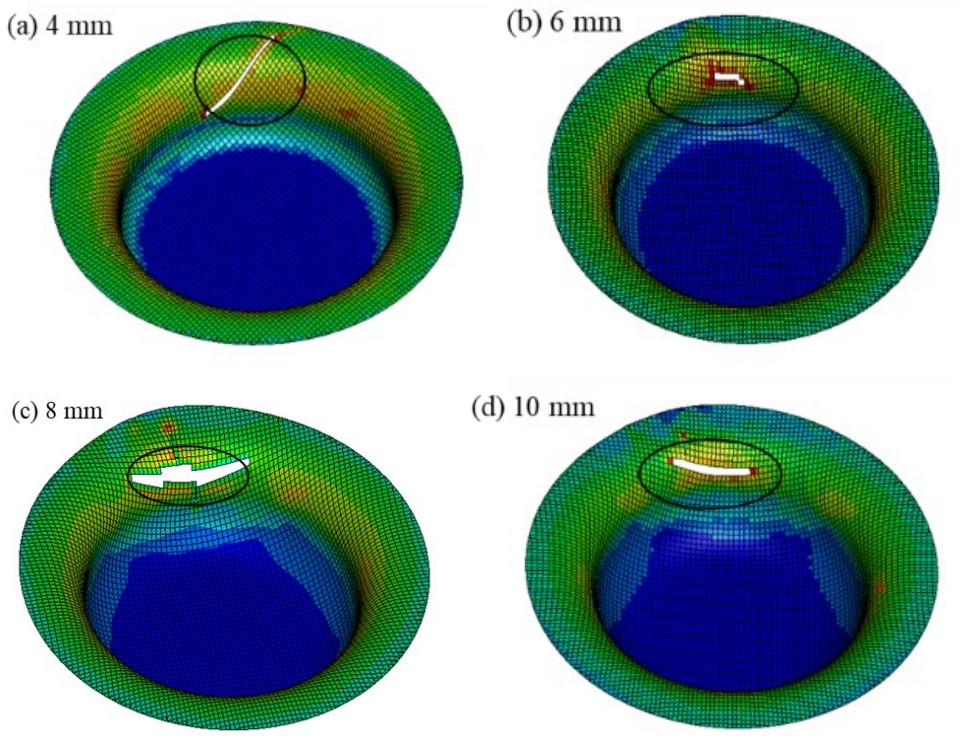

Figure 3.43: Failure locations of the deep drawn cup at different punch corner radius.

Failure in the deep drawn cup with different punch corner radius was observed to occur at the die entry radius when the plastic strain exceeds the failure strain as can be seen in Figure 3.43. Figures 3.45-3.47 show the variation in blank thickness, temperature and effective plastic strain at the draw depth just before failure for deep drawing of PP with different punch corner radii.

Table 3.11: Draw depth just before failure and failure region at different punch corner radii (at 500 N blank holder force).

Punch corner radius	4 mm	6 mm	8 mm	10 mm
Draw depth attained just before failure (mm)	17.83	18.20	18.87	19.24
Max. punch force (N)	2557.2	2535.0	2476.4	2355.1
Failure location	Strain exceeding failure strain at the die entry radius			

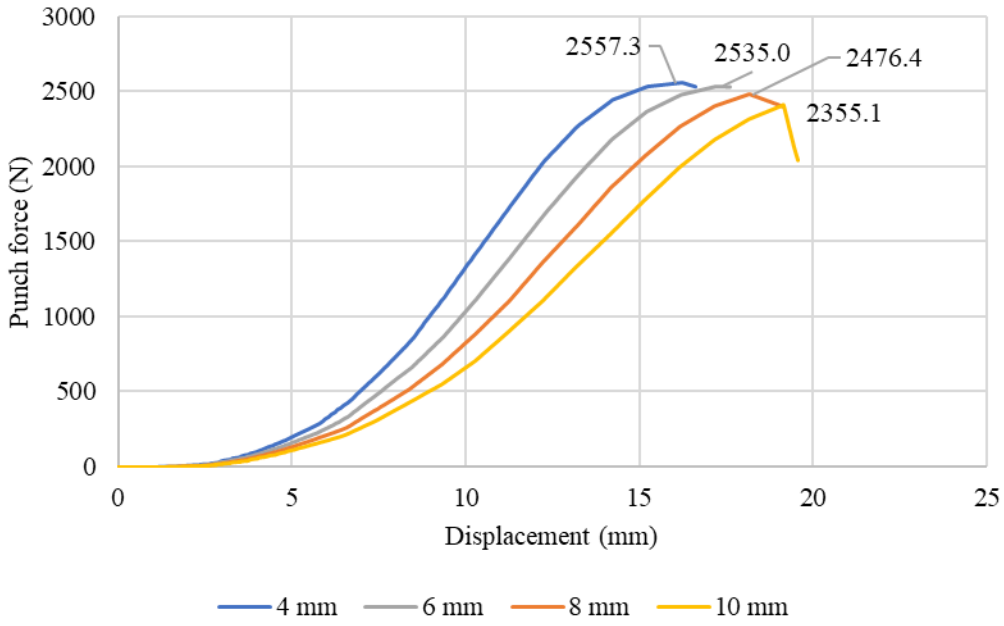

Figure 3.44: Effect of punch corner radius on punch force vs. punch displacement diagrams.

Punch force required to deep draw the PP sheet decreases with increase in punch corner radius as can be seen from Figure 3.44. Cup thickness variation plots in Figure 3.45 show that the thickness remains the same at the cup bottom irrespective of the punch corner radius. The increase in the blank thickness along the flange area was found to decrease with increase in punch corner radius. Cup thickness variation for drawn cup with 4 mm punch corner radius showed a drop in

the value near the cup bottom indicating thinning of the blank material for deep drawing with a sharp punch corner radius. The percentage decrease in thickness or % thinning at the cup bottom decreases with increase in punch corner radius as is evident from Figure 3.45.

Temperature distribution plots along the cup bottom and the flange area was found to be almost similar irrespective of the punch corner radius as can be seen in Figure 3.46. Small difference in temperature distribution can be attributed to the different failure draw depths for deep drawing with different punch corner radii. Temperature drop along the cup bottom shows decreasing trend with increase in punch corner radius indicating heat generation due to plastic deformation as the material gets stretched over the punch with higher corner radius.

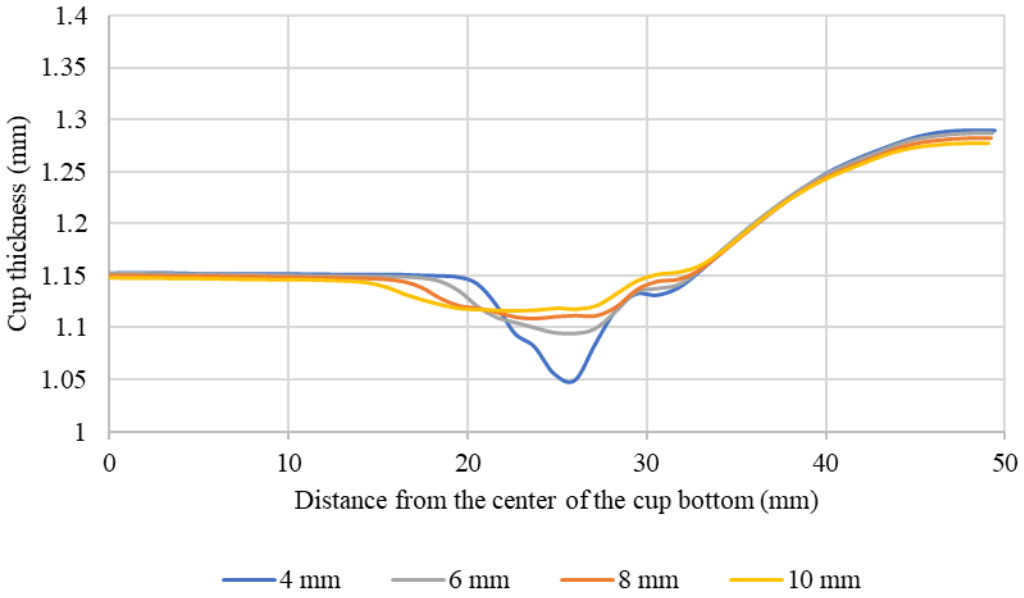

Figure 3.45: Cup thickness variation just before failure for deep drawing at different punch corner radii.

Effective plastic strain variation just before failure shows that the maximum strain occurred at the top corner radius irrespective of the punch corner radius. Plastic strain at the cup bottom was found to be almost same for deep drawn cup until failure with different punch corner radius. Along the flange area the plastic strain decreases with increase in punch corner radius as can be seen from Figure 3.47. Plastic strain for 4 mm punch corner radius shows a peak near the cup bottom indicting

thinning of the blank material and possibility of tearing for the deep drawn cup. In Figure 3.47 we can see that the deep drawn cups with punch having sharp corner radius are more prone to failure by tearing at the cup bottom.

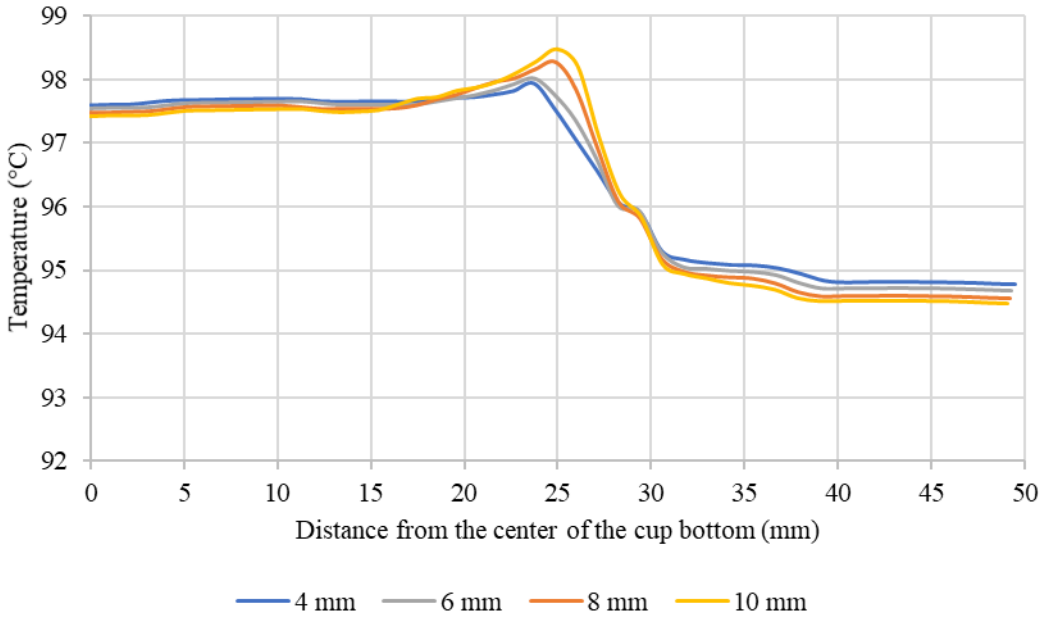

Figure 3.46: Temperature distributions just before failure with different punch corner radii.

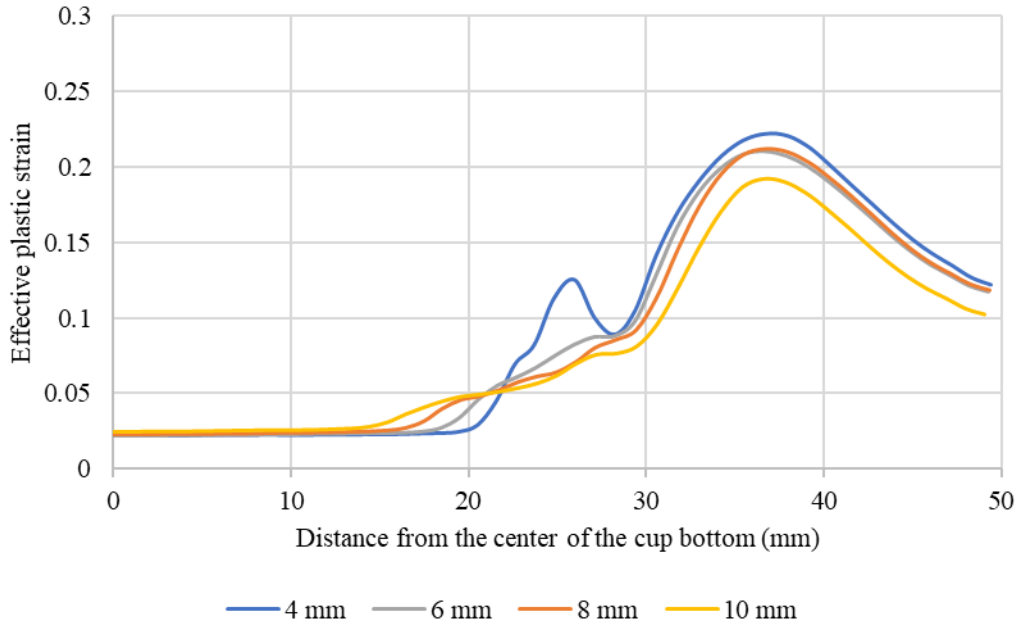

Figure 3.47: Effective plastic strain variations just before failure at different punch corner radii.

3.5.8 Failure Strain

Failure strain is a material parameter which is given as an input for FE simulations. The failure strain values determine the plastic strain at which the elements from the blank mesh are deleted. Deletion of elements occurs when the effective plastic strain reaches the failure limit. In the previous sections, failure strain variation from Figure 3.7 of PP as a function of temperature was given as an input for FE simulations. In this section, deep drawability of PP sheet is studied at four constant failure strain values of 0.3, 0.6, 0.9 and 1.2. No other material parameters are changed. The blank holder force was maintained at 500 N and initial blank temperature at 100°C. The draw depths at corresponding to the four failure strain values are reported in Table 3.12. Figure 3.48 shows the failure locations at different failure strains. As expected, the draw depth increases with increasing failure strain. Even though a full cup without a flange could be formed with 1.2 failure strain, its top edge showed the sign of wrinkle formation.

Table 3.12: Draw depth just before failure and failure location at different failure strains (with a blank holder force of 500 N)

Failure strain	0.3	0.6	0.9	1.2
Draw depth attained just before failure (mm)	18.87	23.59	23.68	25.32
Max. punch force (N)	2476.4	2476.4	2476.4	2476.4
Failure location	Strain exceeding failure strain at the die entry radius	Wrinkling in the flanges		

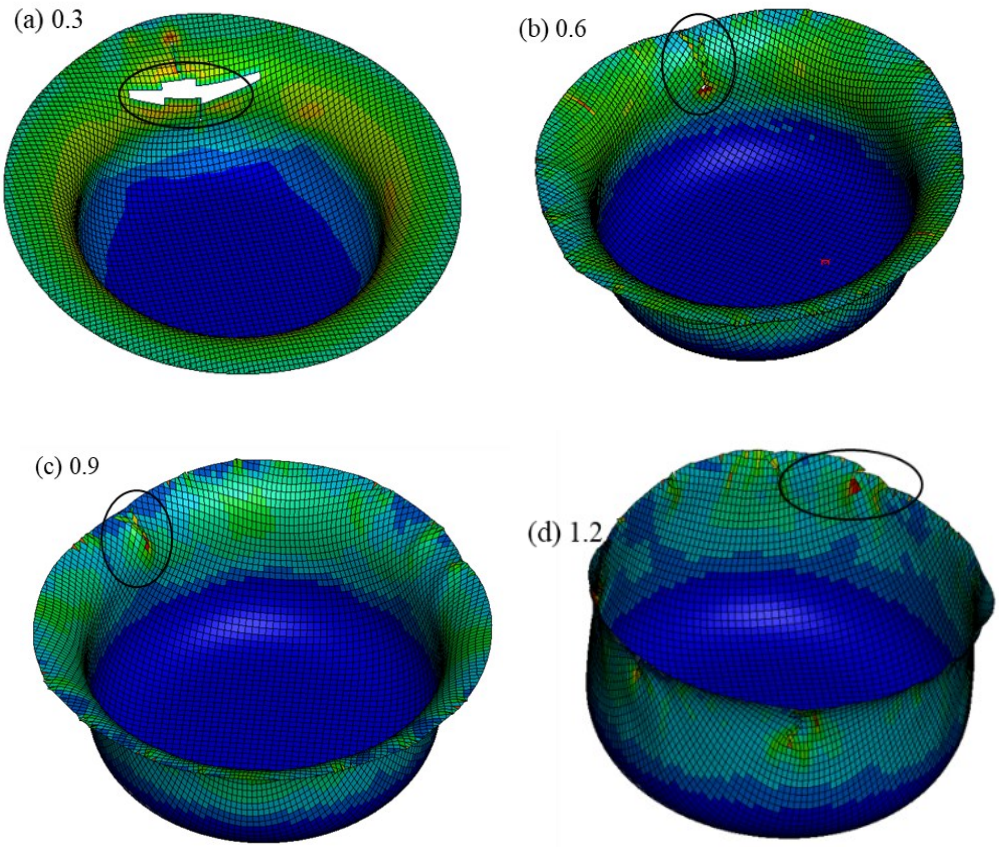

Figure 3.48: Failure locations at different failure strains.

Failure in the deep drawn cups with failure limit at 0.305 occurred when the plastic strain along the cup wall near the die entry radius exceeds the failure strain as can be seen in Figure 3.48. For cup drawn with failure strain at 0.6, 0.9 and 1.2, failure occurs when the blank loses contact with the blank holder after forming to a certain draw depth and the remaining flange portion of the blank is then forced to flow into the space between the die and the punch without any resistance from the blank holder force, thus leading to the folding in the flange area and formation of wrinkles. Wrinkling along the flange increases the effective plastic strain as a result of which failure in the blank occurs.

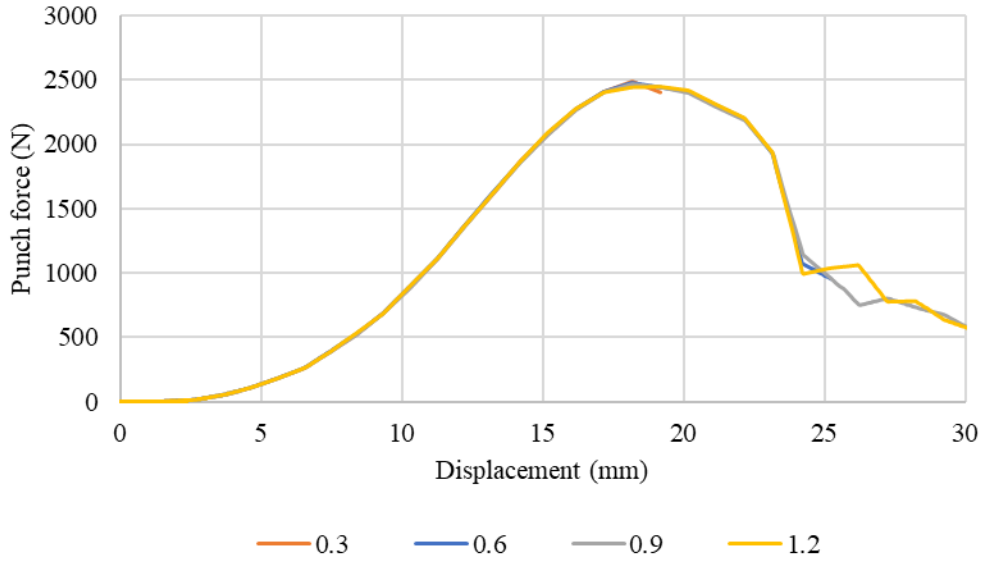

Figure 3.49: Effect of failure strain value on punch force vs. punch displacement diagrams.

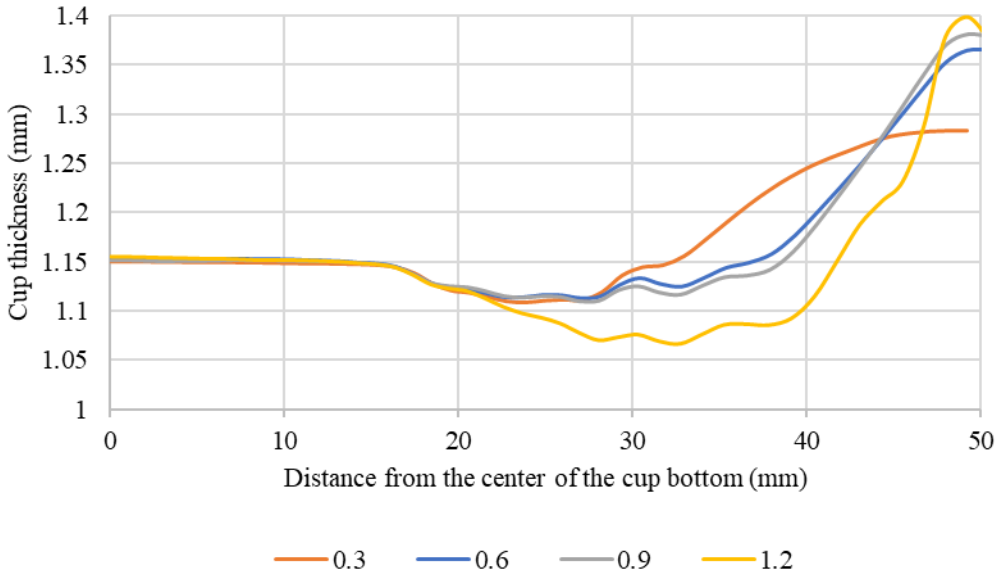

Figure 3.50: Cup thickness variation just before failure for deep drawing at different failure strain values.

Force required to deep draw the PP sheet remains the same irrespective of the failure strain values as can be seen in Figure 3.49. This is expected since other than the failure strain, no other material parameters were changed. Punch force vs. punch displacement curve for deep drawing with 0.3 failure strain shows drop in load curve which can be attributed to the plastic strain along the die entry radius exceeding the failure strain.

Figure 3.50-3.52 show the variations in blank thickness, temperature and effective plastic strain at the draw depth just before failure for deep drawing with different failure strain values. Blank thickness variation from Figure 3.50 along the cup bottom was found to be almost similar irrespective of the failure strain values. However, with increasing failure strain values the decrease in thickness of the blank at the cup wall increases which can be due to the thinning and plastic deformation of the PP sheet as it flows into the space between the dies and punch. Maximum percentage change in thickness was observed for deep drawing with failure strain at 1.2, indicating higher plastic deformation and thinning of the blank material and leading to higher draw depth of 25.32 mm compared to 18.87 mm draw depth with the simulation at the material failure limit of 0.305.

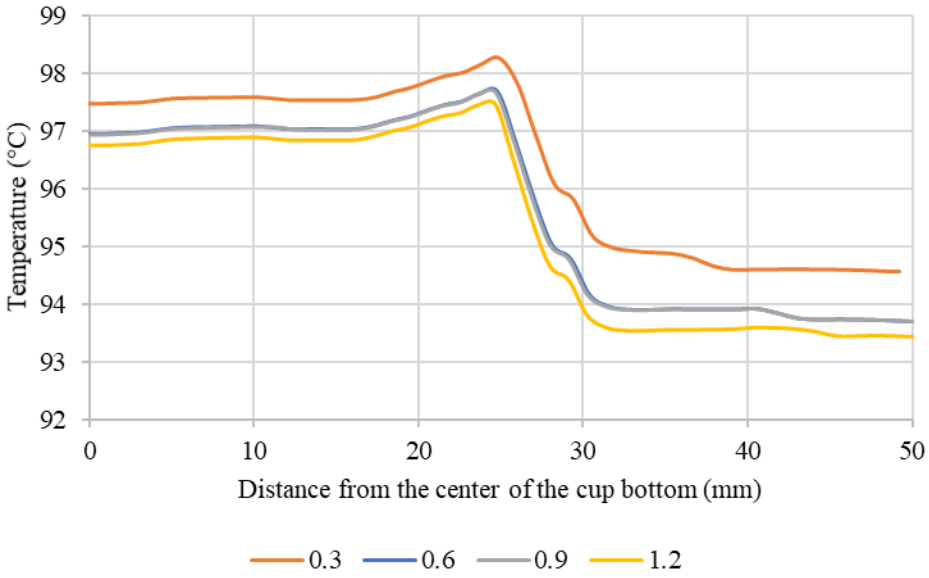

Figure 3.51: Temperature distributions just before failure at different failure strain values.

Temperature distribution profiles shown in Figure 3.51 were similar irrespective of the failure strain values. The difference in temperature values can be attributed to the different draw depths attained by the PP sheet just before failure. The higher the failure strain, the higher will be

the plastic deformation and longer will be the time of contact between the blank and the dies, and higher will be the heat loss from the blank to dies due to conduction heat transfer.

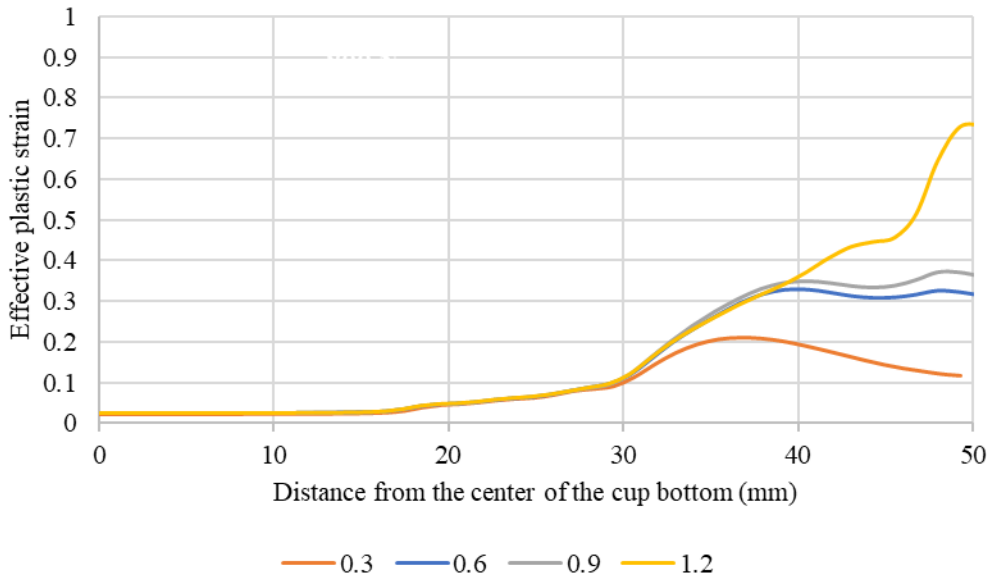

Figure 3.52: Effective plastic strain variations just before failure at different input failure strain values.

Effective plastic strain variation just before failure at the cup bottom remains same irrespective of the failure strain values as can be seen from Figure 3.52. Along the flange area plastic strain increases with increase in failure strain. Maximum plastic strain in the drawn cup with 0.3 failure limit was observed near the die entry radius, while the drawn cups with failure limit at 0.6, 0.9 and 1.2 showed maximum strain at the flange area which can be due to the formation of wrinkles along the cup edge.

3.5.9 Punch Velocity

Punch velocity determines the drawing time, strain rate in the cup wall during forming, and also the time of contact between blank and tool surfaces. The punch velocity used so far is 100 mm/s. A higher punch velocity will reduce the drawing time but will cause higher strain rate that may change the material behavior. At lower punch velocities, the time of contact will be longer which

will cause higher heat conduction and greater reduction in blank temperature that may also change the material behavior. Hence the study of effect of punch velocity is very important to determine the draw depth that can be attained just before failure. In this section, deep drawability of PP is studied at five different punch velocities, namely 5, 20, 50, 100 and 200 mm/s. The blank holder force was maintained at 500 N and the initial blank temperature was 100°C. Draw depth attained just before failure and failure location at different punch velocities are shown in Table 3.13.

Table 3.13: Draw depth just before failure and failure location at different punch velocities (with blank holder force at 500 N)

Punch velocity	5 mm/s	20 mm/s	50 mm/s	100 mm/s	200 mm/s
Draw depth attained just before failure (mm)	11.91	12.42	17.84	18.87	19.17
Max. punch force (N)	*	1481.5	2078.6	2476.4	2358.6
Failure location	Wrinkling in the flange area		Strain exceeding failure strain at the top corner radius		

Failure in the PP sheet at lower punch velocities is due to circumferential buckling in the flange area as can be seen from Figure 3.53. At lower punch velocities, heat transfer from the blanks to the dies will be higher. As the temperature drop in the blank occurs, a more rigid and less ductile behavior exhibited by PP sheet becomes more dominant. At higher punch velocities, failure occurs at the top corner radius when the maximum strain at that particular location exceeds the failure strain.

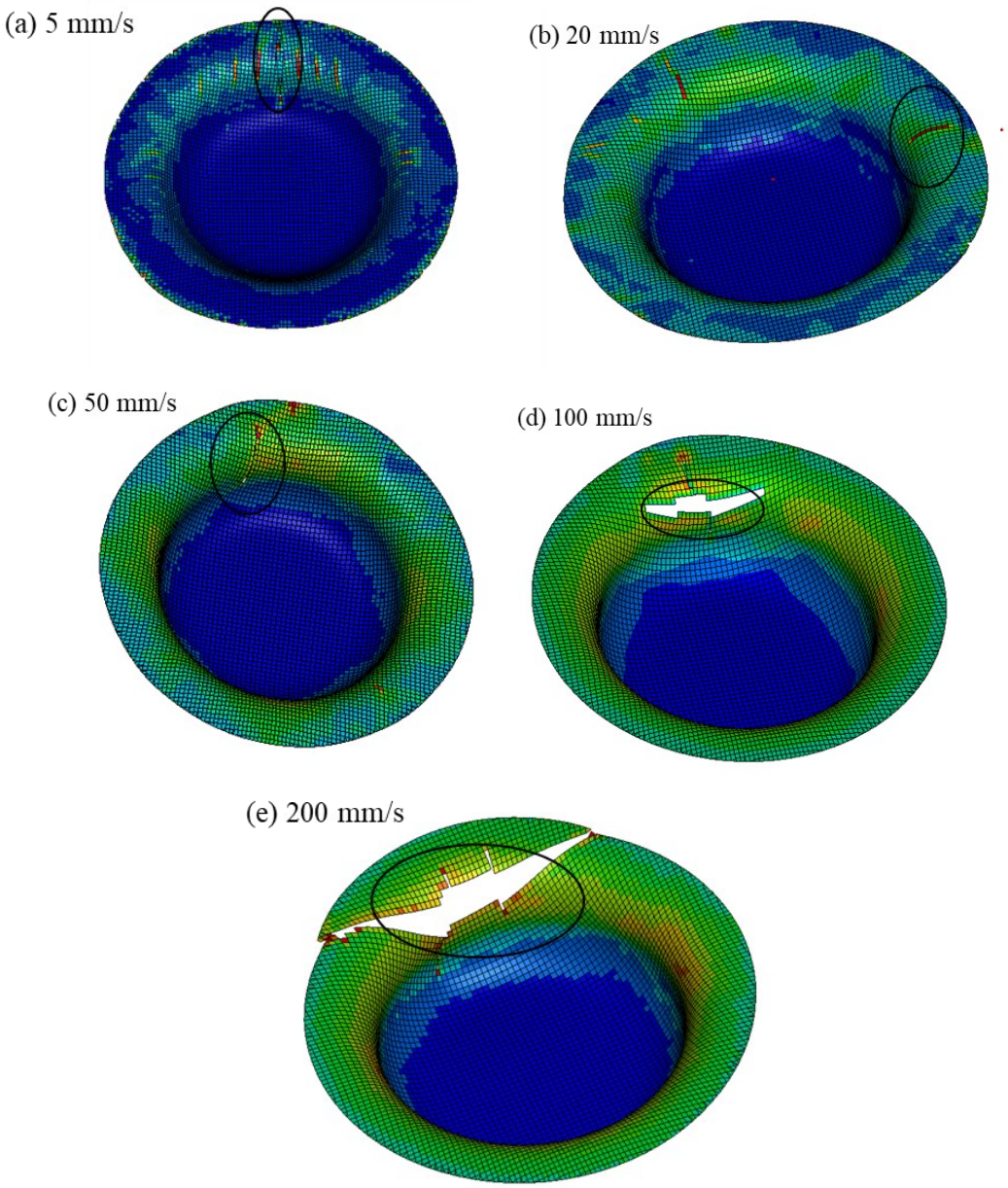

Figure 3.53: Failure locations at different punch velocities.

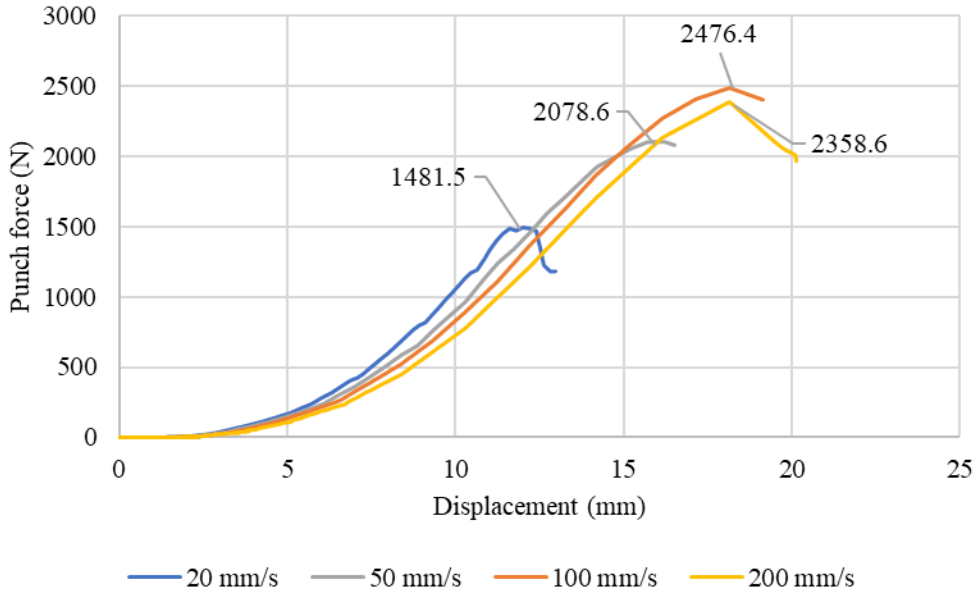

Figure 3.54: Effect of punch velocity on punch force vs. punch displacement diagrams.

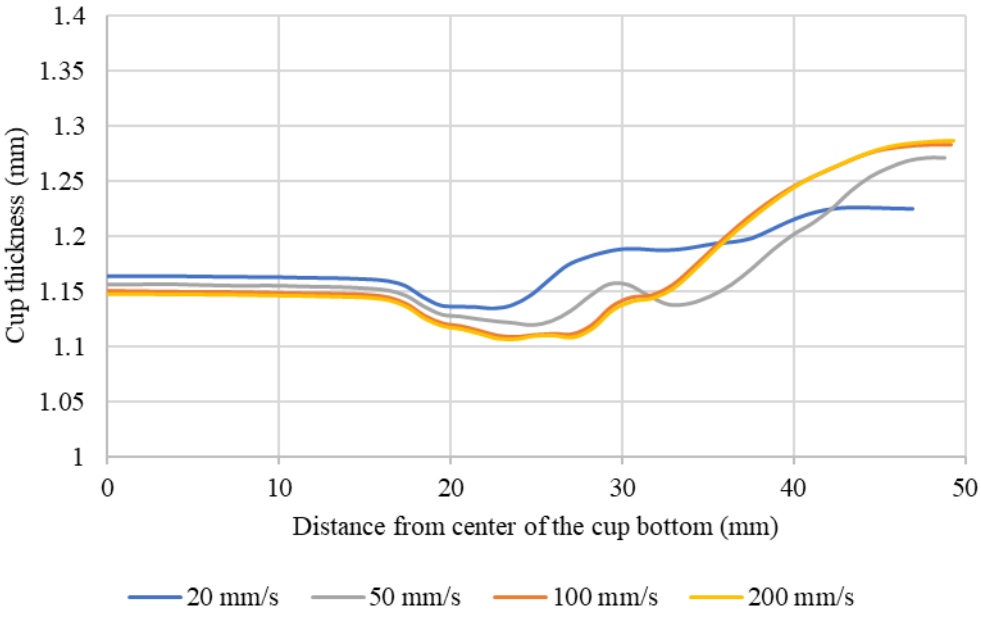

Figure 3.55: Cup thickness variation just before failure for deep drawing at different punch velocities.

Figure 3.55-3.57 show the variations in blank thickness, temperature and effective plastic strain at the draw depth just before failure for deep drawing with different punch velocities. Cup thickness variation as can be seen from Figure 3.55 for 100 and 200 mm/s showed almost similar

behavior. Higher increase in thickness along the flange area was observed for blank with punch velocity at 200 mm/s. The percentage increase in thickness along the flange area for 20 and 50 mm/s was significant when compared to the original thickness which can be attributed to the failure of the PP sheet at lower draw depth.

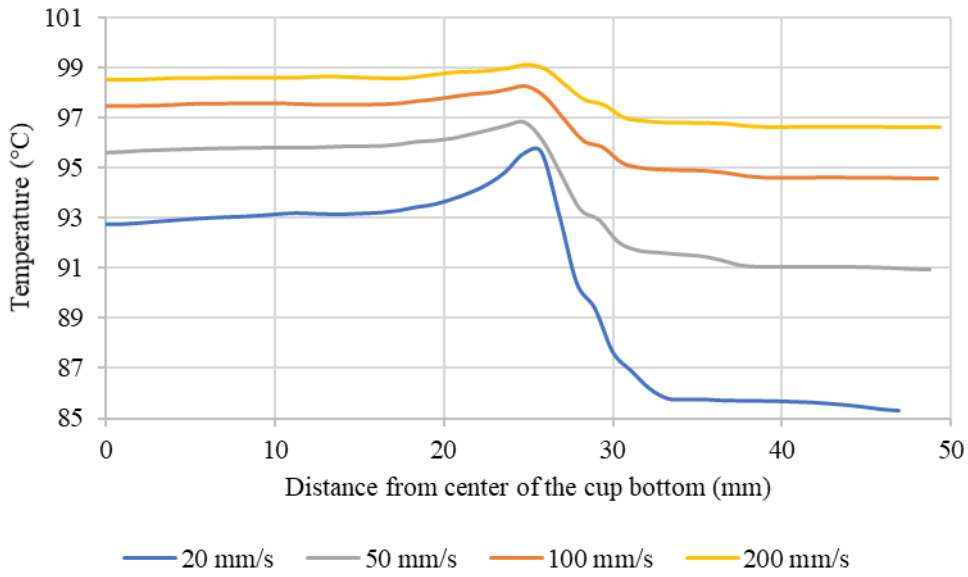

Figure 3.56: Temperature variation profiles just before failure at different punch velocities.

Temperature distribution from Figure 3.56 shows that the temperature drop along the deep drawn cup increases with decrease in punch velocity. Temperature drop in the flange area was higher compared to that in the cup bottom which can be attributed to the blank losing temperature with both the dies while at cup bottom conduction heat transfer occurs only with punch. Temperature drops to almost 86°C at the flange area for deep drawing with punch velocity at 20 mm/s. Effective plastic strain variation until failure shows that irrespective of the punch velocity the maximum strain occurred at the top corner radius as can be seen from Figure 3.57. Plastic strain at the cup bottom reduces with reduction in punch velocity which can be attributed to the failure of the PP sheet at lower draw depth before the deep drawn cup can undergo substantial plastic deformation.

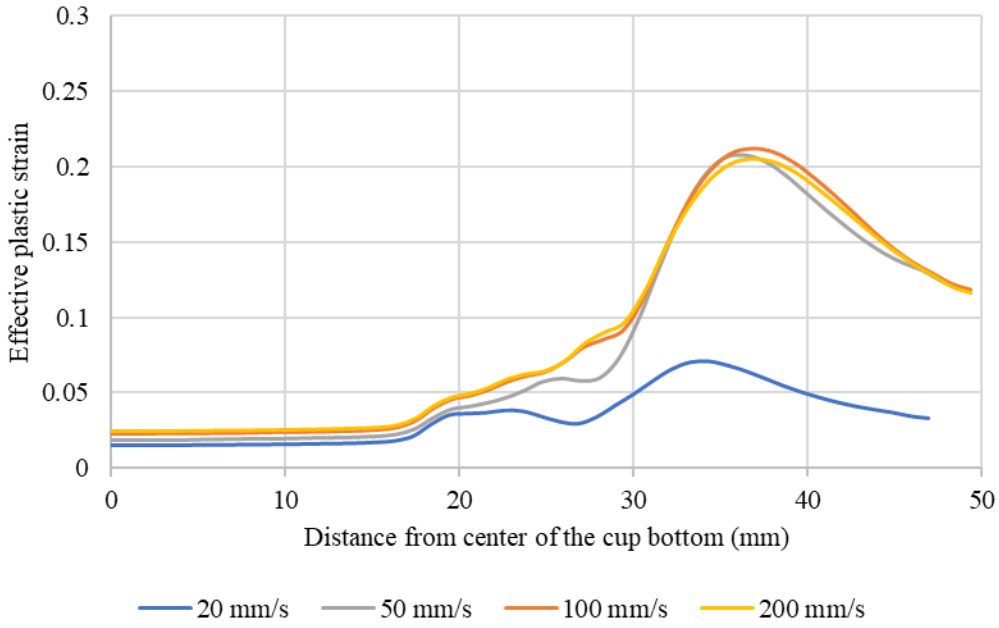

Figure 3.57: Effective plastic strain variation at different punch velocities just before failure.

3.6 Summary and Conclusions

A numerical study of warm deep drawing characteristics of a polypropylene homopolymer was conducted using a circular blank to form a round cup. The forming temperatures and forming speed were selected such that the cups can be formed in a short processing cycle time. Effects of several different process and material parameters on drawing depths, failure modes and final thickness distribution were investigated. These parameters include blank holder force, initial blank temperature, blank diameter, blank thickness, friction co-efficient, die corner radius, punch corner radius, failure strain and punch velocity. Depending on the selection of these parameters, the failure modes observed in the deep drawn cups were flange wrinkling, tearing at the top corner radius and tearing at the end of the vertical wall. In most cases, the cup wall thickness was the lowest at the top of the bottom corner radius and increased in the flange area.

With increasing blank holder force, the punch force required to deep draw polypropylene increases. At low blank holder forces, failure occurs due to wrinkling, while at higher blank holder

forces, excessive thinning along the cup wall results in failure by tearing. There is an optimum blank holder force at which the maximum draw depth is obtained.

The higher the initial blank temperature, the higher is the draw depth which can be attributed to increased plastic deformation, reduction in stiffness of the blank, and increase in failure strain with increase in blank temperature. Hence optimal values of the blank temperature must be considered such that the behavior exhibited by polypropylene is not too stiff, yet the maximum blank temperature is below its melting point.

It was observed the draw depth increases with increasing die corner radius, increasing punch corner radius, increasing failure strain and increasing punch velocity. Friction coefficient does not influence the draw depth. Increasing the blank thickness caused a decrease in draw depth, while increasing the blank diameter decreased the draw depth.

Changing the blank diameter requires selection of the parameters such as blank holder force and die-punch setup (die corner radius and punch corner radius) that would yield the largest draw depth just before failure. For low blank diameter, the blank holder force may not be sufficient to cause enough stretching in the blank and an early release of the blank from the blank holder will lead to failure by wrinkling. For deep drawing of blanks with large diameter, resistance offered to the flow of the material increases which is due to increase in surface area and care must be taken to ensure that the die-punch set up is able to accommodate the increase in flange thickness.

Changing the blank thickness requires changing the parameters such as the die opening diameter, blank holder force etc., since the process parameters suitable for a particular blank thickness will not be suitable for other blank thicknesses. Also, the conduction heat transfer from blank to the die and punch increases with decrease in blank thickness. With increase in blank

thickness, care should be taken to avoid the ironing effect which occurs when the space between the punch and die is not able to accommodate the increase in thickness along the flange area.

Other parameters that may increase the draw depth of polypropylene are its material parameters, such as increased modulus, and process parameters, such as differential heating in which the flange and the punch area of the blank are initially at different temperatures. The experimental work by Machida and Lee [7] has shown the benefit of differential heating; however, more research needs to be done to fully understand the deep drawing characteristics of polypropylene and other polymers under differential heating conditions.

3.7 References

[1] J. A. Schey, Introduction to Manufacturing Processes. (3rd ed.), Boston: McGraw-Hill, 2000.

[2] L. Broutman and S. Kalpakjain, "Cold forming of plastics," *SPE Journal,* vol. 25, no. 10, p. 46, 1969.

[3] R. E. Evans, "The mechanical behavior of thermoplastic materials in the deep drawing process," *Polymer Engineering and Science,* vol. 13, no. 1, pp. 65-73, 1973.

[4] M. J. Miles and N. J. Mills, "The deep drawing of thermoplastics," *Polymer Engineering and Science,* vol. 17, no. 2, pp. 101-110, 1977.

[5] L. J. Broutman, S. Kalpakjain and J. Chawla, "Deep drawability of biaxially rolled thermoplastic sheets," *Polymer Engineering and Science,* vol. 12, no. 2, pp. 150-156, 1972.

[6] D. Lee and P. C. Luken, "Material modeling and solid phase forming of polycarbonate sheet," *Polymer Engineering and Science,* vol. 26, no. 9, pp. 612-619, 1986.

[7] T. Machida and D. Lee, "Deep drawing of polypropylene sheets under differential heating conditions," *Polymer Engineering and Science,* vol. 28, no. 7, pp. 405-412, 1988.

[8] J. L. Throne, Technology of Thermoforming, Cincinnati, OH: Hanser Gardner Publications, 1996.

[9] T. A. Osswald and G. Menges 1923, Materials Science of Polymers for Engineers. (2nd ed.), Munich; Cininnati: Hanser Publishers, 2009.

[10] Y. Zhou and P. K. Mallick, "Effects of temperature and strain rate on the tensile behavior of unfilled and talc-filled polypropylene. Part II: Constitutive equation," *Polymer Engineering and Science,* vol. 42, no. 12, pp. 2461-2470, 2002.

[11] Y. Zhou and P. K. Mallick, "Effects of temperature and strain rate on the tensile behavior of unfilled and talc-filled polypropylene. Part I: Experiments," *Polymer Engineering and Science,* vol. 42, no. 12, pp. 2449-2460, 2002.

[12] C. Donaldson, G. H. HeCain and V. C. Goold, Tool Design. (3rd ed.), New York: McGraw-Hill, 1973.

[13] J. G. Kaufman, Fire resistance of aluminum and aluminum alloys and measuring the effects of fire exposure on the properties of aluminum alloys, Materials Park, OH: ASM International, 2016.

[14] T. A. Osswald and G. Menges, "Thermal Properties of Polymers," in *Material Science of Polymers for Engineers (3rd ed.)*, Munich, Hanser Publishers, 2012, pp. 83-110.

[15] C. I. Chung, W. K. Hennessey and M. H. Tusim, "Frictional behavior of solid polymers on a metal surface at processing conditions," *Polymer Engineering and Science,* vol. 17, no. 1, pp. 9-20, 1977.

[16] E. E. Marotta and L. S. Fletcher, "Thermal contact conductance of selected polymeric materials," *Journal of Thermophysics and Heat Transfer,* vol. 10, no. 2, pp. 334-342, 1996.

Chapter 4 Modeling of Deformation Characteristics and Formability of Dry Fabrics

4.1 Introduction

Fabric-reinforced composites are finding increasing applications in automotive body panels and structures, such as roof panels and B-pillars. The manufacturing process for these components using a thermosetting resin is called resin transfer molding that involves injection of a liquid resin into a dry fabric preform and curing the resin in place [1]. If a thermoplastic polymer is selected as the matrix, then the fabric is first embedded in the matrix, which is followed by press forming operation to make the composite part. One common method of preforming utilizes press forming operation in which a dry fabric or layers of dry fabric are placed on a preforming die and then shaped using a punch that draws the fabric into the die.

During preforming operations to manufacture woven fabric-reinforced composite preforms, the fabrics may be subjected to both shear and tensile stresses at various locations on the preform, such as a corner or a change in curvature in the preforming tool that can cause unacceptable wrinkling, yarn distortion, fiber movement and fiber failure. Most of the studies on the deformation characteristics of fabrics have considered only the shear deformation and used either a uniaxial bias-extension test or a picture-frame test in which the applied load creates shear stresses in the central zone of the fabric specimens used in these tests [2, 3, 4]. As the shear strain in this zone approaches the limit, shear locking occurs and further increase in load results in out-of-plane wrinkling in the fabric. A few studies have shown that a combination of shear and tensile stresses or shear-tension coupling increases the shear stiffness of the fabric, and thereby reduces the amount of wrinkling during the preforming process. Application of in-plane tension with the

help of a blank holder or using a clamping device has shown to mitigate wrinkling through shear-tension coupling and control the final fiber orientation distribution across the component after forming [5].

Currently, there are no standard tests to characterize the shear-tension coupling effect in woven fabrics. Two different tests have been conducted in the past to determine the effect of shear-tension coupling on the shear stiffness of woven fabrics. In one of these tests conducted by Harrison et al. [5], a square fabric specimen with transverse tensile forces was tested in a biaxial bias-extension mode. In the other test conducted by Sharma et al. [6], a cruciform $\pm 45^{o}$-biased fabric specimen was tested in a displacement-controlled mode with its horizontal arms moving outward and its vertical arms moving inward. The results from Harrison et al. [5] and Sharma et al. [6] are contradictory; while Harrison et al. [5] observed an increase in the shear stiffness of the fabric in the presence of applied transverse tensile forces, Sharma et al. [6] did not observe any major changes in the shear stiffness of the fabric for varying transverse loads.

Depending on the press forming conditions used, fabric deformation characteristics and the die-punch design, several defects may form in the fabric preform. Examples of these defects are fiber distortion, wrinkles and tearing. It will be useful if the parameters controlling the defect formation in fabrics can be predicted using a forming limit diagram (FLD) similar to the one used in the metal forming industry to predict the forming behavior of sheet metals.

Forming limit diagram for sheet metals is a graphical representation of the limit strains up to which a thin sheet blank can be shaped in different modes of deformation. The envelope formed by the boundary of the principal strains is called the forming limit curve (FLC), an example of which is shown in Figure 4.1. To avoid failure of the material it is necessary that the strain levels in the stamped part lie below the FLC of the material [7, 8, 9].

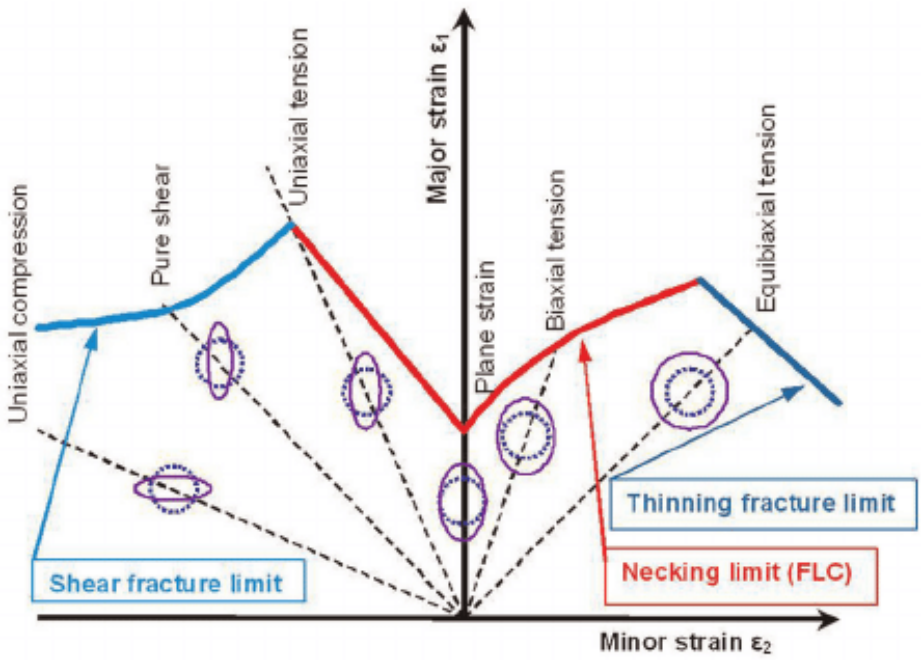

Figure 4.1: Forming limit diagram of a sheet metal [10].

Unlike sheet metals, forming limit studies for fabrics and fabric-reinforced composites have not been explored much. The process of developing FLC for sheet metals cannot be directly applied to fabric-reinforced composites, since the deformation in sheet metals during stamping takes place due to a combination of drawing, bending, and stretching, while the deformation in fabrics during press forming is primarily due to shear between the warp and weft yarns in the fabric. The fibers in the yarns behave in an elastic manner, have low extensibility and also low tensile strain-at-failure; as a result, there may be tearing due to fiber fracture if the tensile stresses acting on them become too high. Furthermore, fabrics have low resistance to buckling and out-of-plane bending deformation.

Some of the defects which arise during press forming of fabrics are fiber distortion, wrinkling and tearing. Wrinkles can form when the fabric is draped over a die with highly curved shapes or corners with small radii that create shear and compressive stresses in the fabric. Since the fabric may not be able to adapt to the geometric form of the die [11], it results in the formation of wrinkles as shown in Figure 4.2. Wrinkling in this case has occurred due to buckling of the yarns at four locations

on the hemispherical cup [12]. Wrinkles are also formed during press forming as the shear deformation between the warp and weft yarns in the fabric reaches a limit, known as shear locking. Until shear locking occurs, the yarns are able to rotate and slide on each other relatively easily. The shear stiffness of the fabric is mainly due to the friction between the yarns; however, at the onset of shear locking, the yarns are closely packed and any further increase in deformation leads to localized wrinkling due to low out-of-plane bending resistance of the fabric. With yarns now laterally compressed, there is further increase in shear stiffness of the fabric [2, 13]. The other form of defects that are observed during press forming of fabrics is tearing. Tearing occurs when the tensile strain in the yarns of the fabric exceeds the ultimate strain-at-failure of the fibers.

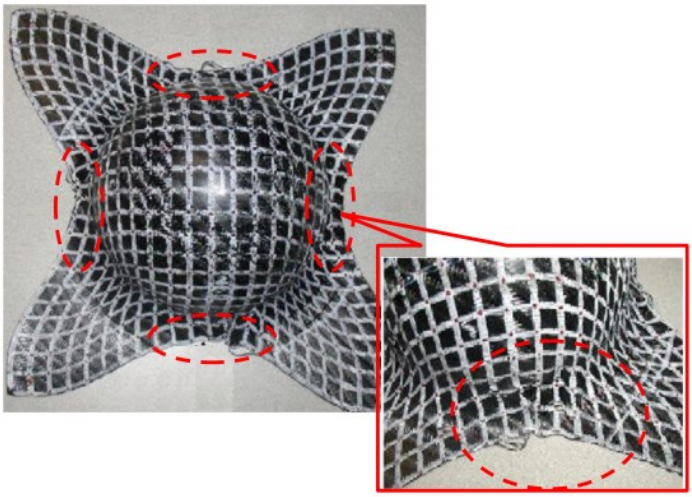

Figure 4.2: Wrinkle formation in the formed hemispherical cup of a fabric reinforced thermoplastic [12].

The concept of forming limit diagrams for composites was first introduced by Dessenberger and Tucker [14]. They used biaxial experiments it to develop FLD for a planar random fiber composite. There are also a couple of references [15, 16] in which forming limit diagrams of fabric-reinforced thermoplastic composites were developed by experiments to predict the onset of wrinkling in fabric-reinforced composites. The possibility of failure by tearing was not addressed in these references. The remaining available literature shows that the past research on this topic is concentrated

principally on understanding the process conditions and the deformation mechanisms during press forming.

This chapter starts with examining the modeling capabilities of woven fabrics using the MAT_234 and MAT_235 material models available in LS-Dyna, a non-linear finite element software used for forming analysis of metals as well as composites. They are assigned to the membrane elements and the simulation results are compared with the experimental work from the available literature. It then deals with using a combination of membrane and shell elements superimposed on one another. The superimposed modeling approach is validated using different case studies and the optimal modeling parameters are determined, which are then used to study the influence of shear-tension coupling on the shear stiffness of plain fabrics using biaxial bias-extension tests with square fabric and cruciform fabric specimens. The fabric orientation is ±45^{o} with respect to the loading directions. Several numerical simulations were performed using LS-Dyna finite element software to determine the influence of specimen design and specimen size on the shear-tension coupling of a plain glass fiber fabric.

The last part of the chapter presents a methodology for the determination of a safe window for press formability of a dry fabric layer using LS-DYNA. The safe forming window, expressed as a function of blank holder force and forming depth, is determined by the ability of the fabric to form and retain the shape without generating wrinkles and tearing. The influence of the punch shape on the safe forming window is also studied.

4.2 Deformation Modeling Approaches for Woven Fabrics

Material models available in LS-Dyna that are used to determine the deformation modes of woven fabrics include Viscoelastic loose fabric model (MAT_234), Micromechanics dry fabric model (MAT_235) and Anisotropic hyper-elastic model (MAT_249) [17, 18]. These material models have

been used by many investigators to predict reorientation of the fabric yarns and to simulate locking phenomenon in uniaxial bias-extension tests, picture frame tests as well as in press forming operations [19, 20]. In a benchmark study, Yildirim and Ozturk [18] compared these three material models for the simulation of press forming of a hemispherical dome and observed that MAT_234 gives a more stable shear angle distribution than MAT_235 and MAT_249. Yildirim et al. [18] also simulated a uniaxial tension test on a plain E-glass fabric and observed that MAT_235 can capture the experimental tensile behavior in the yarn directions in a better way compared to the other two material models.

To study the effect of shear-tension coupling on the deformation characteristics of woven fabrics, it is necessary that the numerical model should be able to capture and replicate both the shear and tensile deformation behavior properly. Also, the numerical model should be able to replicate force vs. shear angle, force vs. displacement, and force vs. theoretical shear angle (obtained using crosshead displacement) behavior of fabrics. Based on the observations from the published literature, it was decided to first study the validity of material models MAT_234 and MAT_235 in simulating the experimentally determined deformation behavior of woven fabrics and then propose a suitable approach to simulate the deformation of woven fabrics in shear-tension coupling tests and also in press forming operations.

4.2.1 Validation of LS-Dyna Material Models to Simulate Dry Fabric Deformation

The current section of the chapter focusses on determining the modeling capabilities for the dry woven fabrics using the LS-Dyna material models MAT_235 and MAT_234. To validate the material models, experimental results from the previously published literature of Hill et al. [21] and Harrison et al. [5] for uniaxial bias extension test were compared with that of the simulation results.

4.2.1.1 Validation of MAT_235

Hill et al. [21] carried out experimental uniaxial bias extension test for silicone-coated plain woven Kevlar fabrics and validated the results using numerical simulations with MAT_235. The material parameters for MAT_235 were optimized using LS-OPT and the optimized values were able to replicate the experimental behavior. The optimized material model input parameters by Hill et al. [21] were used to simulate the uniaxial bias-extension test using MAT_235; this numerical exercise was performed to replicate the results of Hill et al. [21] and to verify the control cards for the fabric deformation. Figure 4.3 shows the comparison of the experimental results of Hill et al. [21] with that of the simulation results using material model MAT_235 assigned to under-integrated membrane and fully integrated membrane elements. Based on the present study, it can be concluded that MAT_235 assigned to either under-integrated or fully integrated membrane shell elements can replicate the fabric deformation behavior.

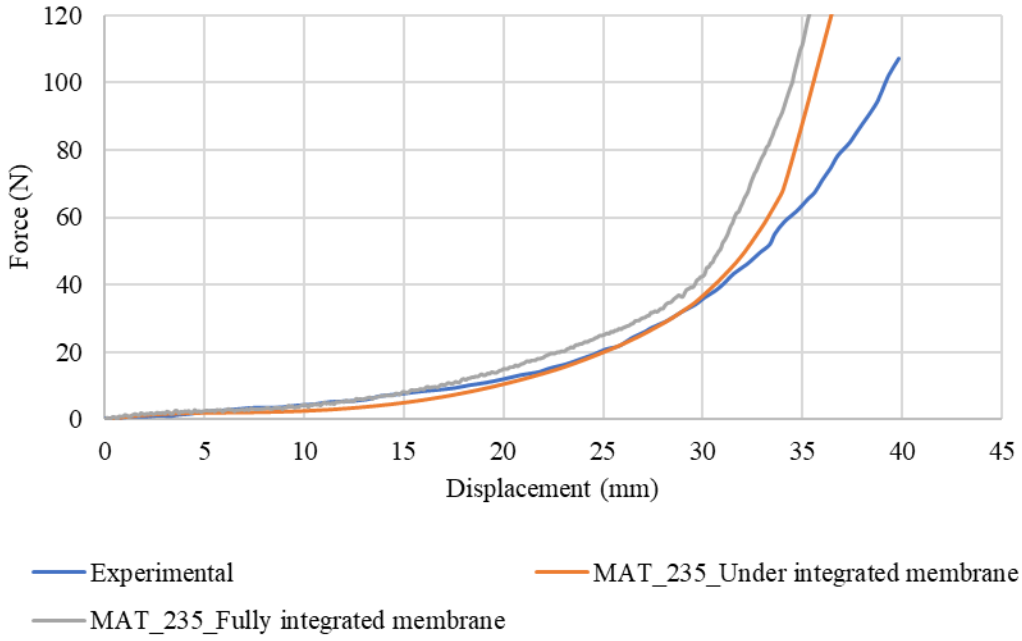

Figure 4.3: Comparison of uniaxial bias extension experimental results (Hill et al. [21]) with simulation results using MAT_235 (with under-integrated and fully integrated membrane elements).

The numerical exercise to validate MAT_235 to study fabric deformation behavior was repeated for ECK 12 plain glass woven fabric and a comparison was made between the experimental results of Harrison et al. [5] and the simulation results. Shear locking angle for ECK 12 glass fabric was determined based on the published experimental results and is shown in Figure 4.4. Harrison et al. [5] provides the normalized shear force vs. shear angle curves based on the experimental uniaxial bias-extension test for ECK 12 glass fabric. Normalization of the experimental results was obtained by dividing the force with the corresponding side length of the pure shear deformation zone. To numerically validate the material model, the side length was assumed to be 77.78 mm owing to the unavailability of the data. The side length was obtained based on the geometrical conditions of the specimen with which the bias-extension test was conducted. The normalized experimental curves were multiplied with the side length to determine the force vs. shear angle response of ECK 12 plain glass woven fabric and a comparison was made with the simulation results using MAT_235 assigned to under-integrated and fully integrated membrane elements.

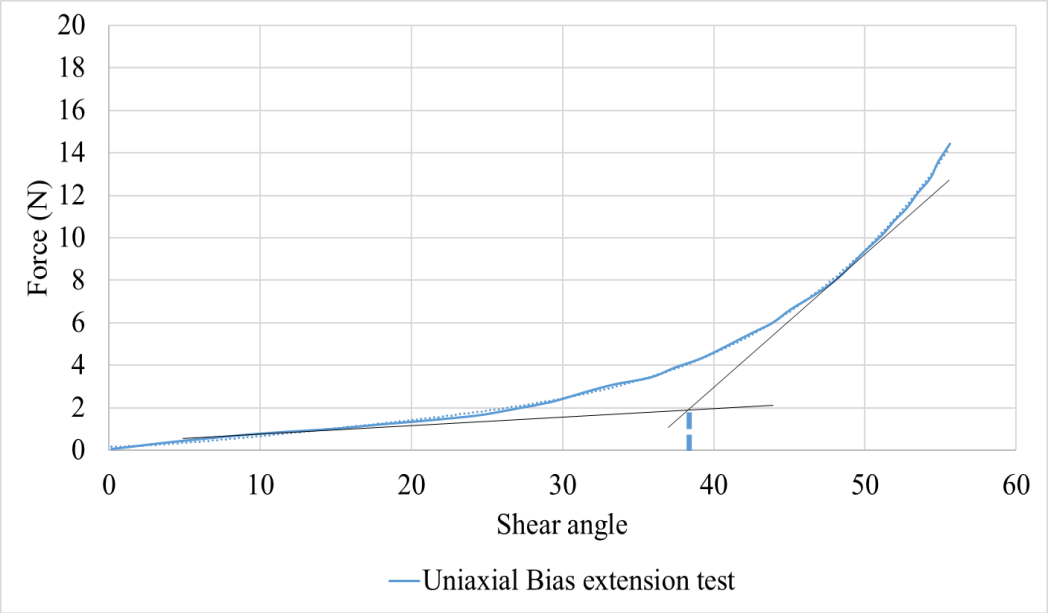

Figure 4.4: Force vs. shear angle curves for ECK 12 plain glass fabric (experimental results by Harrison et al. [5]).

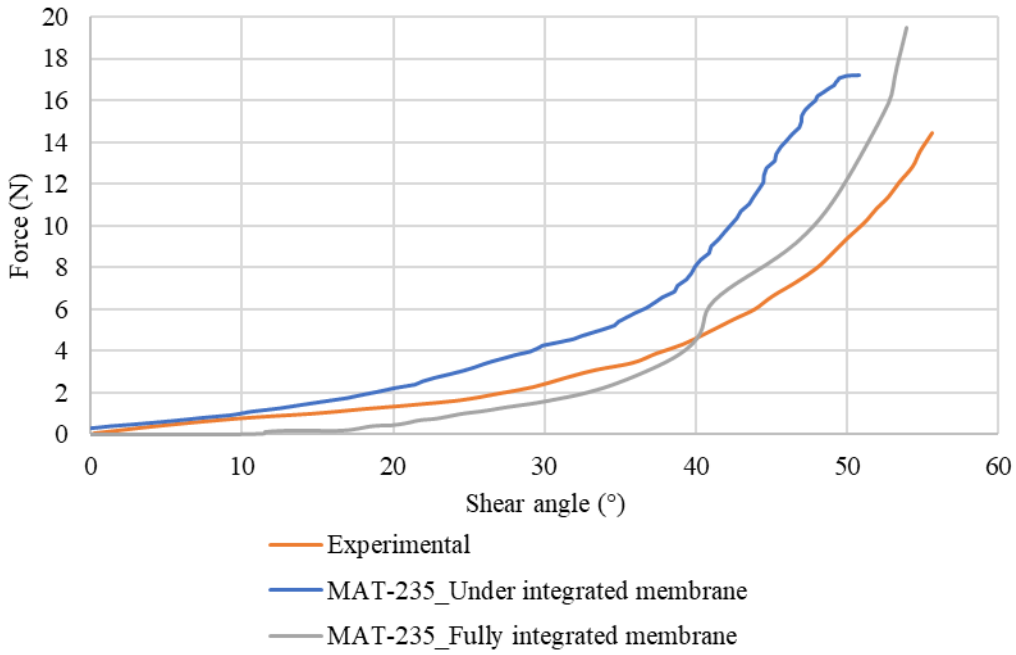

Figure 4.5: Comparison of simulation (MAT_235 with under-integrated and fully integrated membrane elements and experimental (Harrison et al. [5]) force vs. shear angle curves for ECK 12 plain glass fabric.

The shear locking angle determined from Figure 4.4 and the fabric parameters obtained from the thesis by Abdiwi et al. [22] were used to simulate uniaxial biaxial-extension test results for ECK 12. Figure 4.5 shows the comparison of force vs. shear angle data of the experimental test results with simulated curves. Based on the comparison, it can be concluded that MAT_235 with fully integrated membrane elements is able to replicate the fabric deformation behavior exhibited experimentally. There is no tension locking phenomenon exhibited by the fabric as seen from the simulation results. The tension locking phenomenon arises during fabric deformation when the mesh is not properly aligned with the yarns which in turn leads to the spurious tension in the fibers.

Based on the available literature, it was observed that to determine the force vs. shear angle response of the fabrics, it is a common practice to use the crosshead displacement of the testing machine [4, 5] to calculate the theoretical shear angle. Studies have shown that the theoretical shear angle matches the experimental shear angle until shear locking is attained. This practice of

deriving the shear angle data from crosshead displacement for uniaxial bias-extension test can be attributed to the difficulty in obtaining the experimental shear angle data. To further validate the material model MAT_235, shear angle data obtained from the crosshead displacement were validated with that of the experimental curves. To determine the true fabric deformation, it is necessary that the force vs. shear angle data for which the shear angle is obtained using direct measurement should match with the shear angle obtained from the crosshead displacement.

For simulation results using MAT_235 and MAT_234 shear angle data for the uniaxial bias extension test results can be obtained from two sources (a) history variables available in the material model, (b) with the crosshead displacement (using theoretical relationship). Harisson et al. [5] provides a relationship to determine the shear angle from crosshead displacement which is shown in Equation (4.1).

$$\theta_{th} = \frac{\pi}{2} - 2\arccos\left[\frac{1}{\sqrt{2}} + \frac{(d_x - 2\overline{\Delta C_{mu}})}{2L_{mu}}\right] [5] \quad \text{(Eq. 4.1)}$$

Harrison et al. [5] introduced two new parameters C_{mu} and L_{mu}, details of which can be found in Ref. [5]. The accurate determination of the parameters is a time-consuming process. Hence, for the present study these parameters were assumed to be constant obtained from the geometry of the biaxial-extension test specimen. The assumption of the parameters to be a constant simplifies the equation. The simplified equation was then used to calculate the force vs. theoretical shear angle curves and was compared to the experimental results. The results shown in Figure 4.6 are for under- integrated membrane elements. The same behavior as observed with fully integrated membrane elements.

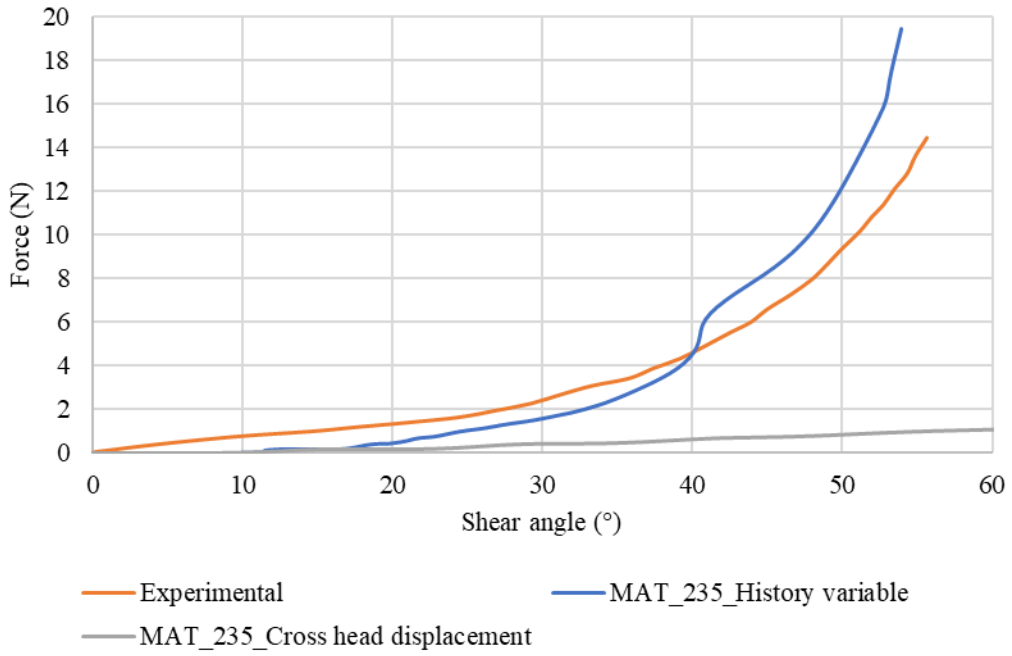

Figure 4.6: Comparison of experimental force vs. shear angle with experimental curves (shear angle determined from history variables and crosshead displacement)

Figure 4.6 shows a comparison of force vs. shear angle curves obtained using the history variable and from crosshead displacement using Equation 4.1. From Figure 4.6, it can be observed that the force vs. theoretical shear angle using MAT_235 does not match with the biaxial bias-extension test experimental results for ECK 12. The force vs. shear angle data obtained from the crosshead displacement shows very low force required for deformation compared to that from experimental results.

From the validation study for MAT_235, we can conclude that the material model is able to replicate force vs. displacement, force vs. shear angle curves but not the force vs. theoretical shear angle curves. The material model predicts higher crosshead displacement to obtain a certain shear deformation compared to the experimental results. Hence, the material model cannot be used to capture the true fabric deformation behavior.

4.2.1.2 Validation of MAT_234

The numerical exercise to validate MAT_235 was repeated with MAT_234 (Viscoelastic loose fabric) model to verify if the material model can be used to determine true fabric deformation behavior, i.e., capture force vs. displacement, force vs. shear angle and force vs. theoretical shear angle behavior and closely replicate the experimental curves for fabric deformation behavior.

Experimental results of Hill et al. [21] for Kevlar woven fabric were validated with the simulation results using MAT_234. Material model input parameters for MAT_234 were inversely calculated based on the optimized material input parameters for MAT_235. Figure 4.7 shows the comparison of the simulation results using MAT_234 assigned to under-integrated and fully integrated membrane elements with that of the experimental results by Hill et al. [21].

For MAT_234, the shear locking angle assigned to the membrane shell elements was a higher arbitrary angle instead of the original locking angle obtained from experiments, with other material parameters being the same. Higher locking angle was assigned since it was observed that the material model predicts high stiffness behavior as soon as the locking angle is attained and is not able to predict the gradual non-linear increase in shear stiffness behavior observed experimentally. By assigning a higher shear locking angle, simulation results were able to replicate the fabric deformation behavior obtained experimentally. From Figure 4.7, it can be concluded that MAT_234 assigned to fully integrated membrane shell elements can replicate fabric deformation behavior obtained experimentally while the MAT_234 assigned to under-integrated membrane shows zero force required for fabric followed by a stiffer response.

The numerical exercise to validate MAT_235 was repeated for MAT_234 and the results are compared to the experimental results of Harrison et al. [5]. Figure 4.8 shows a comparison of the experimental results of uniaxial bias-extension test for ECK 12 glass fabrics with that of the

simulation results assigned to under-integrated and fully integrated membrane shell elements. From Figure 4.8, it can be seen that the MAT_234 assigned to under-integrated membrane shell elements shows zero shear force till the shear locking angle is attained, followed by a very stiff response with rapid increase in the force required for further deformation of the fabric. With MAT_234 assigned to fully integrated membrane shell elements, the predicted force required for fabric deformation shows a very high value compared to the experimental results.

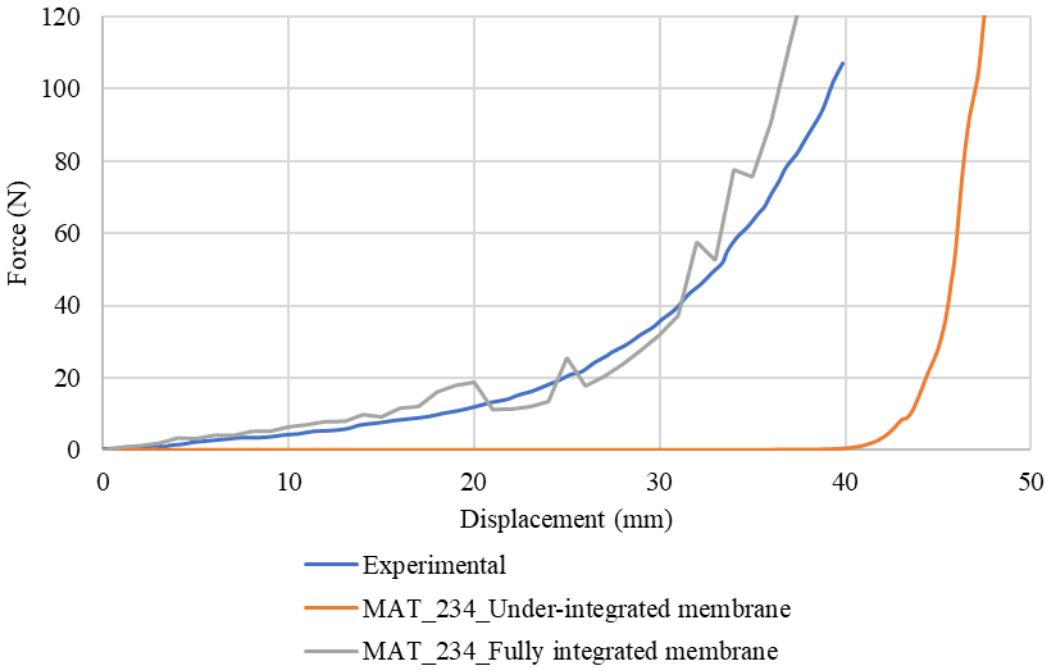

Figure 4.7: Comparison of experimental (Hill et al. [21]) and simulation results with MAT_234 (under-integrated and fully integrated membrane elements).

The high force predicted with the fully integrated membrane shell elements can be attributed to the tension locking phenomenon that occurs when the finite element meshes are not aligned with the yarn directions which in turn leads to the spurious tension in the fibers. This tension arises due to the large tensile rigidity exhibited by the fabric material and to the inability of the finite element software's to give a solution without extension in the fiber directions at the gauss points [23]. Orienting the elements along the tow direction or the direction of fibers avoids

the tension locking phenomenon observed. Figure 4.9 represents the elements oriented in the direction of fibers for uniaxial BE test.

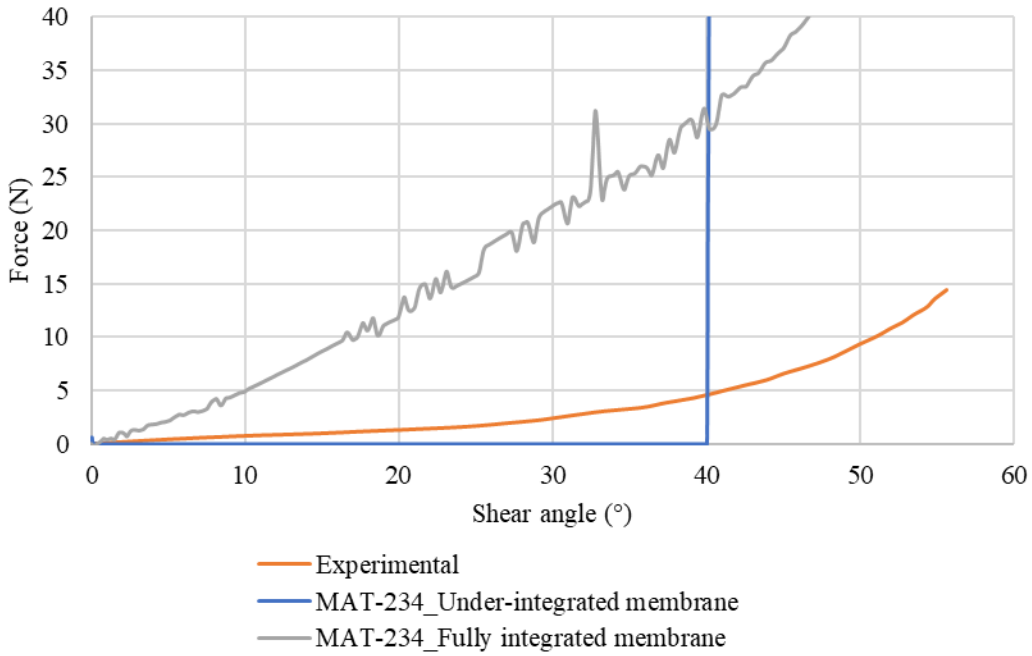

Figure 4.8: Comparison of experimental force vs. shear angle curve with simulated curves using with MAT_234 for ECK 12 plain glass fabric.

Numerical exercise for ECK 12 glass using MAT_234 assigned to fully integrated membrane elements was carried out with the elements oriented along the fiber directions. The Fabric mesh used to determine force vs. shear angle is shown in Figure 4.9. The obtained simulation results are compared with the experimental results. Simulation results with the mentioned approach shows a zero-force required for fabric deformation followed by a stiffer response. This behavior is same as that with the under integrated membrane elements oriented in any direction with respect to the fiber direction.

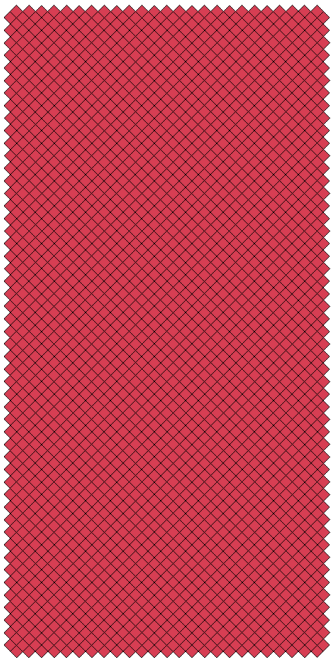

Figure 4.9: Elements oriented along tow direction to avoid spurious tension when the elements are assigned to fully integrated membrane shell element formulation.

Based on the validation study from this section, it was concluded that MAT_234 assigned to reduced or fully integrated membrane elements is not able to capture true fabric deformation behavior as it predicts zero shear force required for fabric deformation. As the material model was not able to replicate force vs. displacement and force vs. shear angle curves, the comparison of force vs. theoretical shear angle curves was not carried out.

4.2.2 Superimposed Modeling Approach

Flexural stiffness of fabrics is quite low in comparison to its tensile stiffness and fabrics are highly susceptible to buckling when subjected to in-plane compression [20]. To simplify numerical determination of the behavior of fabrics, it is common practice to disregard bending stiffness and use only the membrane elements. Forming simulation with only membrane elements predicts the formation of multiple small wrinkles that are not observed experimentally as shown in Figure 4.10,

reason for which can be attributed to the membrane elements not being able to include out-of-plane bending stiffness.

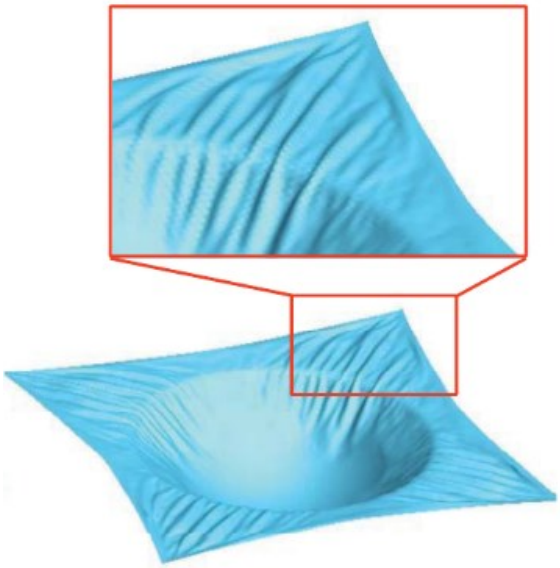

Figure 4.10: Multiple small wrinkles observed for numerical model with membrane elements [24].

Several studies have shown that including the out-of-plane bending stiffness even when they are very low compared to the tensile stiffness will represent the true fabric deformation and play a key role in capturing the wrinkle onset, shape, and size [13, 25]. Element formulation in finite element software which can capture the low out-of-plane bending stiffness while preserving the high tensile stiffness of the fiber directions are not present. To overcome this, different modelling approaches [26, 27, 24] have been used that include the in-plane shear behavior and out-of-plane bending stiffness for the fabrics so that they represent the true fabric deformation.

In the present approach, a superimposed combination of membrane and shell elements was used. The duplicate nodes which arise due to the superimposition were merged so that they are mutually constrained and share the same nodes. Modeling the in-plane shear behavior of the fabrics is governed by the membrane elements while the out-of-plane bending stiffness is governed by the shell elements. The membrane elements are assigned the tensile rigidity and the shear characteristics

of the fabric material, while the shell elements are assigned the tensile modulus whose value is derived from the flexural rigidity of the fabric material [27, 28]. In the absence of the flexural rigidity stiffness of the fabric, the tensile modulus of the shell elements can be assigned a very small value, usually less than 0.01% of the tensile modulus of the fabric material and it can be adjusted to match the experimental force vs. shear angle or force vs. displacement curves. For elements oriented at an angle with respect to the fiber direction, it is preferable to use under-integrated membrane elements. To use fully integrated membrane elements, the elements are to be oriented along the direction of fiber to avoid tension locking [23].

4.2.2.1 Validation of the Superimposed Approach

Based on the numerical exercise in the previous section, it was concluded that MAT_234 and MAT_235 assigned to reduced or fully integrated membrane shell elements cannot be used to capture the true fabric deformation behavior. The reason can be attributed to the membrane elements not being able to capture the out-of-plane bending stiffness. To capture the out-of-plane bending stiffness, superimposed approach was utilized. Modeling approach of superimposed model includes superimposed membrane and shell elements and assigning a very low tensile modulus to the shell elements. The superimposed approach was used to simulate the fabric deformation behavior observed in the two previously published uniaxial bias-extension experimental results.

The membrane elements were assigned the material model MAT_234 and the shell elements were assigned the isotropic elastic material model MAT_01. Experimental results of Hill et al. [21] for silicone-coated plain woven Kevlar fabric in uniaxial bias-extension tests were first utilized to verify the superimposed modeling approach. As the flexural rigidity values of the fabric are unknown, the tensile modulus values assigned to the shell elements were varied to match the

simulation results with the experimental curves. Based on this approach, a tensile modulus of 4 MPa which is 0.0067% of the tensile modulus of the fabric has shown to match the experimental results. Figure 4.11 compares the experimental results of Hill et al. [21] with the simulation results using the approach of superimposed elements and using only MAT_234 membrane elements. It shows that the simulation results of superimposed elements match the experimental results closely and the in-plane shear properties of the fabric material are not affected since the assigned modulus to the shell elements is very low. With only MAT_234 membrane elements, the force does not increase until a displacement of 22.5 mm is reached, which is contrary to the experimental results.

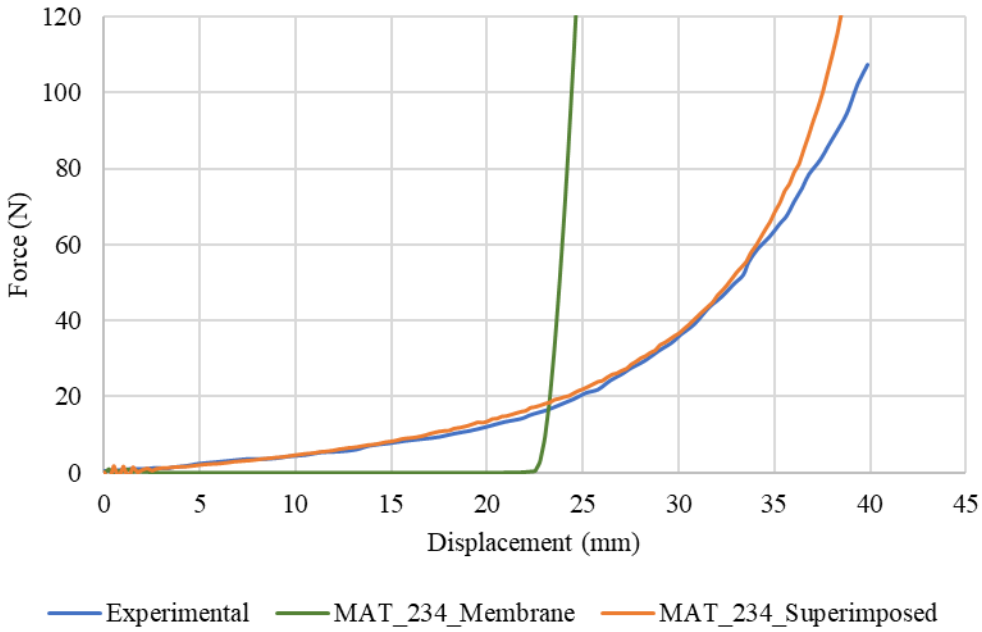

Figure 4.11: Comparison of two numerical models (MAT_234 membrane elements only and superimposed elements) with uniaxial bias-extension test results of Hill et al. [21].

The same exercise was repeated to validate the modeling approach using the experimental results of Harrison et al. [5] on the uniaxial bias-extension tests of ECK-12 plain glass fiber fabric. Figure 4.12 represents the comparison of the simulated and the experimental force vs. shear angle curves. It can be seen that the superimposed elements approach can capture the behavior of the

ECK-12 fabrics determined experimentally. The value of tensile modulus assigned to the shell elements was 1.5 MPa which is 0.0021% of the tensile modulus of the fabric material. Such a small value would not affect the in-plane shear properties of fabric material. Force vs. shear angle curves with shear angle measured from crosshead displacement using theoretical equations (Equation (4.1)) by Harrison et al. [5] are also included in Figure 4.12. The curves obtained using the shear angle from simulation history variables and from the crosshead displacement matches closely with the experimental curve. Based on these results, it is concluded that finite element modeling with the superimposed elements can replicate force vs. displacement behavior, force vs. shear angle behavior and the shear angle variation with cross head displacement. i.e., the superimposed model can be used to simulate the fabric deformation behavior.

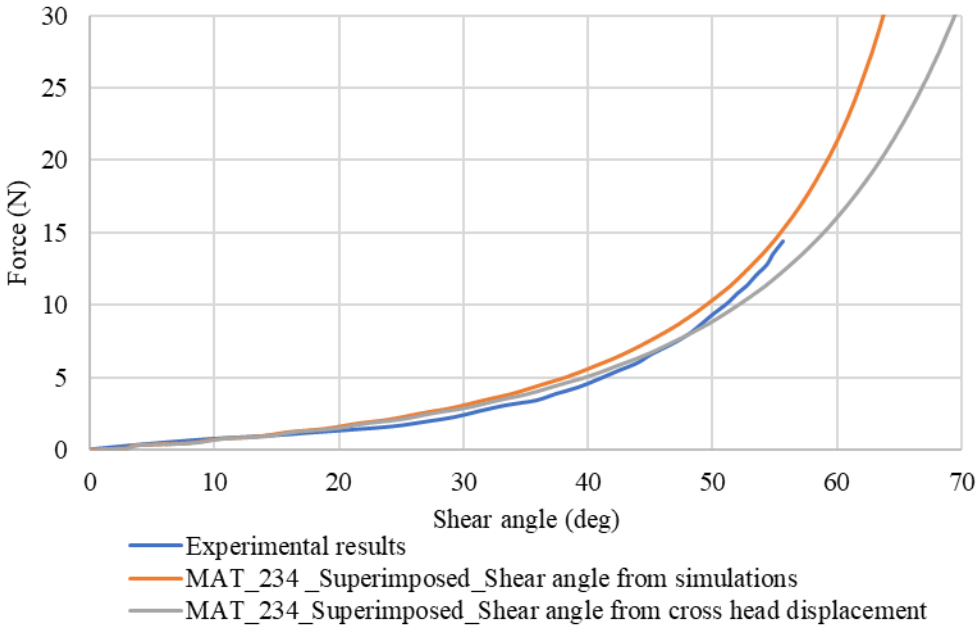

Figure 4.12: Comparison of numerical models (MAT_234 superimposed; shear angle from history variables and from crosshead displacement) with uniaxial bias extension test results of Harrison et al. [5].

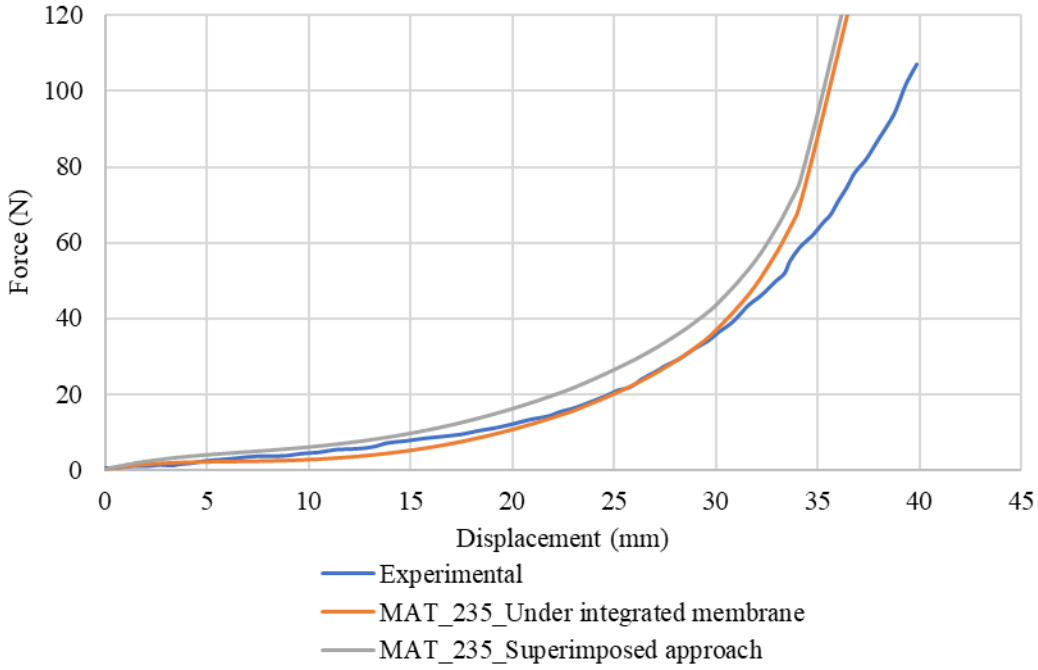

Figure 4.13: Comparison of numerical models (MAT_234 superimposed; shear angle from history variables and from crosshead displacement) with uniaxial bias-extension test results of Harrison et al. [5].

The method of superimposed membrane and shell elements was used with MAT_235 to verify if the approach alters the fabric deformation behavior significantly. Figure 4.13 shows the comparison of the experimental results with simulation results for MAT_235 with only membrane elements and with the superimposed approach. From Figure 4.13, we can see that the superimposed approach with MAT_235 does alter the behavior, but it is observed to be very minimal. Based on the numerical exercise, we can conclude that superimposed method can replicate the fabric deformation behavior exhibited experimentally with material models assigned to under integrated membrane shell element formulations. If the elements are assigned to fully integrated membrane shell elements, then the elements are to be oriented along the direction of fibers to avoid tension locking phenomenon.

4.3 Shear-Tension Coupling

Harrison et al. [5] have emphasized the importance of studying the shear-tension coupling to determine the true fabric deformation. Simulations were run first with the same test conditions at which their experiments were carried out to verify if the superimposed model can replicate experimentally obtained results. The material model parameters were the same as those used in uniaxial bias-extension test simulation for ECK-12 glass fabric described in the previous section. Then, several test parameters were varied to study their effects on the shear-tension behavior of the fabrics considered.

4.3.1 Biaxial Bias Extension (BBE) Test of Square Fabric Specimen

To determine shear-tension coupling in fabrics, Harrison et al. [5] used biaxial bias-extension (BBE) tests in which a square fabric specimen was clamped over a fraction of the length along its four edges. This is shown in Figure 4.14. The specimen was fixed at the bottom clamp and pulled in the upward direction at the top clamp, while applying transverse tensile forces F_C in the outward directions at the right and left clamps. The experiments were conducted on a tensile testing machine and the transverse forces were applied using a pulley arrangement shown in Figure 4.15. Two different specimen sizes were used: 210 mm x 210 mm and 240 mm x 240 mm. The clamping lengths were 70 mm for the first specimen and 60 mm for the second specimen so that the clamping ratios were 3:1 and 4:1, respectively. The vertical load on the top clamp F_T increased with increasing vertical displacement of the top clamp. Force vs. shear angle curves showed an increase in slope with increase in the applied transverse tensile force representing an increase in shear stiffness of the woven fabrics.

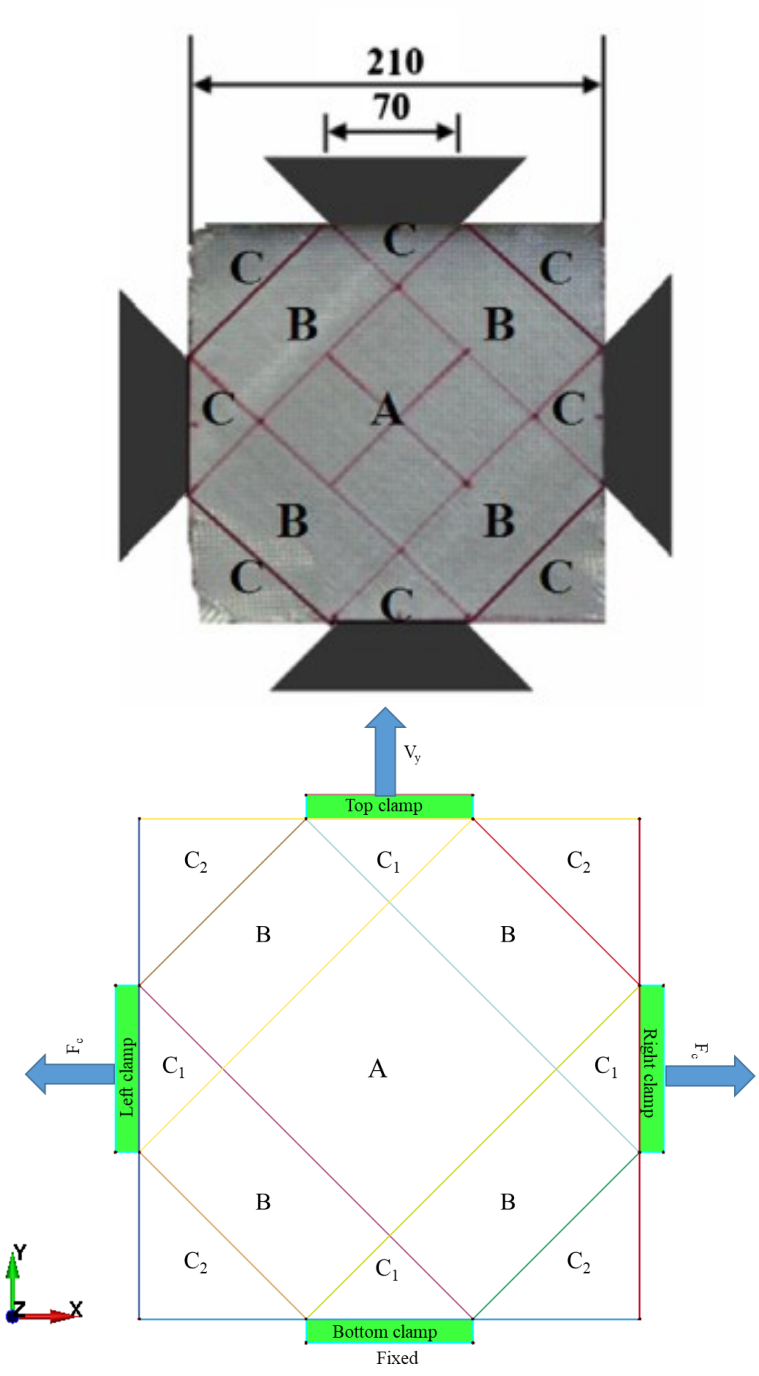

Figure 4.14: Square biaxial bias-extension test specimen (top) according to Harrison et al. [5] and (bottom) a schematic of the specimen with clamping edge lengths represented in color and showing pure shear (A), half shear (B) and zero-shear (C_1 and C_2) zones.

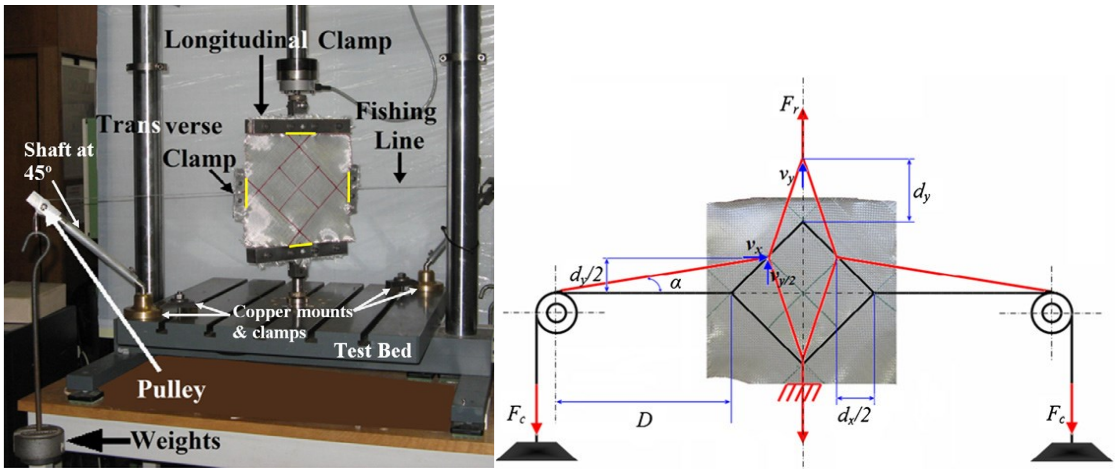

Figure 4.15: (a) Biaxial bias-extension test araangment using square fabric specimen and (b) schematic representation of the deformed square specimen under increasing vertical load [5].

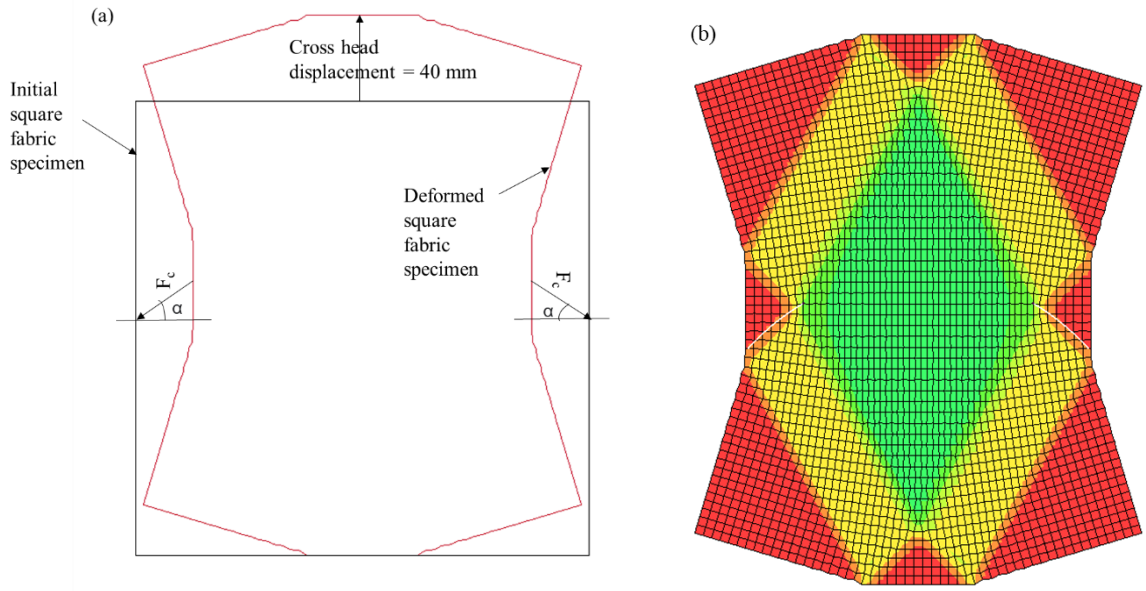

Figure 4.16: Deformed shape of the square fabric specimen with 4:1 clamping ratio and a transverse load of 50 N at 40 mm vertical displacement: (a) Schematic, (b) Simulated (white lines represent the path traversed by the corner of the pure shear zone).

Harrison et al. [5] noted several zones of deformation on the fabric specimens as shown in Figure 4.14: a zone of pure shear in the center of the specimen represented as A, a zone of half shear in areas B, and two zones of zero shear deformation in areas C_1 and C_2. Area C_1 is the region next to the clamping length where the tensile forces are acting and area C_2 is the region free from

any constraints. C_2 shows zero shear deformation due to the absence of any forces acting in that region. The deformed BBE specimen shows that the moving top horizontal edge is displaced upward from the fixed bottom horizontal edge and the two vertical edges where the transverse forces are applied in the outward direction move inward (Figure 4.16). However, because of the loading arrangement used in the experiments, the points of application of the transverse forces also were displaced and their lines of action became inclined by an angle 'α' with the horizontal direction. As a result, there was not only a tensile force on each vertical edges, but also a shear force acting on the vertical edges. Because of this, the true material deformation force on the fabric will be different than the vertical force acting on the top clamp.

4.3.1.1 Modeling of Biaxial Bias-Extension Test (Square Fabric Specimen)

A square ECK-12 fabric specimen of 210 mm x 210 mm in size with clamping length of 70 mm along each side was used to simulate the BBE tests. Clamping ratio, defined as the ratio of total edge length to the clamping length, was 3:1. The bottom edge nodes were constrained in all directions and the top nodes were displaced in the +y direction at a constant velocity of 100 mm/s as shown in Figure 4.14. The clamping nodes on the right and left sides were subjected to a constant transverse force F_C of 5 N, 50 N and 100 N, and the corresponding vertical force F_T vs. shear angle curves were obtained from the history variable which were then compared with the experimental results. Quadrilateral elements of 4 mm in size were used to mesh both the membrane and shell layers superimposed on one another. The duplicate nodes which occur due to the superimposition were merged. Under-integrated membrane elements were used to avoid tension locking since the direction of the finite elements were not oriented with that of the yarn directions.

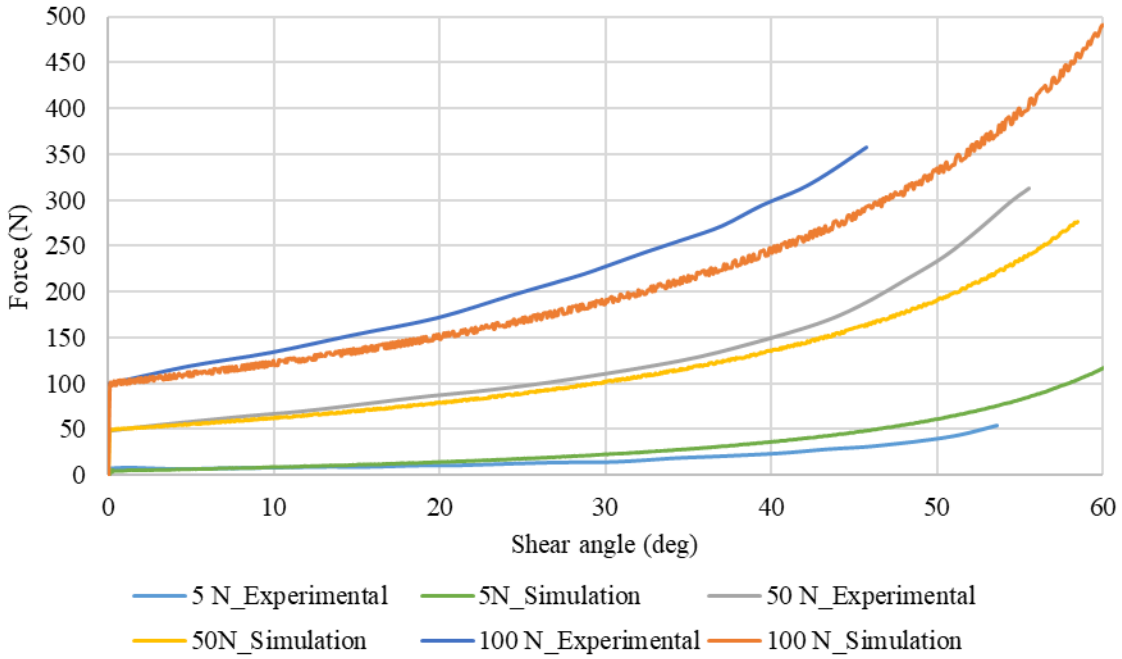

Figure 4.17: Comparison of BBE test results of total force vs. shear angle by Harrison et al. [5] with the simulation results.

Figure 4.17 shows a comparison of the force vs. shear angle curves for biaxial bias-extension test obtained from the simulation results with that of the experimental results by Harrison et al [5]. It can be seen in Figure 4.17 that the superimposed approach is able to closely replicate the BBE test results. The slope of the force vs. shear angle increases with increase in the applied transverse load, which is the same behavior exhibited by ECK 12 plain glass fabric both experimentally and from simulation results. Increase in slope with increasing transverse force of 5, 50 and 100 N indicates stiffer response exhibited by the fabric due to the application of tensile force.

4.3.1.2 Material Deformation Force

To calculate the material deformation force F_m, the reaction force F_r due to the transverse force F_C must be subtracted from the total force F_T. Since in the experiments conducted by Harrison et al. [5], F_C is inclined at an angle 'α', they proposed Equation 4.2 to determine the reaction force F_r. In this

equation, $V_{horizontal}$ and $V_{vertical}$ are the velocities of the horizontal and vertical corners of zone A. The x and y coordinates at each time step can be obtained as output from LS-Dyna which can then be used to calculate the angle 'α'.

$$F_r = F_C\left(\frac{V_{horizontal}}{V_{vertical}}cos\alpha + sin\alpha\right) \quad \text{(Eq. 4.2)}$$

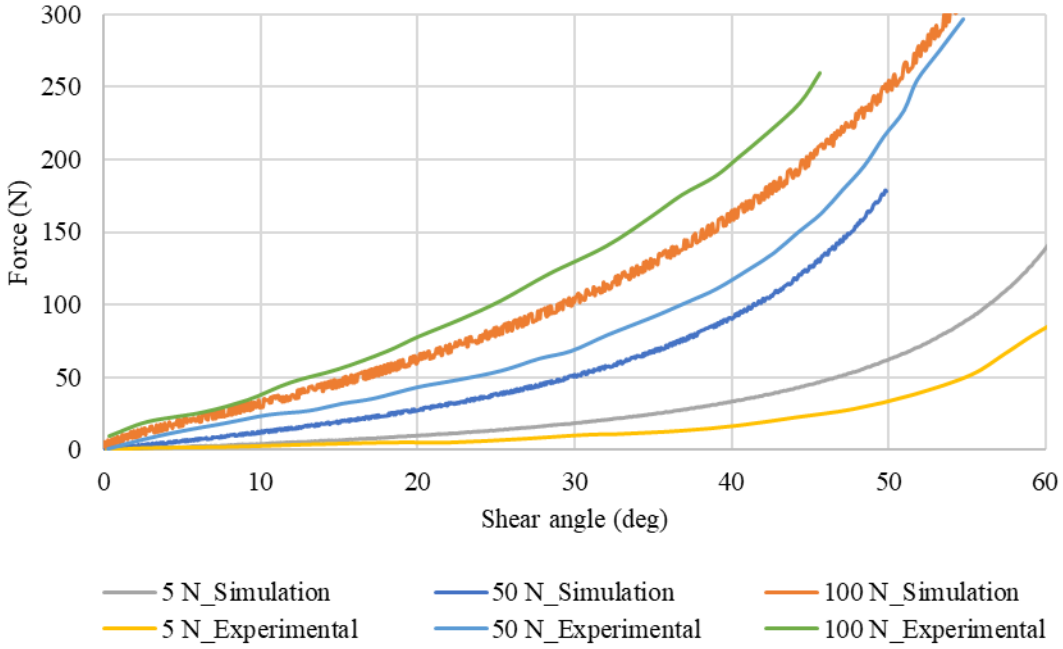

Figure 4.18: Material deformation force vs. shear angle curves at different applied transverse tensile forces.

As can be seen in Figure 4.18, the material deformation force F_m increases with increasing transverse tensile force indicating higher fabric stiffness behavior exhibited by the fabrics. The simulated material deformation force curves were compared with the experimental material deformation force curves and the trends represented by both simulation and experimental results are similar.

4.3.1.3 Effect of Clamping Ratio

To determine the effect of the clamping ratio on the deformation behavior of the fabric, five different clamping ratios were considered: 1.04:1, 2:1, 3:1, 4:1 and 5:1. For the 210 mm x 210 mm

fabric specimen, the corresponding clamping edge lengths are 202, 105, 70, 52.5 and 42 mm, respectively.

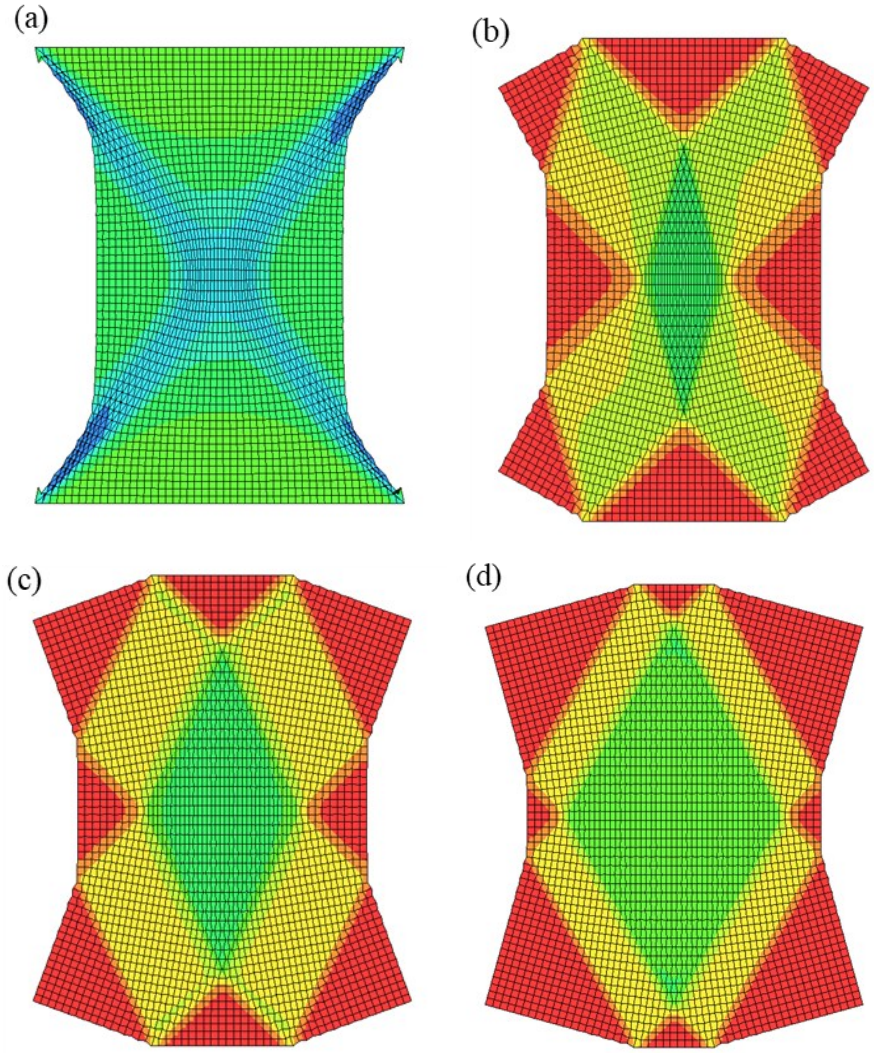

Figure 4.19: Fabric deformation shape for different clamping ratios (a) 1.04:1, (b) 2:1, (c) 3:1, (d) 5:1. Fabric deformation shape for 4:1 clamping ratio is shown in Figure 4.16.

Figure 4.19 represents the fabric deformation shapes at a vertical displacement of 40 mm. Force vs. shear angle response was recorded for different clamping ratios and the results are shown in Figure 4.20. Shear angle was measured at the center of the fabric specimen. From Figure 4.20, it can be seen that the force vs. shear angle response is almost the same for clamping ratios of 2:1,

3:1, 4:1 and 5:1. The 1.04:1 clamping ratio shows a different behavior compared to the other ratios which can be attributed to the wrinkle formation along the diagonal ends of the square fabric. The force vs. displacement curves plotted in Figure 4.21 show that the higher the clamping ratio, the greater is the displacement at which full shear locking occurs for the square fabric. The shear locking in the central zone for the 2:1 ratio occurs at a displacement of 45 mm, for the 3:1 ratio it occurs at a displacement of 60 mm, and for the 4:1 and 5:1 ratio, the fabric starts to exhibit a stiffer behavior at 60 mm and shear locking can be expected to be at an even higher displacement.

Table 4.1: Effect of clamping ratio on deformation zone areas as percentages of total fabric area*.

Clamping Ratio	Zone A (Pure shear)	Zone B (Half shear)	Zone C_1 (Zero shear)	Zone C_2 (Zero shear)
2:1	7%	11%	7%	4%
3:1	16%	13%	3%	5%
4:1	24%	8%	2%	7%
5:1	27%	8%	1%	8%

(*): Different deformation zones are shown in Figure 4.19.

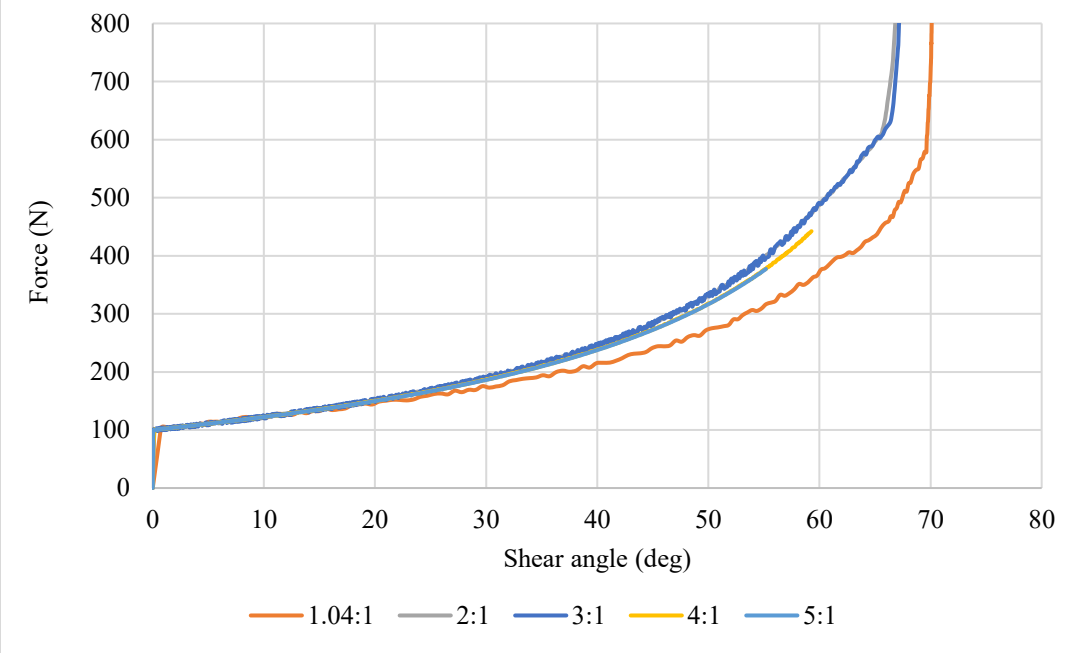

Figure 4.20: Comparison of simulated total force vs. shear angle curves at five different clamping ratios.

Another difference that arises in the BBE test specimens with different clamping ratios is the areas of shear deformation, which can be seen in Figure 4.19. Table 4.1 lists the percentage areas of different deformation zones in the 210 mm x 210 mm square fabric specimen. Areas of the shear deformation zone at 1.04:1 clamping ratio were not considered due to the formation of wrinkles along the diagonals of the square fabric. For the other clamping ratios, the area of pure shear increases with increasing clamping ratio, while the areas of zero shear in zone C_1 decreases and zone C_2 increases with increase in the clamping ratio.

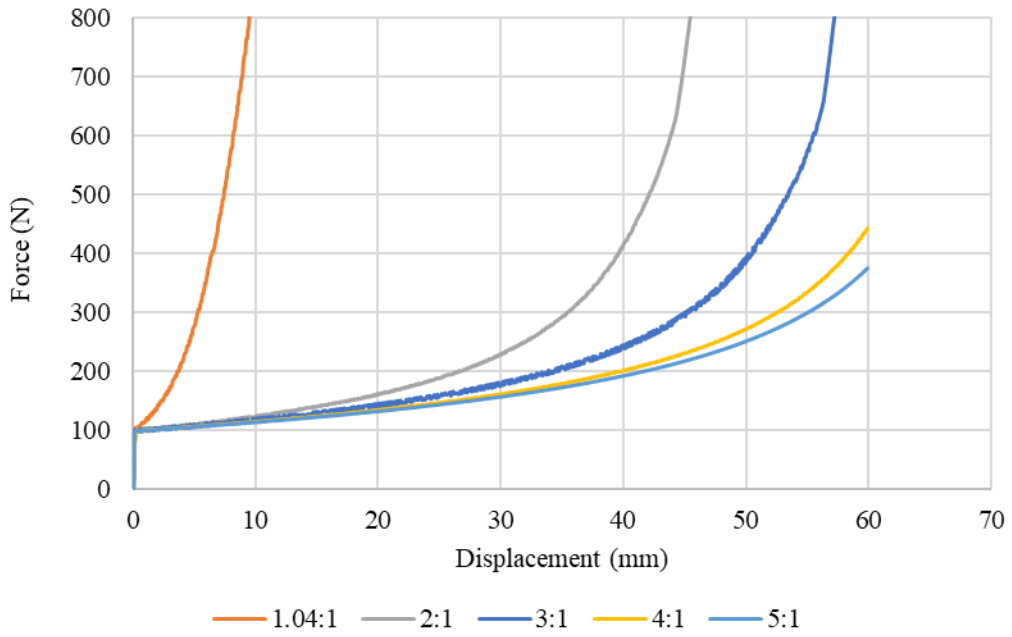

Figure 4.21: Comparison of simulated total force vs. displacement curves at four different clamping ratios.

4.3.1.4 Effect of Fabric Specimen Size

To study the effect of BBE test specimen size, simulations were carried out with 210 mm x 210 mm and 240 mm x 240 mm fabrics. The clamping ratio for both specimens was 4:1 and the applied transverse load was 50 N. The area of the shear deformation zones, shown in Figure 4.22, is higher for the fabric with higher surface area; however, the percentage areas of shear deformation

compared to the total area for both fabric specimens are the same. Figure 4.23 shows that the force vs. shear angle curves for the two fabrics are also the same. However, at all crosshead displacements, the 210 mm x 210 mm fabric specimen shows a higher shear deformation zone when compared to the 240 mm x 240 mm fabric specimen.

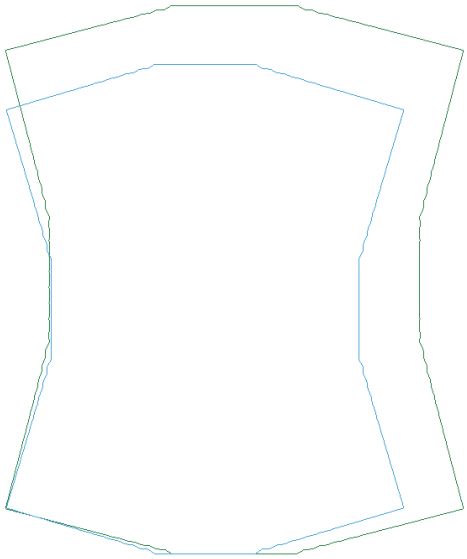

Figure 4.22: Deformed shapes of 210 mm x 210 mm and 240 mm x 240 mm fabric specimens with 4:1 clamping ratio and 50 N applied transverse force.

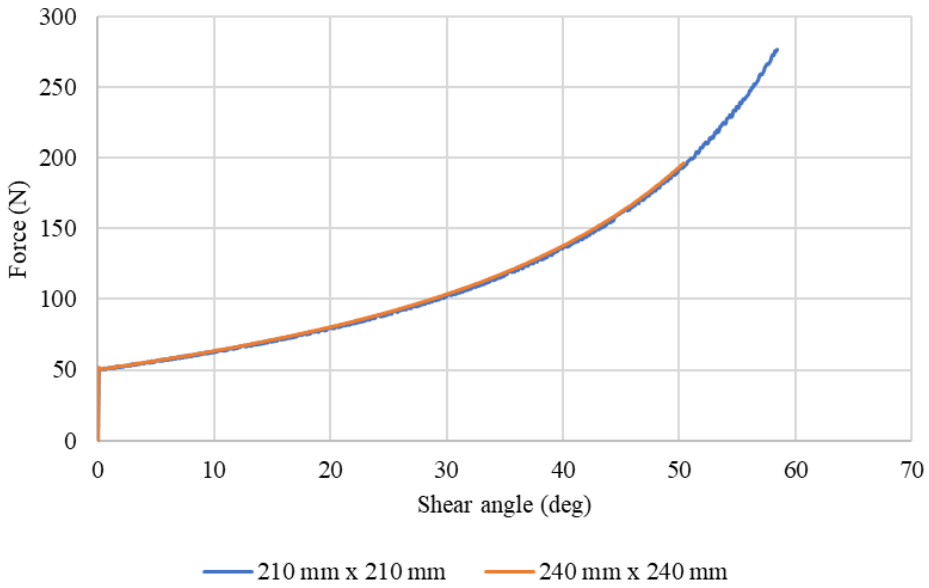

Figure 4.23: Comparison of total force vs. shear angle curves for two different fabric sizes with 4:1 clamping ratio and 50 N applied transverse force.

4.3.1.5 Effect of Specimen Constraints

In the previous sections, the bottom clamp of the BBE specimens was fixed and the top clamp was displaced upward at a constant velocity. This was the test method used by Harrison et al. [5], and as mentioned earlier, due to the change in the lines of action of the applied transverse loads, the total force had to be corrected to determine the material deformation force using Equation 4.2. To determine the effect of specimen constraints, the top and bottom clamps were displaced in opposite directions with equal velocity so that the lines of action of the transverse forces applied on the right and left clamps remained horizontal, and therefore, $\alpha = 0$, which can be seen in Figure 4.24. The total force vs. shear angle curves for 4:1 clamping ratio with 50 N applied transverse load for the two constraint conditions are compared in Figure 4.25. It can be seen in this figure that the total forces are the same for both constraint conditions; however, as shown in Figure 4.26, the material deformation force required to attain a certain shear deformation in the fabric is much higher with the first constraint condition.

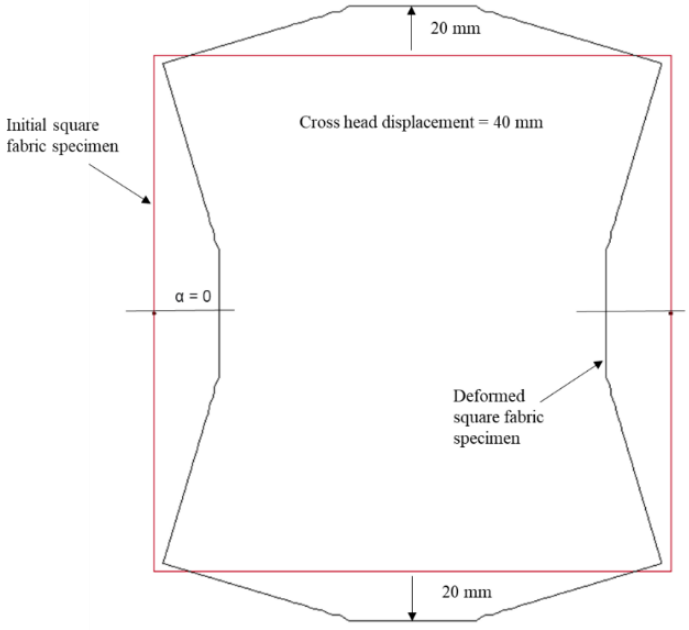

Figure 4.24: Deformed shape of the square fabric with velocity applied to both the top and bottom nodes.

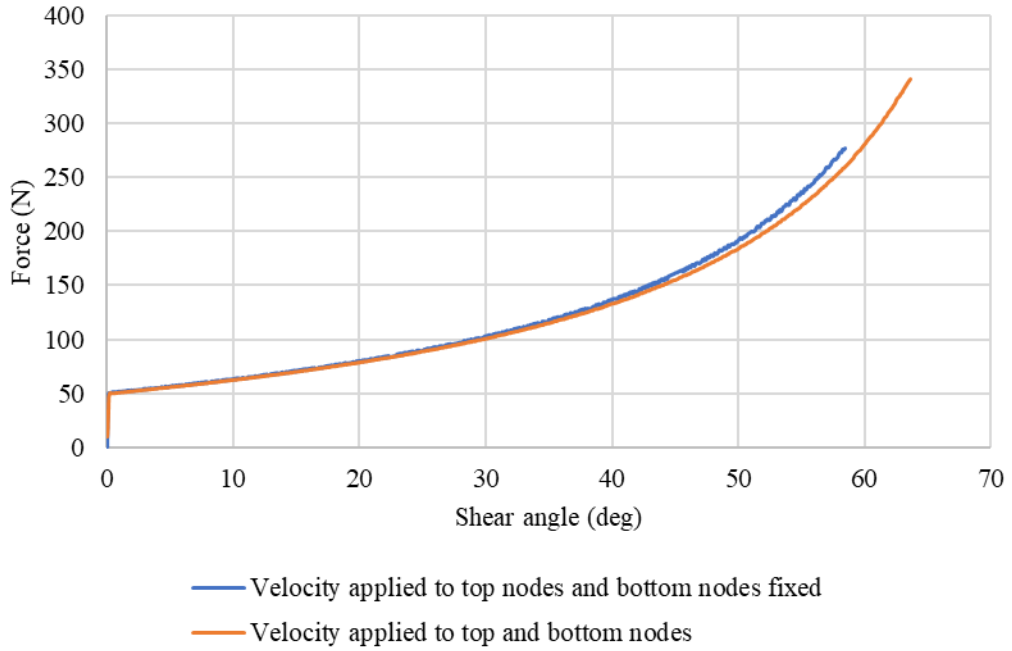

Figure 4.25: Comparison of total force vs. shear angle curves for the square fabric specimen with velocity applied to the top edge with that of the velocity applied to both the top and bottom edges.

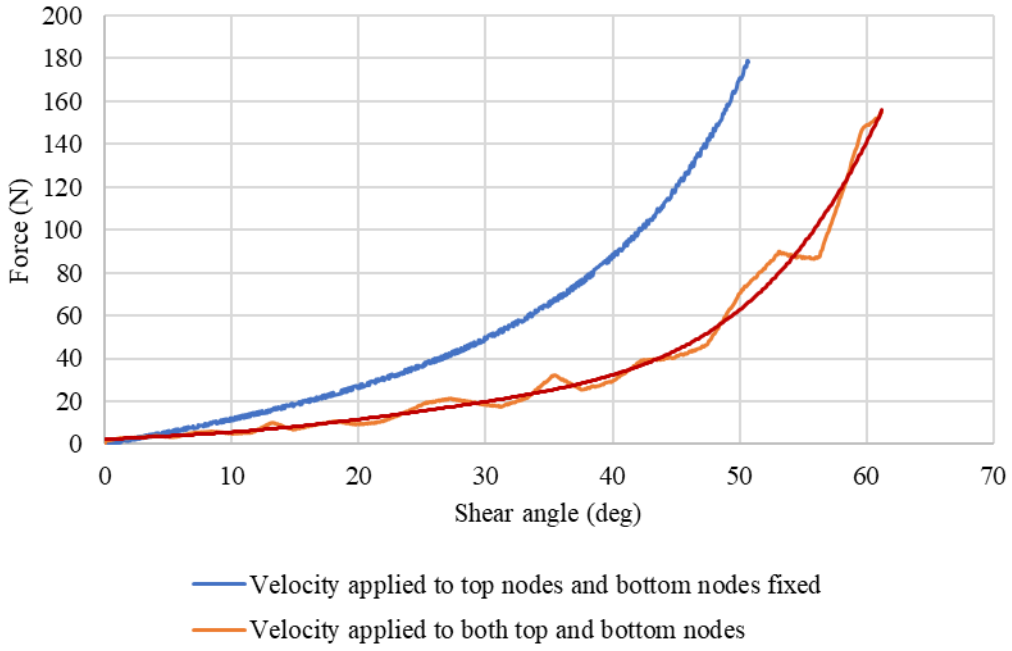

Figure 4.26: Material deformation forces: (a) with the bottom nodes fixed and displacement applied to the top nodes, (b) with displacement boundary conditions applied to both top and bottom nodes.

4.3.2 Biaxial-Bias Extension Test with Cruciform Fabric Specimen

Sharma et al. [6] studied the shear-tension coupling effects on the fabric behavior using a cruciform fabric specimen shown in Figure 4.27 (a). The lengths of the horizontal and vertical arms were 200 mm and the gage section at the center of the fabric specimen was 75 mm x 75 mm. The biaxial bias-extension test in their experiments was velocity controlled with the arms of the specimen along the horizontal direction moving apart and the arms along the vertical direction approaching each other. The ratio of the horizontal and vertical arm velocities was varied from 0.8 to 1.2. In these experiments, Sharma et al. [6] did not observe much interaction between shear and tension in the gage section of the cruciform specimens.

In this section, a cruciform specimen of the same size as that in Sharma et al. [6] is used; but instead of applying constant velocities in the vertical and horizontal arms, the vertical arms are displaced in the opposite directions with a velocity of 50 mm/s (so that the relative velocity between them is 100 mm/s) and a constant tensile force is applied in the opposite directions in the horizontal arms as shown in Figure 4.27 (b). The transverse tensile forces were 5, 50 and 100N. This experiment is similar to the BBE experiments conducted by Harrison et al. [5] except that the transverse forces in this modified cruciform test were introduced away from the gage section. As can be seen in Figure 4.28, the 75 mm x 75 gage section experiences only pure shear and does not contain any zones of half or zero shear. This is because the forces are introduced to the arms away from the gage area. However, there is evidence of wrinkling at the sharp corners between the horizontal and vertical arms. This can perhaps be reduced by using more rounded corners.

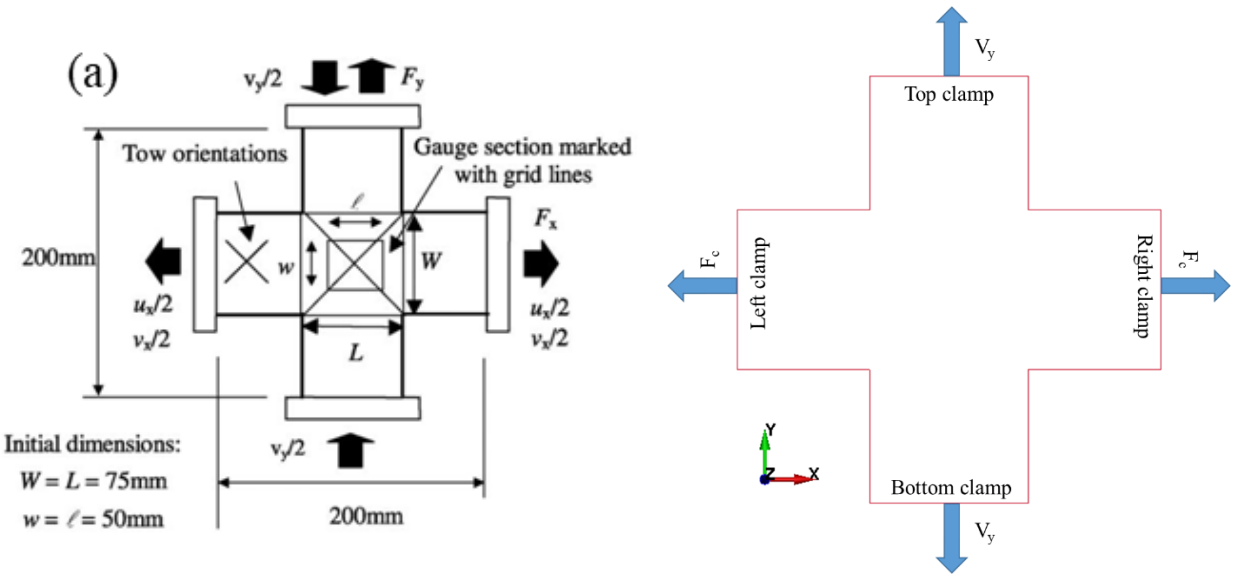

Figure 4.27: Cruciform fabric specimens: (a) velocity-controlled test conditions by Sharma et al. [6], (b) simulation test conditions in which top and bottom arm are made to move apart from each other with a constant velocity while left and right arms are subjected to constant transverse tensile forces.

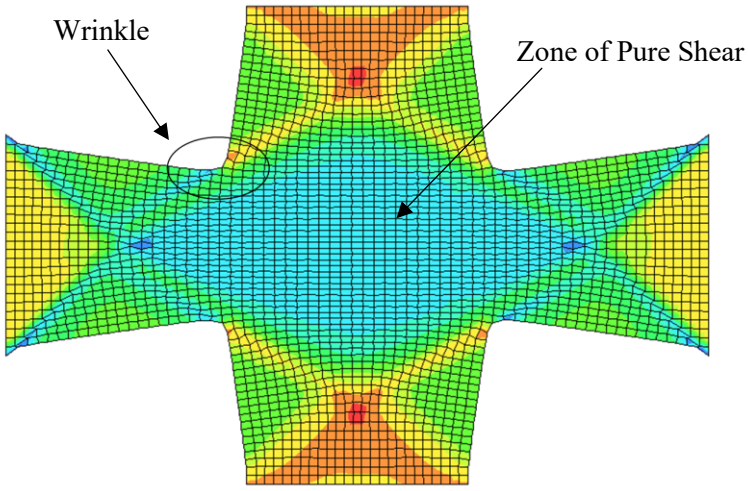

Figure 4.28: Deformed cruciform fabric test at a total vertical displacement of 40 mm (20 mm for both top and bottom vertical arms away from each other) showing pure shear zone in the gage area and formation of wrinkles at the corners joining vertical and horizontal arms.

Figure 4.29 shows a comparison of the force vs. shear angle curves for the BBE test simulations with square and cruciform fabric specimens. The force vs shear angle curves for the square fabric specimen are for a clamping ratio of 3:1, i.e., the clamping edge length is 70 mm

while for the cruciform fabric specimen the clamping edge length is 75 mm. The cruciform fabric specimen exhibits little stiffer behavior compared to the square fabric specimen; however, the trends exhibited by both types of specimens are the same for all three transverse tensile force conditions. Unlike the results reported by Sharma et al. [6], the simulated results with the modified cruciform test show that increasing the transverse tensile force increases the shear stiffness of the fabric.

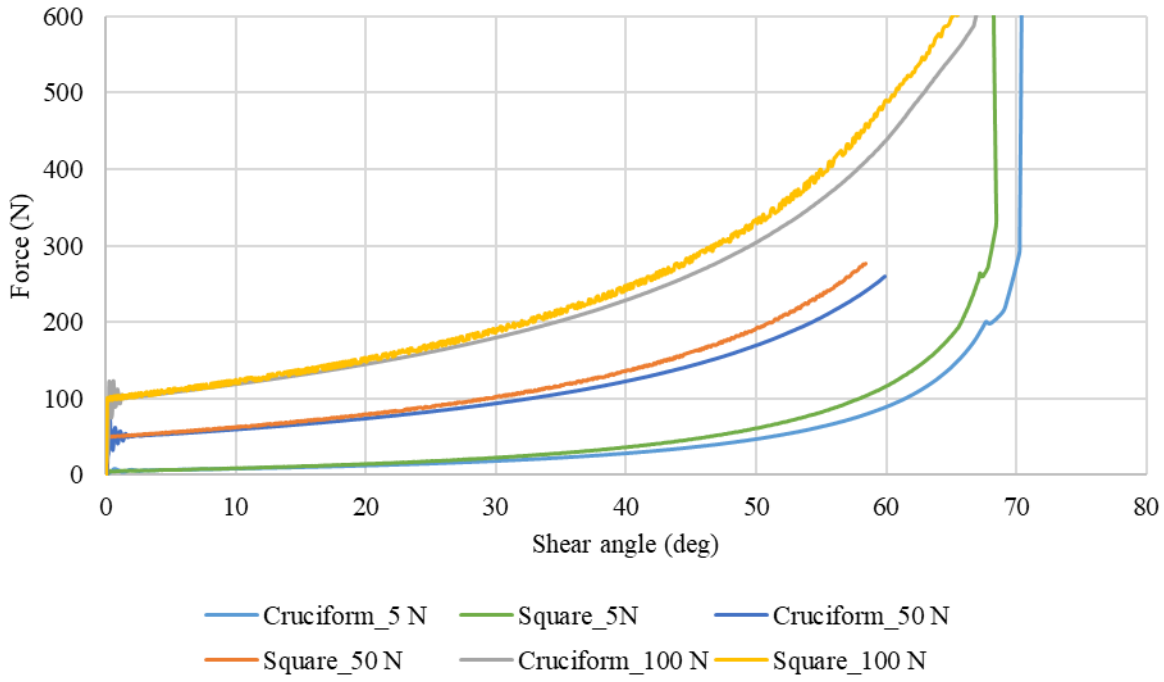

Figure 4.29: Comparison of force vs. shear angle curves for square and cruciform fabric specimens with 5, 50 and 100 N transverse tensile forces.

4.4 Forming Limit Diagrams

The fabric under consideration in this study to develop safe forming window is ECK 12 which is a plain-woven glass fabric with the following properties: weft tow width = 2.18 ± 0.038 mm, warp tow width = 2.12 ± 0.052 mm, areal density = 311 g/m^2, thickness = 0.206 ± 0.012 mm (product code = ECK12, Allscot) [5].

4.4.1 Fabric and Press Forming Setup

Figure 4.30 shows the die-punch setup used for finite element modeling of the press forming operation to produce a cup-shaped fabric preform. It consists of an open round die, a blank holder, and a punch. The die and punch materials are an aluminum alloy. The die opening radius is 40 mm and the punch radius is 38 mm so that the radial gap between the die wall and the punch is 2 mm. Four different punch bottoms were considered: (1) a hemispherical bottom with 38 mm radius, (2) a flat bottom with 15 mm corner radius, (3) a flat bottom with 5 mm corner radius, and (4) a flat bottom with sharp corner. The die corner radius was kept constant at 10 mm, which was selected based on the guidelines prescribed by Donaldson et al. [29] for metal forming applications. A punch velocity of 100 mm/s was selected for this study. To develop the forming limit window for the ECK 12 fabric, the blank holder force was varied between 0 and 80,000 N for each punch configuration and the forming depth corresponding to either wrinkling or tearing was obtained by simulation. A square fabric measuring 160 mm x160 mm was found suitable for the forming experiments using the mentioned die-punch setup.

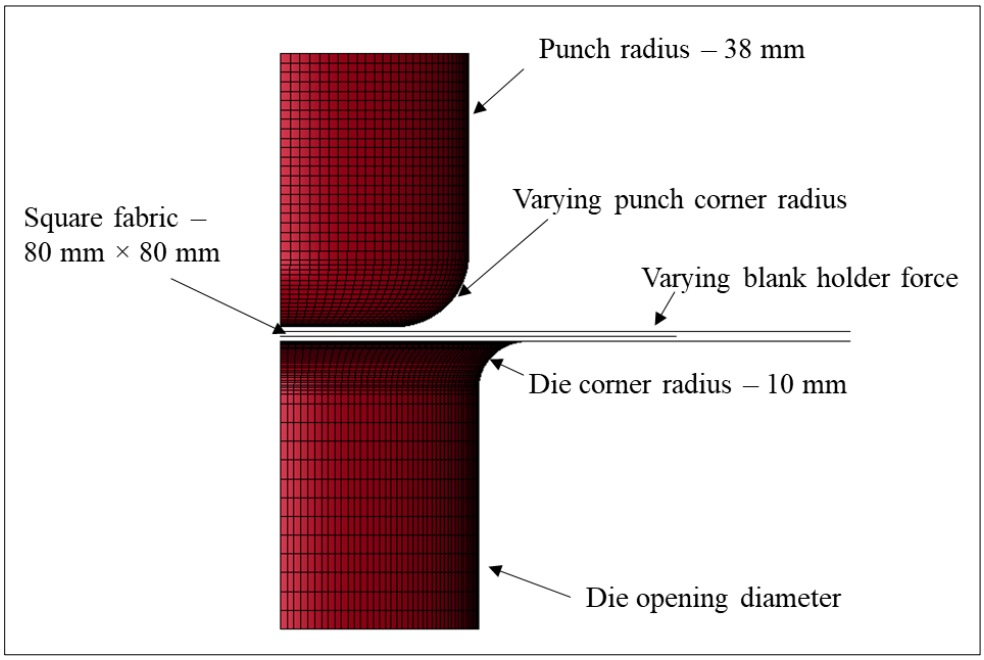

Figure 4.30: Press forming setup.

4.4.2 Modeling of Fabric Press Forming

The finite element model to develop the forming limit diagrams for ECK-12 plain glass fabrics is the same as that described in the superimposed model. The material model MAT_234 superimposed with material model MAT_001 was selected to develop the forming limit diagrams for dry fabrics. The membrane elements account for the fabrics in-plane shear deformation and is assigned the material model MAT_234. The shell elements are used to account for the out-of-plane bending and are assigned the isotropic elastic material model MAT_001. The tensile modulus assigned to the shell elements is same as that for which the simulation results of uniaxial bias-extension test results were validated with the experimental results.

The yarn orientation in the square fabric was 0/90 and so was the element orientation. The mesh size for the die and the punch was selected to be 2 mm; however, a higher mesh density at both punch and die corner radii was used to accommodate the geometrical inconsistencies during press forming. The mesh size of the quadrilateral elements used for the 160 mm x 160 mm fabric was selected to be 1.5 mm. Because of symmetry, simulations were carried using a quarter model to achieve faster computational time. To represent the quarter model of the fabric, a square blank of 80 mm x 80 mm was used in the simulations and the necessary boundary conditions were applied. The total blank holder force was also divided by 4 to represent the quarter model.

To accommodate the in-plane shear properties of the fabric, the fabric was assigned the under-integrated membrane elements using MAT_234. The mechanical and the mesoscopic properties for ECK 12 plain glass fabric were kept the same as the parameters with which the uniaxial bias-extension simulations were carried out in Section 4.3. The ultimate strain at fiber failure for ECK-12 glass fabric is taken from literature as 4.8% [30]. To account for the out-of-plane bending stiffness, MAT_001 was assigned to the shell elements and a tensile modulus of 1.5

MPa that matched the experimental results of uniaxial bias-extension tests were used. The shell and membrane elements were superimposed on one another. Duplicate nodes which arise due to superimposition were merged to represent the fabric behavior. The aluminum die-punch set was modelled using rigid shell elements and material model MAT_020 (MAT_RIGID). Since the experimental data for the coefficient of friction between the warp and weft direction yarns of ECK 12 were not available, it was assumed to be 0.41 based on the recommendation by Yildrim et al. [18].

Three regions of contact were considered for this study: (a) contact between the punch and the blank, (b) contact between the blank holder and the blank, and (c) contact between the die and the blank. The coefficient of friction between aluminum and glass fabrics was selected as 0.2 based on the simulation results by Peng and Ding [31] who validated their results with experimental results and showed a correlation between the two using the friction co-efficient value of 0.2.

4.4.3 Forming Limit Diagrams for ECK 12 Glass Fabric

Fabric press forming simulations on dry ECK 12 glass fabric were carried out using LS-Dyna to study the variation of the successful forming depths (without wrinkling and tearing) with blank holder force and punch corner radius. For each punch corner radius considered, the blank holder force was varied, and the formed shape of the fabric was observed for any forming defects. The forming depth at which the defects were first observed was recorded and was used to plot the forming limit diagrams.

4.4.3.1 Defects Observed during Fabric Press Forming

The following defects were observed during the dry fabric forming:

- Wrinkling due to yarn (tow) buckling at the intersection between the flanges
- Wrinkling due to shear locking at the die entry radius and along the diagonals

- Wrinkling at the punch corner radius
- Tearing of the fabric (tearing at the cup wall and cup bottom)

Wrinkles observed due to shear locking during press forming of dry fabrics is shown in Figure 4.31. Tearing of the fabric was observed at very high blank holder forces when the strain in the yarns exceeded the ultimate strain-at-failure of the fibers. At lower blank holder forces, wrinkling observed in the formed fabric shape can be attributed to the compressive stresses at the locations shown in Figure 4.32 which later resulted in the formation of folds. With the increase in blank holder force, the wrinkles due to compressive stresses were reduced as can be seen in Figure 4.33 and only the wrinkles due to shear locking were observed. Wrinkles due to shear locking were observed at almost the same forming depth irrespective of the blank holder force. This can be attributed to the dry fabric conforming to the shape of the die corner radius and to the shear deformation as the fabric passed over the die corner radius. Wrinkles were also observed at the cup bottom when the punch with very sharp corner radius was used; however, these wrinkles were reduced with increase in the punch corner radius.

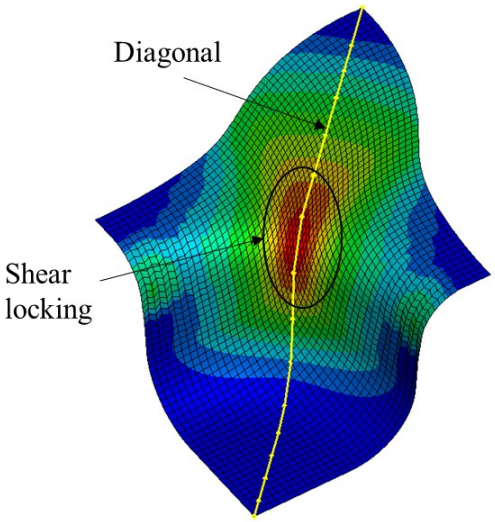

Figure 4.31: Wrinkling due to shear locking (15 mm punch corner radius, 37 mm forming depth).

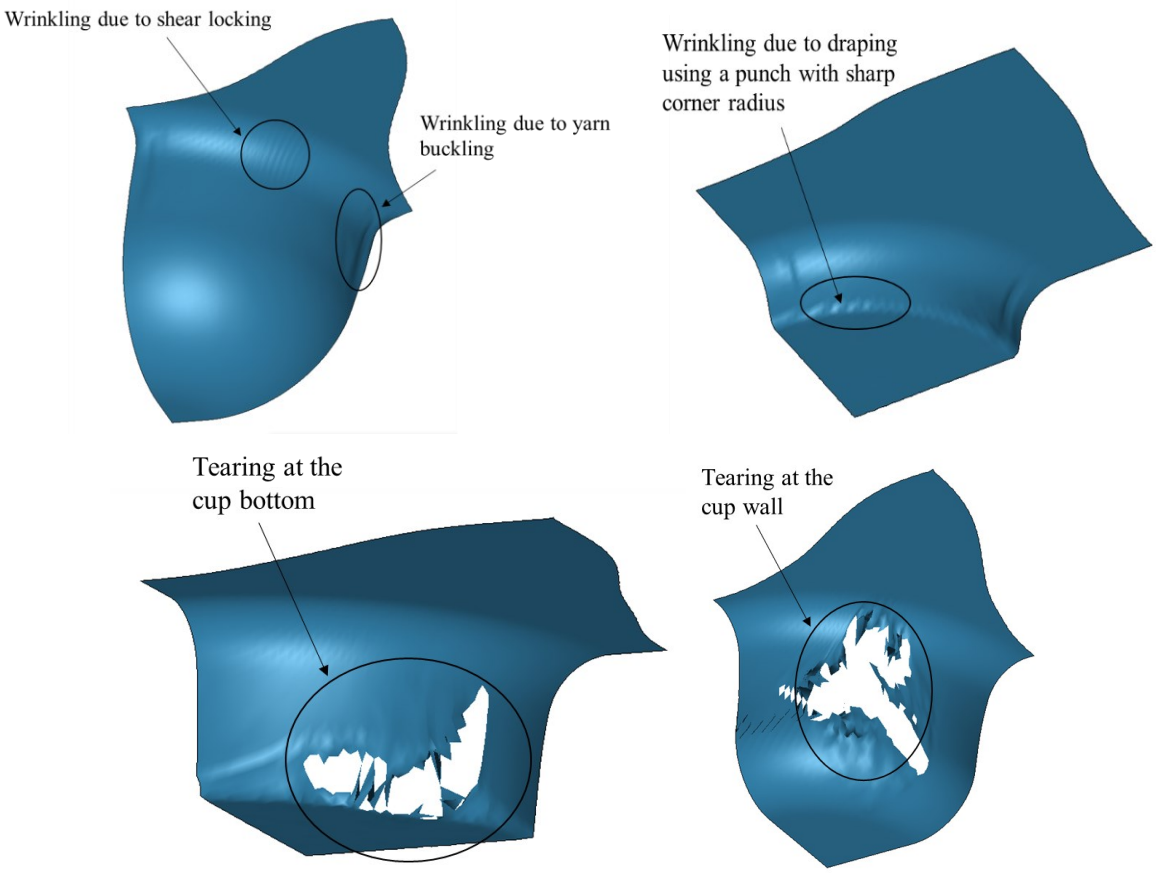

Figure 4.32: Defects observed during dry fabric forming: (a) wrinkling due to yarn buckling (0 mm punch corner radius), (b) wrinkling due to shear locking (0 mm punch corner radius), (c) wrinkling at the cup bottom (0 mm punch corner radius), (d) tearing at the cup bottom (0 mm punch corner radius), (e) tearing at the cup wall (15 mm punch corner radius)

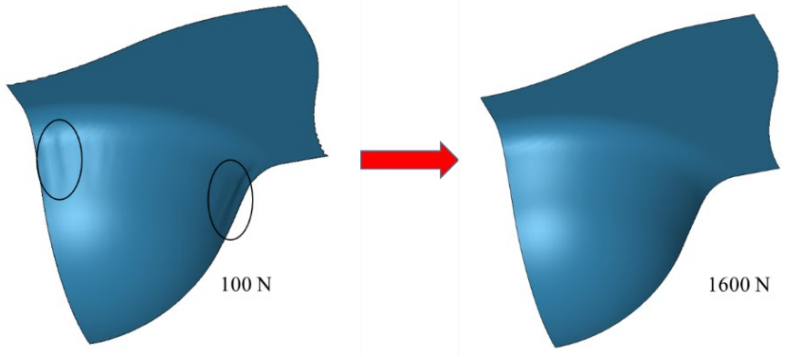

Figure 4.33: Reduction of wrinkles due to yarn buckling with increase in blank holder force from 100 N to 1600 N (with hemispherical punch bottom of radius 38 mm and at 40 mm forming depth).

4.4.3.2 Safe Forming Window

The recorded forming depths without any defects at different blank holder forces and for various punch corner radii were utilized to determine the safe forming windows for the ECK-12 glass fabric shown in Figure 4.34 (a-d). The region to the left side of these figures represents the safe forming window for the ECK-12 fabric, whereas the region to the top right represents the tearing behavior and the region in the bottom right represents the wrinkling behavior. The dashed line marks the transition between wrinkling and tearing; below the dashed line, wrinkling defects were observed on the formed fabric which at higher blank holder forces ultimately led to tearing defects. Blank holder forces shown in Figure 4.34 are the values for the full model.

As can be seen in Figure 4.34, the safe forming window decreases with decrease in punch corner radius. With increasing blank holder force, the safe window initially increases which can be attributed to a reduction in the formation of wrinkles due to yarn buckling with applied punch load, however at high punch loads, tearing defects were observed in the formed fabric, which in turn reduces the formability window.

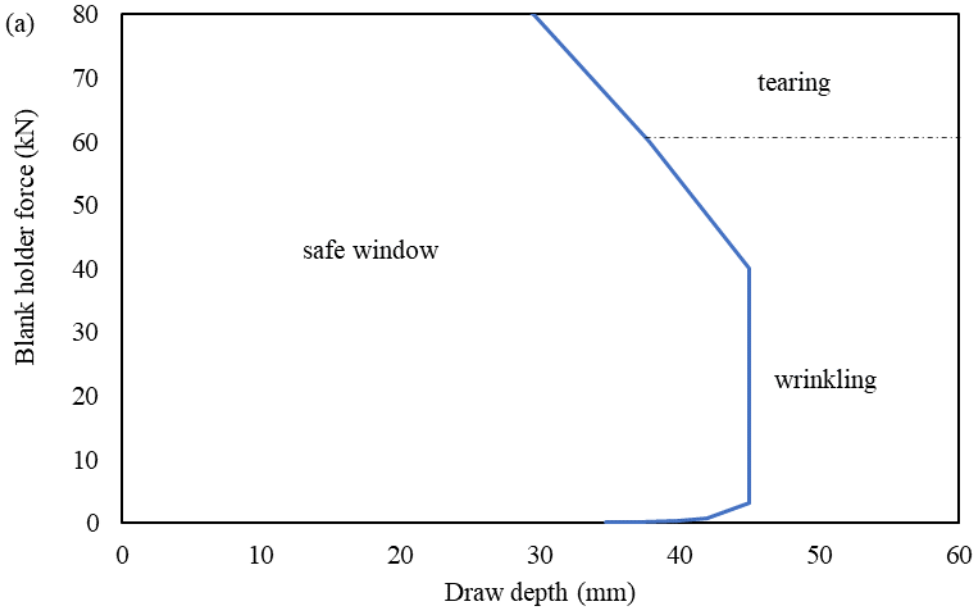

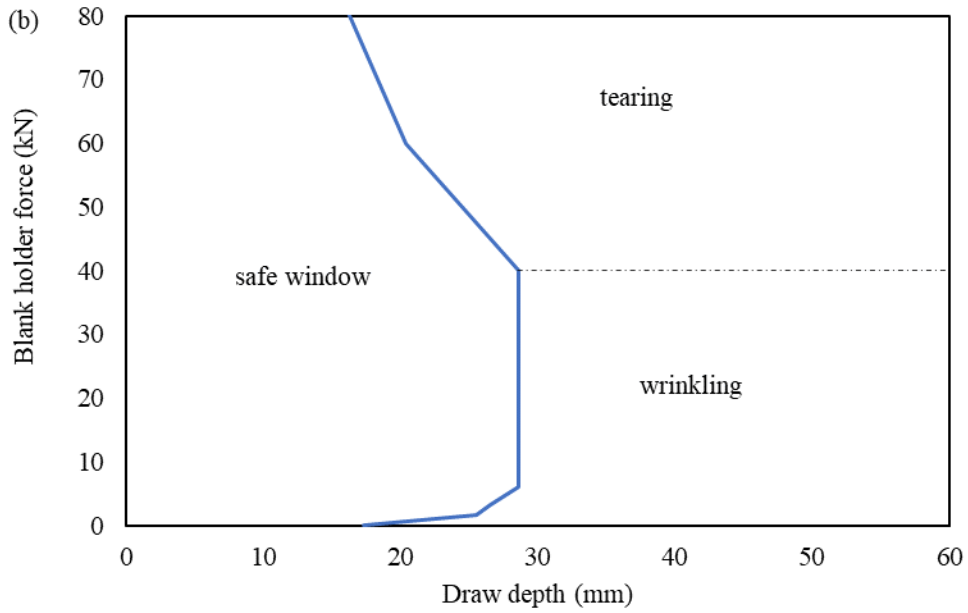
(b)
Blank holder force (kN)
80
70
60
50
40
30
20
10
0
tearing
safe window
wrinkling
0
10
20
30
40
50
60
Draw depth (mm)

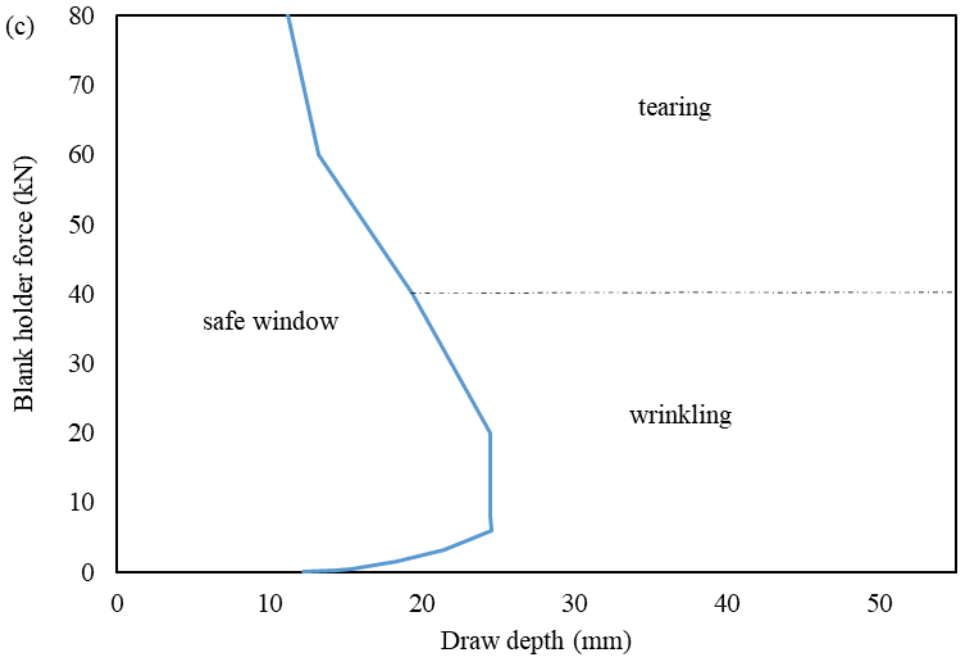
(c)
Blank holder force (kN)
80
70
60
50
40
30
20
10
0
tearing
safe window
wrinkling
0
10
20
30
40
50
Draw depth (mm)

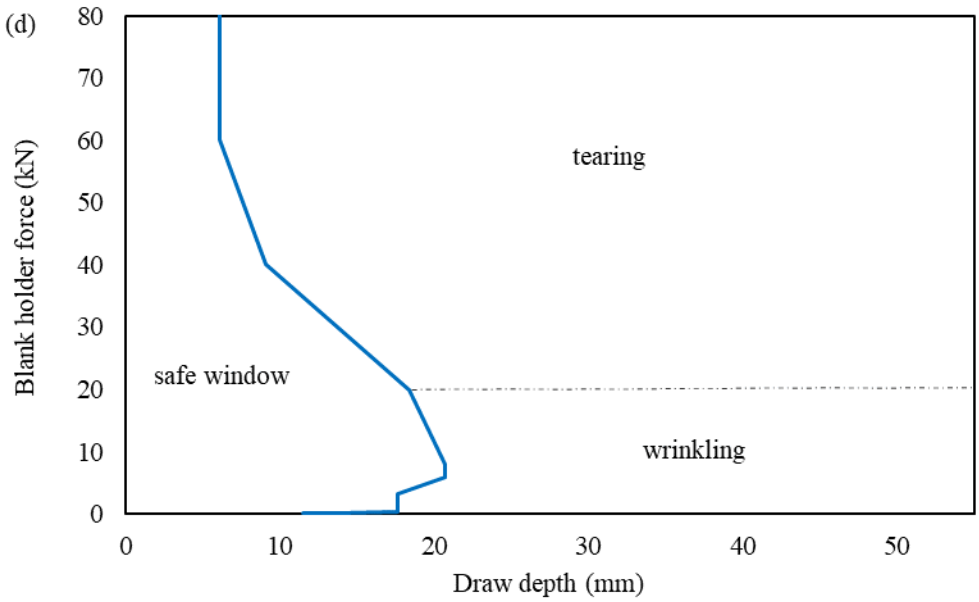

Figure 4.34: Safe forming window: (a) 38 mm punch corner radius (hemispherical punch), (b) 15 mm punch corner radius, (c) 5 mm punch corner radius, and (d) 0 mm punch corner radius.

4.4.3.3 Outer Shape Contour

The outer shape contours of one quarter of the press formed fabric at 40 mm and 55 mm forming depths for 38 mm punch corner radius are shown in Figure 4.35. It can be observed in this figure that there was little or no difference of the shape contours at 40 mm forming depth, however the wrinkle formation and the outer shape contours showed significant variation at 55 mm forming depth. At 55 mm forming depth, the shape contour with 100 N blank holder force was different from the shape contours with the other blank holder forces. Above 400 N blank holder force, the outer contour was almost the same as with the other blank holder forces. Thus, these observations show that the effect of the blank holder force on the final shape formation is reduced above a limiting value, which for this fabric and with forming parameters used was 400N; however, it is important to note that the blank holder force has a significant role on the formation of wrinkles and tearing.

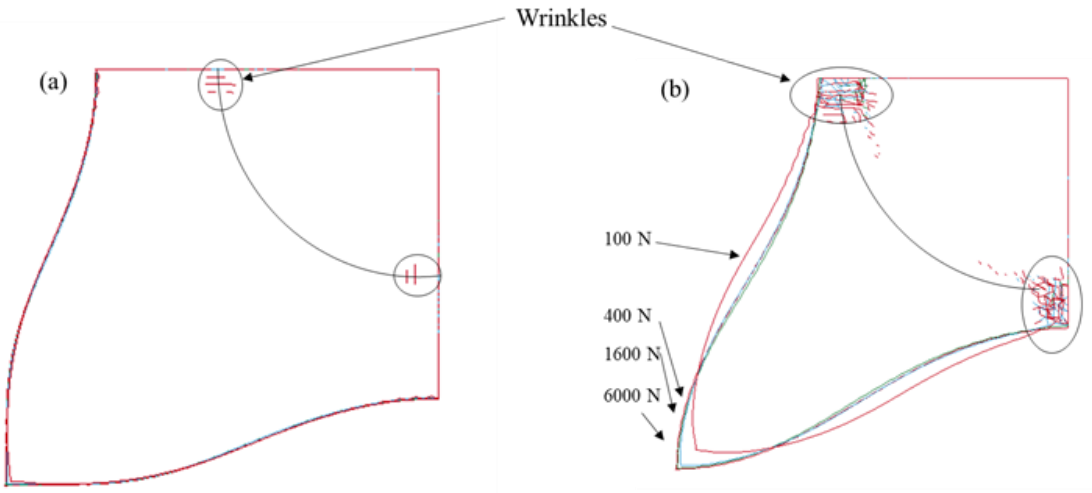

Figure 4.35: Flange shape contours shown for the quarter model of the press formed fabric as viewed from the top at (a) 40 mm, (b) 55 mm punch displacements with 100, 400, 1600 and 6000 N applied blank holder forces.

4.4.3.4 Press Forming Force vs. Punch Displacement Diagrams

Figure 4.36 shows press forming force vs. punch displacement diagrams at 100 N, 400 N and 1600 N blank holder forces. As anticipated, the press forming force required for preforming the fabric increases with increasing blank holder force. In Figure 4.37, the press forming force is plotted at a high blank holder force of 60 kN. Sudden drop in the press forming force indicates tearing of the fabric which occurred when the tensile strain in the yarns of the fabric exceeded the ultimate strain-at-failure for the fibers at a punch displacement of 37.78 mm.

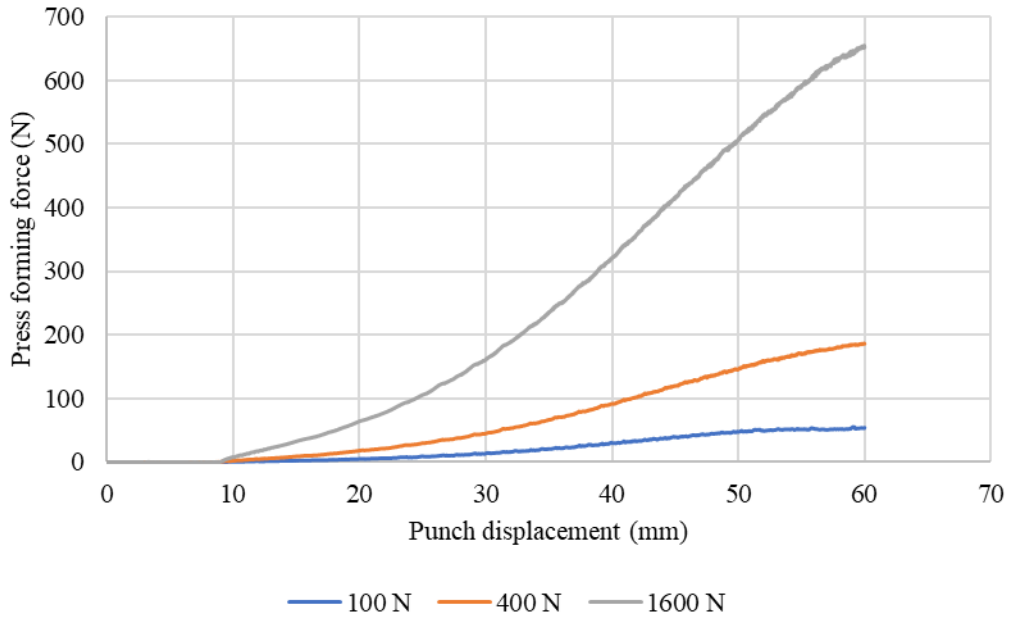

Figure 4.36: Press forming force vs. punch displacement at 100, 400 and 1600 N blank holder forces.

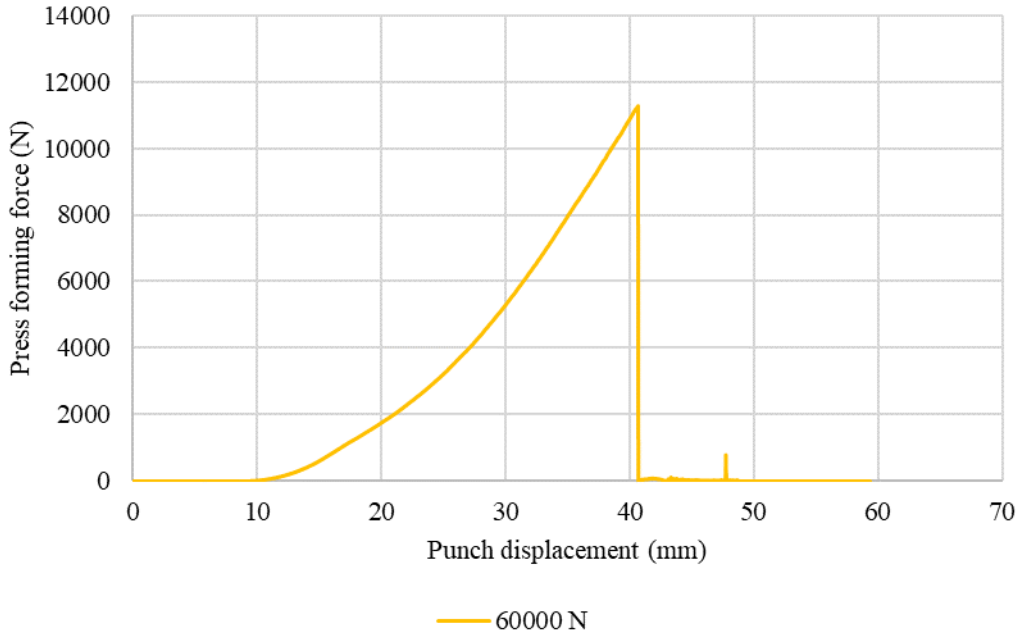

Figure 4.37: Press forming force vs. punch displacement at 60 kN blank holder force.

4.5 Conclusions

The following conclusions are made from the study presented in this chapter. Superimposed model in which membrane and shell elements are superimposed on one another can predict the force

required for shear deformation of fabrics in both uniaxial and biaxial bias-extension tests. Modulus value to be assigned to the shell elements should be very low so that it does not affect the in-plane behavior of the fabric material.

Force required for fabric deformation in biaxial bias-extension tests using square fabric specimens with partially clamped edges increases with increase in transverse tensile force. The square fabric specimen does not show any shear response variation with changes in clamping ratio or fabric size. However, the displacement at which shear locking occurs changes with both clamping ratio and fabric size. The percentage area of pure shear deformation zone increases with increasing clamping ratio and does not vary for different fabric sizes provided that the clamping ratio is kept the same.

Square fabric test specimen in which both the top and bottom clamps are moved with the same velocity, but in opposite directions to keep the angle of inclination of the applied transverse forces at zero exhibits a lower shear stiffness behavior compared to the square fabric with one end fixed and other end moving. The higher shear stiffness exhibited by the latter can be attributed to the introduction of shear component in addition to the transverse forces.

Cruciform fabric specimen with two vertical arms moving in opposite directions and two opposing transverse tensile forces applied to the horizontal arms can be used to characterize shear-tension coupling for fabrics. The trends exhibited by force vs. shear angle curves for both square and cruciform fabric specimens are similar. Unlike the square fabric specimen which exhibits pure shear, half shear and no shear zones, the cruciform specimen exhibits only pure shear zone in the gage area. Cruciform fabric specimen exhibits wrinkling tendency at the sharp corners between the vertical and horizontal arms. Further experimental studies are needed to develop the cruciform fabric specimens to characterize the shear-tension coupling of fabrics.

Based on the study for the development of a formability window for dry fabrics, the following conclusions can be made. At lower blank holder forces, wrinkles are observed at the intersections between the flanges due to yarn buckling. With increase in blank holder force, wrinkles due to compressive stresses are reduced. Wrinkles are also formed due to shear locking at the die entry radius along the diagonals of the square fabric specimen and when a punch with a sharp corner radius is used. When the fabric is pulled over the die corner radius, shear deformation occurs in the fabric and as the forming depth is increased, wrinkles start to appear in the fabric due to shear locking phenomenon. Wrinkle formation due to shear locking does not appear to depend on the blank holder force. Increasing the punch corner radius reduces the formation of wrinkles at the cup bottom. Hence, an optimum punch radius must be selected while press forming fabrics to avoid wrinkle formation at the cup bottom.

The forming limit diagrams for fabrics in which a safe forming window is expressed as a function of blank holder force and punch corner radius gives the limits for press forming fabrics. The safe forming window decreases with decrease in the punch corner radius, and with the applied blank holder force, the forming window increases initially due to a reduction of wrinkles formed due to compressive stresses. However, at higher blank holder forces the safe window again decreases with the applied load as the fiber strain in the yarns of the press formed fabric exceeds the ultimate strain-at-failure of the fibers.

4.6 References

[1] P. K. Mallick, Processing of Polymer Matrix Composites, Boca Raton, FL: CRC Press: Taylor & Francis Group, 2018.

[2] W. Lee, J. Padvoiskis, J. Cao, E. d. Luycker, P. Boisse, F. Morestin, J. Chen and J. Sherwood, "Bias-extension of woven composite fabrics," *International Journal of Material Forming,* vol. 1, pp. 895-898, 2008.

[3] P. Boisse, N. Hamila , E. Guzman-Maldonado, A. Madeo, G. Hivet and F. dell'Isola, "The bias-extension test for the analysis of in-plane shear properties of textile composite reinforcements and prepregs: a review," *International Journal of Material Forming,* vol. 10, no. 4, pp. 473-492, 2017.

[4] I. Taha, Y. Abdin and S. Ebeid, "Comparison of picture frame and bias-extension tests for the characterization of shear behaviour in natural fibre woven fabrics," *Fibers and Polymers,* vol. 14, no. 2, pp. 338-344, 2013.

[5] P. Harrison, F. Abdiwi, Z. Guo, P. Potluri and W. R. Yu, "Characterising the shear–tension coupling and wrinkling behaviour of woven engineering fabrics," *Composites. Part A, Applied Science and Manufacturing,* vol. 43, no. 6, pp. 903-914, 2012.

[6] S. B. Sharma, M. P. F. Sutcliffe and S. H. Chang, "Characterisation of material properties for draping of dry woven composite material," *Composites. Part A, Applied Science and Manufacturing,* vol. 34, no. 12, pp. 1167-1175, 2003.

[7] S. Holmberg, B. Enquist and P. Thilderkvist, "Evalutaion of sheet metal formability by tensile tests," *Journal of Material Processing Technology,* vol. 145, no. 1, pp. 72-83, 2004.

[8] S. Kumar, T. Amjith and C. Anjaneyulu, "Forming limit diagram generation of Aluminum alloy of AA2014 using Nakazima test simulation tool," *Procedia technology,* vol. 24, pp. 386-393, 2016.

[9] S. P. Keeler, "Determination of forming limits in automotive stamping," *SAE tehcnical paper series ,* 1965.

[10] S. K. Paul, "Theoretical analsis of strain-and stress-based forming limit diagrams," *Journal of Strain Analysis for Engineering Design,* vol. 48, no. 3, pp. 177-188, 2013.

[11] R. Azzouz, S. Allaoui and R. Moulart, "Composite preforming defects: a review and a classification," *International Journal of Material Forming,* vol. 14, no. 6, pp. 1259-1278, 2021.

[12] A. A. Skordos, C. Monroy Aceves and M. Sutcliffe, "A simplified rate dependent model of forming and wrinkling of pre-impregnated woven composites," *Composites Part A: Applied Science and Manufacturing,* vol. 38, no. 5, pp. 1318-1330, 2007.

[13] P. Boisse, N. Hamila, E. Vidal-Salle and F. Dumont, "Simulation of wrinkling during textile composite reinforcement forming. Influence of tensile, in-plane shear and bending stiffnesses," *Composites Science and Technology,* vol. 71, no. 5, pp. 683-692, 2011.

[14] R. Dessenberger and C. L. Tucker III, "Forming limit measurements for random fiber mats," *Polymer composites,* vol. 19, no. 4, pp. 370-376, 1998.

[15] V. Viisainen, J. Zhou and M. P. Sutcliffe, "Development of a composite forming diagram: A feasibility study," in *22nd Internatiional Conference on Composite Materials*, Melbourne, Australia, Aug 2019.

[16] K. Vanclooster, S. V. Lomov and I. Verpost, "On the formability of multi-layered fabric composites," in *ICCM Inernational Conferences on Composite Materials*, Edinburgh, Scotland, 2009.

[17] "LS-Dyna Keyword User's Manual Volume II R11.0," Livermore Software Technology Corporation (LSTC), 2018.

[18] H. Yildirim and F. Ozturk, "A benchmark study of the material models for forming simulation of woven fabrics," *Journal of the Textile Institute,* vol. 113, no. 6, pp. 1027-1038, 2021.

[19] A. Tabiei and R. Murugesan, "Thermal structural forming simulation of carbon and glass fiber reinforced plastics composites," *International Journal of Composite Materials,* vol. 5, no. 6, pp. 182-194, 2015.

[20] A. Tabiei and I. Ivanov, "Computational micro-mechanical model of flexible woven fabric for finite element impact simulation," *International Journal for Numerical Methods in Engineering,* vol. 53, no. 6, pp. 1259-1276, 2002.

[21] J. L. Hill, "Mechanical property determination for flexible material systems," Ph.D. Thesis, Georgia Institute of Technology, 2016.

[22] F. A. A. Abdiwi, "Characterisation and modelling of the shear-tension coupling and variability of woven engineering fabrics," Ph.D. Thesis, University of Glasgow, 2013.

[23] N. Hamila and P. Boisse, "Locking in simulation of composite reinforcement deformation. Analysis and treatment," *Composite. Part A, Applied science and Manufacturing,* vol. 53, pp. 109-117, 2013.

[24] M. Nishi and T. Hirashima, "Approach for dry textile composite forming simulation," *19th International Conference on Composite Materials,* pp. 7486-7493, 2013.

[25] B. Liang, N. Hamila, M. Peillon and P. Boisse, "Analysis of thermoplastic prepreg bending stiffness during manufacturing and of its influence on wrinkling simulations," *Composites Part A, Applied Science and Manufacturing,* vol. 67, pp. 111-122, 2014.

[26] D. Jauffres, J. A. Sherwood, C. D. Morris and J. Chen, "Discrete mesoscopic modeling for the simulation of woven-fabric reinforcement forming," *Internation Journal of Material Forming,* vol. 3, no. 2, pp. 1205-1216, 2010.

[27] P. Harrison, "Modelling the forming mechanics of engineering fabrics using a mutually constrained pantographic beam and membrane mesh," *Composites. Part A, Applied Science and Manufacturing,* vol. 81, pp. 145-157, 2016.

[28] A. J. Thompson, J. P. Belnoue and S. R. Hallett, "Modelling defect formation in textiles during the double diaphragm forming process," *Composites. Part B, Engineering,* vol. 202, p. 108357, 2020.

[29] C. Donaldson, G. H. LeCain and V. C. Goold, Tool Design (3rd ed.), New York: McGraw-Hill, 1973.

[30] P. K. Mallick, Fiber-Reinforced Composites: Materials, Manufacturing, and Design, Bosa Roca: CRC Press, 2007.

[31] X. Peng and F. Ding, "Validation of a non-orhtogonal constitutive model for woven composite fabrics via hemispherical stamping simulation," *Composite Part A: Applied Science and Manufacturing,* vol. 42, no. 4, pp. 400-407, 2011.

Chapter 5 Formability of Dry E-glass Fabrics and Fabric-Reinforced Polypropylene

In this chapter, shear deformation characteristics of dry fabrics and their press formability are studied by both finite element simulations and experiments. In addition, press formability of fabric-reinforced polypropylene is investigated using finite element simulation. Uniaxial bias-extension tests were conducted to determine the shear deformation characteristics of three different dry plain-weave E-glass fabrics. The results of the uniaxial bias-extension tests were used to determine the tensile modulus of the fabrics needed for the simulations of their press formability using superimposed approach presented in Chapter 4. Press forming experiments were conducted with the three dry fabrics and the experimental load-displacement diagrams were compared with the simulations results to confirm the validity of the simulations approach.

In the second part of the chapter, different methods to simulate press forming of fabric-reinforced polypropylene were explored and the draw depth attained before failure was compared with that of the draw depth attained for press forming of single layer polypropylene using the same die setup.

5.1 Uniaxial Bias Extension Test for Plain E-Glass Fabrics

The present section provides the details of the uniaxial bias-extension tests conducted for determining the shear deformation characteristics of dry fabrics. Three different plain-weave E-glass fabric styles were selected, namely 1610, 1522 and 3733. Table 5.1 lists the catalog information on these three fabrics as listed by Fibreglast, the supplier of the fabric. Yarn width and yarn span for each fabric were measured using the image analysis of 50 mm x 50 mm square fabric specimens. Enlarged images of the fabric specimens are shown in Figure 5.1. The warp and weft

yarn counts determined using the image analysis fall within the range mentioned by the supplier [1].

Table 5.1: Catalog information on the plain-weave E-glass fabrics [1].

Fabric Style	Fabric Weight	Fabric Thickness	Warp and Weft (Fill) Counts	Yarn Description
1610 (2 oz fabric)	2.38 oz/yd^2 (80 g/m^2)	0.004 in (0.1 mm)	32/in and 28/in (12.59/cm and 11.02/cm)	ECG 150 1/0 (US) EC9 33 (SI)
1522 (4 oz fabric)	3.67 oz/yd^2 (124 g/m^2)	0.006 in (0.15 mm)	24/in and 22/in (9.4/cm and 8.7/cm)	ECG 150 1/2 (US) EC9 33 x 2 (SI)
3733 (6 oz fabric)	5.8 oz/yd.^{2} (197 g/m^2)	0.007 in (0.2 mm)	18/in and 18/in (7.09/cm and 7.09/cm)	ECG 37 1/0 EC9 134 (SI)

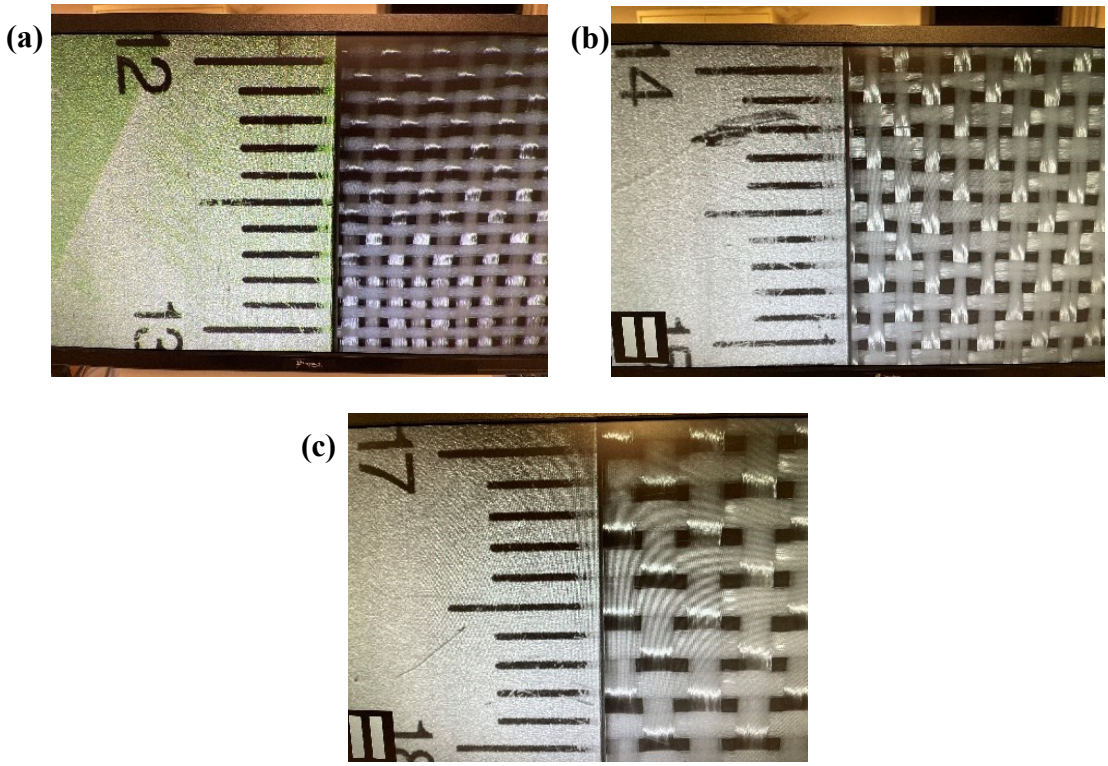

Figure 5.1: Enlarged images of the E-glass fabrics: (a) 1610 (2 oz), (b) 1522 (4 oz), and (c) 3733 (6 oz).

5.1.1 In-plane Shear Characterization of E-glass Fabrics

In-plane shear characteristics of the fabrics were determined by conducting uniaxial bias-extension tests on an Instron testing machine_5967 with 1 kN load cell. The fabric specimens were rectangular in shape, 170 mm in length × 50 mm in width. Test specimens were taped to 50 mm wide aluminum end clamps over a length of 25 mm at each end, which were then gripped on to the Instron crossheads. The schematic representation of the experimental uniaxial bias-extension set up is shown in Figure 5.2. The resultant length and width of the specimens were 120 mm × 50 mm so that the length to width ratio was 2.4. This follows the recommendation by Taha et al. [2] that the specimen length should be more than twice its width to ensure uniform deformation zones and a region of pure shear deformation in the center region where the restraining effects of the clamps become insignificant.

The bottom crosshead of the testing machine was stationary, while the top crosshead was moved upward with a velocity of 10 mm/min, creating a tensile force in the fabric specimen. Proper care was taken to align the warp and weft directions of the fabric in ± 45° orientations with respect to loading direction. Crisscrossed lines with a 90^{o} included angle between them were drawn along the warp and weft directions in the central zone of the fabric where the region of pure shear deformation was expected. A total of 5 tests were carried out for each fabric. The first three tests were continued until a displacement of 40-45 mm was reached. The remaining two tests were carried out in increments of 5 mm displacements. These tests were stopped at each 5 mm displacement increment and an image of the fabric specimen was captured which was then used to measure the angle between the fiber yarns. The Instron testing machine on which the uniaxial bias-extension tests for fabrics were conducted is shown in Figure 5.3. The shear angle was then calculated using Equation (5.1).

$$\gamma = 90° - 2\theta \quad \text{(Eq. 5.1)}$$

where, 'θ' is the angle between the warp and weft yarns and 'γ' is the shear angle.

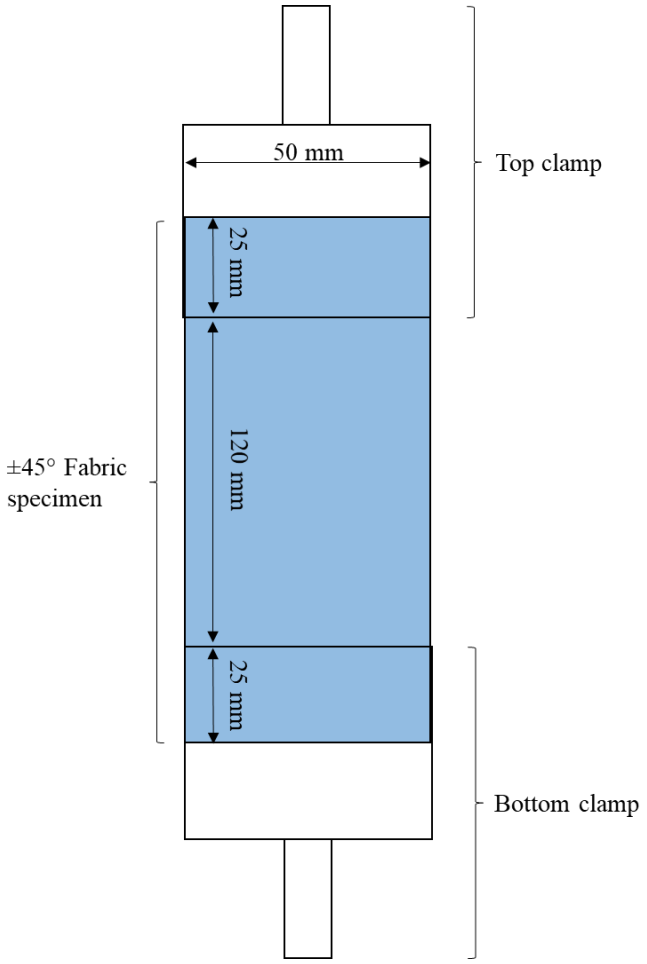

Figure 5.2: Schematic representation of the experimental uniaxial bias-extension set up.

The deformed shapes of the fabric specimens at intervals of 5 mm are shown in Figure 5.4, 5.5 and 5.6 for 1610, 1522 and 3733 fabrics, respectively. At displacements higher than 25-30 mm, the fabric specimens either pulled out from the end clamps or showed folding inwards at the edges and wrinkling.

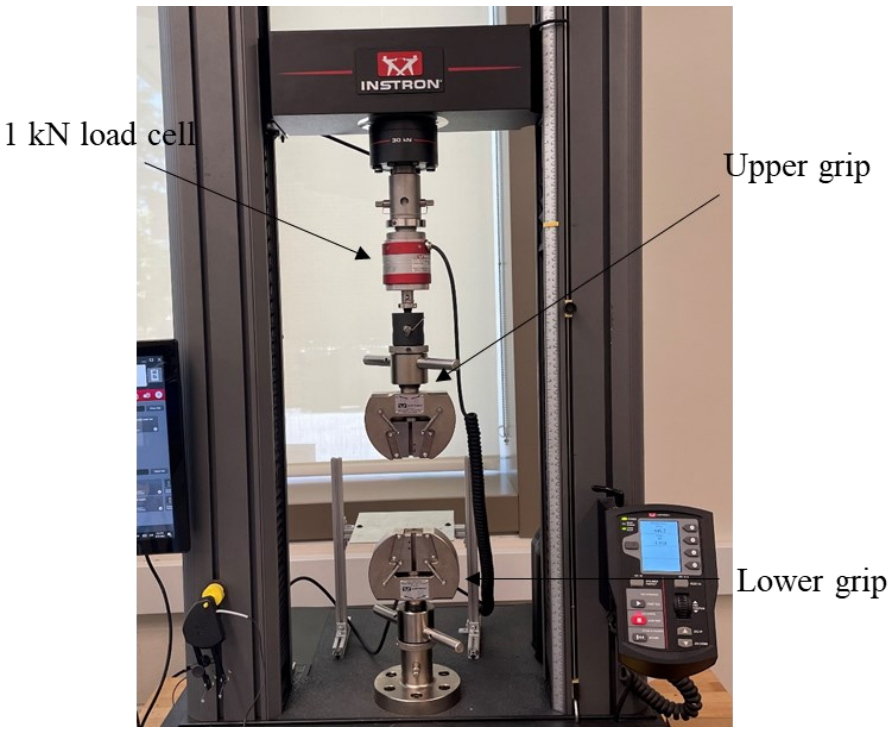

Figure 5.3: Instron testing machine on which uniaxial bias-extension tests of fabrics were conducted.

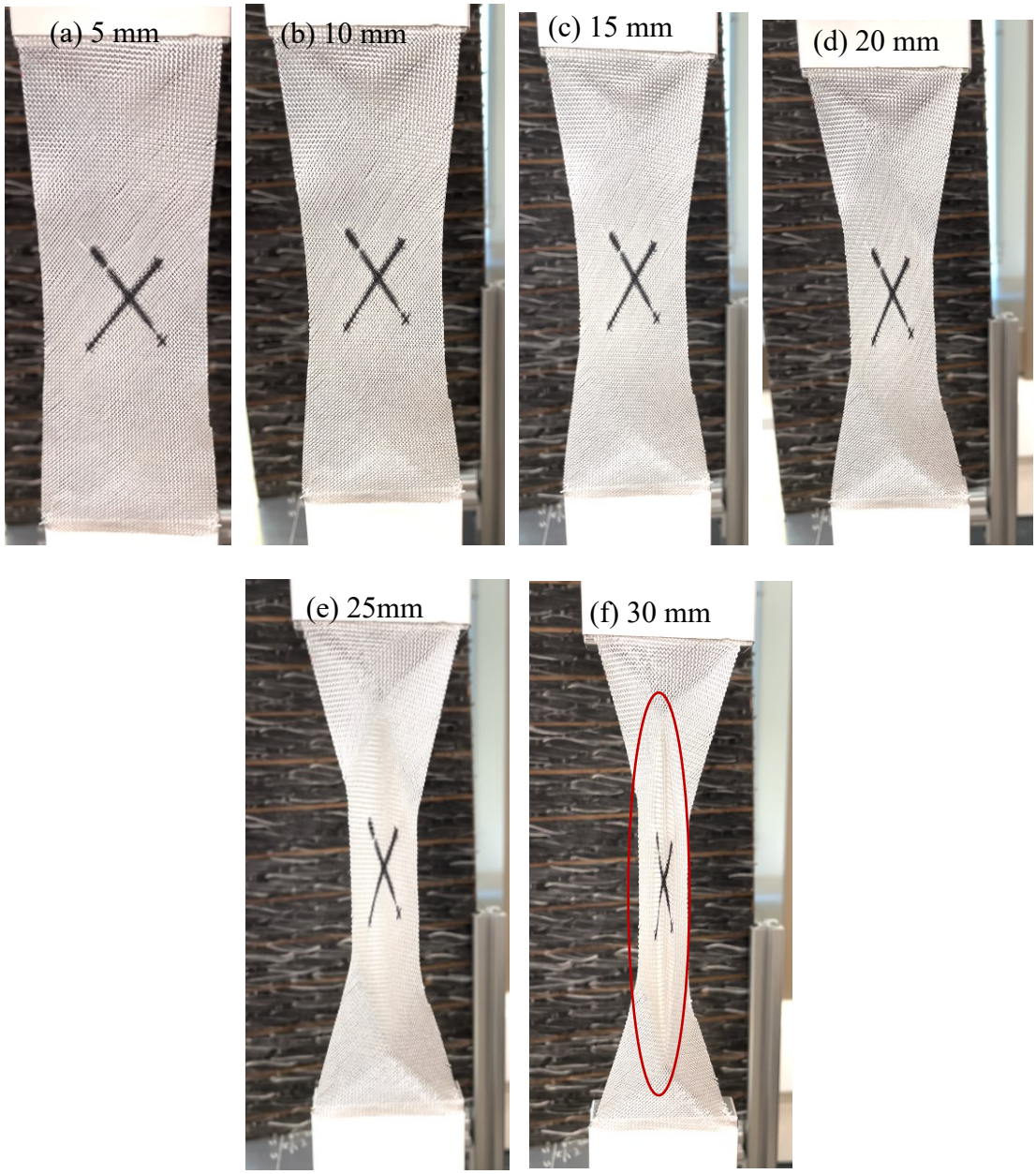

Figure 5.4: Deformed 1610 fabric (2 oz) specimens at an increasing interval of 5 mm. Shear deformation in (e) and (f) were not considered as the fabric shows wrinkling tendency due to shear locking.

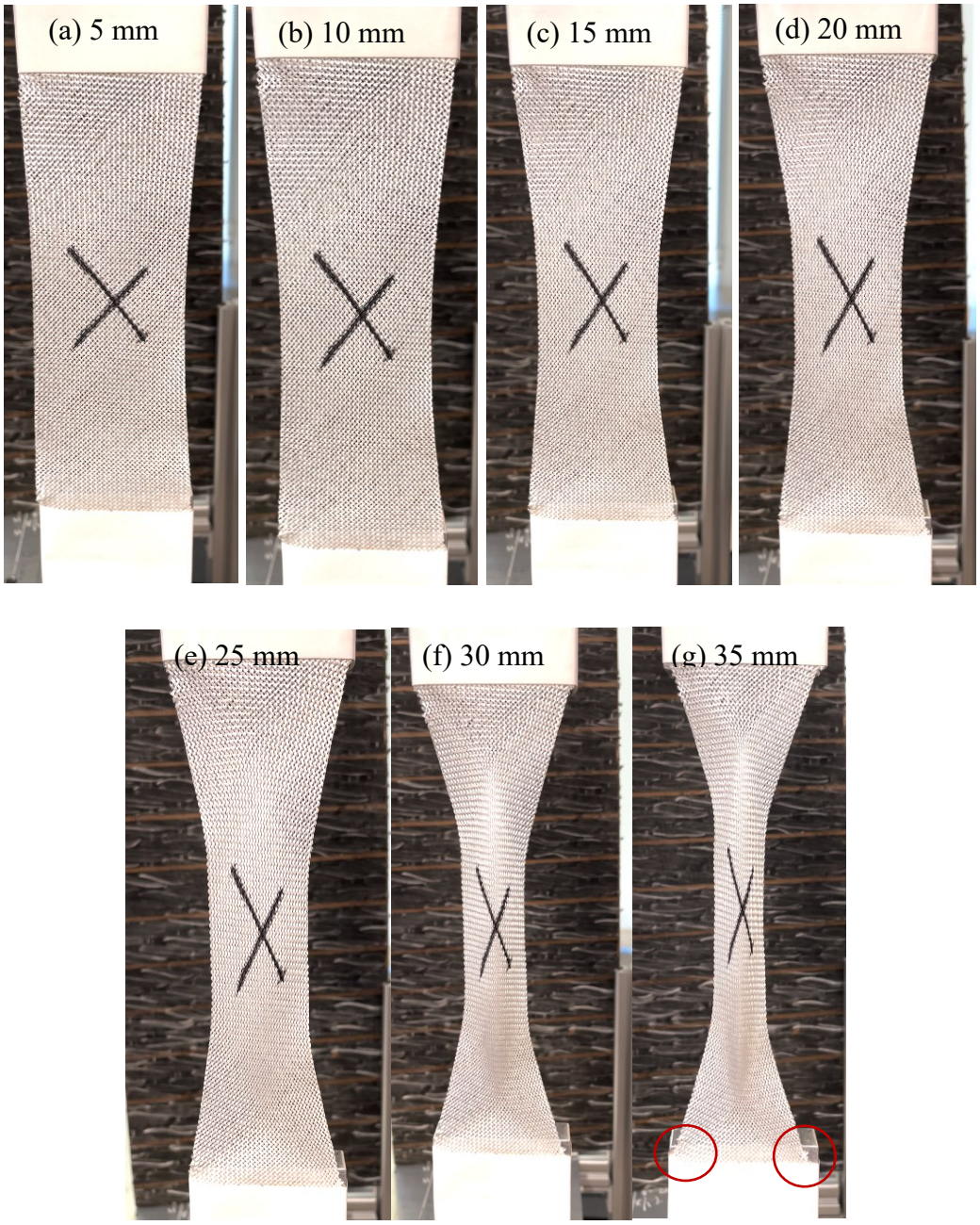

Figure 5.5: Deformed 1522 (4 oz) fabric specimens at an increasing interval of 5 mm. Shear deformation in (f) and (g) was not considered as the fabric shows drawing out from the tape along with wrinkling behavior due to shear locking.

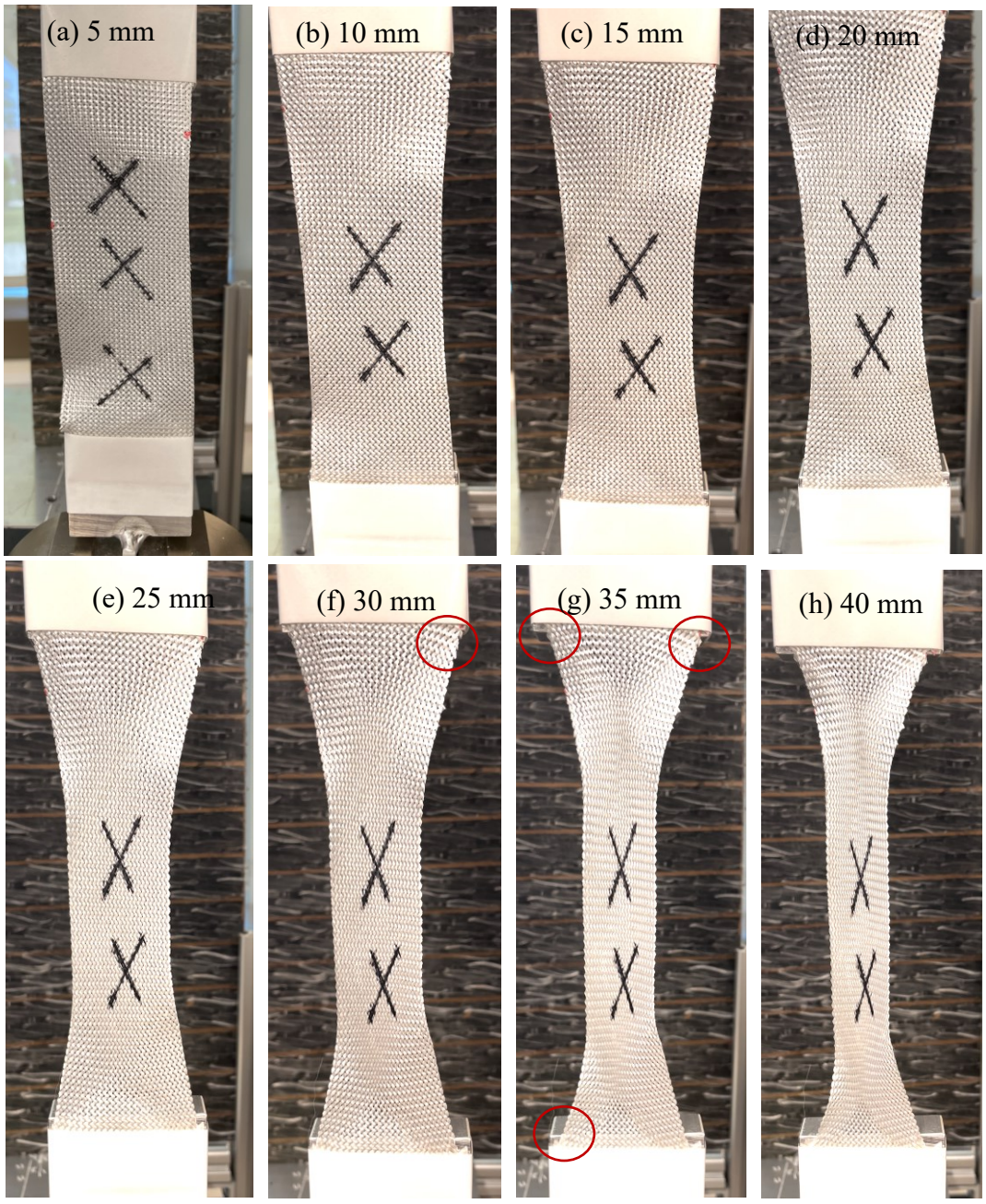

Figure 5.6: Deformed 3733 (6 oz) fabric specimens at an increasing interval of 5 mm. Shear deformation in (f), (g) and (h) were not considered as the fabric shows pull out from the tape along with wrinkling behavior due to shear locking.

The force vs. shear angle diagrams obtained from the uniaxial bias-extension tests for the three E-glass fabrics are shown in Figure 5.7. It can be observed in Figure 5.7 that the fabrics exhibit stiffer shear deformation behavior with an increase in areal density. The force vs. shear

angle curves represented here also include the data that correspond to the force required for fabric deformation during the fiber pull out from tape end, during folding of edges and during wrinkle formation.

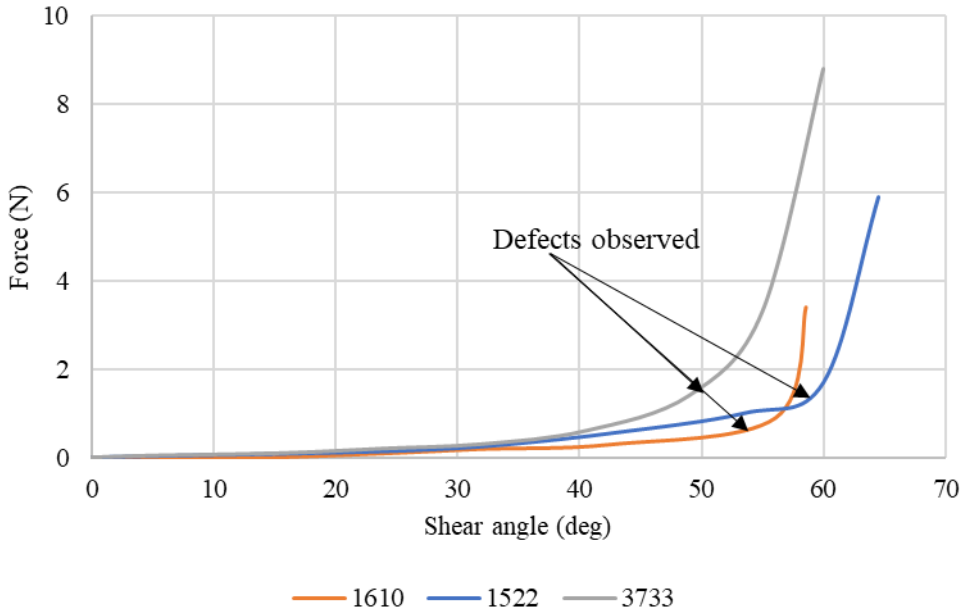

Figure 5.7: Experimental force vs. shear angle curves for E-glass fabrics obtained from uniaxial bias extension tests.

5.1.2 Material Parameters for Finite Element Simulation of Press Forming

Simulations of press forming operations were conducted using under-integrated membrane elements with material model MAT_234 superimposed on shell elements with material model MAT_001. The superimposition of the membrane and shell elements with shared nodes between them accounts for both in-plane deformation and out-of-plane bending of the fabrics. The material properties needed as input for MAT_234 are described in Appendix A and listed in Table 5.2 for 1601, 1522 and 3733 fabrics. The tensile modulus needed for modeling out-of-plane bending stiffness with the shell elements were determined by iteratively matching the simulated force vs. shear angle curves to the experimentally determined force vs. shear angle curves in Figures 5.7.

Table 5.2: Material input parameters for plain-weave E-glass fabrics.

Parameters	Fabric_1610 (2 oz)	Fabirc_1522 (4 oz)	Fabric_3733 (6 oz)
Density (kg/m^3)		2540	
Longitudinal Young's modulus MPa		73.1	
Transverse Young's modulus MPa		8.04	
Longitudinal shear modulus MPa		30.19	
Transverse shear modulus MPa		30.19	
Yarn locking angle (THL)°	30.21	27.44	25.43
Ultimate strain at failure (EU)		0.048	
Initial braid angle°		45	
Transition angle to locking (TA)°		1	
Span between the yarns (*S*) mm	0.7968 (image)	1.13 (image)	1.4276 (image)
Yarn width *w* (mm)	0.3924 (image)	0.71 (image)	0.89 (image)
Real yarn thickness (*T*) mm	0.09	0.13	0.18
Effective yarn thickness (*H*)	0.03177	0.049	0.077
Yarn cross-section area (*S*) mm^2	0.01261	0.02727	0.05463
Elastic constant of element a MPa		146.2	
Elastic constant of element b MPa		146.2	
Co-efficient of friction between fibers *C*		0.4	
Areal density (kg/m^2)	0.081	0.125	0.197

For the simulation of the uniaxial bias-extension tests, the mesh elements were oriented in the 0^o direction to the loading axis, i.e., at a 45^o angle to the yarn direction in the test specimen. To avoid shear locking tendency exhibited by the fabrics during simulation, under-integrated membrane elements were used to determine the in-plane shear behavior. Since the experimental data for the coefficient of friction between the warp and weft directions was not available, it was assumed to be 0.41 based on the recommendation by Yildrim et al. [3]. Different values of tensile modulus in the range of 0.05 and 0.2 MPa were assigned to the shell elements and the corresponding force vs. shear angle diagrams were generated. The tensile modulus assigned to the

shell elements that produced the best match between the simulated and experimental force vs. shear angle diagrams was selected for press forming simulations described in Sections 5.2 and 5.3.

Figure 5.8-5.10 show the comparison of the force vs. shear angle curves obtained experimentally and from simulation results. Based on the superimposition approach, the values of the tensile modulus assigned to the shell elements derived by matching the simulated and experimental force-shear angle curves are shown in Table 5.3.

Table 5.3: Value of the tensile modulus to be assigned to the shell elements to capture out-of-plane bending stiffness.

Parameters	Fabric 1610 (2 oz)	Fabric 1522 (4 oz)	Fabric 3733 (6 oz)
Tensile modulus assigned to the shell elements	0.1 MPa	0.14 MPa	0.12 MPa
% of modulus compared to fabric tensile modulus	0.00014%	0.00019%	0.00016%

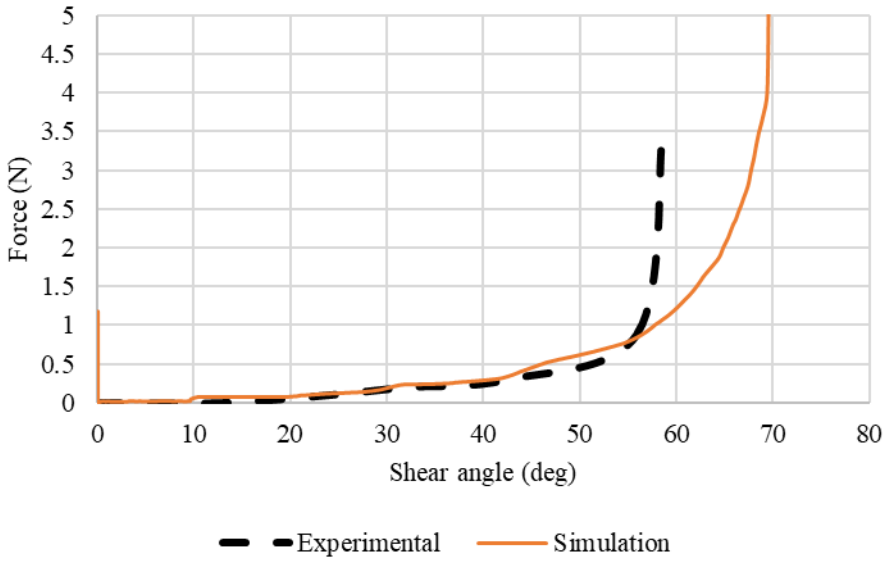

Figure 5.8: Comparison of experimental and simulation force vs. shear angle curves for Fabric_1610 (2 oz).

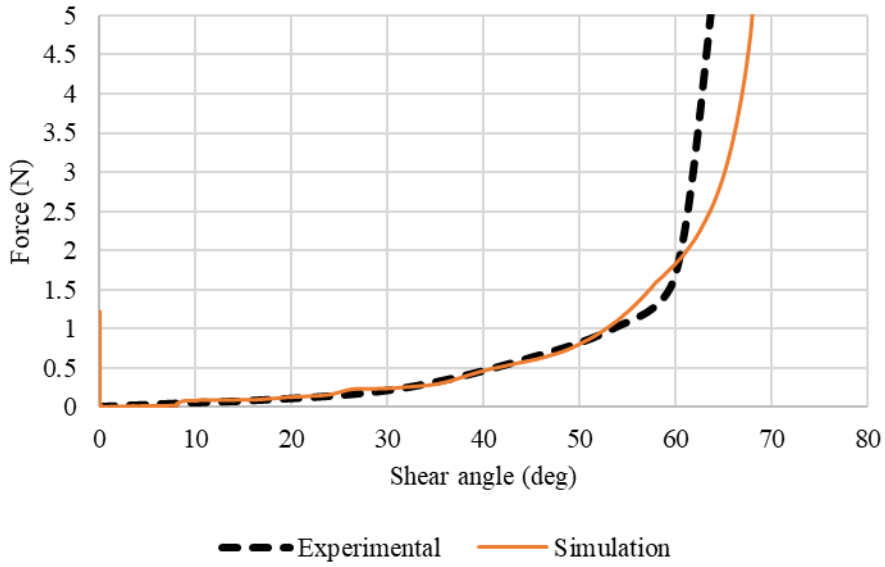

Figure 5.9: Comparison of experimental and simulation force vs shear angle curves for Fabric_1522 (4 oz).

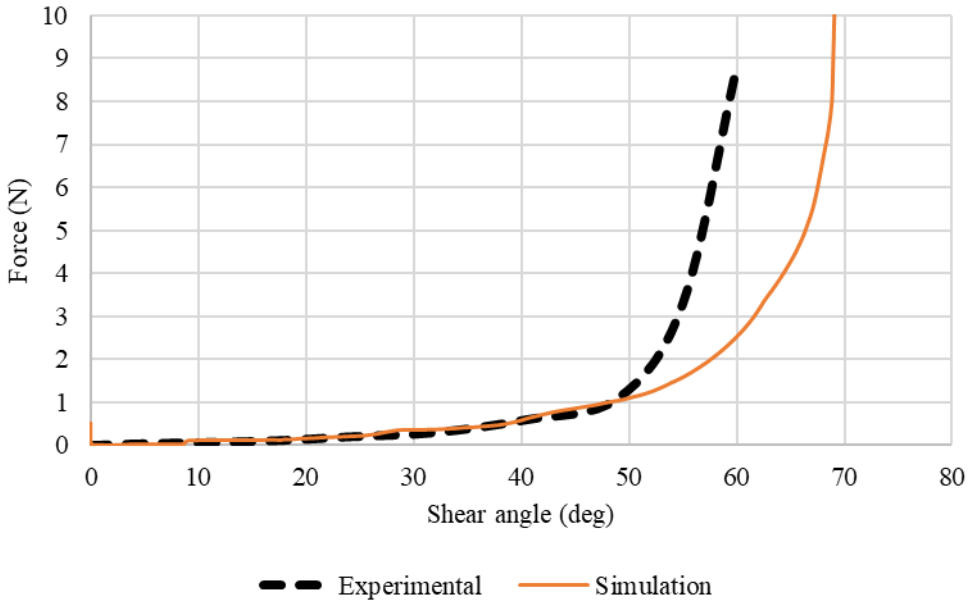

Figure 5.10: Comparison of experimental and simulation force vs. shear angle curves for Fabric_3733 (6 oz).

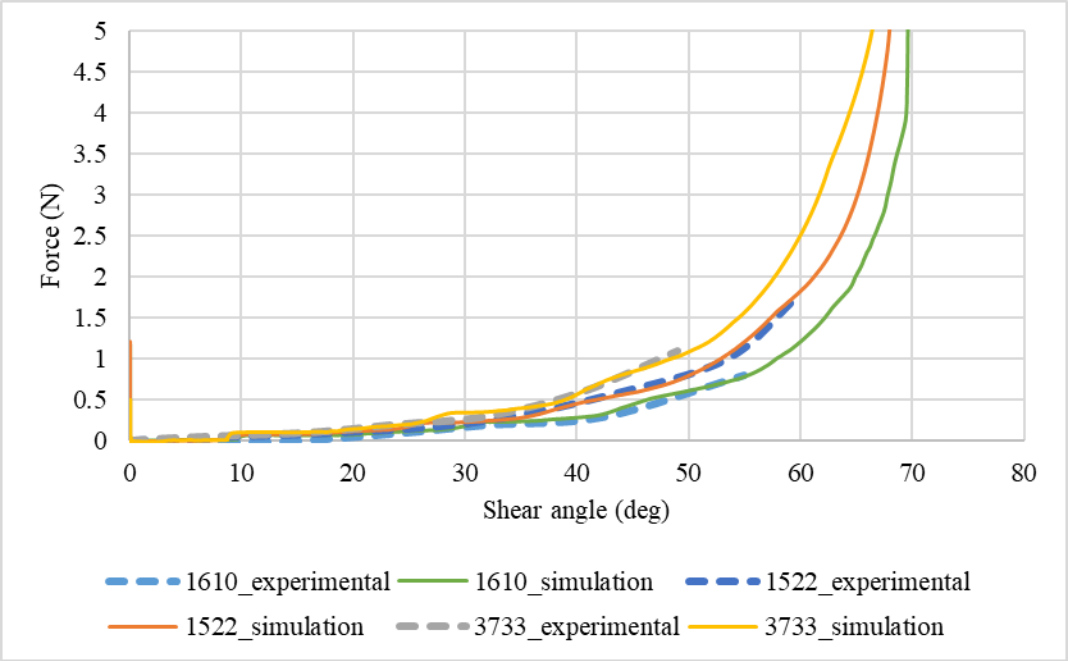

Figure 5.11: Comparison of experimental and simulation force vs. shear angle curves for E-glass fabrics.

Simulation results of the uniaxial bias-extension test match with the experimental results as can be seen from Figures 5.8-5.10. The combined comparison of the force vs. shear angle curves for all three fabrics without considering the data corresponding to the defects are shown in Figure 5.11. Both the experimental and simulation results show an increase in the fabric stiffness behavior with an increase in the areal density of the fabrics.

5.2 Press Forming of Dry Fabrics

5.2.1 Press Forming Experiments

Press forming experiments with E-glass fabrics 1601, 1522 and 3733 were conducted with an aluminum die-punch set up shown in Figure 5.12. The fabric specimens were 160 mm x 160 mm in size and the yarn orientation in them was 0/90 deg with respect to its square edges.

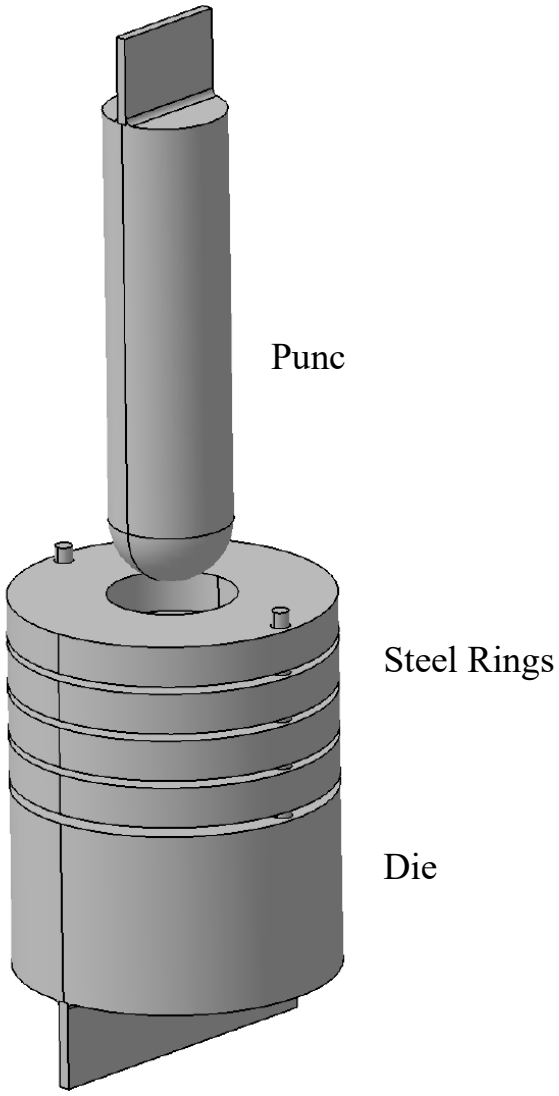

Figure 5.12: Die-punch setup used for press forming experiments with dry fabrics.

The die opening diameter and the punch diameter were 80 mm and 76 mm, respectively so that there was a radial gap of 2 mm between the die opening and the punch. The die corner radius was 10 mm and the die depth was 100 mm. Three different punch bottoms were used: a hemispherical bottom with 38 mm radius (shown in Figure 5.13), a flat bottom with 15 mm corner radius, and a flat bottom with 8 mm corner radius. The fabric blanks were placed on top surface of the die that had an outside diameter of 200 mm. A thin acrylic ring of 200 mm outside diameter and 80 mm inside diameter was placed on top of the fabric blank. To apply the blank holder force

on the fabric blank, circular steel rings with an internal diameter of 80 mm and an external diameter of 200 mm and each weighing 50 N, were placed on top of the acrylic ring. Two different blank holder forces were used, namely 50 N for which one steel disk was placed on top of the acrylic ring and 200 N for which four steel disks were placed on top of the acrylic ring (Figure 5.13).

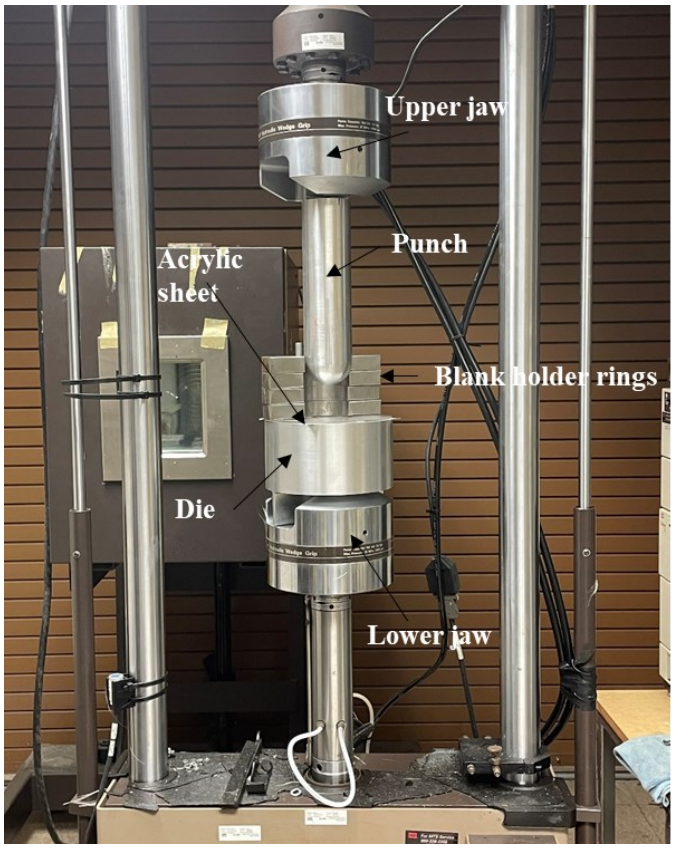

Figure 5.13: Experimental press forming setup for dry fabrics installed on an MTS machine. (Note: Only half of the blank holder rings are shown in the figure).

The press forming experiments were conducted on an MTS servo-hydraulic testing machine The punch was gripped in the upper jaws and the die was mounted in the lower jaws. The lower jaws were moved upward at a speed of 10 mm/sec until the forming depth of 40-55 mm was reached. The lower jaw was then returned to the home position and the outer shape profile of press-formed fabric was photographed. The acrylic ring held the fabric in place and undisturbed after

the punch was retracted and the steel rings were removed, and since it was transparent, photographing its outer profile was relatively easy.

5.2.2 Modeling of Press Forming Experiments

The finite element model of the press forming experiment is shown in Figure 5.14. Because of symmetry conditions and to reduce computational time, only a quarter model was used for which the blank size was 80 mm x 80 mm. The total blank holder forces of 50 N and 200 N were also divided by 4 to represent them appropriately in the quarter model. The mesh size for the die and the punch was selected to be 2 mm; however, a higher mesh density at both punch and die corner radii was used to accommodate the geometrical inconsistencies during press forming. The mesh size of the quadrilateral elements used for the fabric was selected as 1.5 mm. To simulate the press forming of the E-glass fabrics under study, superimposed approach was utilized. Material model MAT_234 accounts for the in-plane shear behavior of the fabrics considered. The material parameters which are to be given as input for the finite element simulations and assigned to MAT_234 are shown in Table 5.2. The material model MAT_001 account for the out-of-plane bending stiffness and the values of the tensile modulus that is to be assigned to the shell elements for the individual fabrics are listed in Table 5.3.

The die and punch materials were aluminum and were modeled using MAT_020 (MAT_RIGID). The coefficient of friction between the dry fabrics and die-punch surfaces was kept at 0.15. The value of 0.15 was selected for the tool-fabric interaction instead of 0.2 which was used by Yildrim et al. [3] and Peng et al. [4], since the top surface of the fabrics in this study was in contact with the acrylic ring surface instead of a metallic surface. The coefficient of friction between the fibers (warp and weft direction) in the E-glass fabric was taken as 0.41 from the benchmark study by Yildrim et al. [3].

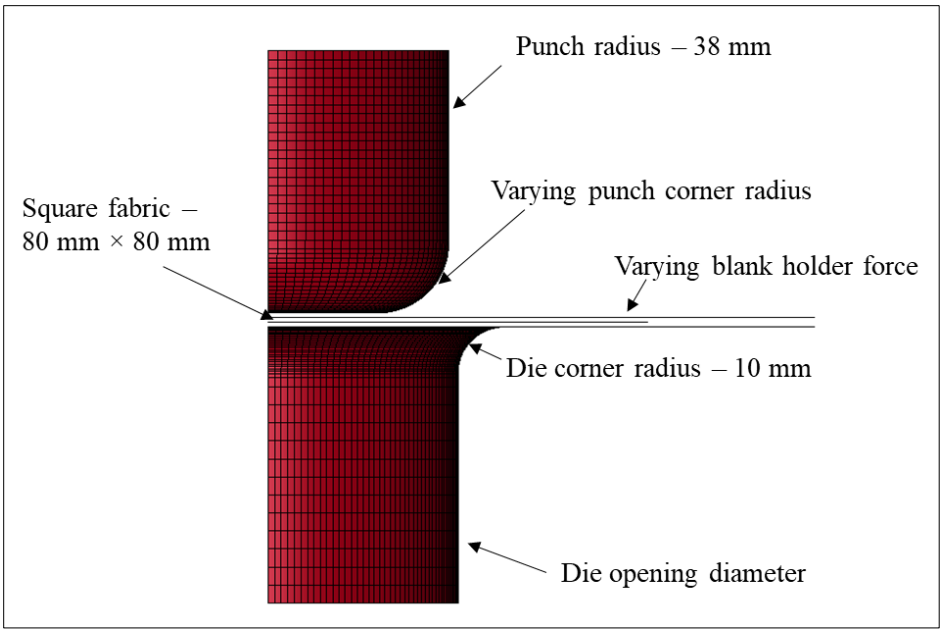

Figure 5.14: Finite element model of the quarter of the press forming setup (Note: Dimensions of the blank shown here are for quarter model).

5.2.3 Outer Shape Profile for Press Forming with 38 mm Hemispherical Punch

The simulated outer shape profile of the press formed dry E-glass fabric are compared to the experimental outer shape profile in Figures 5.15–5.28. The outer shape profile obtained from the simulation results matches well with the experimental outer shape profile. Outer shape profiles were also compared for a few intermediate draw depths for press forming with 33 mm punch corner radius to check if the simulation can replicate the experimental behavior.

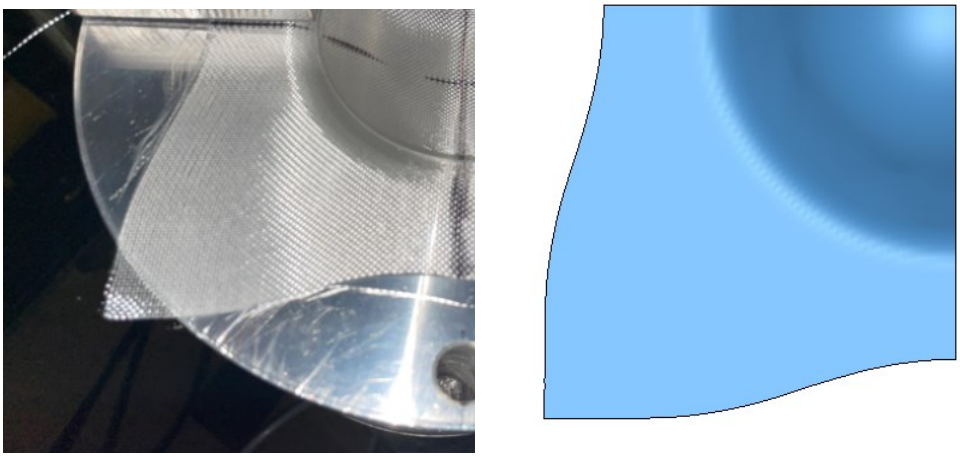

Figure 5.15: Comparison of the experimental and simulation outer shape profiles for Fabric_1610 with 50 N blank holder force at 33 mm displacement.

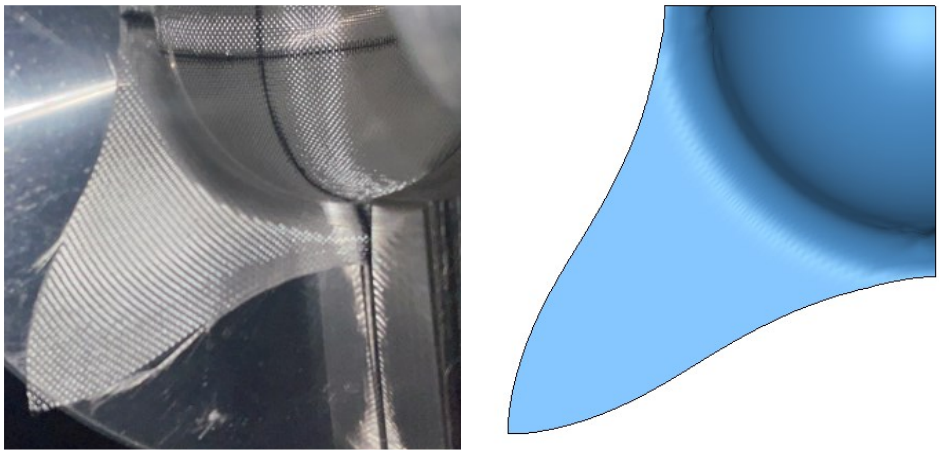

Figure 5.16: Comparison of the experimental and simulation outer shape profiles for Fabric_1610 with 50 N blank holder force at 55 mm displacement.

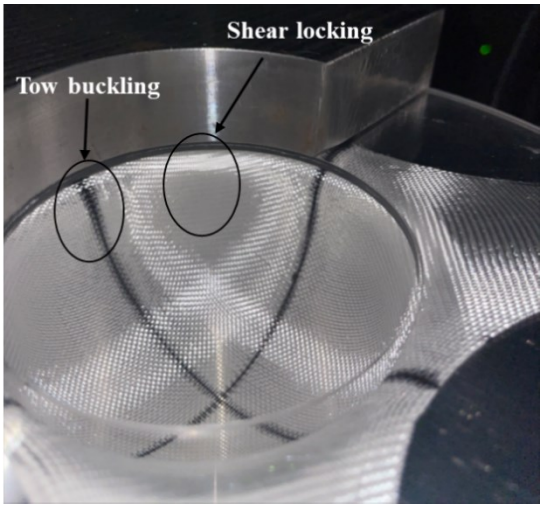

Figure 5.17: Press formed dry Fabric_1610 at 55 mm displacement showing the wrinkles formed due to tow buckling and shear locking.

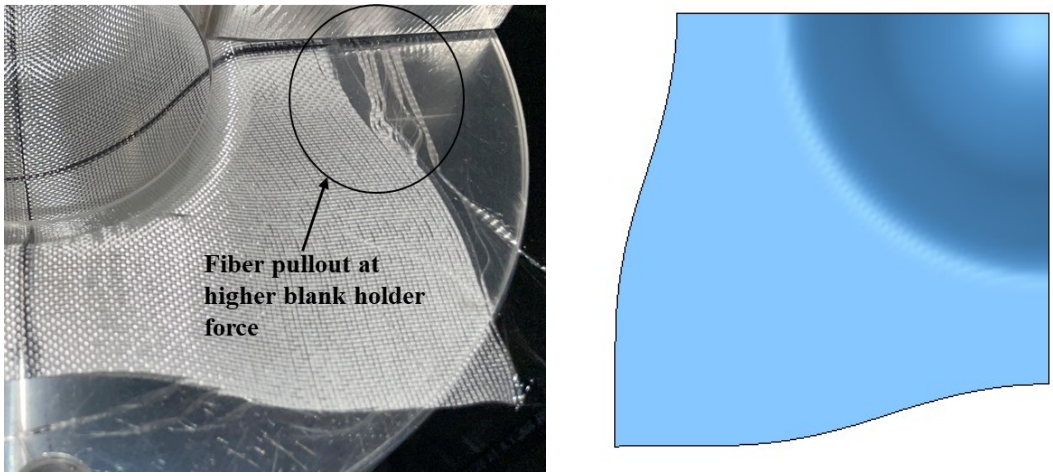

Figure 5.18: Comparison of the experimental and simulation outer shape profiles for Fabric_1610 with 200 N blank holder force at 33 mm displacement.

Figure 5.18 shows a comparison of the experimental and simulation outer shape profile for Fabric_1610 with 200 N of applied blank holder force. Experimental press forming for dry fabric shows fiber pull out defects at higher blank holder forces which are not captured in the simulation results.

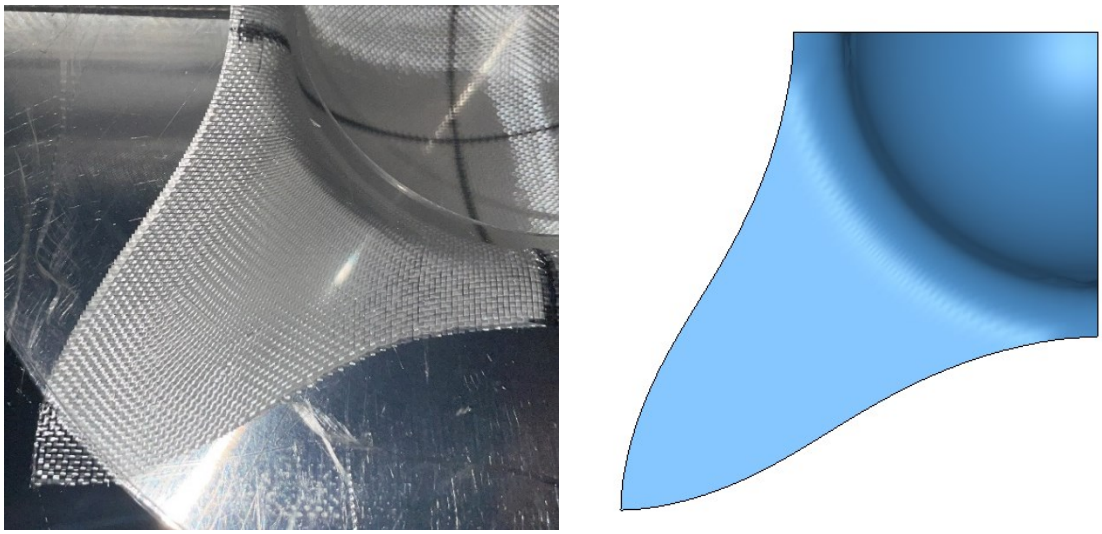

Figure 5.19: Comparison of the experimental and simulation outer shape profiles for Fabric_1610 with 200 N blank holder force at 55 mm displacement.

A comparison for the press formed fabrics at 55 mm displacement with 50 N and 200 N blank holder force (Figures 5.16 and 5.19) shows that wrinkle formation due to yarn buckling reduces with the increase in blank holder force. Wrinkles due to yarn buckling at the intersection of the flanges were more dominant for the fabric with 50 N blank holder force, however these wrinkles were less dominant with 200 N blank holder force as can be seen in Figure 5.19.

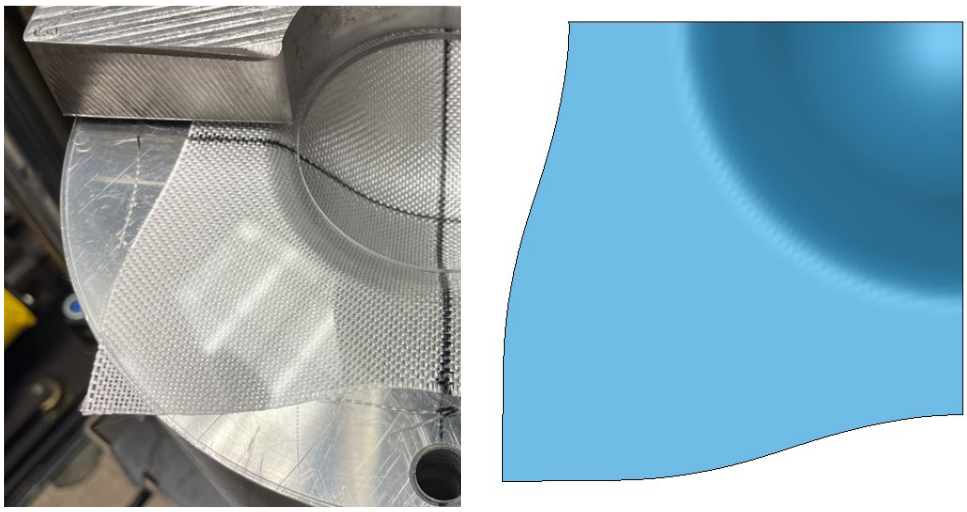

Figure 5.20: Comparison of the experimental and simulation outer shape profiles for Fabric_1522 with 50 N blank holder force at 33 mm displacement.

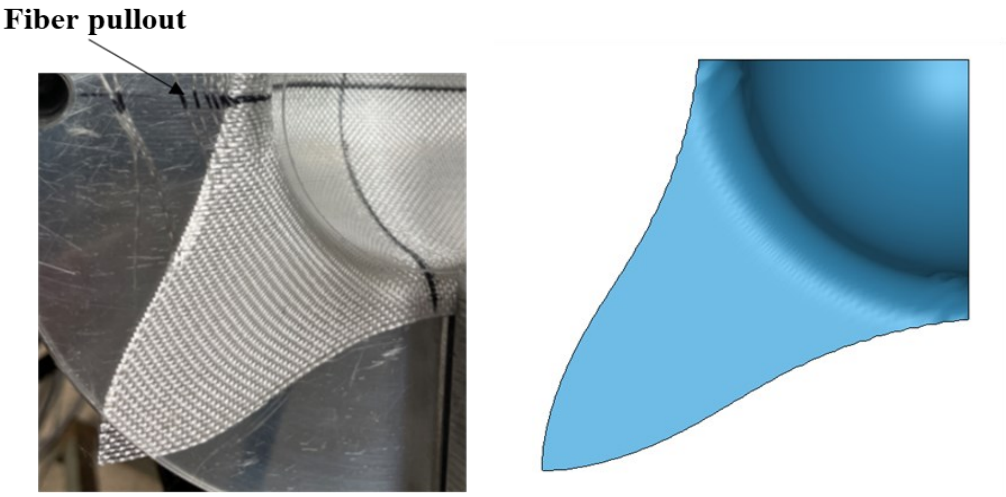

Figure 5.21: Comparison of the experimental and simulation outer shape profiles for Fabric_1522 with 50 N blank holder force at 55 mm displacement.

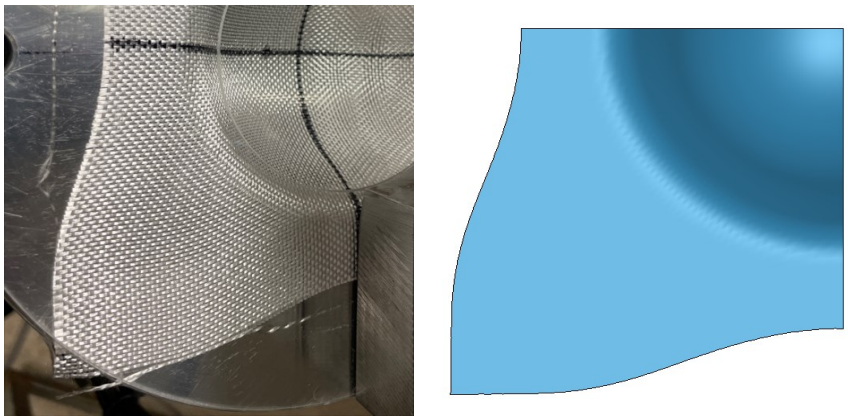

Figure 5.22: Comparison of the experimental and simulation outer shape profiles for Fabric_1522 with 200 N blank holder force at 33 mm displacement.

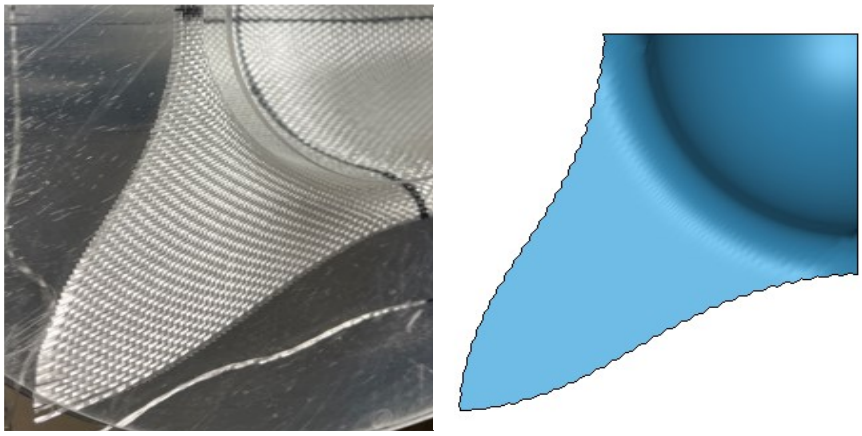

Figure 5.23: Comparison of the experimental and simulation outer shape profiles for Fabric_1522 with 200 N blank holder force at 55 mm displacement.

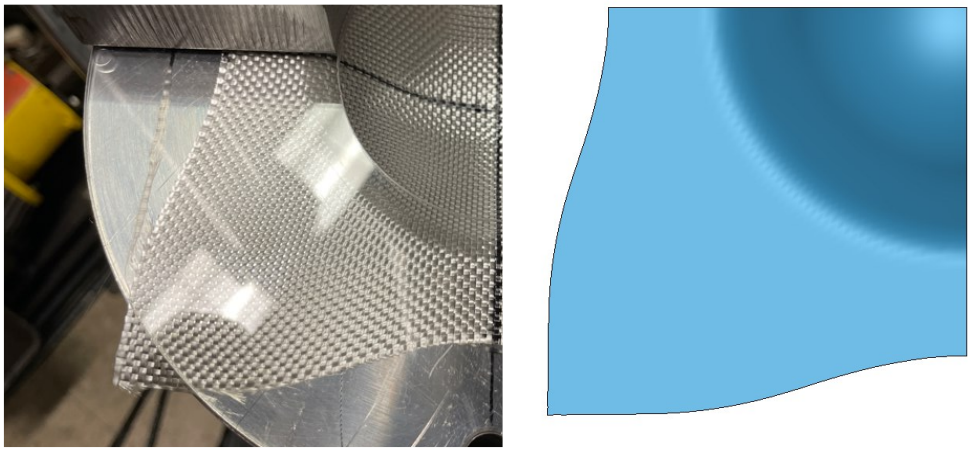

Figure 5.24: Comparison of experimental and simulated outer shape profiles for Fabric_3733 with 50 N blank holder force at 33 mm displacement.

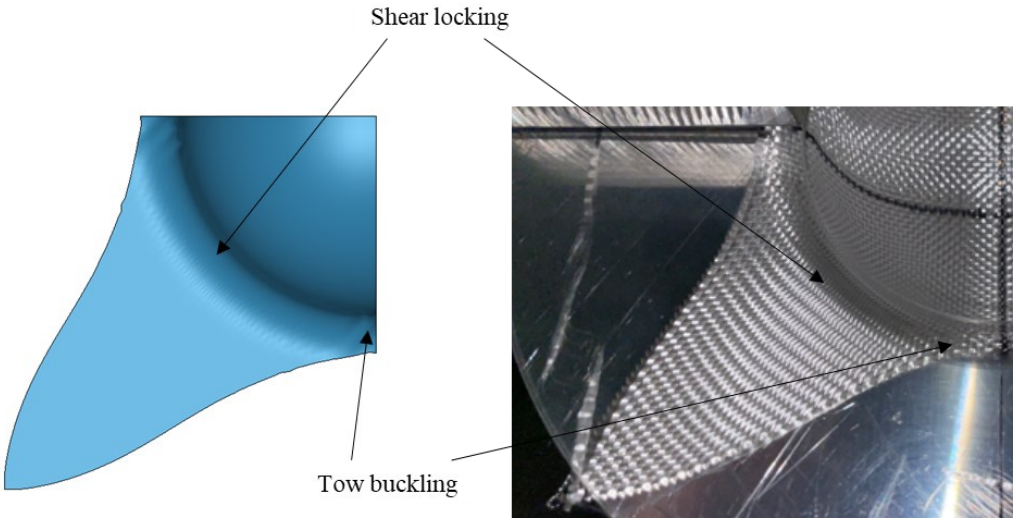

Figure 5.25: Comparison of the experimental and simulation outer shape profiles for Fabric_3733 with 50 N blank holder force at 55 mm displacement.

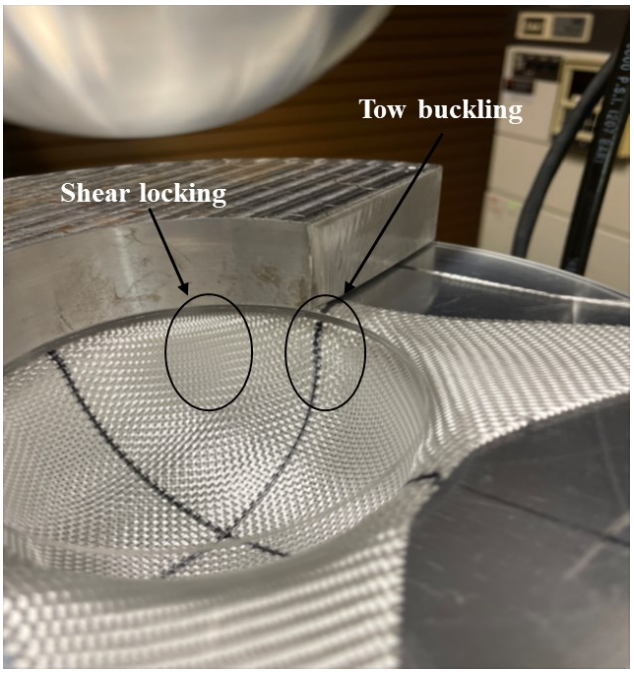

Figure 5.26: Formed Fabric_3733 at 55 mm displacement showing wrinkles due to tow buckling and shear locking.

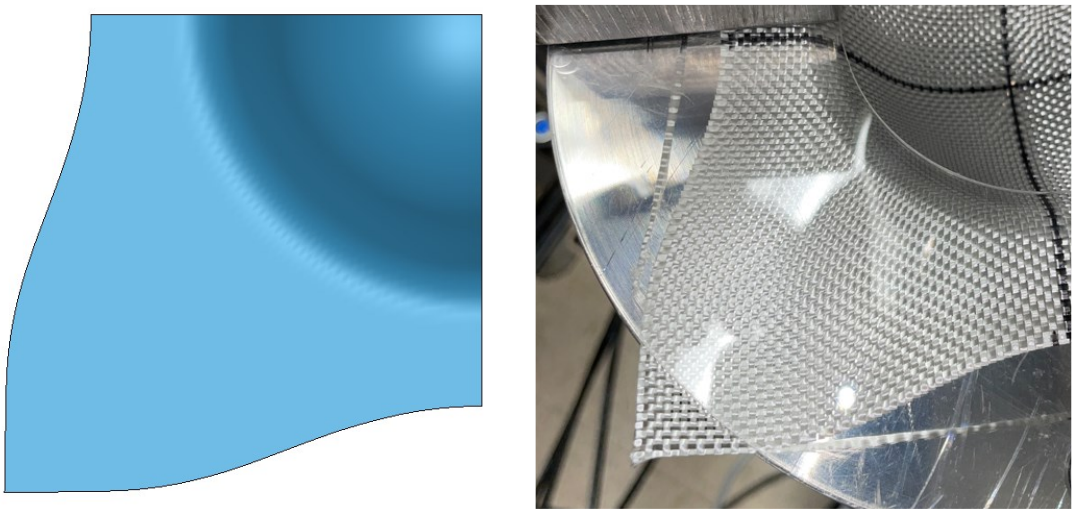

Figure 5.27: Comparison of the experimental and simulation outer shape profiles for Fabric_3733 with 200 N blank holder force at 33 mm displacement.

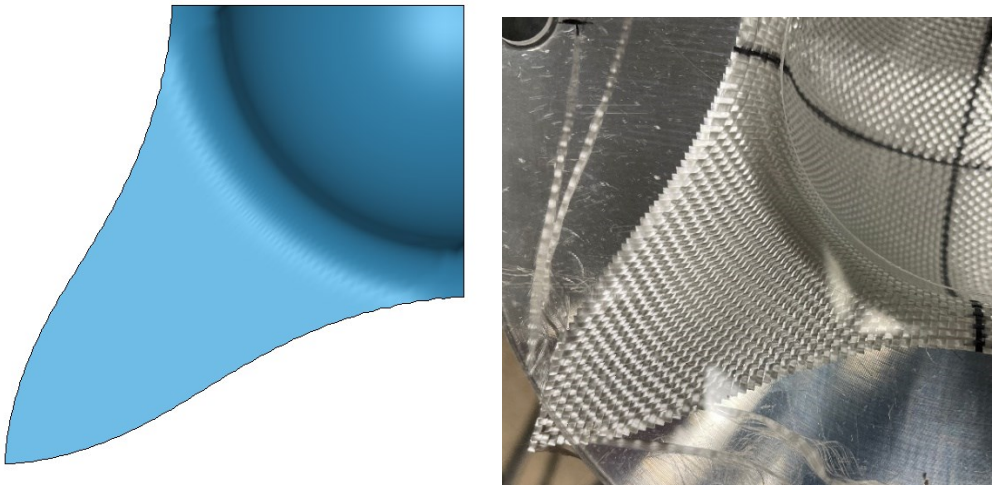

Figure 5.28: Comparison of the experimental and simulation outer shape profiles for Fabric_3733 with 200 N blank holder force at 55 mm displacement.

5.2.4 Outer Shape Profile for Press Forming with 15 mm Punch Corner Radius.

A comparison was made to verify if the superimposed model is able to capture the outer shape profile for press forming of the dry fabrics. Figures 5.29-5.34 shows the comparison of the experimental and simulated outer shape profile for the press formed dry fabric. From the comparison, we can see that the superimposed approach is able to capture the outer shape profile and also it is able to capture the defects (i.e. wrinkling) that occurs in the formed fabrics.

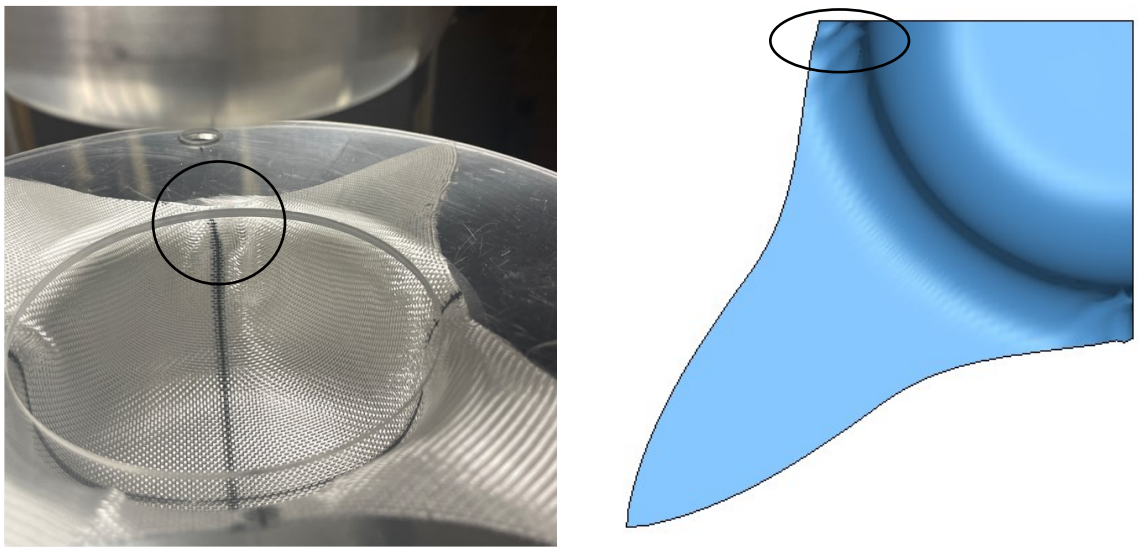

Figure 5.29: Comparison of the experimental and simulation outer shape profiles for Fabric_1610 with 50 N blank holder force at 45 mm displacement.

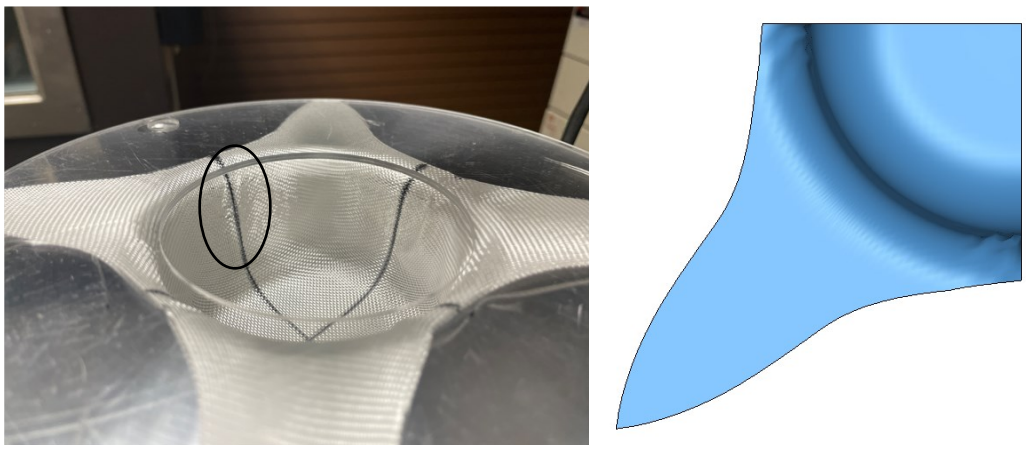

Figure 5.30: Comparison of the experimental and simulation outer shape profiles for Fabric_1610 with 200 N blank holder force at 45 mm displacement.

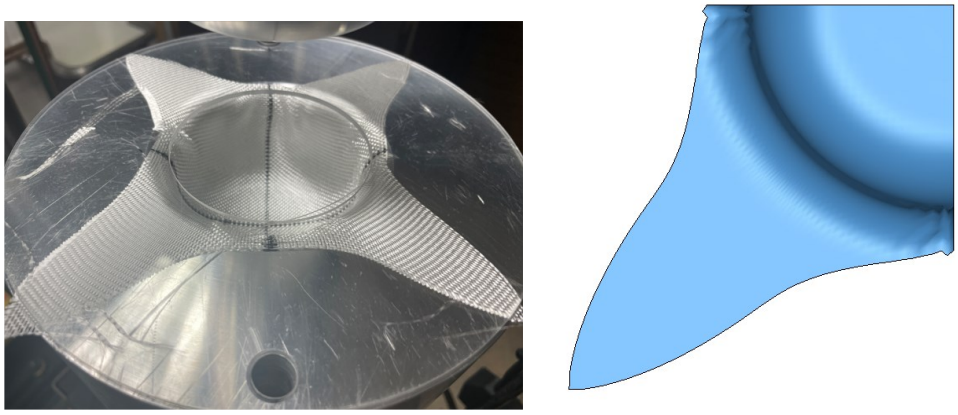

Figure 5.31: Comparison of the experimental and simulation outer shape profiles for Fabric_1522 with 50 N blank holder force at 45 mm displacement.

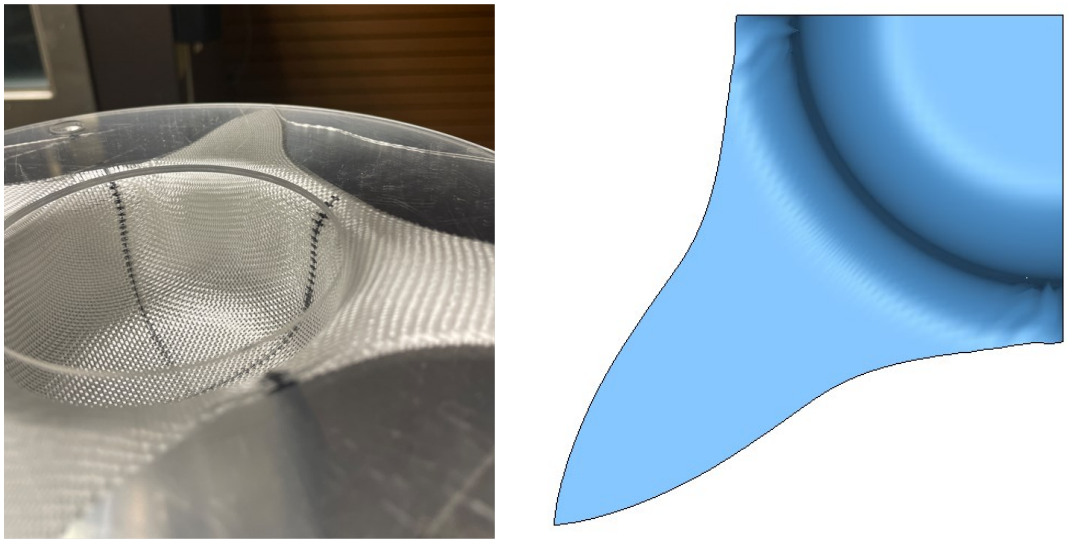

Figure 5.32: Comparison of the experimental and simulation outer shape profiles for Fabric_1522 with 200 N blank holder force at 45 mm displacement.

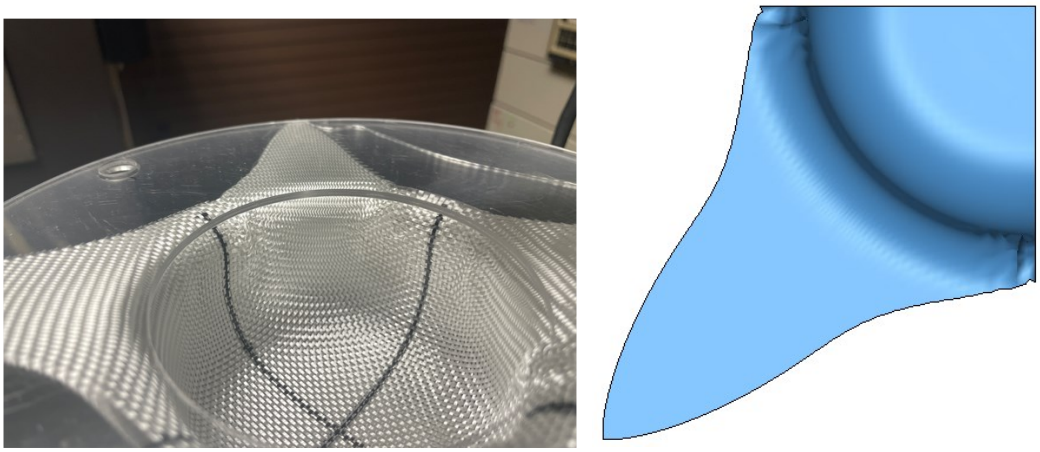

Figure 5.33: Comparison of the experimental and simulation outer shape profiles for Fabric_3733 with 50 N blank holder force at 45 mm displacement.

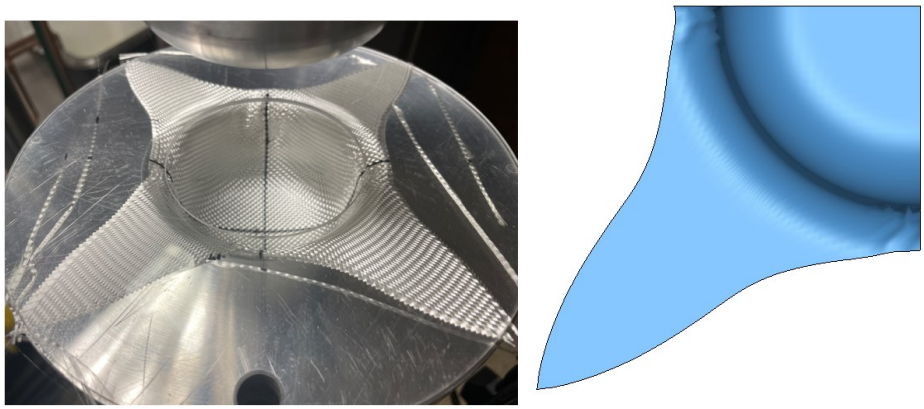

Figure 5.34: Comparison of the experimental and simulation outer shape profiles for Fabric_3733 with 200 N blank holder force at 45 mm displacement.

5.2.5 Outer Shape Profile for Press Forming with 8 mm Punch Corner Radius

The press forming operation for dry E-glass fabrics using a punch with 8 mm corner radius were simulated using the superimposed approach and the outer shape profile obtained from the simulation results were compared to the experimental results. The comparison of the outer shaper profile for the press formed parts with 8 mm punch corner radius are shown in Figures 5.35-5.40. From these figures we can see that the simulated outer shape profile using the superimposed approach is able to replicate the experimental results.

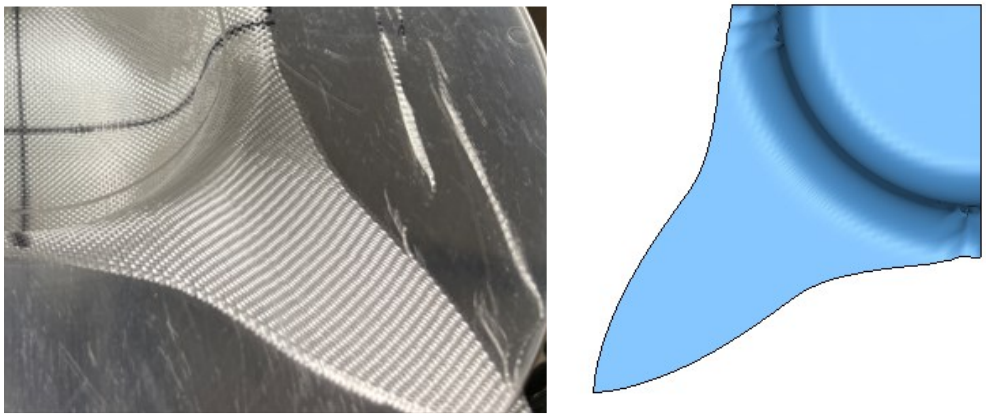

Figure 5.35: Comparison of the experimental and simulation outer shape profiles for Fabric_1610 with 50 N blank holder force at 40 mm displacement.

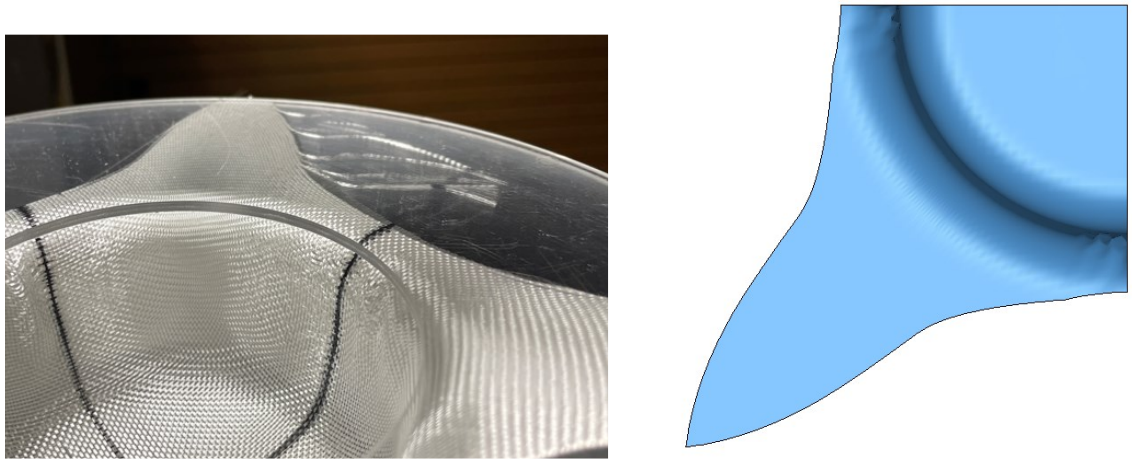

Figure 5.36: Comparison of the experimental and simulation outer shape profiles for Fabric_1610 with 200 N blank holder force at 40 mm displacement.

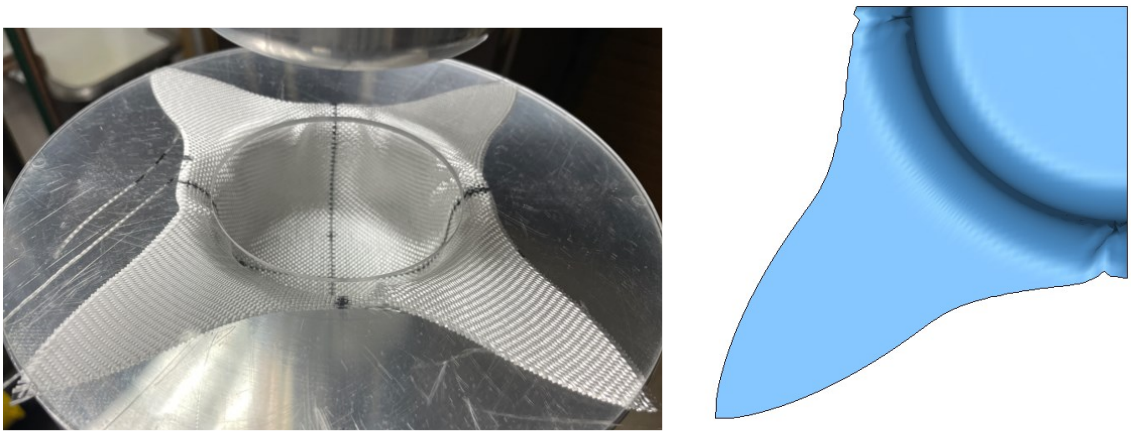

Figure 5.37: Comparison of the experimental and simulation outer shape profiles for Fabric_1522 with 50 N blank holder force at 40 mm displacement.

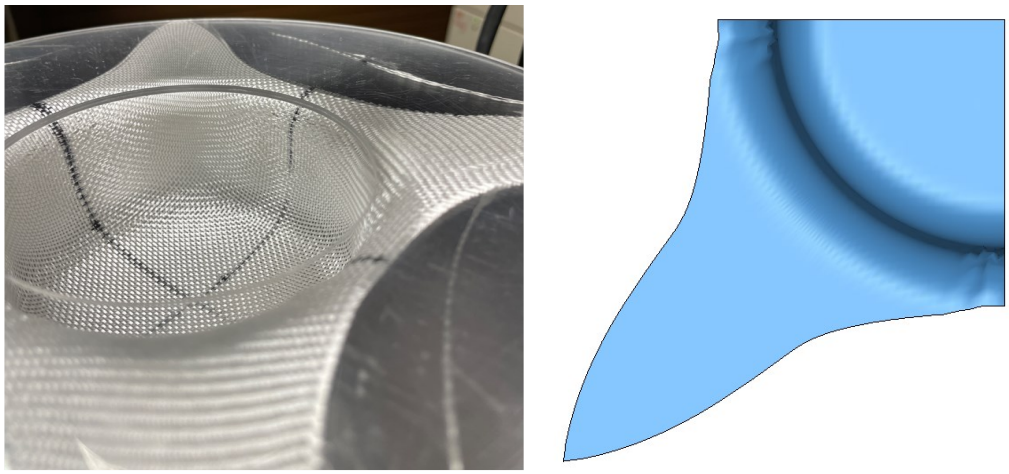

Figure 5.38: Comparison of the experimental and simulation outer shape profiles for Fabric_1522 with 200 N blank holder force at 40 mm displacement.

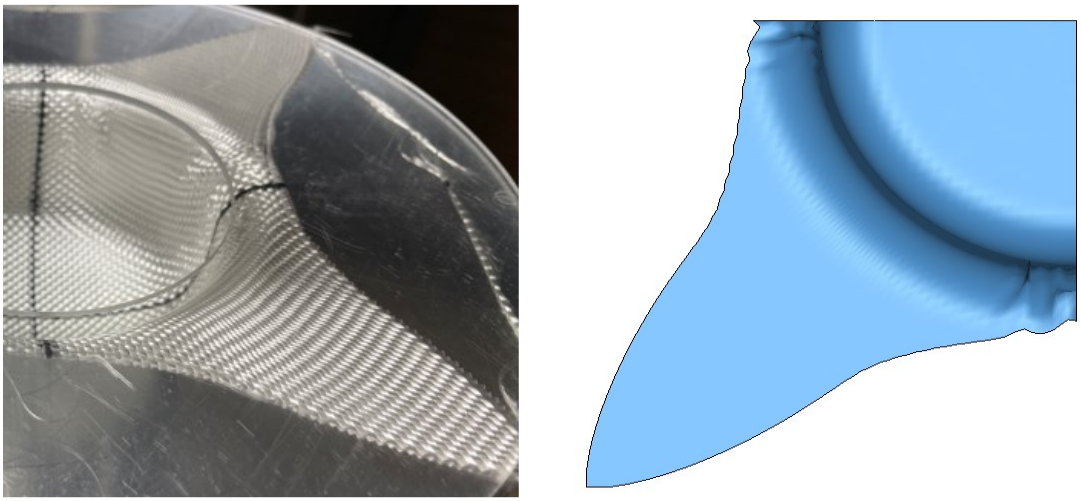

Figure 5.39: Comparison of the experimental and simulation outer shape profiles for Fabric_3733 with 50 N blank holder force at 40 mm displacement.

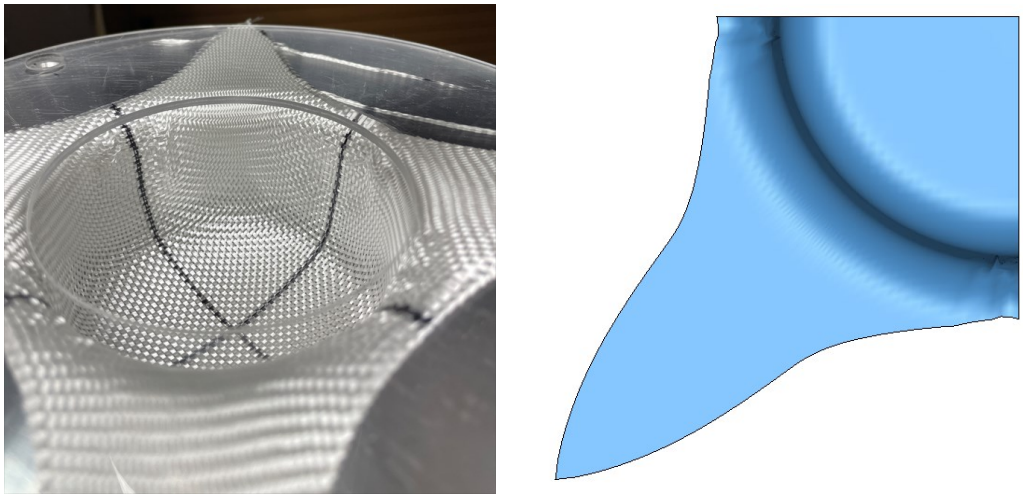

Figure 5.40: Comparison of the experimental and simulation outer shape profiles for Fabric_3733 with 200 N blank holder force at 40 mm displacement.

5.2.6 Punch Force vs. Punch Displacement Curves

Punch force vs. punch displacement curves were studied for the press forming operation of dry fabrics using different process and material variables to study their effects on the force required to press form the dry fabrics. A comparison was also made between the experimental and simulated punch force vs. punch displacement. This exercise was done to check if the superimposed modeling approach is able to predict reasonably accurately the force required to deep draw the fabrics.

5.2.6.1 Effect of Blank Holder Force and Areal Density

Experimental punch force vs. punch displacement graphs were plotted for the three different fabrics to study the effect of the blank holder force on the force required to press form the dry fabrics. Figures 5.41- 5.43 shows the variation of the force vs. displacement graphs for the three fabrics under study with different punch corner radius of 38 mm, 15 mm, and 8 mm, respectively.

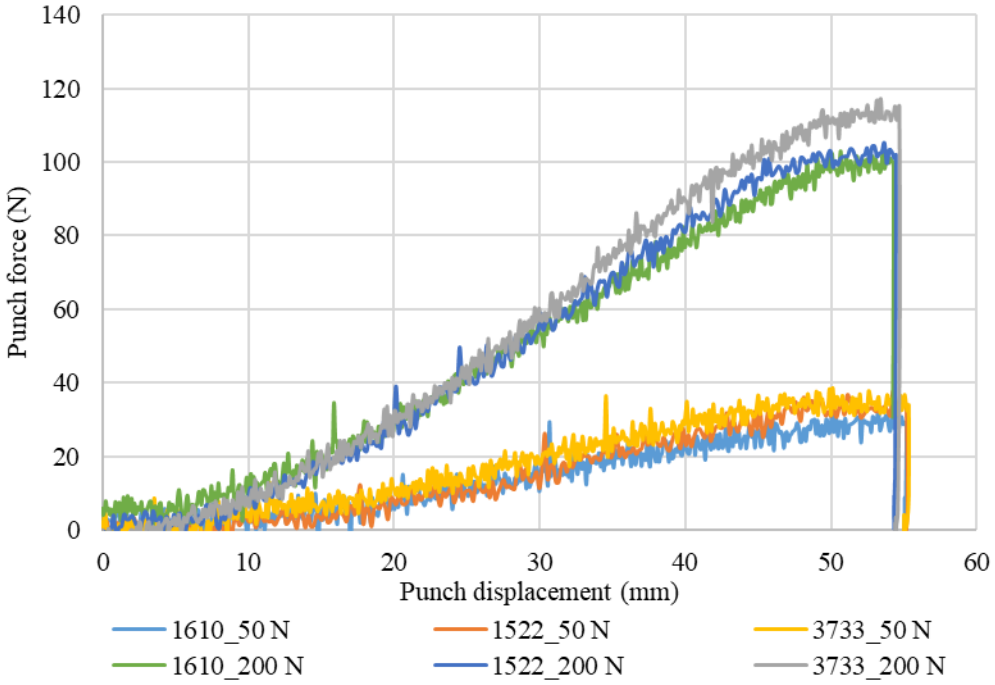

Figure 5.41: Punch force vs. punch displacement graphs for the press formed fabric with a punch of 38 mm corner radius at different blank holder forces.

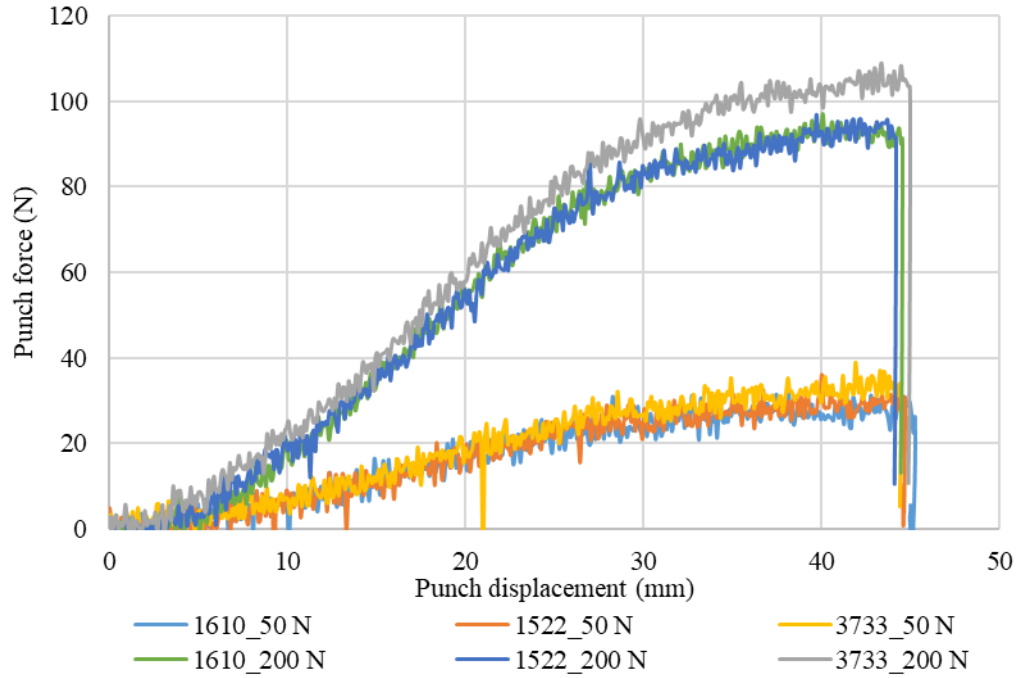

Figure 5.42: Punch force vs. punch displacement graphs for the press formed fabric with a punch of 15 mm corner radius at different blank holder forces.

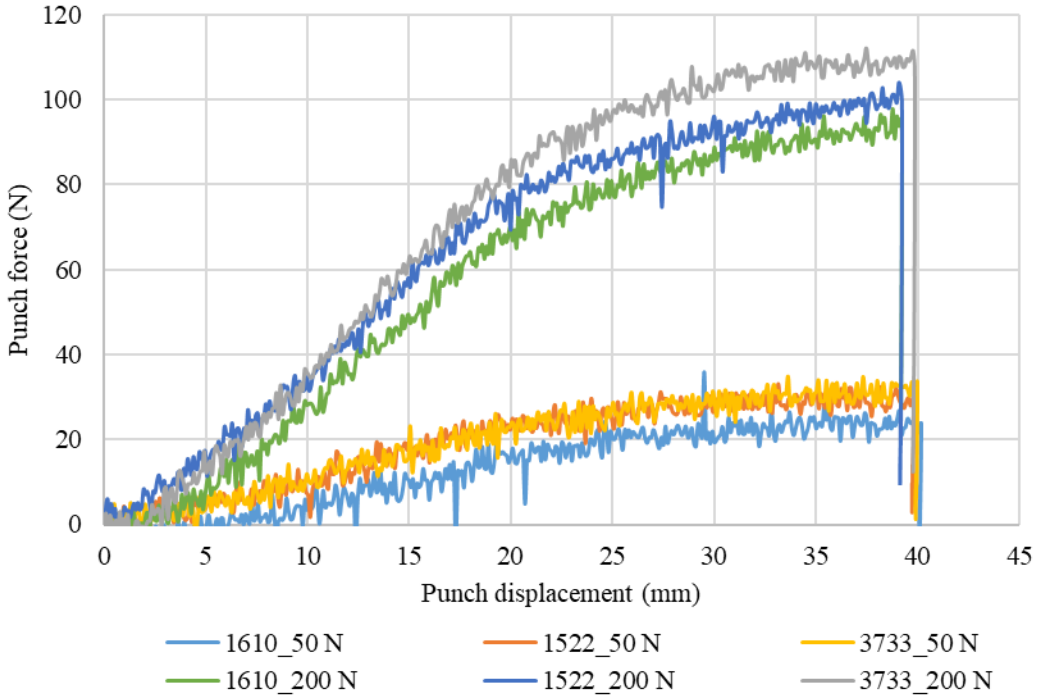

Figure 5.43: Punch force vs. punch displacement graphs for the press formed fabric with a punch of 8 mm corner radius at different blank holder forces.

Figures 5.41-5.43 show that the force required for press forming increases with increase in the applied blank holder force, i.e., with increase in blank holder force, higher punch forces are required to overcome the applied transverse load. Force required to press form the dry fabrics also increases with increase in the areal density of the fabrics as can be seen from the Figures 5.41-5.43.

5.2.6.2 Effect of Punch Corner Radius

The effect of the punch corner radius on press forming of dry fabrics is studied by plotting the punch force vs. punch displacement graphs for the formed fabrics with three different punch corner radii of 38 mm, 15 mm and 8 mm for an applied blank holder force of 200 N. Figures 5.44–5.46 show the force vs. displacement for Fabric_1610, Fabric_1522 and Fabric_3733, respectively.

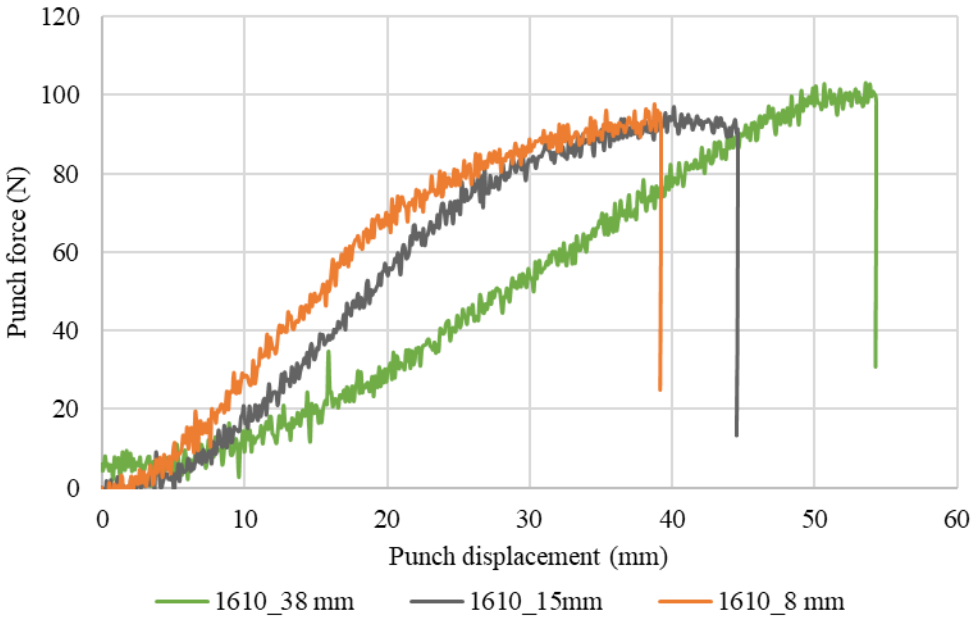

Figure 5.44: Punch force vs. punch displacement graphs for the press formed Fabric_1610 with punch having different corner radius and at blank holder force of 200 N.

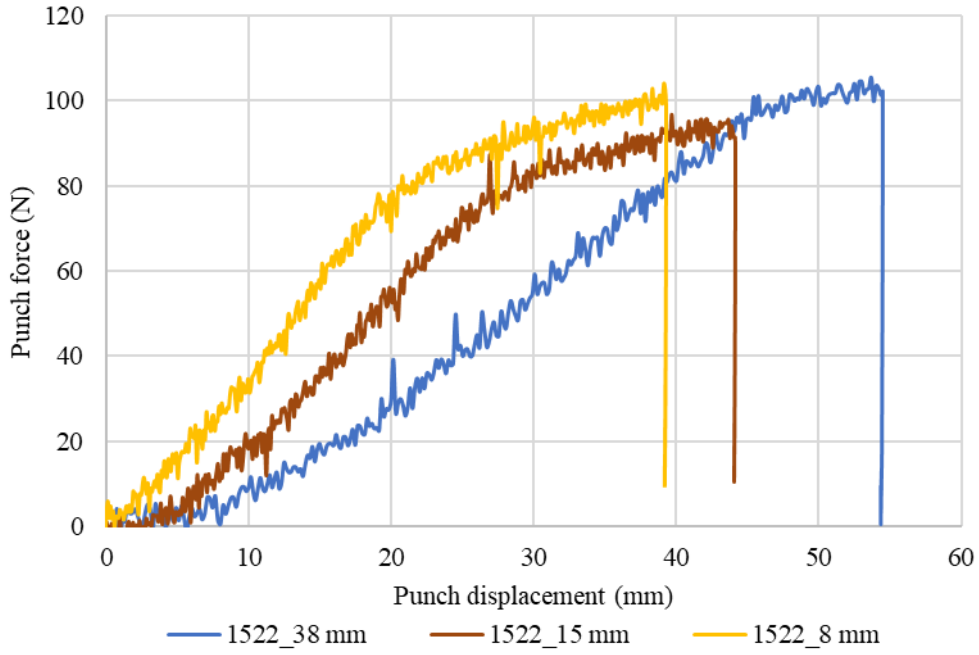

Figure 5.45: Punch force vs. punch displacement graphs for the press formed Fabric_1522 with punch having different corner radius and at blank holder force of 200 N.

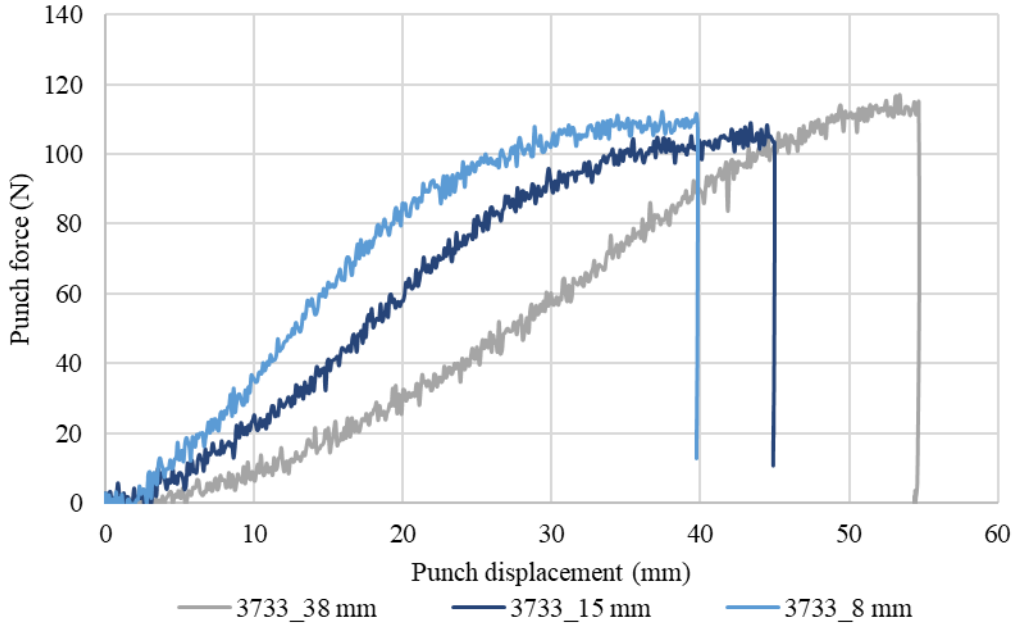

Figure 5.46: Punch force vs. punch displacement graphs for the press formed Fabric_3733 with punch having different corner radius and at blank holder force of 200 N.

From Figures 5.44-5.46, it can be seen that the force required for forming the dry fabric increases with a decrease in the punch corner radius which can be attributed to the higher resistance offered by the fabric during draping with a punch having sharper corner radius. The wrinkles that are formed due to yarn buckling and shear locking also increases with the decrease in the punch corner radius. At higher blank holder forces, the tendency of tearing defects along the cup wall or at the cup bottom increases with the decrease in the punch corner radius.

5.2.6.3 Comparison of Experimental and Simulated Force vs. Displacement Curves.

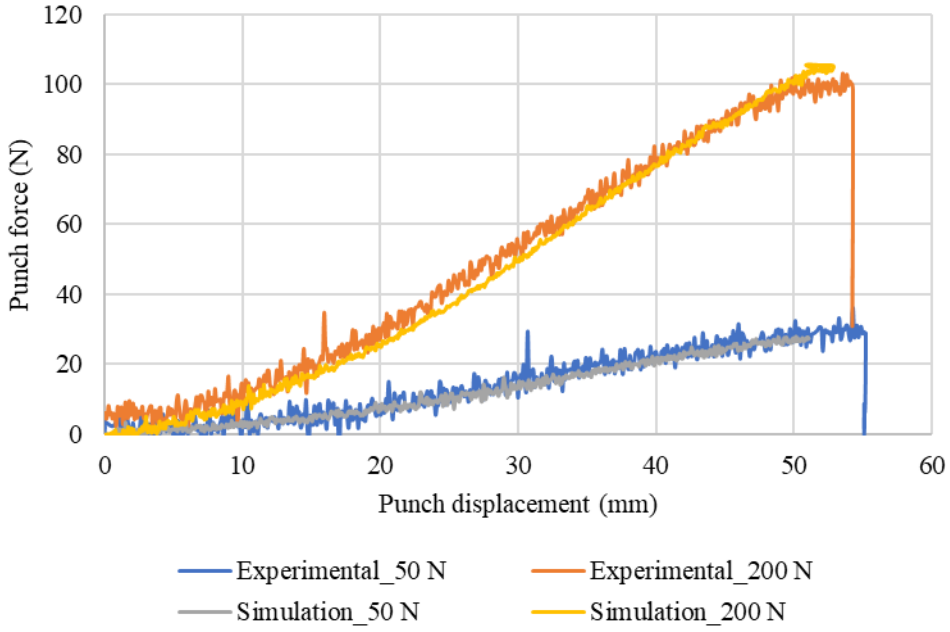

Figure 5.47: Comparison of experimental and simulated punch force vs. punch displacement graphs for Fabric_1610 (2 oz) at different blank holder forces with 38 mm punch corner radius.

Comparisons were made between the experimental and simulated punch force vs. punch displacement curves at 50 N and 200 N applied blank holder forces for press forming operation of dry fabrics with punch having different corner radii. This exercise was carried out to validate the superimposed approach and to check if the approach is able to determine and replicate the forces required for fabric deformation during press forming operation. Figures 5.47–5.55 show the

comparison of the experimental and simulated punch force vs. punch displacement curves for three different dry fabrics at different applied blank holder forces for press forming with punch having different corner radius. Figures 5.47-5.55 show that the superimposed modeling approach is able to predict reasonably accurately the force required for press forming of fabrics.

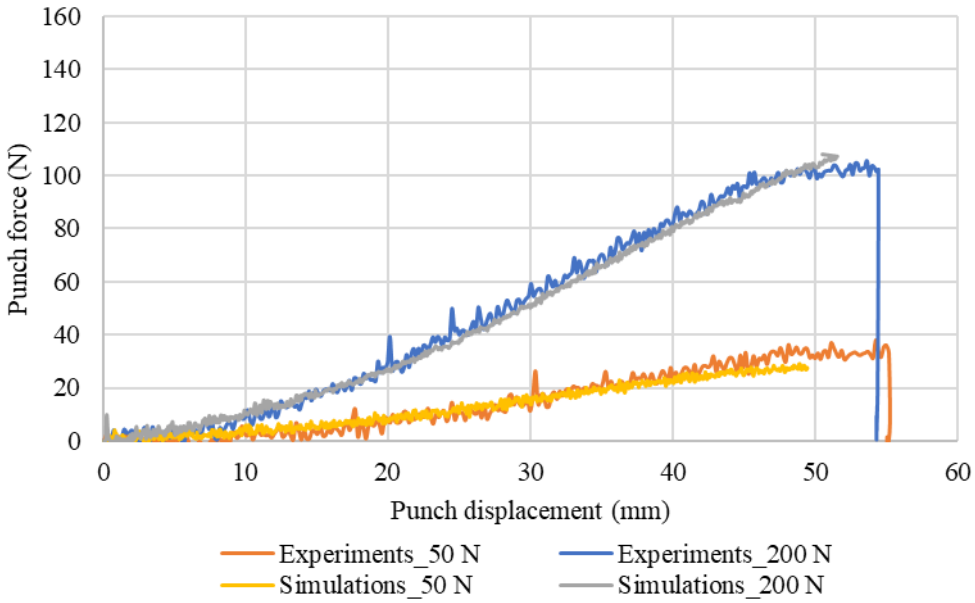

Figure 5.48: Comparison of experimental and simulated punch force vs. punch displacement graphs for Fabric_1522 (4 oz) at different blank holder forces with 38 mm punch corner radius.

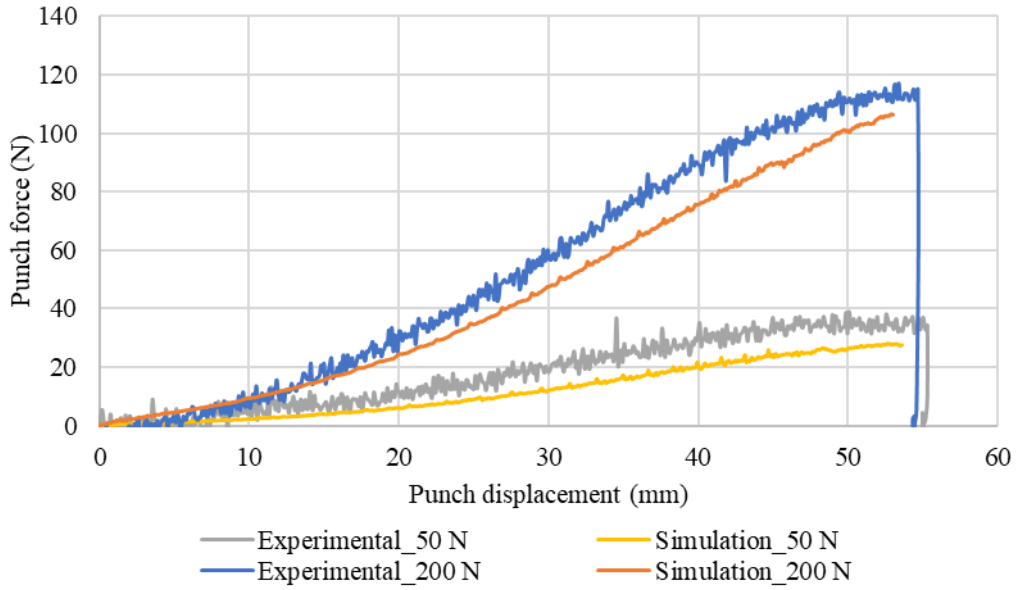

Figure 5.49: Comparison of experimental and simulated punch force vs. punch displacement graphs for Fabric_3733 (6 oz) at different blank holder forces with 38 mm punch corner radius.

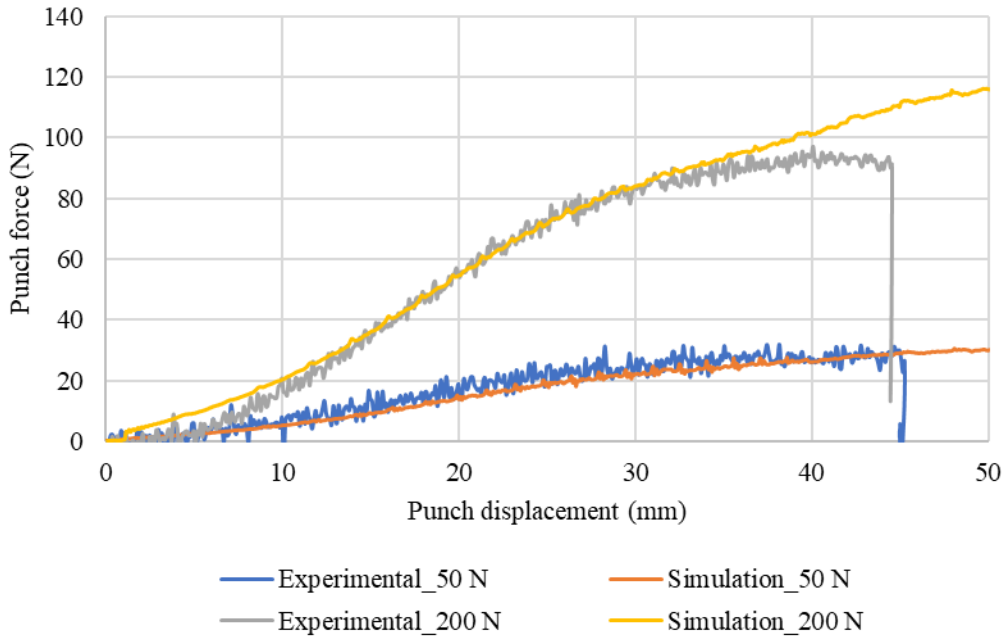

Figure 5.50: Comparison of experimental and simulated punch force vs. punch displacement graphs for Fabric_1610 (2 oz) at different blank holder forces with 15 mm punch corner radius.

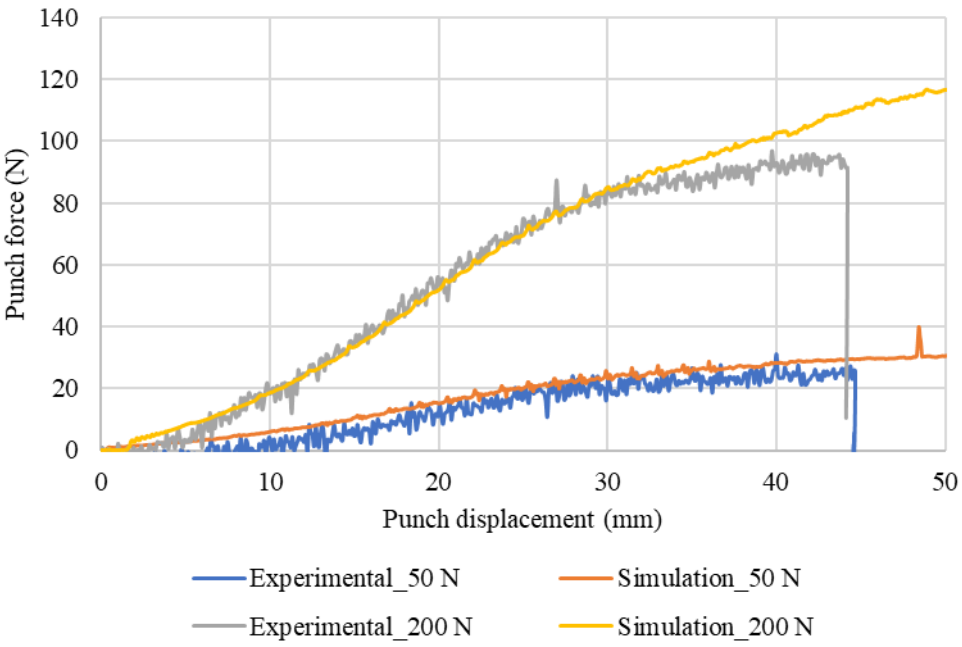

Figure 5.51: Comparison of experimental and simulated punch force vs. punch displacement graphs for Fabric_1522 (4 oz) at different blank holder forces with 15 mm punch corner radius.

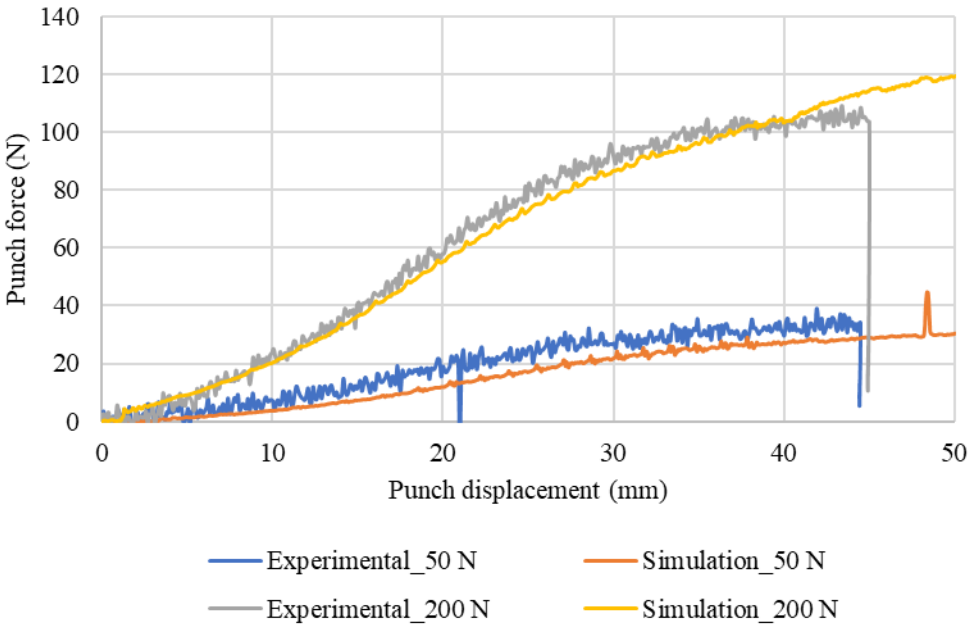

Figure 5.52: Comparison of experimental and simulated punch force vs. punch displacement graphs for Fabric_3733 (6 oz) at different blank holder forces with 15 mm punch corner radius.

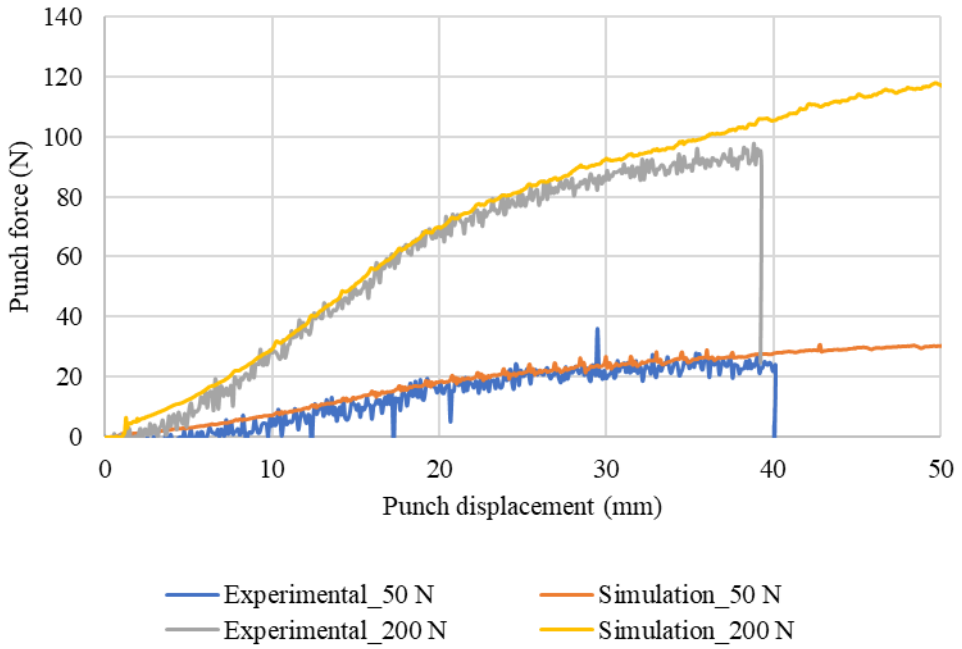

Figure 5.53: Comparison of experimental and simulated punch force vs. punch displacement graphs for Fabric_1610 (2 oz) at different blank holder forces with 8 mm punch corner radius.

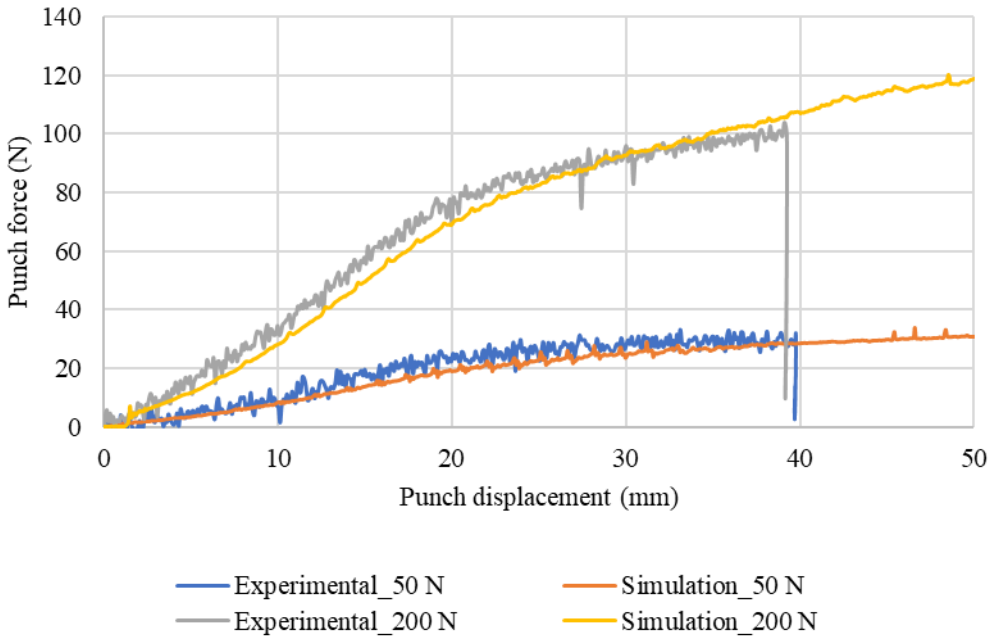

Figure 5.54: Comparison of experimental and simulated punch force vs. punch displacement graphs for Fabric_1522 (4 oz) at different blank holder forces with 8 mm punch corner radius.

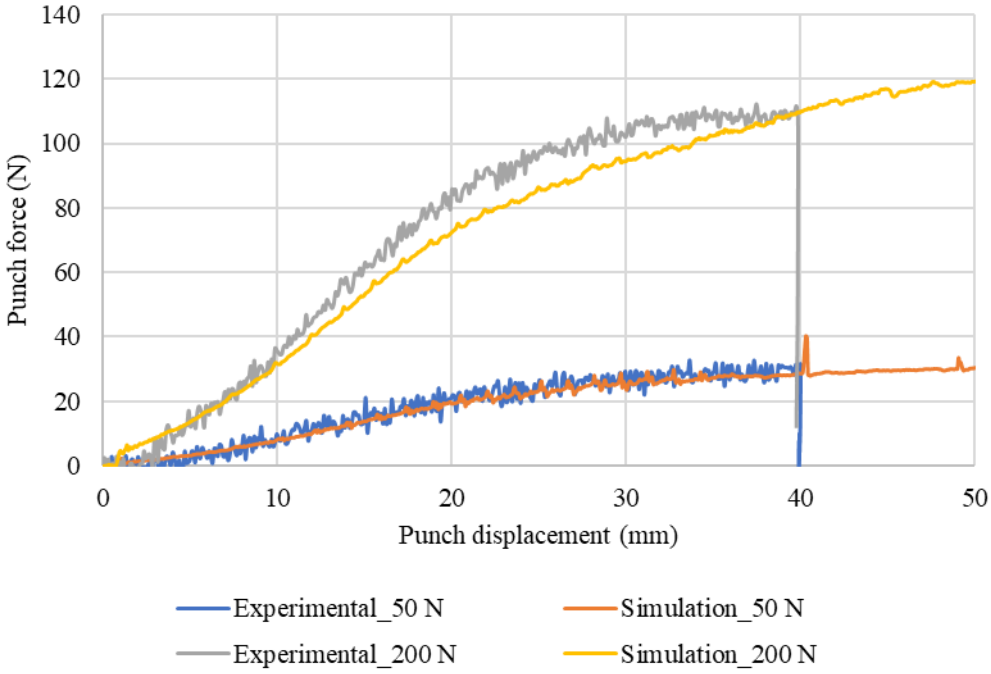

Figure 5.55: Comparison of experimental and simulated punch force vs. punch displacement graphs for Fabric_3733 (6 oz) at different blank holder forces with 8 mm punch corner radius.

5.3 Press Forming of Fabric-Reinforced Polypropylene

In this section, a numerical study was performed on press forming of fabric-reinforced polypropylene using LS-Dyna and an optimum combination of the simulation parameters was identified which can be successfully utilized to simulate the press forming of fabric-reinforced polypropylene.

The matrix material used in the study is unfilled polypropylene (PP), which has the same material properties as in Chapter 3. The reinforcement material is Fabric_3733 (6 oz) E-glass fabric. Material properties of the fabric material are provided in Table 5.2. The total thickness of the fabric-reinforce PP blank was 1 mm. The punch velocity was 100 mm/s. The friction coefficient between the die-punch material (which is aluminum) and the fabric-reinforced PP were the same as that used in the numerical study of press forming of PP (Figure 3.8). This value was selected based on the initial temperature of the fabric-reinforced PP blank. All numerical studies were carried out at isothermal conditions, assuming that the blank remained at a constant temperature of 100°C and there was no heat loss due to thermal conduction from the fabric-reinforced PP blank to the die or the punch. The thermal conductivity of E-glass fibers was taken to be 0.05 W/m.°K [5] and the heat capacity of E-glass fibers is 810 J/kg.°K.

The finite element model of die-punch set up in this study was the same as shown in Figure 5.14. A flat-bottomed punch with a corner radius of 15 mm was selected. A blank holder force of 800 N (i.e., 200 N for the quarter model) was applied on the blank to avoid wrinkle formation at very low draw depths due to yarn buckling at the intersection of the flanges as was observed in press forming experiments with dry fabrics at lower blank holder forces.

The modeling approach for fabric-reinforced PP involves a prepreg sheet of a 0.077 mm (Fabric_3733) fabric layer embedded in the PP matrix on its top and bottom (Figure 5.56). The

total thickness of the prepreg was 1 mm. The fabric and PP layers were superimposed on one another and the duplicate nodes arising due to superimposition were merged into single common nodes. The fabric was assigned under-integrated membrane elements of MAT_234 and the PP layers were assigned fully integrated shell elements of MAT_106. The total stress obtained during the deformation is the sum of the stress required for forming of fabric material and the stress for forming of PP layers. The superimposed PP layers account for out-of-plane bending stiffness.

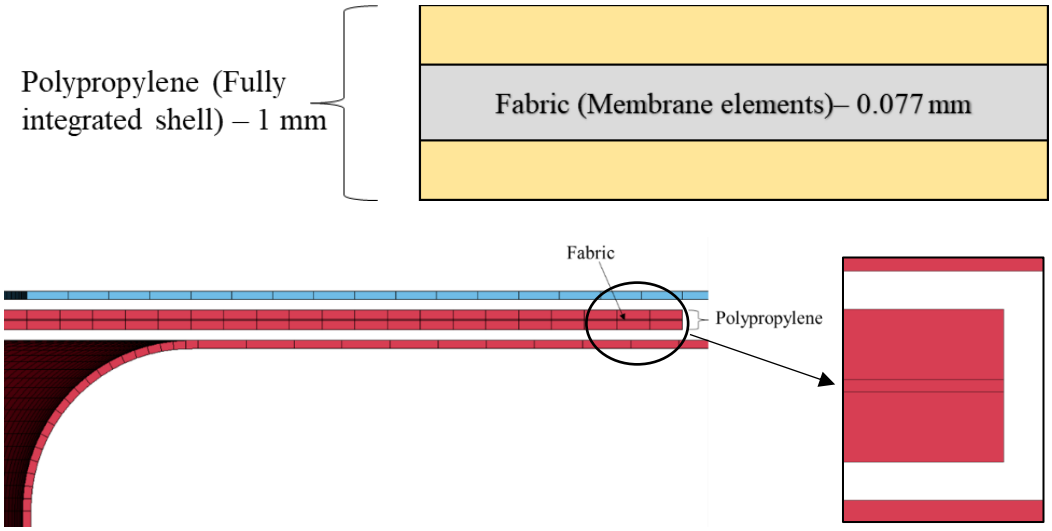

Figure 5.56: Modeling approach for fabric-reinforced PP.

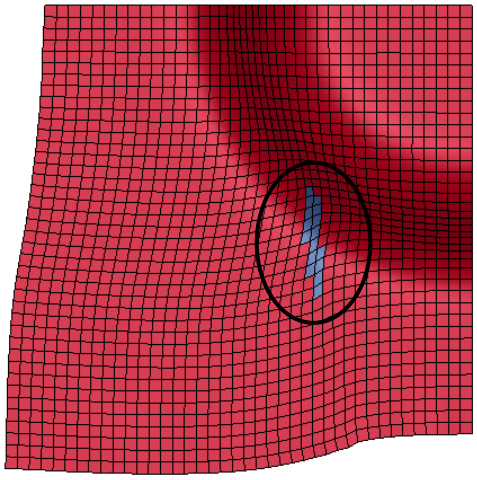

Figure 5.57: Failure locations as predicted by prepreg (superimposed approach of fabric and PP) approach for press forming of fabric-reinforced PP composite.

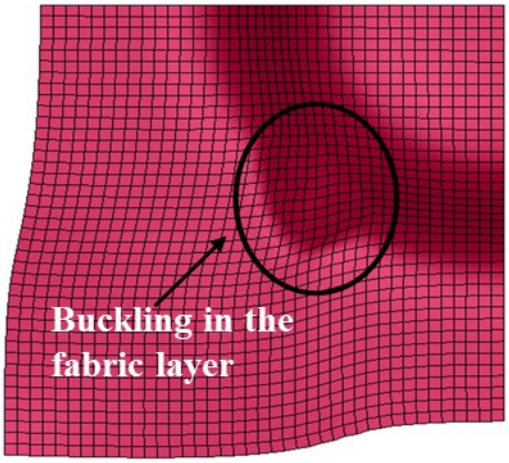

Figure 5.58: Buckling of fabric layer at the top corner radius after failure in the PP layer.

The numerical studies on fabric-reinforced PP forming with preperg approach showed the failure location at the top corner radius where the plastic strain in PP layer exceeded the failure strain of PP. This is shown in Figure 5.57. The fabric exhibits buckling behavior after failure was observed in the PP layer. Buckling observed in the fabric after failure in the PP at the top corner radius is shown in Figure 5.58.

5.3.1 Effect of Forming Temperature

5.3.1.1 Press Forming with 15 mm Punch Radius

The prepreg method was used in this section to study the press forming of fabric-reinforced PP at different forming temperatures, namely 25, 75, 100, 125 and 150°C. The blank thickness was 1 mm, and the blank holder force was 800 N (i.e., 200 N for the quarter model). Table 5.4 shows the draw depths attained by the fabric-reinforced PP and the single layer PP blank at various forming temperatures. It can be observed in this table that the draw depth for both materials increased with increasing forming temperature, primarily due to the increase in failure strain of

PP. Finite elements were carried out for other fabrics; Fabric_1610 and Fabric_1522 at 125°C to study the effect of the fabric weight on the draw depth.

Table 5.4: Draw depth attained at various forming temperatures for a blank thickness of 1 mm and a blank holder force of 800 N (punch corner radius = 15 mm).

Forming Temperature	Draw depth (mm)			
	Single layer PP	Fabric_3733	Fabric_1610	Fabric_1522
25°C	19.10	17.56		
75°C	23.11	18.5	*	
100°C	26.63	19.11		
125°C	29.15	19.63	20.09	20.14
150°C	30.00 (failure in cup wall)	21.55	*	*

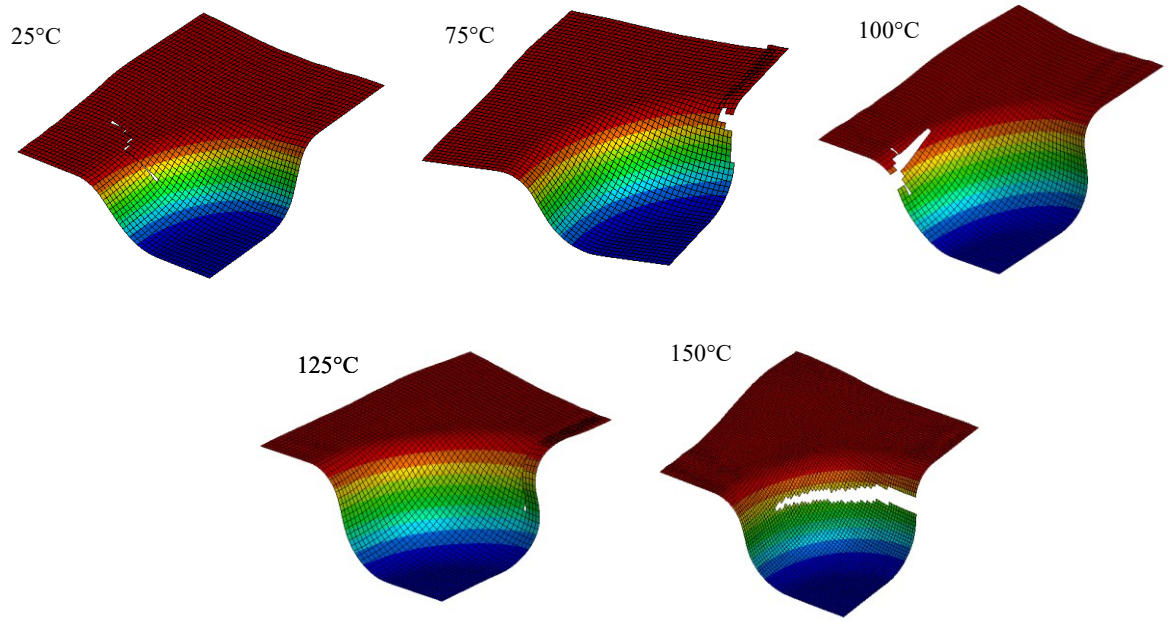

Figure 5.59: Failure locations of the deep drawn PP cups at different forming temperatures.

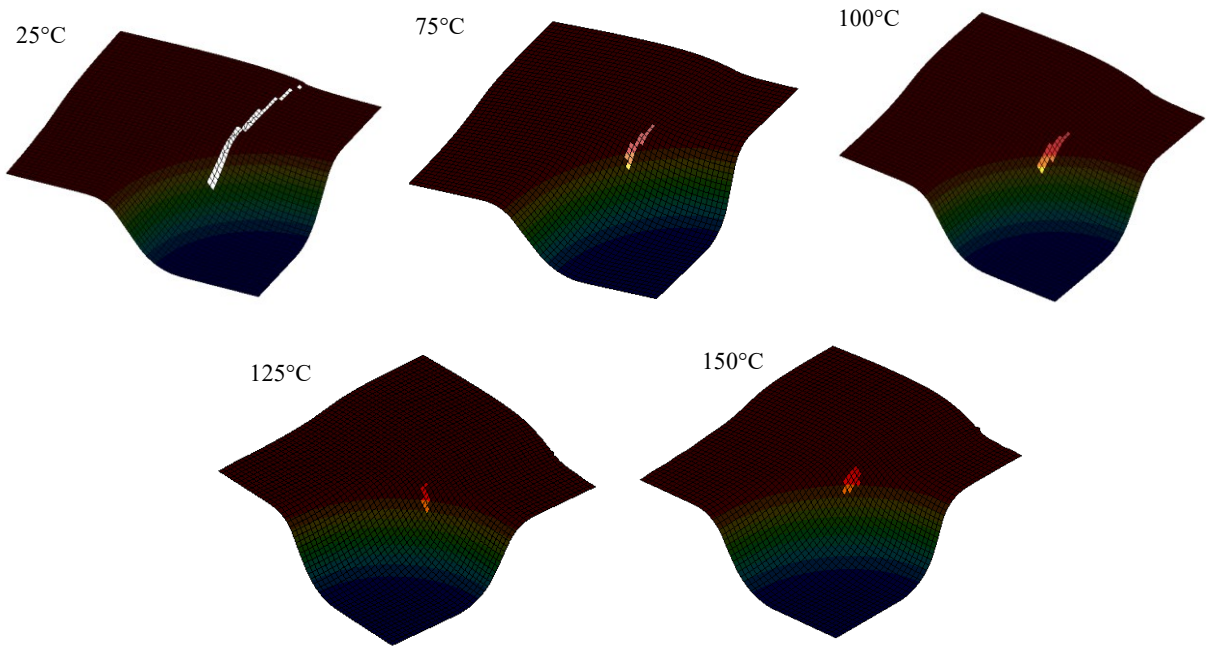

Figure 5.60: Failure locations of the deep drawn fabric-reinforced PP cups at different forming temperatures.

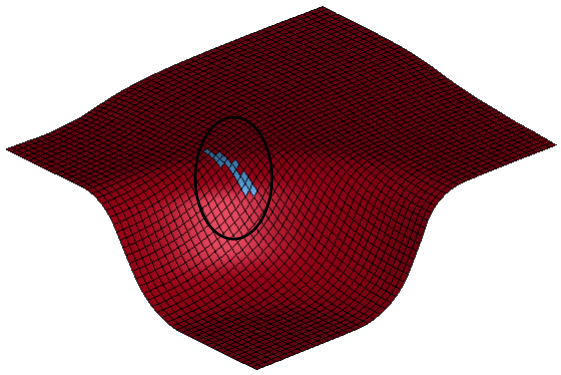

Figure 5.61: Failure locations of the deep drawn fabric-reinforced PP (Fabric_1610) cups at different forming temperatures.

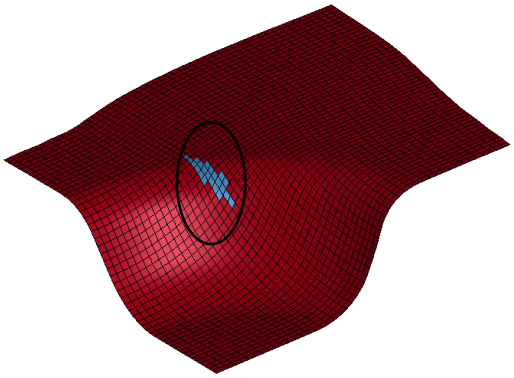

Figure 5.62: Failure locations of the deep drawn fabric-reinforced PP (Fabric_1522) cups at different forming temperatures.

From Table 5.4, it can be seen that the draw depth for press forming of single PP increases with increasing forming temperature, while for superimposed model of fabric and PP the draw depth attained before failure does not show any major variation. Failure in the single layer PP was observed at the die entry radius as shown in the Figure 5.59 for all temperatures except for press formed part at 150°C for which failure was observed along the cup wall. At 25°C, failure can be attributed to wrinkling along the flange area, and for 75, 100 and 125°C, failure was observed when the plastic strain at the top corner radius exceeded the failure strain.

The draw depth attained before failure during press forming of fabric-reinforced PP did not show much variation as can be seen from Table 5.4. Failure was observed in the PP layer when the plastic strain exceeded the failure strain, as shown in Figures 5.60-5.62. Small difference in the draw depth for drawn cups can be attributed to the difference in the failure strain at different temperatures, which increases with increase in temperature. Failure for all the cups was observed at the top corner radius where the shear deformation is maximum in the fabric layer irrespective of temperature or the fabric size. Due to the shear deformation in the fabric layer, PP layer undergoes compressive stress and failure occurs in the PP layer at top corner radius. The wrinkles that are formed due to shear locking are shape dependent and process parameters independent, and hence the reason for almost the same draw depth for fabric-reinforced PP irrespective of temperature or fabric type.

5.3.1.2 Press Forming with 8 mm Punch Radius

Table 5.5 gives the draw depths attained before failure for single layer PP and fabric-reinforced PP prepreg sheet, each with 1 mm thickness. The blank holder force was 800 N.

Table 5.5: Draw depth attained at various forming temperatures for a blank thickness of 1 mm and a blank holder force of 800 N (punch corner radius = 8 mm).

Forming Temperature	Draw depth (mm)	
	Single layer PP	Prepreg method (Superimposed model)
100°C	22.03	16.04
125°C	26.50	16.08

From Table 5.5, the draw depth attained before failure using the single layer PP showed a decrease in their values compared to the draw depth attained with 15 mm punch corner radius, indicating that with the decrease in the punch corner radius the draw depth attained decreased. For fabric-reinforced PP drawn cups, the draw depth was observed to be same irrespective of the blank temperature. Failure was observed when the shear deformation in the drawn cup reaches shear locking angle in the fabric layer which creates compressive stresses in the PP layer thus leading to failure. After the failure of the PP, buckling was observed in the fabric layer leading to ultimate failure of the composite.

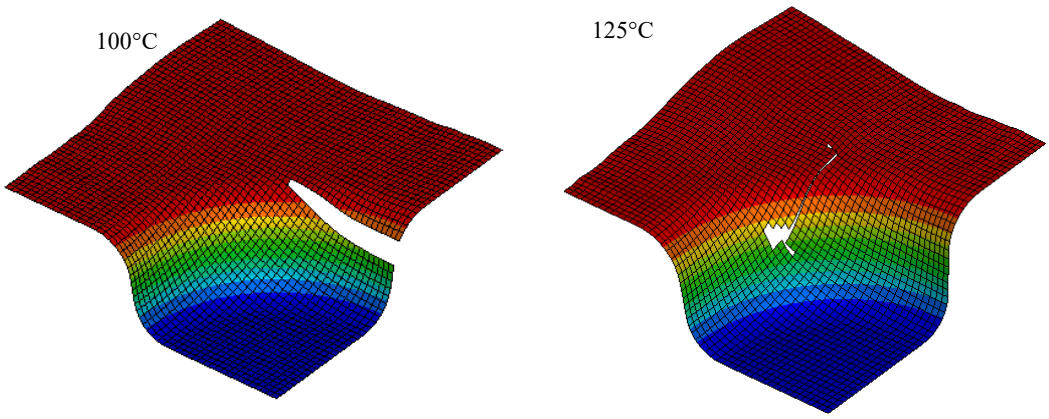

Figure 5.63: Failure location of the deep drawn PP cups at different temperatures using a punch corner radius of 8 mm.

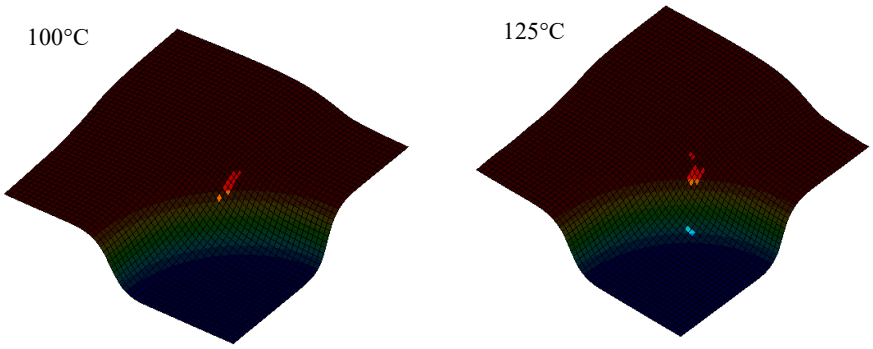

Figure 5.64: Failure location of the deep drawn composite cups at different temperatures using a punch corner radius of 8 mm.

Failure locations for the drawn cup with single layer PP and superimposed model of fabric-reinforced PP are shown in Figure 5.63 and 5.64, respectively. Figure 5.65 denotes the shape of the drawn cup at draw depth just after failure with individual layer, i.e. . PP and fabric layers. Fabric layer buckles as soon the plastic strain in the PP exceeds the failure strain.

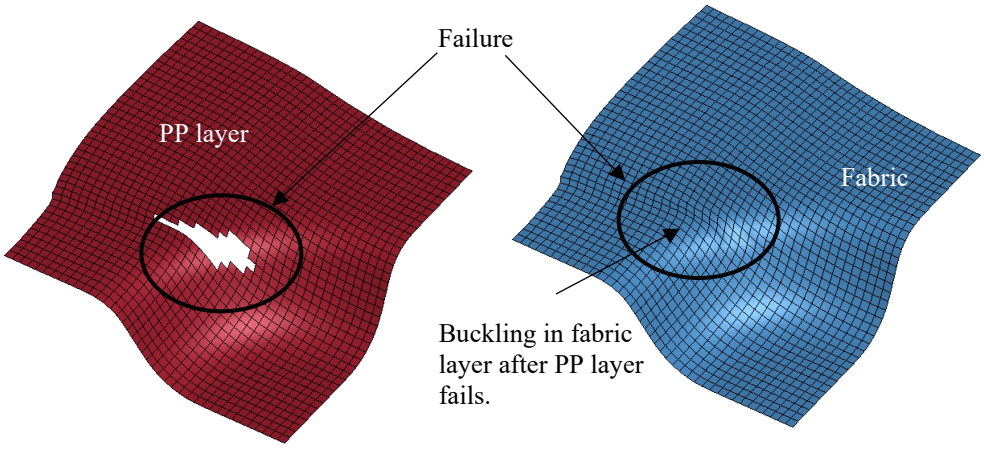

Figure 5.65: Failure location in the individual layers of fabric and PP for press forming of fabric-reinforced PP.

5.4 Conclusions

The following conclusions are made from the study of press forming of fabrics and fabric-reinforced PP. The fabrics exhibit stiffer behavior with increase in the areal density of the fabrics and the value of the tensile modulus assigned to the shell elements to replicate the uniaxial bias-

extension behavior for E-glass fabrics is very low (less than 0.001% of the fabric modulus). For press forming of dry fabrics, finite element simulations with superimposed approach (i.e., superimposition of membrane and shell elements) are able to closely predict the outer shape profile at different displacements during press forming and predicts reasonably accurately the force required for fabric deformation.

Press forming simulations of the fabric-reinforced PP using the superimposed method in which the fabric is assigned to membrane elements and matrix PP is assigned to the shell elements so that it replicates the prepreg structure are presented. Press forming with single PP shows an increase in the draw depth with increase in the forming temperature and decrease in the draw depth with decreasing punch corner radius, while the fabric-reinforced PP failed at almost similar draw depths with first failure observed in PP layer. The failure in the PP was observed when compressive strains in that particular layer exceeded the failure strain, the compressive strains are created due to the shear locking exhibited by the fabric. The maximum shear deformation was observed along the diagonal at the die entry radius and the same was the location of failure observed in the PP layer. Fabric layer exhibits buckling tendency after failure is initiated in the PP matrix layer.

5.5 References

[1] "https://www.fibreglast.com/category/Fiberglass_Fabric," Fiberglast, [Online]. Available: https://www.fibreglast.com/category/Fiberglass_Fabric. [Accessed 05 March 2022].

[2] I. Taha, Y. Abdin and S. Ebeid, "Comparison of picture frame and bias-extension tests for the characterization of shear behaviour in natural fibre woven fabrics," *Fibers and Polymers,* vol. 14, no. 2, pp. 338-344, 2013.

[3] H. Yildirim and F. Ozturk, "A benchmark study of the material models for forming simulation of woven fabrics," *Journal of the Textile Institute,* pp. 1-12, 2021.

[4] X. Peng and F. Ding, "Validation of a non-orhtogonal constitutive model for woven composite fabrics via hemispherical stamping simulation," *Composite Part A: Applied Science and Manufacturing,* vol. 42, no. 4, pp. 400-407, 2011.

[5] S.-J. Park and M.-K. Seo, "Chapter 6 - Element and processing," in *Interface Science and Technology*, vol. 18, 2011, pp. 431-499.

Chapter 6 Conclusions

6.1 Conclusions

This dissertation presents the numerical modeling approaches to study press forming and press formability characteristics of polypropylene, dry E-glass fabrics, and E-glass fabric-reinforced polypropylene under various material and process parameter conditions and material variables. Polypropylene and E-glass fabrics were selected as the thermoplastic polymer matrix and reinforcement materials based on their applicability in high-volume production composite parts, such as in the automotive industry. A safe press forming window for the fabrics, determined by their ability to form the shape and retain it without defects such as fiber distortion, wrinkling and fracture, is presented.

Press forming of polypropylene was studied using a cup deep drawing process at temperatures much lower than its melting temperature. The influence of several different processes and cup design conditions on the depth of draw attained before failure was determined. Both temperature and strain rate dependency of polypropylene at the deep drawing conditions was taken into account. The failure modes observed in the deep-drawn cups were flange wrinkling and cup wall tearing near the top as well as the bottom cup corners. Blank holder force, initial blank temperature, die corner radius and punch speed showed the greatest influence on the press formability of polypropylene.

To study the deformation characteristics of dry fabrics, superimposed finite element modeling approach was utilized. In this approach, membrane elements for in-plane shear

deformation and shell elements for out-of-plane bending deformation are superimposed on one another and tied at their common nodes are utilized to study the fabric deformation characteristics needed for preforming fabric shapes. The superimposed modeling approach is used to study fabric deformation characteristics under shear-tension coupling in biaxial bias-extension tests of square fabric specimens with $\pm 45^{o}$ warp and weft orientations. It is shown that the stiffness of the fabric increases with the increase in the applied biaxial tensile loads. An important test parameter of this test is found to be the clamping arrangement, since the percentage area of the pure shear deformation zone increases with increase in the clamping ratio; however, it does not depend much on the fabric specimen size provided that the clamping ratio is kept the same. Also, the displacement at which the shear locking occurs changes with clamping ratio and fabric size.

During press forming of fabrics, wrinkling and tearing defects are observed in the formed part. Wrinkles can form due to yarn buckling, shear locking or draping with a punch having sharp corner radius. Tearing of the fabric occurs with higher blank holder force or draping with a punch having a sharp corner radius. Safe forming window determines the limits of the press forming operation, which is determined by the ability to form the shape and retain it without defects such as fiber distortion, wrinkling and fracture. With an increase in the blank holder force, the safe forming window increases initially attributed to the reduction in wrinkles formed due to yarn buckling which later reduces due to the tearing defects observed at higher blank holder forces. Wrinkles that form due to shear locking occurs at the same draw depth irrespective of the blank holder force and are dependent on the shape to which it is conformed to. The shape to which the fabric is being conformed to plays an important role on the forming limit of the fabric.

A comparison of the simulation and experimental press forming of E-glass fabrics shows that the superimposed model is able to reasonably accurately predict the outer shape profile and

forces required for the fabric deformation during press forming. The force required for the fabric deformation increases with increasing blank holder force and areal density of the fabric and decreases with increasing punch corner radius.

A numerical modeling approach for forming of a fabric-reinforced polypropylene prepreg is presented. This model utilizes the superimposed approach in which the membrane elements are assigned to the fabric and shell elements are assigned to the thermoplastic polymer. The press forming at different temperatures of the prepreg shows almost similar limiting draw depth with failure observed in the polypropylene layer at the location of the maximum shear deformation in the fabric layer. The fabric layer exhibits buckling tendency after failure occurs in the polypropylene layer.

6.2 Intellectual Merit and Broader Impact

The superimposed finite element modeling approach utilized in this dissertation can reasonably accurately predict the outer shape profile and the forces required for fabric deformation during the press forming of dry fabrics. This method of superimposition to capture different behavior is more computationally efficient and requires lesser calibration of the material parameters compared to the other methods mentioned in the previously published literature.

The safe forming window for fabrics predicts the forming limit of fabrics for draping with a punch having a particular corner radius. It can determine the minimum blank holder force required to press from the fabric up to the required draw depth without producing wrinkles and tearing in the fabric. This forming limit curve can serve as a guideline for forming a particular fabric in the composite industry.

6.3 Scope for Future Work

The press forming of polypropylene under non-isothermal conditions was presented in this dissertation. Based on the published literature, it was observed that the cup draw depth attained before failure increases for different heating conditions such as isothermal heating (i.e., dies and blank maintained at warm forming temperatures) and differential heating conditions (with dies at warm forming temperature and blank at room temperature). Numerical simulations and experimental work using isothermal and differential heating conditions should be performed to successfully press form polypropylene and other thermoplastic polymers to greater draw depths without any defects.

Press forming for dry fabrics with different fabric orientations (i.e., the yarns oriented at angles other than 0/90) can be performed to determine the optimum orientation at which the maximum draw depth can be attained without any defects and with no or small flange formations. Also, experimental and numerical studies can be performed with different fabric blank shapes, such as circular shapes, to check if the use of such shapes yields fewer earing defects that occur in the flange area. Such an exercise will require preprocessing the fabric; however, the post-processing can be avoided after press forming the part.

The concept of forming limit diagram or forming window can be further explored to determine the process and material parameters that should be selected to not only press form fabric preforms, but also fabric-reinforced thermoplastics with fewer defects. This can be initially done using experiments, but analytical relationships can also be developed to predict the forming limits of different fabrics and related composites.

Another area of future research is the experimental validation of press-forming of fabric-reinforced thermoplastics to check the validity of the superimposed finite element modeling

approach utilized in this study. The effects of prepreg consolidation, prepreg thickness, die/punch design and processing conditions, such as blank temperature and punch speed can be included in such a study.

Appendix A Input Parameters of Viscoelastic Loose Fabric Model (MAT_234) in LS-Dyna

A.1 Geometric Properties of Fabric

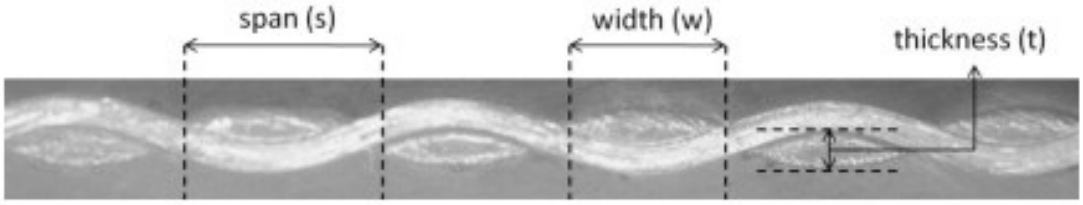

Figure A.1: Micrograph of plain weave fabric showing geometric properties of fabric [1].

a. Yarn width (*w*): This value is determined experimentally in a stress-free, un-deformed state, preparing a cross-section of the sample and measuring geometry of the un-deformed yarns with a microscope. It represents the average width of the warp and fill yarns.

b. Span between fibers (*s*): This value is determined by considering the geometry of the un-deformed fabric with microscope.

c. Real yarn thickness (*T*): This value represents the fabric thickness.

d. Effective yarn thickness (*H*)*:* This value is defined in the LS-Dyna material model as the quotient of the areal density to the mass density.

e. Yarn cross-sectional area (*S*): It can be approximately calculated as:

$$Yarn\ mass = \frac{Areal\ density}{Total\ yarn\ count} \quad \text{(Eq. A.1)}$$

$$Yarn\ volume = \frac{Yarn\ mass}{Mass\ density} \quad \text{(Eq. A.2)}$$

$$Yarn\ cross\ sectional\ area = \frac{Yarn\ volume}{Yarn\ length} \quad \text{(Eq. A.3)}$$

A.2 Material Properties

a. Longitudinal Young's modulus (E_1): The value can be determined from the static tensile test carried out for yarns in the fabric. This value is assumed to be equal to the Young's modulus of the fiber.

b. Transverse Young's modulus (E_2): Fein et al. [2] states that it is not possible to characterize transverse Young's modulus experimentally and approximates it to a value corresponding to approximately 11% of the longitudinal Young's modulus.

c. Longitudinal shear modulus (G_{12}): This parameter can be determined by performing an experimental test by measuring the torsional response of a mass suspended from a known length of the yarn.

d. Transverse shear modulus (G_{23}): This value can be approximated to be the same value as the longitudinal shear modulus.

e. Ultimate strain at failure (E_U): This value is to be determined experimentally. It represents the strain at peak stress for a single yarn specimen from the woven fabric. A notable characteristic of woven fabrics is crimping in yarns. Studies by Shim et al. [3] showed that the areal density reduces by 3% if the yarns are fully straightened. The authors found that the straightening of yarns accounts for up to 1.5% of the total strain. Figure A.2 shows the stress-strain behavior for Twaron fabric for which the initial slack of 1.5% corresponds to straightening of the crimped yarns. They gave a quantitative relation between actual, total and crimp stain of the form

$$\varepsilon_{actual} = \varepsilon_{total} - \varepsilon_{crimp} \left[1 - exp\left(-\frac{\varepsilon_{total}}{\varepsilon_{crimp}}\right) \right] \qquad \text{(Eq. A.4)}$$

where ε_{crimp} is the maximum strain attributable to crimp.

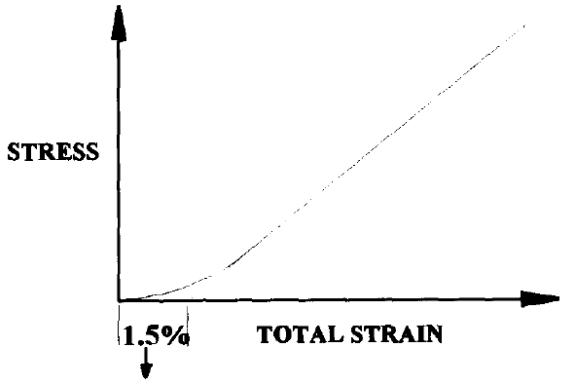

Figure A.2: Schematic stress-strain curve for Twaron fabric (1.5% represents initial slack due to straightening of crimped yarns) [3].

f. Yarn locking angle (*THL*): Can be obtained using the relationship mentioned in Ref. [4]. To determine the yarn locking angle, it requires the geometric parameters such as span and width of the fabrics.

g. Initial braid angle (*THI*): The initial braid angle of the material is half of the total angle between warp and fill direction in the un-deformed state. Because the fill and warp yarns are initially orthogonal, the value of *THI* can be set to 45°.

h. Transition angle to locking (*TA*): The transition angle to locking provides a small angle through which the locking mechanism between the yarns can take effect. The value of *TA* is set at 1°-3° based on observation by Ala Tabiei et al. [5] and Shim et al [3].

i. Elastic constant of element '*a*' (*EKA*): If the effect of viscoelasticity can be ignored for press forming operation of fabrics considering quasi-static analysis due to the high punch velocity then the equation can be written

$$(K_a + K_b)\sigma = K_a K_b \varepsilon \qquad \text{(Eq. A.5)}$$

Assuming K_a, K_b of the phenomenological material model (Figure 2.22) to be equal then

$$K_a = K_b = 2E_1 \qquad \text{(Eq. A.6)}$$

Studies by Shim et al. [3] recommended the reference value as $K_a = 2\,E_1$.

If the effects of the viscoelasticity cannot be ignored, then the method defined by Fein et al. [2] has to be used to determine the values of K_a and μ_b. Fein et al. [2] used the Cowper-Symonds model to generate the modulus values of the fabric yarn under consideration for different strain rate values and a response curve for fabric yarn was generated. Values of elastic constant K_a and damping coefficient of element *b* (*VMB*) can be obtained by curve fitting the response curve evaluated at typical strain rates. By varying the strain increment as 0.001 and varying strain rates, the value of K_a and $\mu_b$can be selected such that the resulting curve closely resembles the curve.

j. Damping co-efficient of element *'b'* (*VMB*): As stated, the value can be obtained by curve fitting the stress-strain curves of fibers at different strain rates. The value can also be taken as zero for press forming operation ignoring the viscoelasticity effect due to high punch velocity.

k. Co-efficient of friction between fibers (*C*): For impact loads changing the friction factor can change the number of yarns taking the impact load and yarn slip. For press forming operations, this value can be taken as 0.1 [4, 5]. Yildirim et al. [6] and Fang et al. [7] made an approximation for the value using the reverse analysis. They estimated the value of the yarn-yarn interaction to be 0.41. Rajan et al. [8] though their studies of fabric-to-fabric friction testing measured the coefficient of friction between the fabric yarns as 0.2. This values can be utilized in case of modeling multiple layers of fabric with frictional contact between the layers.

l. Elastic constant of element '*b*' (*EKB*)*:* Its value can be obtained using the relation specified in Item i above.

A.3 References

[1] G. Nilakantan, M. Keefe, J. W. Gillespie Jr, T. A. Bogetti and R. Adkinson, "A study of material and architectural effects on the impact response of 2D and 3D dry textile composites using LS-Dyna," in *7th European LS_DYNA Conference*, Salzburg, Austria, May 14-15, 2009.

[2] J. Fein, "Improvements in numerical modeling methodology of dry woven fabrics for aircraft engine containment system," MS Thesis, Arizona State University, 2012.

[3] V. P. W. Shim, V. B. Tan and T. E. Tay, "Modelling deformation and damage characteristics of woven fabric under small projectile impact," *International Journal of Impact Engineering,* vol. 16, no. 4, pp. 585-605, 1995.

[4] I. Ivanov and A. Tabiei, "Loosely woven fabric model with viscoelastic crimped fibers for ballastic impact simulations," *International Journal for Numerical Methods in Engineering,* vol. 61, no. 10, pp. 1565-1583, 2004.

[5] A. Tabiei and R. Murugesan, "Thermal structural forming simulation of carbon and glass reinforced plastics composites," *International Journal of Composite Materials,* vol. 5, no. 6, pp. 182-194, 2015.

[6] H. Yildirim and F. Ozturk, "A benchmark study of the material models for fomring simulation of woven fabrics," *Journal of the Textile Institute,* vol. 113, no. 6, pp. 1027-1038, 2022.

[7] H. Fang, E. Palta and M. Gutowski, "Numerical simulation of high-speed impacts involving metallic and non-metallic materials," *International Journal of Computational Methods and Experimental Measurements,* vol. 6, no. 3, pp. 463-475, 2018.

[8] S. D. Rajan, B. Mobasher, Z. Stahlecker, S. Bansal, D. Zhu, M. Morea and K. Dhandapani, "Explicit finite element modeling of multilayer composite fabric for fas turbine engine containment systems, Phase III," U.S. Department of Transportation, Federal Aviation Administration, Washington DC, 2011.